3-24-2016

Methods for Passive Remote Turbulence Characterization in the Planetary Boundary Layer

Lee R. Burchett

METHODS FOR PASSIVE REMOTE TURBULENCE CHARACTERIZATION IN THE PLANETARY BOUNDARY LAYER

DISSERTATION

Lee Robert Burchett

AFIT-ENP-DS-16-M-058

DEPARTMENT OF THE AIR FORCE
AIR UNIVERSITY

AIR FORCE INSTITUTE OF TECHNOLOGY

Wright-Patterson Air Force Base, Ohio

AFIT-ENP-DS-16-M-058

METHODS FOR PASSIVE REMOTE TURBULENCE CHARACTERIZATION IN THE PLANETARY BOUNDARY LAYER

DISSERTATION

Presented to the Faculty

Graduate School of Engineering and Management

Air Force Institute of Technology

Air University

Air Education and Training Command

in Partial Fulfillment of the Requirements for the

Degree of Degree of Doctor of Philosophy

Lee Robert Burchett, B.S.P.*c.l.*, M.S.P.

24 March 2016

AFIT-ENP-DS-16-M-058

METHODS FOR PASSIVE REMOTE TURBULENCE CHARACTERIZATION IN THE PLANETARY BOUNDARY LAYER

DISSERTATION

Lee Robert Burchett, B.S.P.*c.l.*, M.S.P.

Committee Membership:

Dr. S. T. Fiorino
Chairman

Dr. M. Temple
Member

Lt.Col R. Wacker, PhD
Member

Dr. M. Oxley
Dean's Representative

Abstract

This work presents several new methods for measurement of turbulence in the Planetary Boundary Layer (PBL). These methods use data from WSR 88-D Next-Generation Radar (NEXRAD) weather radars, Numerical Weather Prediction (NWP) forecasts, and cell phone scintillation in order to estimate C_n^2, a common scalar measure of PBL turbulence, as measured by a visible light or Infra-Red (IR) system. The methods presented here can estimate C_n^2 from NWP alone, or NWP can be combined with NEXRAD or cell signals (RF instruments) to remotely and passively estimate C_n^2 with high spatial and temporal resolution. Previously, no method was known for accurately estimating the effects of turbulence on visible and IR systems based on measurements from RF instruments.

In order to show how well these new approaches perform in comparison to existing techniques, estimates of C_n^2 are made using the various methods and are compared with measurements taken using standard $880nm$ large aperture scintillometers. Comparisons are made in every month of the year in two environments: temperate suburban, and high-mountain desert. Results show consistent improvement of accuracy by the newer methods over existing estimation methods. The results also suggest removing the common assumption that visible and IR C_n^2 can be estimated from temperature field perturbations alone. Instead, water content and non-hydrostatic pressure perturbations should be included when estimating C_n^2.

A survey of noise and uncertainty is also presented. This analysis of different noise sources in the radar, cell phone, and NWP data is of practical utility as it outlines limits of applicability, and performance that can be expected for each method under a variety of conditions.

To Sara

Acknowledgements

For sustaining me and my family through this work and providing the many people who have made this work possible, I give thanks to the LORD my God. This document and research has been at times exciting, frustrating, and always humbling. I cannot imagine how it could have been completed without the many sacrifices and patient understanding of my wife. Thank you.

I also would like to thank Dr. Fiorino for his persistent guidance and support during my Masters and PhD research. I thank Dr. Terzuoli for originally bringing me to AFIT as an undergraduate student researcher and providing many research projects to work on as a student researcher. Thank you to my committee members, Dr. Temple and Lt Col Wacker for your help along the way. While I will refrain from listing them all by name, the AFIT faculty and staff have helped me enormously, and I am grateful to have been able to work with and learn from them.

For support of this work, I would like the thank the AFIT Engineering Physics Department, the Center for Directed Energy and Air Force Office of Scientific Research. For their support of my research position under Dr. Terzouli, which provided good work and useful experience, I would like to thank the Wright-Patterson Multi-Intelligence Development Consortium, the Air Force Research Laboratory, and the National Air and Space Intelligence Command.

Lee Robert Burchett

Table of Contents

Page

List of Figures

Figure Page

List of Tables

List of Symbols

List of Abbreviations

Abbreviation		Page
CFL	Courant-Friedrichs-Levy	78
GFS	Global Forecast System	78
RAP	Rapid Refresh	80
VCP	Volume Coverage Pattern	86
NOAA	National Oceanic and Atmospheric Administration	86
TRMM	Tropical Rainfall Measurement Mission	86
RSL	Radar Science Library	86
OS	Operating System	93
CDMA	Code Division Multiple Access	95
GPS	Global Positioning System	96
RAOB	RAwindsonde OBservation	112
AFIT	Air Force Institute of Technology	210

METHODS FOR PASSIVE REMOTE TURBULENCE CHARACTERIZATION IN THE PLANETARY BOUNDARY LAYER

I. Introduction & Background

This dissertation presents and compares several methods for measuring turbulence in the atmosphere. This research was motivated by a need to characterize the PBL with respect to its impact on visible-light and IR systems. Turbulence in the PBL limits the capabilities of free-space optical communications, imaging, and High-Energy Laser (HEL) systems. The impact of turbulence on these systems is commonly characterized by the so-called *index of refraction structure function constant*, C_n^2. Larger values of C_n^2 indicate worse propagation conditions for these systems.

For several reasons, it would be desirable to be able to measure C_n^2 within a region of operation. As a part of product development, systems will be tested in a variety of environments, and knowing C_n^2 allows a system's performance to be evaluated for validation. For HEL systems, there is also an operational need for real-time turbulence measurement. While HEL systems measure the impact of turbulence just before firing. It only does so on the path to each target (often assumed to be a high-speed vehicle, like a missile). In the case where a HEL is best suited, engaging several inbound high-velocity targets at once, a wide-area volumetric measure of C_n^2 would allow for a fire control system to prioritize targets to assure the highest probability of successful engagement.

Available C_n^2 measurement methods do not provide adequate tools to meet these needs. Systems with sufficient accuracy and resolution are limited by cumbersome instrumentation. Methods which allow for sufficiently large volume measurements

are limited to very coarse resolutions, or poor accuracy. The techniques presented here are the first which simultaneously provide the accuracy, resolution, and volume sufficient to be of practical use for product validation in the PBL, or as the basis for a HEL fire-control system.

New techniques adapted from existing research, and physical interpretations of turbulent eddy structure will be compared against conventional methods. This first chapter reviews past research and literature which has been an immense help in developing this subject. The first three sections of the chapter will present an introduction of contemporary turbulence theory, and practical motivation for turbulence research. Following this will be an overview of some of the most common methods for characterizing turbulence. This is followed by a section describing what new techniques are being presented. Finally, the remaining sections present a short primer on NWP, NEXRAD radar, and cell phone signals.

The next chapter will describe in detail both existing and novel methods and techniques presented here, as well as metrics for comparing their performance to more contemporary techniques. Following this is a chapter describing the sources of uncertainty and noise in both the standard and new methods. The impact of these factors is also presented with the hope of providing a metric for when and where the various techniques are appropriate. The following chapter will present the results of the research, and is organized by technique. The final chapter presents a summary of conclusions, and suggestions for follow-on research.

1.1 Why Measure C_n^2

There are two sides to the pragmatic motivation for this research: why turbulence detection and measurement is important, and how Radio Frequency (RF) measurements may improve and extend our capability to measure turbulence, even turbulence

which affects optical wavelengths. This section will address why turbulence measurement is important, and the limitations of current methods. A technical motivation for the use of RF is presented in Section 1.5.

A significant driver of this research is the need for a better understanding of PBL turbulence. Our understanding is limited by our inability to adequately measure or predict (model) turbulence in the atmosphere. Current methods are only able to measure a limited volume of the atmosphere. Because they require in-situ instrumentation, there is significant cost in setting up and maintaining measurements in a given area. Practical prediction and modeling methods are computationally limited to resolution of time and space which is much greater than than the scales involved in turbulence. Turbulence studies are important in many disciplines. Turbulence affects the drag on objects as small as a bullet in flight and is a critical to the formative processes of stars. Understanding found in PBL turbulence studies like this one can have impacts in a wide range of other engineering and theoretical endeavors.

Developing the capability to overcome current measurement and modeling limitations have practical utility, beyond satisfying our need to better understand the world around us. We know that PBL turbulence is the primary mechanism for mixing and advection within the PBL. [33] NWP and plume-dispersion models can both be improved if current, wide-area turbulence information is available for inclusion. Furthermore, turbulence is a critical component of the atmosphere and surface interactions which affect our ability to predict weather. Improved measurements of turbulent activity can help improve our ability to model energy and moisture diffusion in the PBL.

Anyone who has flown through turbulent air knows that turbulence can create violent jarring of aircraft in flight. In addition to being unpleasant, this increases stress and wear on the aircraft structure. Both safety, comfort, and system longevity

can be improved by modifying flight paths to avoid turbulence. Adequate real-time turbulence detection could allow aircraft to reroute through smoother air, and has been the subject of research. [3, 18]

In addition to flight concerns, turbulence also has a significant effect on optical systems. These effects include the well known twinkle of starts, limitations on the resolution of large telescopes, data throughput limitations in laser communications systems, and impairment of the effectiveness of high-powered laser weapons [56]. For a given path between two points the ability to predict turbulence-induced scintillation would allow for improved system optimization. A characteristic of turbulence first noted by Taylor [69] is that turbulent eddies evolve slowly when compared to typical rates of advection in the atmosphere. Dubbed the *frozen flow* hypothesis, it predicts that the impact of turbulence in the near-future (on the order of minutes) can be predicted if one knows the current, volumetric state of turbulence in a sufficiently large area, and the direction and magnitude of the mean wind. For example, say turbulence can be predicted in the short term for a transmitter to receiver path in a laser communication system. Communications-encoding schemes could be switched as needed to best suit the propagation conditions. Similarly, a HEL fire control system, tracking a fast moving target would be better able to choose when to fire in order to ensure a high probability of success on every firing. In addition to performance enhancement, improved measurement methods are helpful for testing and evaluation of a system's response to turbulence. In many cases, the methods presented in this work can provide a convenient, cost effective measure of the turbulence present during testing, where measurement or modeling by conventional methods is not available or sufficient.

Knowing that turbulence affects aviation, weather, aerosol dispersion, and optical systems leads to the question: "when and where do we have to cope with turbulence?"

Here at the bottom (lowest $1000m$ or so) of the atmosphere, turbulence is essentially constant. [33,66] Since most of what we humans do occurs in this region, it's apparent that turbulence is around us most of the time. Perhaps it's better said that most of us are working in or near the presence of turbulence all of the time. So PBL turbulence has a persistent and direct impact on the performance of many endeavors.

In order to present additional capabilities that RF can provide for turbulence measurement, it's helpful to understand other ways that we measure turbulence. Turbulence is typically studied using statistical methods which focus on correlation theory and structure functions [12, 32, 67]. Techniques for obtaining structure functions are presented in Section 1.4 and their use is summarized here.

These structure functions describe, in a statistical sense, the spatial and temporal perturbations of a field. In this case, the perturbations are assumed to be due to turbulence. A structure function for a particular field can be computed directly based on functions which describes the field. While these functions are not known, based on statistical arguments, it is assumed that the structure functions have a specific algebraic form. Measurements are used to estimate the structure function constant, C_ϕ^2. Here, ϕ is the functional value of the field. It can be real, complex or of vector field. This process is much the same as statistical approaches used in other disciplines. For example, many processes are assumed to have a probability distribution function (PDF) with a Gaussian form. Data are then sampled (realizations from the true distribution with noise), and the mean and variance of a Gaussian PDF are estimated from the sampled data. This process is analogous the one used for structure functions, where the structure function is like the PDF, the structure function form is like the Gaussian form, and fitting the constant C_ϕ^2 is much like fitting the mean of the assumed form of a Gaussian PDF to the data. While it is true that all approaches here *estimate* C_ϕ^2, use of established techniques will be referred to as *measurement* of

C_ϕ^2, while estimation using new techniques is referred to as *estimation* of C_ϕ^2.

Measurement of structure function constants may be accomplished by using appropriate measurement instruments (often thermal and wind probes) which are distributed over a given area. Similarly, samples may be taken from NWP volumetric grids. Alternatively the structure function constant of the index of refraction C_n^2 can be inferred using a point source or laser scintillometer. This device simplifies turbulence measurement by requiring only a transmitter and receiver to be set up. An example of the scintillometer measurement method is also outlined in Section 1.4 and further details are available from scintillometer manufacturers [62]. It is also possible to convert between related structure function constants, like temperature, C_T^2, and index of refraction, C_n^2.

1.2 Turbulence and Structure Functions

Fluid flows can be categorized as either laminar or turbulent. Turbulent flows are chaotic in nature and are characterized by swirls of varying size and shape (Figure 1). These whorls make up a complex but identifiable structure. In the short term, it is possible to predict the evolution of the flow. However, as with other chaotic processes, as time goes on predictions become more and more likely to be invalid.

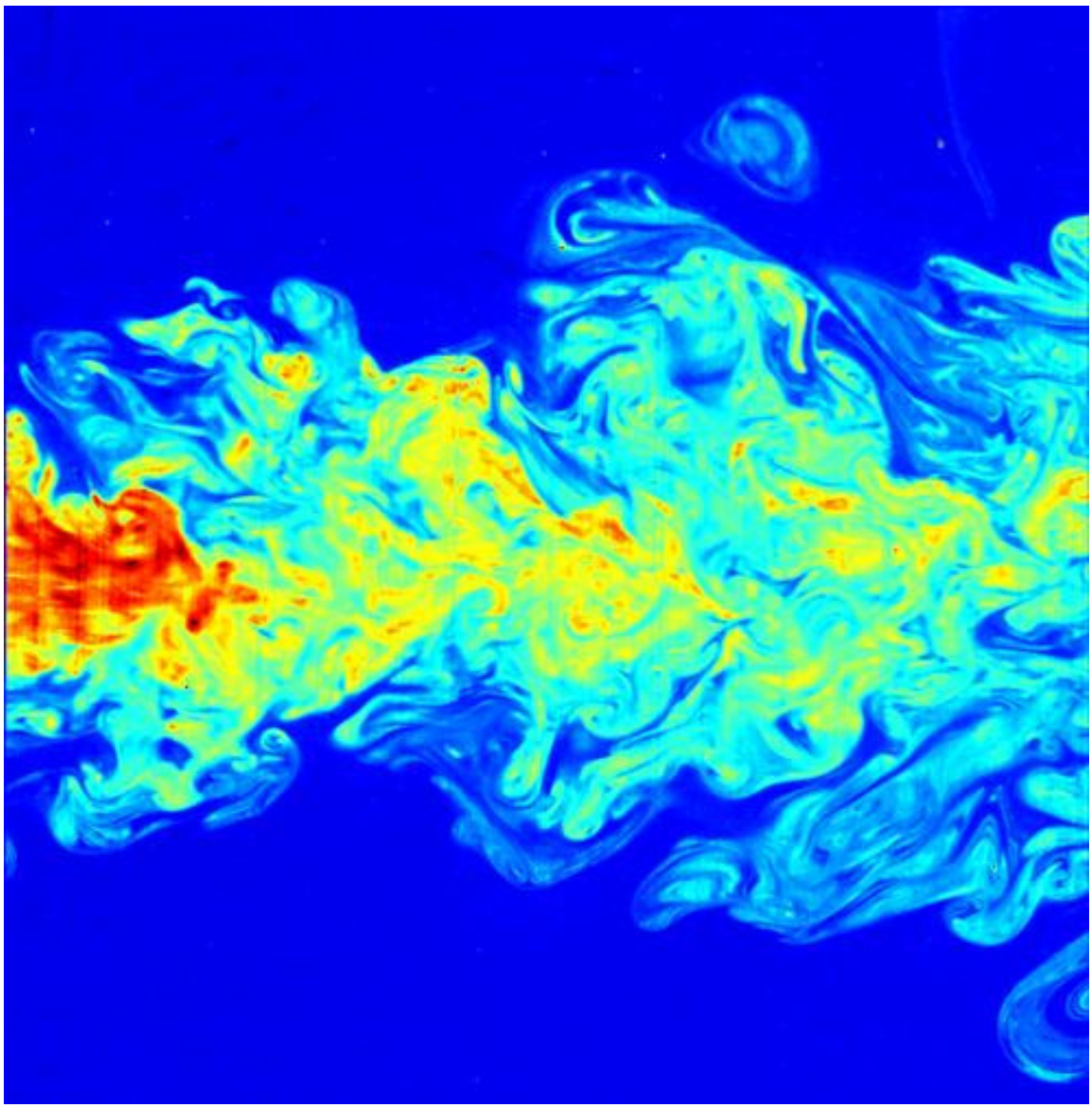

Figure 1. False color image of turbulence induced by a submerged jet made visible by laser induced fluorescence. The image is owned by C. Fukushima and J. Westerweel, Technical University of Delft, The Netherlands, and is used without permission or endorsement of this work under the Creative Commons license.

The PBL is the lowest part of the troposphere, the layer which contains most of the mass of the atmosphere. It is characterized by air that is generally well-mixed due to turbulent motions. The depth of the layer varies from a few meters to well over a

kilometer [57]. The dynamical variations are closely tied to the turbulence measurements investigated here, and will be discussed in the next section. One direct impact that this layer has on modern technologies is the disturbance of EM propagation by turbulence [32, 68]. These disturbances are usually a hindrance to achieving "good" propagation, and degrade system performance [12, 14, 39, 76, 77]. The primary reason why turbulent flows disturb EM propagation is that they create a complex spatial and temporal structure of the index of refraction, n. A measure of how much one can expect n to vary over a given distance is C_n^2. Generally, the larger C_n^2, the greater the impact that turbulence has on system performance.

Throughout this dissertation, turbulence will be characterized by the value C_n^2. C_n^2 is *the structure function constant for the index of refraction structure function.* In practice, this term is used as a scalar measure of how turbulent an atmospheric flow is. As mentioned in Section 1.1, this parameter is based on fitting measured data to an expected form of the structure function for index of refraction. This section will attempt to present a description of C_n^2 which provides an adequate familiarity with what this scalar represents. For a more thorough technical development, the reader may with to look at the works of Tatarskii, [67, 68], and Volumes I and III of the series by Rytov, Tatarskii, and Kravtsov, [60].

Other structure function constants used in this work include the structure function constant for temperature, C_T^2, pressure, C_P^2, wind speed C_v^2, and vapor pressure $C_{e_v}^2$. The remainder of this section will present structure functions themselves, and how they relate to turbulence. The role of the structure function is to describe how the correlation of measurements varies with distance. For example, consider an experiment where temperature is measured simultaneously at many locations above a football field. Selecting one particular measurement, T_0 one could then consider how similar surrounding measurements might be to T_0. It would be expected that mea-

surements taken a few centimeters away (nearby) would be very similar to T_0, while measurements taken many meters away (distant) would be less similar to T_0. The *temperature structure function* for these measurements should describe how similar one expects measurements to be as a function of spatial displacement. Within the scope of a statistical description of measurements taken within a turbulent field, it has been shown [36,37,52] that structure functions for particular quantities (including those listed above) have the form of (4).

Structure functions address a need for a statistical theory which allows for analysis of non-stationary functions. A non-stationary function is a function whose mean is not fixed. For example, temperature over time in the atmosphere is a non-stationary process. Consider taking temperature measurements every minute for a period of time. If these temperatures are plotted over time, one would notice high and low frequency variation. If these measurements are then averaged over each hour and plotted, these hourly means will also show high and low frequency variation. This process can be repeated, and regardless of the time span, days, weeks, months, years, decades, and so forth there will still be variation in the plots. Therefore, the mean of temperature is sensitive to the choice of which measurements to include, and does not head to a fixed value as the number of measurements increases. The difficulty that non-stationarity presents is that common tools which describe the process (spectral density, probability density, and cumulative density) are no longer fixed.

A common way to measure turbulence, is to consider how much variance one would expect to see in a measurable physical aspect of the fluid which is mixed by the turbulence, say temperature as a function of position and time, $T(\vec{r}, t)$. It was found that correlation theory was insufficient to describe the statistics of $T(\vec{r}, t)$ as it did not have a stationary mean. Instead, the so-called structure-function was proposed by Kolmogorov [36]. The structure function generalizes correlation theory

to allow for a statistical description of functions without stationary means.

For many atmospheric processes, even while the mean is not stationary, the *first increment* is approximately stationary. The first increment in the example temperature field is the difference in temperatures taken at two times or locations, but separated by a fixed interval. Say, the difference in measurements taken 1 minute apart. Structure functions also describe expected differences in measurements taken at different locations (as in the volume over a football field above), where variation is taken with respect to $\vec{r}$ instead of t. For processes with stationary first increments, similar techniques to those developed for stationary processes may be applied. For a complex field $\tilde{\zeta}(\vec{r})$ that varies over space, the structure function is defined as

$$D_{\tilde{\zeta}}(\vec{r}_1, \vec{r}_2) = \left\langle \left| \tilde{\zeta}(\vec{r}_1) - \tilde{\zeta}(\vec{r}_2) \right|^2 \right\rangle . \tag{1}$$

Further development of structure functions and correlation theory is presented in [60, 67] and other sources. For purposes of this research, $\zeta(\vec{r})$ is a real-valued field which represents the local distribution of index of refraction, temperature, pressure, vapor pressure, zonal wind, or meridional wind (n, T, P, e_v, U, V). By computing the first increments of $\zeta(\vec{r})$, the short range variation which is related to turbulence induced perturbations is separated from the long range variation which is attributed to other processes.

Further assumptions about the statistical nature of PBL fields are commonly made, and carried through here. First, it is assumed that the structure function is homogeneous. That is

$$D_\zeta(\vec{r}_1, \vec{r}_2) = D_\zeta(\vec{r}_1 - \vec{r}_2) = D_\zeta(\vec{r}) \tag{2}$$

so that the structure function only depends on the difference between the points,

not the points themselves. Second, the structure function is assumed to be isotropic. That is

$$D_\zeta(\vec{r}) = D_\zeta(r) \tag{3}$$

where $r = |\vec{r}|$. These assumptions are not always valid, but within the PBL, results based on the locally homogeneous and isotropic assumption for eddies within the inertial subrange agree well with observation [16, 32, 68].

Based on the statistically homogeneous, isotropic, and stationary first increment assumptions, Kolmogorov and Obukov were able to show that there is a range of lengths, $r \ll L_0$ for which the spatial structure function of conserved passive additives has the form [36, 37, 52]

$$D_\phi(r) = \begin{cases} C_\phi^2 r^{2/3} & l_0 \ll r \ll L_0 \\ C_\phi^2 l_0^{2/3} \left(\frac{r}{l_0}\right)^2 & r \ll l_0 \end{cases}. \tag{4}$$

In (4), ϕ is some scalar quantity, r is distance, l_0 is what is known as the *inner scale* of the turbulence, and L_0 is the *outer scale* of the turbulence. It's common to see structure function constants for temperature (C_T^2), velocity (C_v^2), vapor pressure (C_{ev}^2), and index of refraction (C_n^2). These structure function constants depend on, and describe how strongly each quantity varies within a field. Here it is assumed that perturbations in the field are generated by advection of fluid parcels by a turbulent flow. While turbulent flows are present in a range of applications, this work is concerned with turbulence in the PBL where l_0 is on the order of a few centimeters and L_0 can be tens to hundreds of meters.

It can be seen from (4) that the structure function within a certain size, $l_0 \ll r \ll L_0$, can be described using only the distance between measurements, r, and a constant C_ϕ^2. This form of the structure function is used to derive much of modern

theory about the interaction of turbulence with propagating waves (such as EM and sound waves). The range of eddy sizes $l_0 \ll r \ll L_0$, where $D_\phi(r) = C_\phi^2 r^{2/3}$ is known as the *inertial subrange*.

Structure functions are closely related to correlation functions. For processes with a statistically homogeneous field, the covariance is

$$\Psi_\zeta(\vec{r}) = \langle \zeta(\vec{r}_1)\zeta^*(\vec{r}_1 - \vec{r})\rangle - \langle \zeta(\vec{r}_1)\rangle \langle \zeta^*(\vec{r}_2)\rangle \,, \tag{5}$$

and it can be shown [60] that the structure function is

$$D_\zeta(\vec{r}) = 2[\Psi_\zeta(\vec{0}) - \Psi_\zeta(\vec{r})]. \tag{6}$$

The advantage of structure functions over correlation is that they exist for fields where the correlation (and covariance) does not exist, and can be used to check for stationarity before attempting to use correlation functions [16]. For PBL turbulence studies, structure functions are often appropriate. In Section 1.4 methods are presented for determining the structure function constants based on measurement.

1.3 Dynamics of The Planetary Boundary Layer

At the bottom of the Earth's atmosphere is a relatively thin layer known as the planetary boundary layer (PBL). The depth of this layer varies with time and location, but is typically from several hundred meters to over a kilometer. The evolution of winds, temperatures, aerosol concentrations, water vapor concentrations, and other atmospheric quantities within the PBL is driven by the interaction forces between the free atmosphere above and the Earth's surface below. The dynamic evolution of these quantities is directly related to turbulence. It is known that turbulence does affect the EM propagation environment [12, 32]. The question to be answered is"by

how much?" Understanding some of the atmospheric interactions is important for determining if the sum of their effects on an EM signal is detectible, measurable, and finally usable as a tool for inferring the state of turbulence in the PBL.

Whenever a fluid flows over a rigid surface, there is an interaction area called a *boundary layer* where the dynamics of the fluid are controlled by the sheer stresses between the flowing fluid and the stationary surface. [66] What happens in this layer depends on the physical characteristics of the fluid, surface, and the flow. Flows are generally divided into laminar (smooth) flows and turbulent flows. The Reynolds number:

$$R \propto \frac{v}{viscosity}, \tag{7}$$

parametrizes how laminar or turbulent a given flow is. Very large Reynolds numbers indicate turbulent flows. A combination of very low viscosity for air, and high values for the wind velocity in the free atmosphere causes the Earth to have a persistent boundary layer. This layer varies in depth, as mentioned above, but the depth and turbulent intensity can be attributed to a combination of several different processes [30,66] The amount of turbulent kinetic energy (TKE) in a given area is controlled by a balance of processes which transfer energy into and out of turbulent flows. Molecular diffusion is constantly removing kinetic energy from turbulent flows and converting it into heat. Mechanical production occurs in regions where velocity shear between winds creates turbulence. This includes interaction with objects on the surface as well as wind shear between adjacent streams of differing velocity. Advection by the mean wind can serve to increase or decrease TKE in a given region. Buoyant forces that arise from the vertical temperature profile can also act as a source or sink of TKE. The TKE budget can be expressed symbolically as [30]:

$$\left\langle \frac{D(TKE)}{Dt} \right\rangle = MP + BPL + TR - \varepsilon. \tag{8}$$

As used here and throughout the remainder of the document, the $\langle \cdot \rangle$ indicates the expected value when referring to processes (like the rate of change of TKE), or as the arithmetic mean when referring to discretely sampled data. D indicates the total derivative (the derivative in a coordinate frame following an air parcel), MP indicates mechanical production, BPL is buoyant production or loss, TR is energy lost or gained by transport and pressure forces, and ε is frictional dissipation of TKE into heat.

The dynamics of the PBL are quite complex, as the various quantities are all inter-related. For example, to track what happens with temperature just above the surface one could start with considering the balance of heat flux from solar heating, ground reflection, and ground emission. This can help to estimate changes in the local temperature distribution. Next, one must consider how the winds will mix and advect air of differing temperatures, so it's important to know the local distribution of temperatures and winds. At the same time, it's important to consider how the temperature gradients will affect the motion of the winds. As the air is being moved to locations of different pressures, the parcel's pressure will almost instantly equalize with local pressure and acceleration induced gradients (more on those in Section 2.4) and the temperature will change (more or less) in accordance with adiabatic thermodynamic principals. So it's important to know the local pressure gradients as well. These changes in temperature, in conjunction with the pressure and moisture content may cause water vapor to change state, adding or removing heat from the air. So the relative humidity, temperature, pressure and aerosol content (aerosols may affect nucleation of water) are all important parts of TKE production and loss. At the same time, evaporation rates and pressure gradients are dependent on the local

temperature, humidity and winds as well. If a bit of warm, moist air is moved up (as often happens due to wind convection or buoyant forces and heating of the air by the surface) the water vapor may condense into a cloud. The cloud will, in turn, change the original solar heating process. While simple compared to full PBL dynamics, this scenario shows how none of the different parameters: solar heating, temperature, wind, humidity, and precipitation can be considered independently. This interrelation makes it hard to understand any one process without knowledge of several others, but it also means that the state of one parameter (say temperature) carries with it information about all the others. In developing the radar C_n^2 corrections, this made it possible to do the correction using just a few parameters rather than trying to track every one that could affect the refractivity of air for the radar. This section will attempt to outline a basic model for the dynamics of the PBL. A more complete treatment is available in meteorology texts including [30, 33, 66].

While the total interaction is complicated, general PBL dynamics can be understood in relation to the diurnal cycle. Because turbulence moves air about, causing the temperature to respond adiabatically to changes in pressure, temperature discussions can often be simplified by the introduction of *potential temperature*, θ. Potential temperature is defined as the temperature a parcel of air would be at, if it were brought adiabatically to standard pressure ($1000mb$).

Land tends to heat quickly during the day. Because of this, the temperature of the air near the surface becomes warmer than the air in the upper PBL. Under these conditions the potential temperature θ decreases with height, $d\theta/dz < 0$. An air parcel that begins to rise cools adiabatically due to the pressure drop, but because $d\theta/dz < 0$, the parcel is still warmer than the air around it. Buoyant forces accelerate the air upward toward the capping temperature inversion at the top of the boundary layer (where θ increases quickly with height). This air then displaces cooler air down,

which can then be heated by the ground and continue the cycle. This process creates TKE through buoyant production, and tends to mix the air throughout the PBL. Thus, during the day the PBL is typically *unstable*, deep and well-mixed. At dusk, insolation drops off and the ground begins to cool. Under clear or partly cloudy skies, the surface cools more quickly than the air, and $d\theta/dz$ will begin to increase. Buoyant production ceases as the atmosphere goes through a quiescent period of neutral stability ($d\theta/dz$ becomes approximately zero). As night goes on, $d\theta/dz$ continues to increase (unless cloudy skies absorb and re-radiate energy back toward the ground) creating a *stable* PBL. Under these conditions buoyancy damps vertical motions because air which is advected up has a lower temperature than the surrounding air and thus sinks back down. This PBL is typically much more shallow than the daytime PBL, and is characterized as stable because of the buoyant feedback which suppresses vertical motions. Above this stable PBL is a residual layer where turbulent eddies from the previous day gradually spin down over the night.

As C_n^2 is closely related to how turbulent an atmosphere is, it can be used to signify (roughly) TKE. For example, Figure 2 shows C_n^2 vs height and time from a full day on September 4, 2013. Nearby observations recorded clear skies throughout the day, with a high of 27.2^oC and a low of 8.9^oC. Surface winds were calm in the early morning, increased to about $6kn$ $(3.1m \cdot s^{-1})$ by noon, and stayed steady throughout the afternoon. The reduction in C_n^2 at dawn is readily apparent, and to a lesser extent the dusk quiescent period may also be seen. During these times, the potential temperature gradient, $d\theta/dz$, goes to zero, and the BPL term of (8) also becomes minimal. As the ground warms though the day, $d\theta/dz$ becomes negative (unstable).

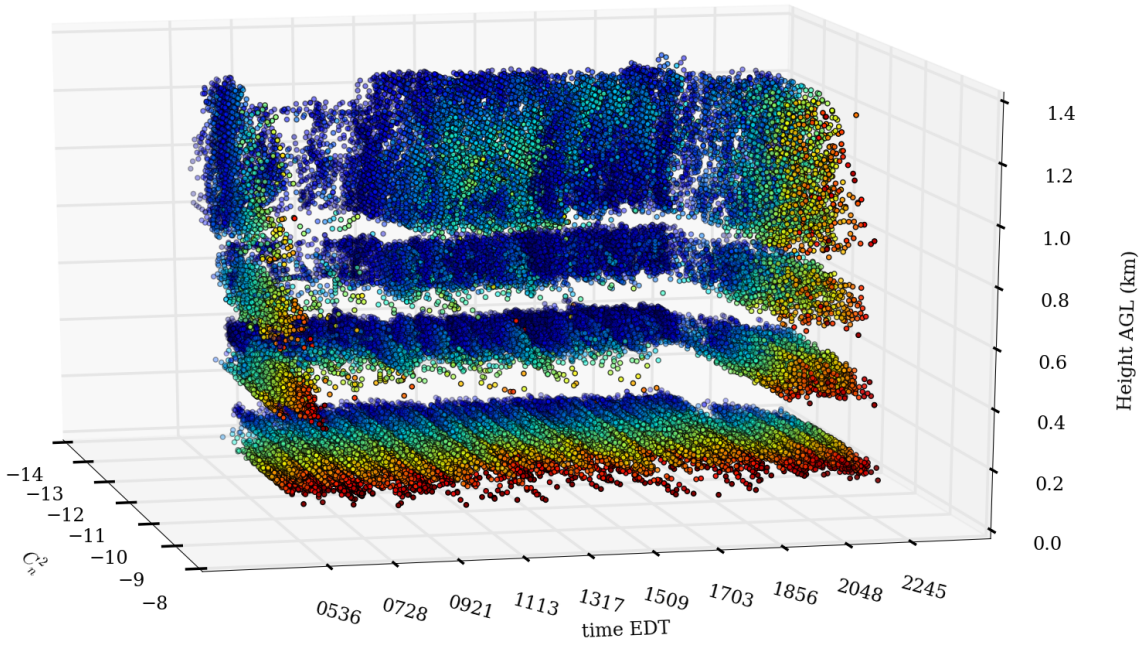

Figure 2. NEXRAD measured C_n^2 vs height AGL and local time of day from 4 September 2013 . Each sphere represents one measurement from a NEXRAD bin. The sphere color and placement on the x-axis indicate the measured $log_{10}(C_n^2)$ value. The location on the y-axis indicates which time the spheres came from. The location on the z-axis indicates the height of the center of the $250 \times 250 \times 250m$ radar bin each measurement came from. Data are taken from a $2 \times 2 \times 1.5km$ volume approximately $14.5m$ from the Wilmington Ohio (KILN) NEXRAD. Local sunrise occurred at 0706 EDT and sunset occurred at 2001 EDT.

The increased C_n^2 after sunset is not indicative of typical PBL dynamics, but is often seen in NEXRAD measured data (and sometimes to a lesser extent in scintillometer data). This increase may be due to the increased refractive bending that occurs at night. The vertical hydrostatic pressure gradient causes the radar beam to bend down toward the earth (with a radius of curvature about four-thirds of the Earth's radius). The vertical temperature gradient also causes the beam to bend. During the day, the vertical temperature gradient is significantly reduced. Reduction in the resulting bending causes the beam to remain higher and less of the beam and

side-lobes to intersect the ground. At night, the ground cools quickly due to radiative loss, and the potential temperature begins to increase more strongly with height. This causes the beam to bend more sharply downward, increasing ground clutter (which manifests as raised C_n^2). Doppler filtering and surface clutter maps are used to reduce clutter. Section 4.8 explores this topic in detail, with the conclusion that significant clutter remains in the NEXRAD data, even after filtering. In addition to the ground clutter, there may also be biological echoes in the data.

The increased nocturnal C_n^2 values may not be entirely due to clutter and noise. Scintillometer data from the nearby ($30km$ away) Dayton scintillometer often showed nighttime C_n^2 which is as high as daytime C_n^2. For example, in Figure 3 the measured C_n^2 on the evening of 4 September was nearly as high as the daytime C_n^2. This is unusually high for the scintillometer, for which it is typically expected that nighttime C_n^2 will be 1 to 2 orders of magnitude below daytime C_n^2. Data from 2, 3, and 6 September showed the more common pattern of lower nocturnal C_n^2. Because the radar sees a much greater nocturnal increases than the scitillometer, it may be that while TKE is dropping, the water vapor structure function $C_{e_v}^2$ is increasing. As NEXRAD C_n^2 depends much more on $C_{e_v}^2$ than the scintillometer C_n^2 does, an increase in $C_{e_v}^2$ would be expected to impact the NEXRAD measurements much more. The combination suggests that these elevated C_n^2 values may be due, in part, to increased TKE on this evening. The elevated nocturnal C_n^2 may also be due to the height of the scintillometer path. Typically, scintillometer measurements are taken within the first few meters above the surface. Turbulence within this surface layer is strongly influenced by surface interactions, and behavior which is typical close to the surface will not necessarily be observed at the height of the scintillometer paths used here, 60 to $70m$ above the surface.

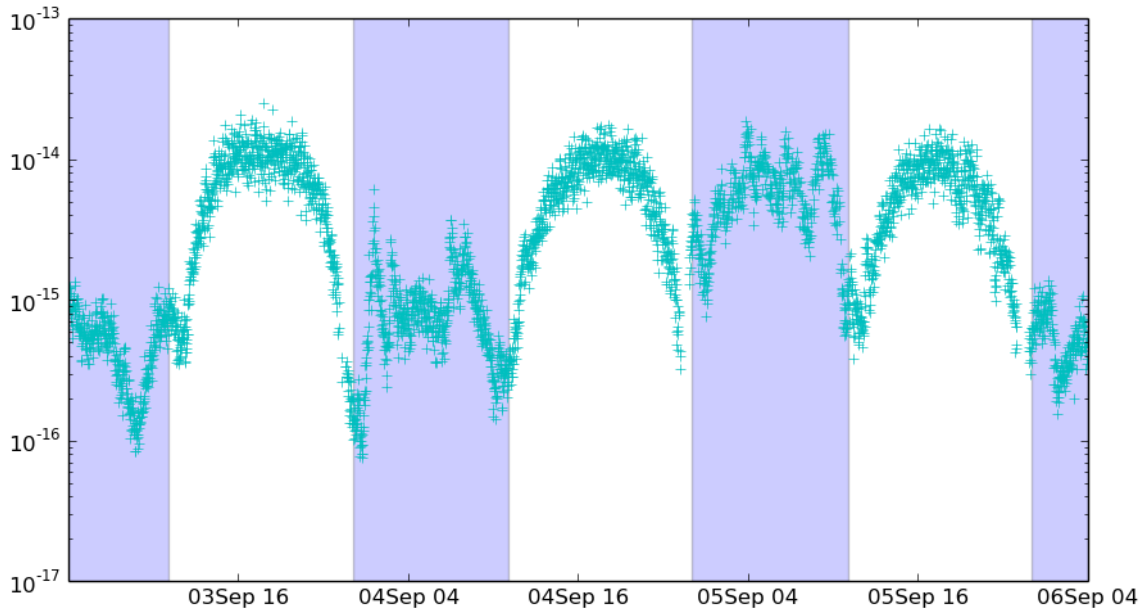

Figure 3. Scintillometer measured C_n^2 vs. time from the Dayton scintillometer path. Dark regions indicate nighttime with transitions at sunrise and sunset. All times are local, EDT.

1.4 Current Methods for Determining C_n^2

Five sources of real-time turbulence data are investigated here: scintillometer, NWP, NEXRAD, Image Differential Motion, and cell phone signals. Because it is a well-established method, scintillometry will be used as the standard to compare against, when available. Currently, there is significant interest in using NWP to estimate C_n^2, [2, 46–48] and results using the standard NWP approach will be presented. C_n^2 estimated via standard techniques [16] which use NEXRAD clear-air reflectivity are also presented. Recent research has also shown that C_n^2 may be determined based on image analysis [4]. Using images taken over a long path (several kilometers), differential motion within the image can be used to determine C_n^2.

These methods will be compared with C_n^2 estimated using the new approaches presented in this work. The new methods include modifications to the standard

NWP approach, and a new method which estimates C_n^2 from cell phone signal strength variation. It will also be shown that NWP can be fused with either NEXRAD or cell phone C_n^2 data to provide improved performance. As an example NWP and NEXRAD data are fused and used as a validation tool for the new Image Differential Motion technique [4]. This section will present a brief summary of the standard methods compared in this work. Later sections will develop methods which fuse NEXRAD and NWP to provide improved measurement capabilities, and show how some of these techniques are suitable for extension to improve cell phone scintillometry.

Scintillometers use a calibrated laser or LED source with a specialized receiver known to measure C_n^2, [28, 29, 41, 44, 62]. Turbulence-induced refractive index variations distort the propagating wavefront. Due to mutual interference and path-bending induced by spatial variation in n over the propagation path, the intensity measured at the receiving aperture varies, or scintillates, in time and space. By tracking the scintillation, and making some assumptions about the propagation path, turbulence parameters can be estimated [32,68]. By measuring scintillation over a period of time, and in some cases over the pupil-plane area, an estimate of C_n^2 over the propagation path can be created. Scintillometers have been developed which operate in bands which range from the microwave to visible-light regime.

Large aperture scintillometers are used for both the Dayton and Albuquerque locations. The Dayton device is a Scintec® BLS2000, which uses two arrays of $880nm$ LEDs which are modulated at two different frequencies. The receiver is a telescope which collimates received radiation onto a high-sensitivity photo-diode. By modulating the two arrays at different rates, the receiver can differentiate scintillation from both paths. The two transmitting apertures are circular LED arrays, spaced $30cm$ apart. This creates a triangular measurement geometry (Figure 4). This type of scintillometer weights its measurement of C_n^2 toward the center of the path with zero

weighting at the path ends. Because there are two transmitters and one receiver, the paths forms a triangle. Because of the triangular geometry, the $30cm$ separation at the base of the triangle, and the measurements being weighted toward the center, the scintillometer can measures C_n^2 for two regions whose centroids are separated by $15cm$. Using C_n^2 from both paths allows for detection of transverse wind velocity and reduction of saturation effects [62]. The scintillometer also has a weighting which emphasizes the portion of the turbulence size spectrum from 0.1 to $10cm$ with the peak weighting being at around $3cm$ [62]. The scintillometer used at the Albuquerque location is similar to that used at the Dayton site.

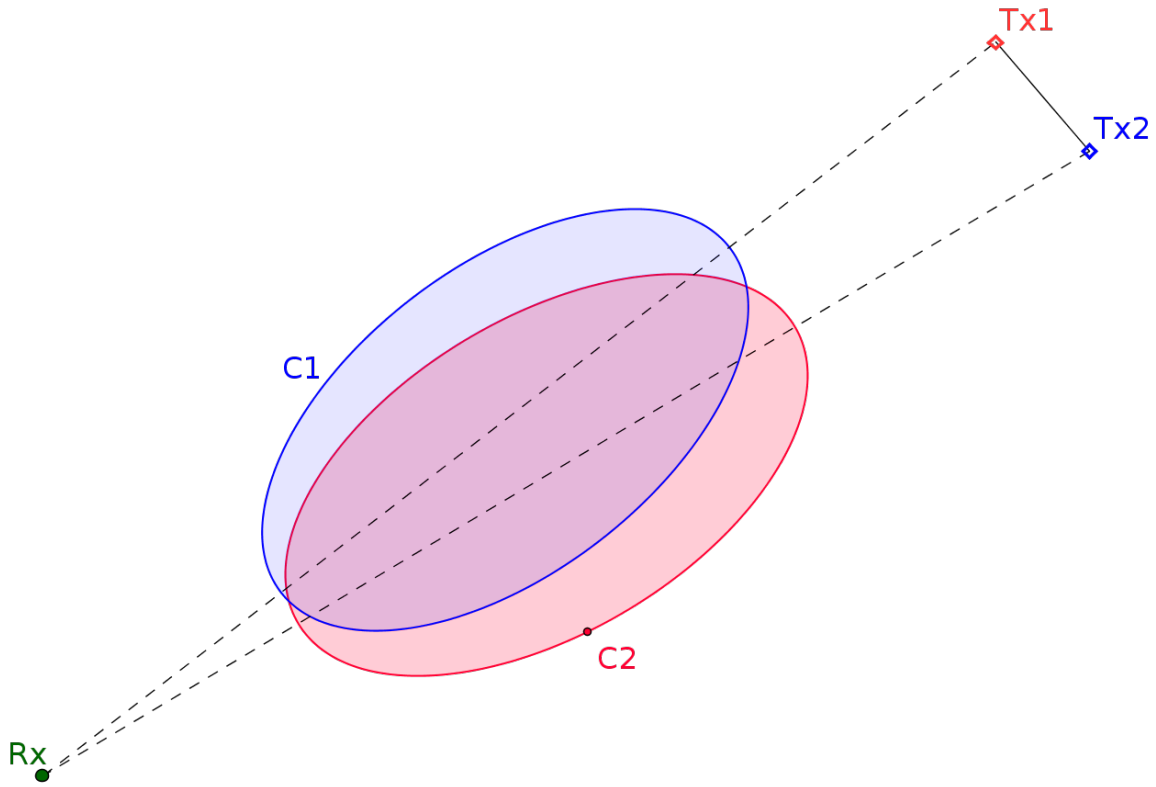

Figure 4. Illustration of the BLS2000 measurement geometry for the Dayton path (not to scale). The scintillometer consists of two transmitters, Tx_1 and Tx_2, spaced $0.3m$ apart with the receiver, Rx $7km$ away. Each path from transmitter to receiver measures integrated C_n^2 over the path, with a much stronger weighting of C_n^2 toward the center of the path. Ellipses $C1$ and $C2$ illustrate that each path gives the structure function constant for similar sized regions of the atmosphere, with some lateral separations.

In addition to scintillometry, NWP is used to estimate C_n^2. Development of techniques for determining structure function constants from NWP, which cannot resolve the scale of turbulent structure, is possible for fields whose perturbations are primarily due to PBL turbulence. This is made possible by the energy cascade theory, first proposed by Kolmogorov. The theory is based on the idea that eddies in fully developed turbulence have a steady state balance between generation and dissipation. Considering the amount of energy present in eddies as a function of eddy size,

there is a spectrum of eddy sizes known as the *inertial subrange* wherein the primary generation and dissipation mechanism is the cascade (breaking apart) of larger eddies into smaller eddies. As the eddies become smaller, the rate at which their energy is dispersed due to the cascade becomes smaller. At some size, the rate of dissipation into smaller eddies becomes less than the rate at which the energy is dispersed into heat, ε. The size of eddies where heat dissipation overcomes cascade dissipation is the so called *inner scale* of the inertial subrange, l_0. The largest eddies, receive their energy from various eddy generation mechanisms which are 'outside' the largest scale of the turbulence, L_0. While the scale of l_0 is generally agreed upon to be on the order of a few centimeters in the typical PBL [28], estimates of the outer scale vary over many orders of magnitude [78]. The true value of L_0 has practical implications for the applicability of Kolmogorov's energy cascade theory, but if the energy dissipation rate, ε, can be determined then the energy spectrum of the turbulence can be estimated, and has been shown to agree well with measurement [68].

In cases where Kolmogorov's energy cascade theory is applicable, Tatarskii developed a relationship between the vertical gradient of a *passive additive* and its structure function constant,

$$C_\zeta^2 = a^2 \varepsilon^{-1/3} K_\zeta \left(\frac{d\langle \zeta \rangle}{dz} \right)^2 . \tag{9}$$

In (9) a is a universal constant, ε is the rate of dissipation of TKE into heat, K_ζ is the rate of diffusion of the passive additive ζ, and $d\langle \zeta \rangle / dz$ is the vertical gradient of the mean state of the passive additive (the gradient without turbulence induced perturbations). For a quantity to be *passive* it must not affect the turbulent flow when advected. To be *additive* the quantity cannot change value due to advection by the turbulent eddy. For example, temperature is not additive because if a parcel of air is advected vertically, the pressure will change to maintain hydrostatic balance resulting in an adiabatic change of temperature. However, equivalent potential tem-

perature θ is additive because its value does not change due to vertical advection. Equivalent potential temperature (hereafter referred to as "potential temperature") is the temperature that a parcel of moist air would have if it were brought to a reference pressure using a reversible moist adiabatic process. Tatarskii's equation is often used to estimate structure function constants for turbulence research using vertical gradients of passive additives determined from NWP (or other sources of vertically sampled weather data live rocketsonde, radiosonde, and IR sounders). [3, 16, 21, 34, 35, 58, 78]. Once found, the gradients of potential temperature and vapor pressure can be converted to index gradients used to determine C_n^2.

Scattering techniques may also be used to measure C_n^2. Purpose built lidar and radar systems have been used to remotely measure turbulence [18, 40, 54, 58] at moderate (up to $15km$) ranges. Even when comparing measurements from similar instruments, it is common for there to be significant disagreement about C_n^2 and other turbulence parameters [2, 18, 28, 44, 58, 74]. Variations in T, e_v, and P lead to changes in the index of refraction, n, of air. While these changes in n are slight, there effects are measurable using a variety of techniques. Radar and lidar may be used to detect Bragg scattering off turbulence induced index variations [9, 10, 16, 18, 20, 26, 58, 59]. Under the assumption that all back-scattered energy is from clear-air turbulence, then the value of C_n^2 measured by radar can be found using [16, 19, 21]

$$C_n^2 = 2.63\pi^5\lambda^{-11/3}\left|K_w\right|\frac{10^{dBZ/10}}{1000^6}, \tag{10}$$

where λ is the wavelength, K_w is the complex index of refraction for water, and dBZ is the NEXRAD reflectivity factor. Often, wind-profiling radars operate at wavelengths between 1/3 and $frac2/3m$, where reflections from hydrometers are relatively weak. Later in this work, results will be presented which argue for the inclusion of non-hydrostatic pressure gradients in estimation of C_n^2 values. If the turbulent eddies do

have a velocity structure similar to the proposed Lamb-Oseen irrotational vortex [61], then (10) may no longer be valid. The common assumption is that the "size" of the eddy is the same when considering (1) the energy present due to its circulation, and (2) the eddy's scattering properties. This assumption is an oversimplification. While there is no analytic solution for 3-D vortex structures, numerical 3-D vortex solutions have a radial velocity structure which converges to a similar form under conditions considered for PBL turbulence [47,61]. More detail of the resulting refractive structure will be given in Section 2.4, where the non-hydrostatic pressure term is introduced. What is found is that the size of the eddy as a scattering body (property 2) is smaller than its size as a vortex structure (property 1). This difference in size leads to (10) overestimating C_n^2. This comes about because Doviak uses Kolmogorov's five-thirds law,

$$E(k) = C\varepsilon^{\frac{2}{3}}k^{-\frac{5}{3}} \tag{11}$$

to obtain the relationship between scattering and eddy size. Doviak does show that clear-air back-scatter is dominated by eddies with diameter in the Bragg-scattering regime, $D \approx \lambda/2$. However, if the effective scattering body size, D_s, is less than the actual vortex size, D_v, then C_n^2 will be over-estimated by a factor of $(D_s/D_v)^{5/3}$.

While they provide good resolution and accuracy, standard turbulence-measurement instruments such as scintillometers, LIDARs, rocketsondes, radiosondes, and wind-profiling radars are severely limited in the temporal and spatial extent of the atmosphere they can sample compared to the immense volume coverage provided by operational NEXRAD coverage, cell phone networks and NWP forecast models. The cost advantage of using freely available data over instrumentation is obvious. While the radar itself is an active device, their data are publicly available for download. Cell phone towers broadcast continuously, and measurement only requires receiving their broadcasts. So using weather radar, cell phone signals, and forecasts to measure C_n^2

has the added benefit of essentially being a 'passive' method. The following sections will outline how NEXRAD and NWP or cell phone and NWP might be combined to provide a more accurate and high-resolution C_n^2 estimate than either system can provide by itself.

1.5 A Better Way to Measure C_n^2

In the previous section, four common methods for determining C_n^2 were presented, but all of these methods fail to provide a reasonable solution for real-time, large-volume C_n^2 measurements. Distributed weather probes have the obvious problem of deployment. Rocketsondes and radiosondes only measure a small column of turbulence at a time, and are expensive to operate continuously. Wind-profiling radars provide a relatively large volume measurement, but are also expensive to install and maintain. Scintillometers are relatively inexpensive and easy to set up, but measure only a small volume of the atmosphere. Because they require alignment of the transmitter and receiver, scintillometers are generally limited to fixed locations. NWP is limited by its resolution, which is usually on the orders of kilometers (horizontally) and hours while turbulence scales require centimeters and seconds. While models can be run at these scales, their validity degrades in a matter of a few seconds after initialization, and they still require a very high-resolution boundary condition for initialization.

Benefits of using NEXRAD as a turbulence measurement instrument have been documented [9, 10] and can be summarized as providing a persistent, passive, wide-area, historically archived measurement method. This makes NEXRAD a convenient and useful source for large-volume high-resolution turbulence information. A particular benefit of the NEXRAD over more conventional instrumentation is its ability to measure turbulence in the upper PBL. This can be leveraged for PBL structure stud-

ies as shown in Section 4.4 or for comparison results to be used for system verification and validation as shown in Section 5.3.

Cell phone signals (and other RF emitters of opportunity) provide potential augmentation and extension of the radar capabilities. While NEXRAD measurement range extends several hundred kilometers, the range at which they detect turbulence appears to be limited to about $50km$. As a result, the area where weather radars (NEXRADs included) can measure turbulence is large, but is far from complete (a map of NEXRAD locations is presented in Figure 15). Cell phone towers can provide coverage in areas that are beyond the reach of the NEXRAD network. Because the cell phone base-station signals are always available, they provide a more constant measurement source. NEXRAD measurements take between 5 to 10 minutes to complete and a given location is only measured once in this period. Therefore, NEXRAD does not provide the constant coverage available from cell phone base-station signals. Cell phones provide a point-to-point measurement like scintillometers, but do not require alignment, and many locations have several transmitters within view at any given time. Cell phone measurements update frequently, often on the order of seconds. Also, the process by which cell phones signals are affected by turbulence is not identical to radar, so comparing the two can provide more insight into the physical processes of the PBL turbulence.

In comparison to other methods, RF techniques do suffer from considerable noise and measurement uncertainty, which is described in detail in Chapter IV. NEXRAD data are also limited in range and completeness. Their limitations are especially severe during winter months, or when precipitation is present. Despite these drawbacks. RF techniques provide promising capabilities. They are capable of providing turbulence measurements in a much greater volume than scintillometer, rocketsonde, radiosonde, or distributed probe methods. Compared to NWP, NEXRAD radar pro-

vide over an order of magnitude improvement in temporal and spatial resolution. They are essentially passive methods, as the radiation sources are already active. The radar volumetric scan is unique in its ability to provide a three-dimensional measure of turbulent activity. The fact that historical radar data are available allow for turbulence data to be created for comparison to previous work.

In addition to the standard methods for determining C_n^2 from NWP or NEXRAD alone, this work will present several new techniques which determine C_n^2 based on fusing and extending existing NEXRAD and NWP techniques. These new methods make use of the Ciddor model [13], which is not typically found in PBL C_n^2 literature. Ciddor's equation and Edlén's equation for visible light to IR refractivity, are the standard methods for relating index of refraction to atmospheric pressure, temperature, and vapor pressure [13, 65]. Ciddor's equation is argued to be more accurate over a larger range of environmental conditions and wavelengths so is used here [65]. While there are differences, the difference between n values from the two methods is negligible when compared to the large uncertainty inherent in NWP, NEXRAD, and cell-phone input data.

Despite the fact these equations are the modern standard for visible light to IR refractive index calculation, a much less accurate equation which is intended for use in RF is often used in current PBL turbulence literature. This work will compare the use of Ciddor's equation to the RF equation which is currently in use, and show that when considering the impact of water vapor and pressure, Ciddor's equation does a much better job of predicting C_n^2. The Edlén equation was not used, but is expected to give nearly identical results to the Ciddor equation. In addition, a method for determining C_n^2 from scintillation in terrestrial emitters of opportunity (cell phone signals) is presented. The baselining technique developed for NEXRAD is compared with a new image-based C_n^2 technique, and is also suitable for correcting cell phone

based scintillation.

The new methods presented here are partially based on removal of the common simplifying assumption that vapor pressure and pressure gradients do not play a role in determining C_n^2 for IR and visible systems. This modification is suggested by comparison of the magnitude of pressure, temperature, and vapor pressure contributions to C_n^2. It will be shown that pressure contributions are a natural consequence of turbulent flow and are significant under some atmospheric circumstances, but can be safely ignored at other times. Furthermore inclusion of pressure and vapor pressure perturbations provides a physical explanation as to why C_n^2 values are consistently several orders of magnitude higher than expected during dawn and dusk quiescent periods (when they should not be ignored). The new picture of pressure's role in turbulence makes use of the Lamb-Oseen vortex model [61].

II. Methodology and Theorotical Development

In this work, several novel methods for remotely determining C_n^2 were investigated and compared with standard approaches. A large portion of this document focuses on using NWP and radar to estimate C_n^2 and comparing it to scintillometer measurements. The results show how well C_n^2 can be estimated, and suggest under which conditions the methods work well. The radar and NWP C_n^2 technique is then used to generate comparison data for the cell phone and image differential motion techniques. This section will present the theory and processing techniques for estimation of C_n^2 form radar and NWP, and from cell phone scintillation. The next chapter will present the practical concerns involved when implementing these methods.

2.1 Performance Metrics

When testing new approaches to generating C_n^2 estimates, the need to determine how well the approach woks quickly becomes salient. In the initial research stages, the methods are crude and quick, plot the data and see if it looks as expected. As the methods are developed, it becomes necessary to develop a more objective method to determine how well a *test* method can estimate C_n^2. Scintillometer data are used as truth data for comparison of the NEXRAD-NWP methods. These NEXRAD-NWP methods are then used to evaluate the image based, and cell-phone methods. Previous work has shown that cell phone C_n^2 correlates well with radar C_n^2. So the baselining technique may be used to baseline the cell phone C_n^2 to match optical or radar systems, as needed. In turbulence studies one is often doing well if two methods for determining C_n^2 show about the same order of magnitude and show similar diurnal variation. Compared to other disciplines, this criteria seems to show a paltry agreement between data. It would be hard to imagine a carpenter framing

a house with measurements that are correct to within an order of magnitude, and grouped so that the large studs are mostly with the large studs and small studs are mostly with other small studs. The measure of successful agreement in C_n^2 has its bar set so low for reasons which are closely tied with the need for structure functions to describe turbulence.

The BLS2000 scintillometer, used at the Dayton site has two transmitters set close together and one receiver (Figure 4). Despite having a separation of only $15cm$ in the middle of the path, measurements from each transmitter have a covariance which is only about 1/8 the variance seen in either path [62]. It is apparent that the value of C_n^2, while describing the structure function over a large volume can vary quickly with small changes in the volume centroid. Assuming the outer scale of turbulence is on the order of $L_0 = 50m$ (a commonly used value in the PBL [78]) it is surprising to find that a the structure function constant, which describes the magnitude of variation for structures up to L_0 and centered at one location, is only weakly correlated to a structure function centered only $15cm$ away! Couple this with Taylor's frozen flow hypothesis [69] and one can see that even at low mean wind speeds, say $\langle v \rangle = 0.5m \cdot s^{-1}$, that temporal correlation of measurements quickly becomes weak. It is this weak temporal correlation over short distances in space and time that leads to the need for a relaxed criteria for C_n^2 estimation.

Before making comparisons between instruments, it is necessary to convert measurements to a common sampling rate. Either by low-pass filtering data to a lower sample rate, or interpolating to a faster sample rate. Care must be taken when considering the effect of low-pass filtering C_n^2 data. Unlike stationary processes which tend toward a fixed value when averaged, turbulent processes like $C_n^2(\vec{r}, t)$ has a mean value which can vary significantly from centroid to centroid under processes like the sliding mean. This is a restatement of what is presented in the paragraph above.

For this reason, even when low-pass filtered, measurements from two instruments are not expected to approach each other as they would in a scenario where both instruments sample of the same underlying process with added independent and identically distributed noise.

The instruments used here include scintillometers, cameras, cell phone tower and receiver pars, NEXRADs, and NWP models. These instruments each have their own particular geometry, resolution, and noise considerations. In addition, several choices in how to process these measurements into a C_n^2 estimate are presented. Because estimates from each method will represent locations and times which are only approximately the same as those being compared to, it is expected that agreement in C_n^2 will vary. The goal then becomes to define a quantitative measure which can describe how similar measurements are, and how significant that similarity is.

The performance of C_n^2 estimates are quantified based on the difference of the common log of the C_n^2 between methods. Two measures of performance are used. The first is the Root Mean Squared Error (RMSE) between the *test* method, and *standard* method as defined by

$$RMSE = \sqrt{\frac{1}{N}\sum_{i=1}^{N}(\hat{X}_i - X_i)^2}. \tag{12}$$

Here N is the number of samples being considered, $\hat{X}_i$ is the i^{th} C_n^2 value from the *test* method, and X_i is the i^{th} C_n^2 value from the *standard* method. When more than one test method is being compared to a standard, the test methods can also be ranked by the number of points where the particular method provides the smallest error, $\left|\hat{X}_i - X_i\right|$. The count is normalized by dividing by the number of samples involved

providing the Normalized Best Estimate Count (NBEC).

$$NBEC_j = \frac{100}{N} \times \sum_{i=1}^{N} \left[\left| \hat{X}_{i,j} - X_i \right| = min \left(\left| \hat{X}_{i,1} - X_i \right|, \left| \hat{X}_{i,2} - X_i \right|, \ldots, \left| \hat{X}_{i,M} - X_i \right| \right) \right]. \quad (13)$$

Here M different test methods are being compared at N different points. $X_{i,j}$ is the i^{th} estimate from the j^{th} method. The brackets in the sum are Iverson brackets which are defined as

$$[P] = \begin{cases} 1, & P \text{ is True} \\ 0, & P \text{ is False} \end{cases}. \quad (14)$$

The fraction $100/N$ normalizes the result to a percent of the total data points so that $0 \leq NBEC_j \leq 100$. This allows for the methods to be ranked from that which offers the most agreement to that which offers the least.

Because the methods used here are algebraic manipulations of data, the uncertainty in the results depends on how errors in the original data are propagated through the algorithm, and floating point errors. As none of the data sources provide error or uncertainty information meaningful error bars could not be applied to the RMSE. It is possible for some of the operations to become badly conditioned, and unrealistically large or small values result. These data are omitted from the comparisons. Even if initial error data were available, the non-stationary nature of C_n^2 precludes the ability to determine variance in the traditional sense because the mean itself is a random function of space and time.

RMSE and NBEC are both computed in common-log space. Comparisons were also made in linear space. The over-all ranking of the methods was similar in both spaces, even though the results of individual comparisons may change depending on the space used. The NBEC test has some sensitivity to the choice of computation

space. It is certainly possible for index, j, of the smallest deviation in (13) to change after transformation from the log-space used here back to linear space. RMSE is also affected by the choice of space. As the difference in estimates can often be more than an order of magnitude, periods of over-estimation, even when short, carry significant weight in the linear space-RMSE. Use of log-space estimates is believe to be more practically useful, as most turbulence characterization is presented using log-space.

For the NEXRAD-NWP to scintillometer comparisons, data were taken from each month of the year at both the Dayton and Albuquerque sites. The amount of usable data from each month is limited by the availability and completeness, and quality of both the scintillometer data and radar data. Periods of precipitation, and prolonged periods (greater than $30min$) when the radar or scintillometer data are missing were identified and removed from the RMSE calculations. Before comparison, scintillometer data are low-pass filtered to match the radar measurement times. Therefore, each comparison point corresponds to a radar measurement, which occur on intervals of 5 to $10min$ depending on the radar mode. For the Albuquerque, New Mexico NEXRAD station (KABX), the average C_n^2 points per month is 679, with a minimum of 159 points in September, and a maximum of 1027 points in January. The Wilmington, Ohio NEXRAD station (KILN) data provided an average of 1161 points per month, with a minimum of 111 points in February and a maximum of 4747 from August. Results from the individual months are combined using a weighted average to get the RMSE over the year for each site according to,

$$\langle RMSE \rangle = \sum_{i=1}^{12} w_i RMSE_i. \tag{15}$$

Here $\langle RMSE \rangle$ is the RMSE value in Table 2, and $RMSE_i$ is the RMSE of the i^{th}

month. The monthly weights, w_i, are given by,

$$w_i = \frac{n_i}{\sum_{i=1}^{12} n_i}, \tag{16}$$

n_i is the number of comparison points from the i^{th} month. In addition to the weighted mean, a 12-month mean is also reported as

$$\langle RMSE \rangle = \frac{1}{12} \sum_{i=1}^{12} RMSE_i. \tag{17}$$

Comparing the actual RMSE results to the resampled rates provides a metric for the best possible performance an estimation method could be expected to provide. There are several different combinations of the techniques listed above which can be used to estimate C_n^2. The following list includes the name and a short description of the techniques referenced and presented here.

1. **RF** $N(T)$ Using Tatarskii's method (25), with dN/dT based on RF N in, (24), $d\theta/dz$ obtained from NWP, and ignoring other terms. This is a common method for estimating C_n^2.

2. **Ciddor** $N(T)$ Using Tatarskii's method (25), with dN/dT based on Ciddor's N in, (57), $d\theta/dz$ obtained from NWP, and ignoring other terms.

3. **RF** $N(T, e_v)$ Using Tatarskii's method (25), with dN/dT and dN/de_v' based on the RF N in, (24), $d\theta/dz$, and $de_v dz$ obtained from NWP, and ignoring the dP/dz term. This method is sometimes seen when estimating C_n^2, especially in the RF regime.

4. **Ciddor** $N(T, e_v)$ Using Tatarskii's method (25), with dN/dT and dN/de_v' based on Ciddor's N in, (57), $d\theta/dz$, and de_v/dz obtained from NWP, and ignoring the dP/dz term.

5. **RF** $N(T, e_v, P)$ Using Tatarskii's method (25), with dN/dT, dN/de'_v, and dN/dP' based on the RF N in, (24), $d\theta/dz$, and de_v/dz obtained from NWP, and dP/dz determined from radar Doppler spectrum width, as described in Section 2.4.

6. **Ciddor** $N(T, e_v, P)$ Using Tatarskii's method (25), with dN/dT, dN/de'_v, and dN/dP' based on Ciddor's N in, (57), $d\theta/dz$, and de_v/dz obtained from NWP, and dP/dz determined from radar Doppler spectrum width, as described in Section 2.4.

7. **RF** $N(T, e_v) + WC(T, e_v)$ Here the $RF\ N(T, e_v)$ estimate is corrected using the wavelength correction (46) using RF N for the numerator partial derivatives, and Ciddor's N for the denominator, but with the pressure terms neglected.

8. **RF** $N(T, e_v, P) + WC(T, e_v, P)$ Here the $RF\ N(T, e_v, P)$ estimate is corrected using the wavelength correction (46) using RF N for the numerator partial derivatives, and Ciddor's N for the denominator, and using all 3 terms.

There are also several *baselined* corrections. There refer to the technique described in Section 2.6 where a NWP based C_n^2 estimate is used to correct the radar C_n^2 by removing some of the effects of clutter. These are all named based on the NWP used. So a baselined correction using $RF\ N(T, e_v, P) + WC(T, e_v, P)$ is named *Baselined* $RF\ N(T, e_v, P) + WC(T, e_v, P)$. Image Differential Motion (IDM) C_n^2 have a similar temporal relationship as the radar and scintillometer data. The IDM produces minute by minute C_n^2. The RMSE for the single day of IDM data is not calculated here, however.

2.2 Measurement Methods

Comparison measurements were collected from the scintillometer and the IDM technique. This section describes the site locations and measurement conditions for these instruments. Scintillometer measurements of C_n^2 were provided by two different research groups at two sites. One site is in Dayton, Ohio and the other is near Albuquerque, New Mexico. The Dayton site has been collecting C_n^2 data from a $7km$ path for which has been described previously in literature, [74] and is depicted along with a terrain cross-section in Figure 5. The Dayton site uses an $880nm$ Scintec BLS2000 scintillometer which has been collecting data, when possible, since 2011. The Albuquerque site is a little under half the length of the Dayton path. And passes somewhat closer to the ground with a maximum height near the center of the path which is about $62m$. C_n^2 data from 2013 and 2014 were provided for the Albuquerque site, which also uses an $880nm$ scintillometer.

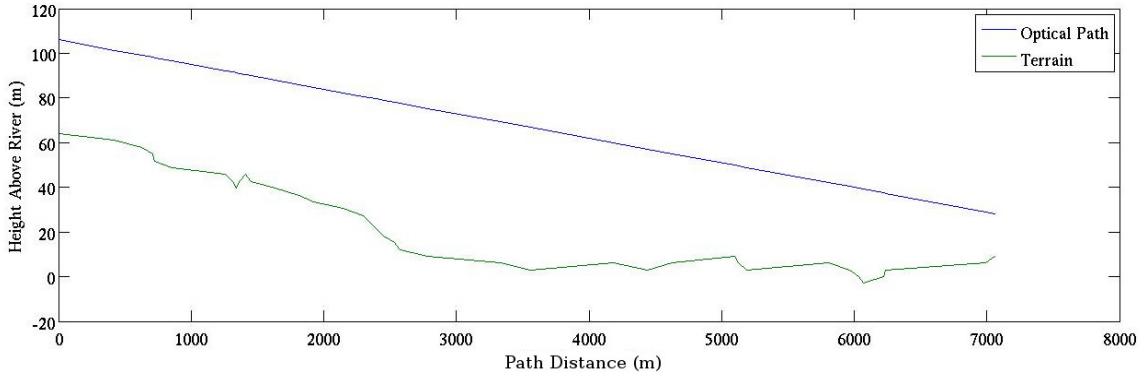

Figure 5. Straight-line path of Dayton scintillometer beam over terrain. The University of Dayton is on the right (East) end of the path and the Dayton VA Medical Center is on the left (West) end. The Great Miami River passes under the path and is about a km from the East end.

The Dayton scintillometer site passes over a river valley and includes both urban, and suburban terrain features. The wide variety of natural and man-made terrain

features creates a complex heating environment in this area. Located at 39.7^oN, the local climate is temperate with large seasonal variability in temperature, precipitation, and humidity. An altitude of around $300m$ results in pressures around $35mb$ below Mean Sea Level (MSL) pressure. The scintillometer path (Figure 5) is oriented in a predominantly East-West direction, with the higher portion of the path on the West. The center of the path is nearly $70m$ Above Ground Level (AGL). As the land slopes down from West to East for the first part of the path, it is expected that the ground will generally receive more direct sunlight at dawn than at dusk. The scintillometer transmitter is inside an enclosure on the roof of the Dayton United States Department of Veterans Affairs (VA) Medical Center. The receiver is located in a University of Dayton (UD) laboratory. It was discovered that the windows of the UD lab blocked most of the $880nm$ light. So for the scintillometer to operate, the window had to be removed. While this would create flows around the window, the path weighting of the scintillometer is nearly zero at the ends so the impact on measurement is negligible.

The Albuquerque site is $3.2km$ long, and located in the Sandia Mountain region. The terrain is high desert with the surface predominantly earth and low shrub. The latitude is similar to the Dayton site, but the elevation is about $1800m$. This leads to significantly lower pressure of about $200mb$ lower than MSL pressure. Albuquerque is unlike Dayton in that its humidity is much lower year-round, and Albuquerque's humidity cycles so that it is greatest in the winter, and the least in the summer. Dayton's humidity is typically greatest in the summer and least in the early spring (Figure 6). Temperature variations show a similar pattern to those in Dayton, but shifted so that the average highs and lows are 10^oF greater throughout the year. Like the Dayton path, the Albuquerque path is elevated partially by passing over a natural valley between two hillsides. However, the center of the path is slightly lower than the Dayton path.

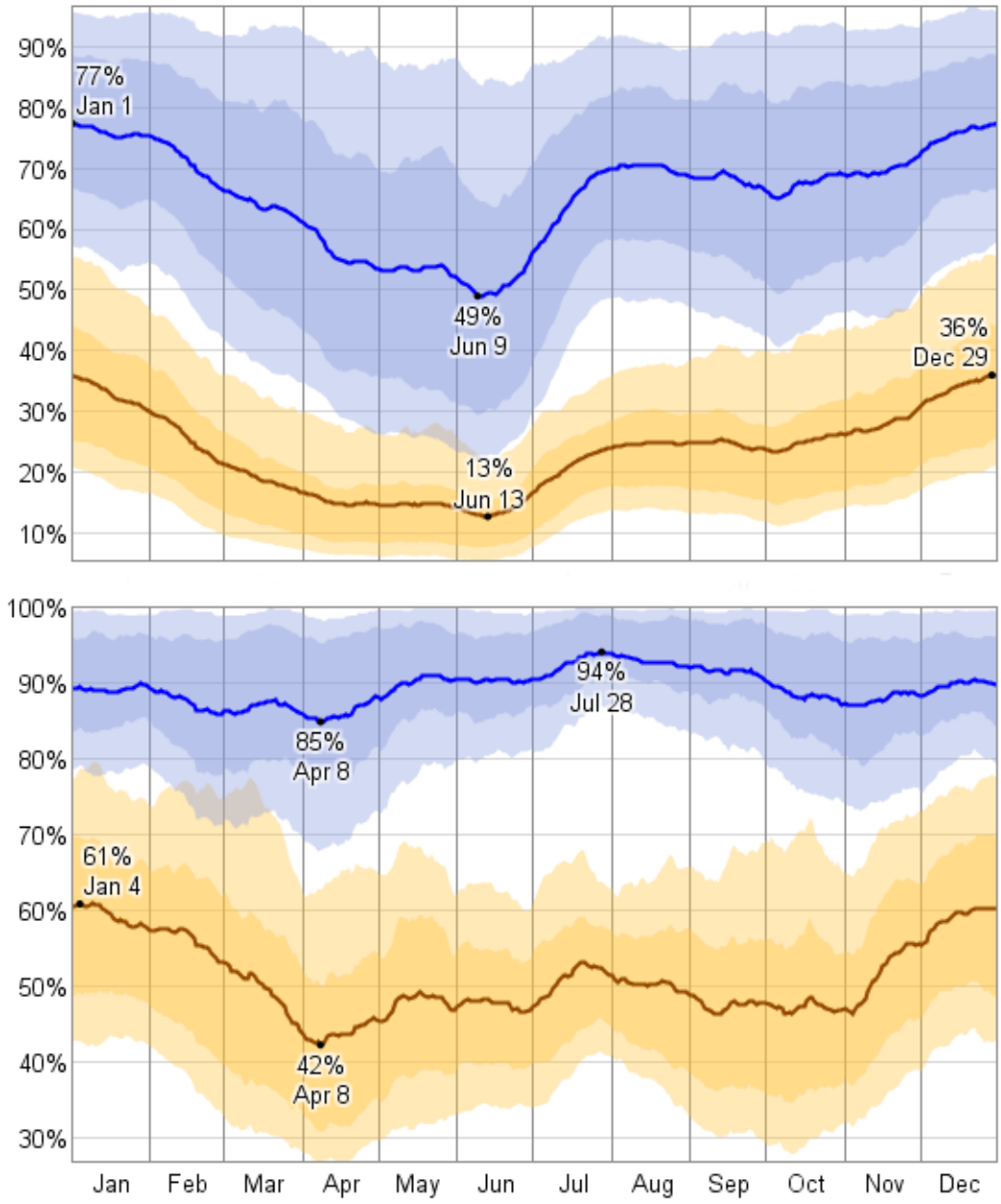

Figure 6. Climatological average daily high (blue) and low (brown) relative humidity for Albuquerque, New Mexico (Top) and Dayton, Ohio (Bottom). Shaded regions indicate 25^{th} to 75^{th} percentile (inner band) and 10^{th} to 90^{th} percentile (outer band). Plots were generated by, and used by permission from WeatherSpark.com [11].

The IDM path is also located in the Greater Miami Valley (Figure 7). It passes from Wright Patterson Air Force Base (WPAFB) to Good Samaritan Hospital. This

path is 12.8km in length, and passes over a wide flat valley. Data are only available from 23 July 2014, a day which was clear in the morning and late afternoon, but was clouded over during midday. Images were collected using a Cannon® 40D digital camera mounted to a tripod with a heat shield to minimize motion due to thermal expansion of the tripod legs. The camera recorded time-lapse images of the hospital over the course of the day. A correlation technique is used to remove vertical variation of the hospital, and then to track the relative motion between portions of the image. By comparing how separate portions of the image move with respect to each other, a path weighted C_n^2 can be extracted [4]. The weighting functions vary depending on which portions of the image are used.

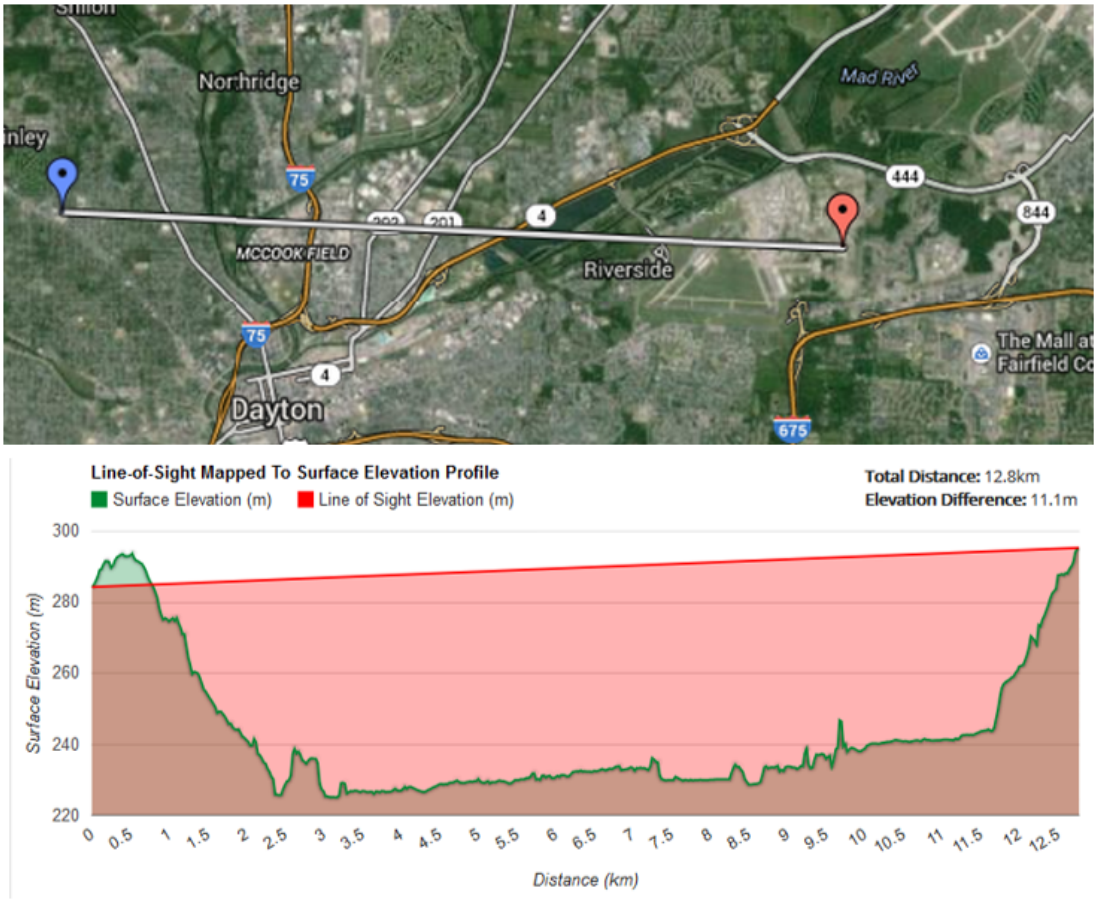

Figure 7. Image Differential Motion path with surface elevation profile. The hospital is on the left and AFIT on the right in the elevation plot. Satellite image ©Google 2015. Figure taken from [4].

2.3 Tatarskii's Method for Determining C_n^2

One of the most common methods for determining the index of refraction structure function constant, C_n^2 is due to Tatarskii [67, 68]. The method often finds C_n^2 as a function of the temperature structure function constant, C_T^2, but may also include the vapor pressure structure function $C_{e_v}^2$ and the cross-temperature-vapor-pressure constant C_{t,e_v}^2. Typically, the $C_{e_v}^2$ and C_{t,e_v}^2 structure function constants are used in the microwave regime, and ignored for visible and IR instruments. The results

section shows that inclusion of these terms degrades RMSE between C_n^2 estimates from Tatarskii's original method and scintillometer C_n^2. Here, this degradation in RMSE is attributed to the fact that an RF equation for $n(T, P, e_v)$ was used by Tatarskii instead of an visible-to-IR $n(T, P, e_v)$. Most modern methods for going back and forth between these structure function constants, and much of turbulence theory is based on his work, and continue to used the RF $n(T, P, e_v)$ and assume that C_n^2 depends solely on C_T^2 in the visible to IR regime [1, 2, 12, 16, 18, 32, 34, 78]. This assumption will be shown to be invalid under some circumstances in later sections.

Regardless of the form of $n(T, P, e_v)$ which is used, Tatarskii's development is still valid. Tatarskii proposed to consider the structure function of index of refraction from the perspective of propagating radiation within a regime appropriate for Klomogorov statistics to apply. If the field is locally homogenous and isotropic in the statistical sense, then the index of refraction structure function has the form, [67]

$$D_n(r) = \left\langle [n(\vec{r} + \vec{x_1}) - n(\vec{x_1})]^2 \right\rangle . \tag{18}$$

In previous work, Obukov showed that for passive additives in a turbulent flow, the structure function will have the form [52]

$$D_\xi(r) = \begin{cases} C_\xi^2 r^{2/3} & l_0 \ll r \ll L_0 \\ C_\xi^2 l_0^{2/3} \left(\frac{r}{l_0}\right)^2 & r \ll l_0. \end{cases} \tag{19}$$

Where ξ is some passive additive, l_0 is the inner scale of the turbulence, and L_0 is the outer scale. Before Obukov, Kolmogorov had shown that the structure function of velocity perturbations within the field also had the same form. Tatarskii went on to show that for PBL turbulence, the structure function constant of a passive additive can be found from the vertical gradient of the mean of the passive additive. A form

of this equation from [16] is

$$C_\xi^2 = a^2 \varepsilon^{-1/3} K_\xi \left(\frac{d \langle \xi \rangle}{dz} \right)^2, \tag{20}$$

where K_ξ is the coefficient of diffusion of the passive additive ξ, ε is the rate of dissipation of turbulent energy into heat, and a is a universal constant on the order of unity.

Certain measurable qualities of the atmosphere can be considered passive additives with respect to turbulence. Being passive means that variations in these parameters do not affect the turbulent flow. By being additive, the quantity does not change on advection. Velocity and pressure perturbations certainly are not passive, but temperature, index of refraction, and vapor pressure are to a good approximation passive. None of these parameters are strictly additive. The reason that parameters like temperature, vapor pressure, and index of refraction are not additive is that hydrostatic balance in the atmosphere creates vertical variation in pressure. Upon advection of an air parcel by turbulence, any change in altitude will change its temperature via an adiabatic equalization to surrounding pressure. Likewise, vapor pressure will change via equalization. Because index of refraction depends on temperature, vapor pressure and pressure, it too must change depending on its vertical displacement. These difficulties are overcome by a change of parameters. Instead of a field of temperature which changes with position and time, $T(\vec{x}, t)$ perturbations of potential temperature $\theta = T \left(P_0 / P \right)^{0.286}$ will be considered. In a similar manner, the potential vapor pressure will be used. Following convention, it will be assumed that any reference in this work to C_n^2 is a reference to the potential index of refraction structure function constant. It is common to use (20) to estimate of C_n^2 in the PBL,

$$C_n^2 = a^2 \varepsilon^{-1/3} K_n \left(\frac{d \langle n \rangle}{dz} \right)^2. \tag{21}$$

Similarly, the temperature structure function can be found using (20). In this and other contemporary work, the variables $\varepsilon^{-1/3}K_\xi$ are transformed so that (20) has the form [2]

$$C_T^2 = a^2 \left(\frac{K_H}{K_M}\right) L_0^{\frac{4}{3}} \left(\frac{\partial\theta}{\partial z}\right)^2, \tag{22}$$

Here a modification has been make to turbulence parameters where $\varepsilon^{-1/3}K_T$ has been replaced by L_0 and the ratio of eddy diffusivity of heat K_H and momentum K_M. Methods for finding K_H/K_M and L_0 from NWP are detailed in [2] and $a^2 = 2.8$. Since C_T^2 can be calculated directly from NWP, it is most common to use Tatarskii's method to find C_n^2 via

$$C_n^2 = \left(\frac{\partial n}{\partial T}\right)^2 C_T^2. \tag{23}$$

Where $\partial n/\partial T$ is the partial derivative of index with respect to temperature. The commonly used parametrization of n is based on refractivity $N = (n-1)\times 10^6$ in the RF regime,

$$RF\ N = \frac{79}{T}\left(P + \frac{4800 e_v}{T}\right). \tag{24}$$

Here T is temperature in K, P is pressure in mb, and e_v is water vapor pressure in mb. While Tatarskii notes that this equation is intended for millimeter waves and longer, it is used in practice for all regimes, from RF to visible light [2, 12, 16, 32, 67, 68, 77].

This method is used here as presented by Alliss and Felton [2] with a difference in that the value of L_0 is set to a fixed value of $100m$ instead of estimating it. A static value was chosen because the approximation of L_0 used by Alliss and Felton relies on thermally stable conditions, but a large portion of data herein was taken under thermally unstable conditions. There is much disagreement in literature as to the typical size of L_0, with estimates ranging from under $5m$ to many hundreds of meters. [78] The $100m$, value was chosen as it works well throughout the year at both locations and will be discussed later in this section.

In this work, this method is extended in two ways. The first is that the assumption that index gradients depend only on potential temperature gradients is removed. Instead the refractive index gradients are expanded in terms of temperature, vapor pressure, and pressure,

$$C_n^2 = a^2 \left(\frac{K_H}{K_M}\right) L_0^{\frac{4}{3}} \left(\frac{\partial n}{\partial T}\frac{d\theta}{dz} + \frac{\partial n}{\partial P}\frac{dP}{dz} + \frac{\partial n}{\partial e_v}\frac{de_v}{dz}\right)^2 . \tag{25}$$

The second modification is that refractivity partial derivatives are calculated two ways. The refractivity equation (24) will still be used for RF systems (NEXRAD and cell phones) In addition to this empirical equation, Ciddor's equation for refractivity is used in the IR to Visible spectrum. Ciddor's equation is given in Section 2.5 and for purposes of this work, can be compactly expressed as

$$N = \frac{P}{ZT}\left(A + x_w B\right). \tag{26}$$

Here Z is the compressibility of moist air; x_w is the molar fraction of water vapor in the air; and A and B are wavelength dependent constants. Implementation of both equations, with inclusion of the various gradients is presented in section Section 2.5, with full parameters and partial derivatives left to the appendix, Section 7.1.

Just as θ is used in place of T, rather than consider the pressure field, $P'(\vec{x},t)$, and vapor pressure field, $e'_v(\vec{x},t)$, which both contain the effects of hydrostatic balance, this work will refer to non-hydrostatic deviations of these two quantities. That is, from here-on $P(\vec{x},t) = P'(\vec{x},t) - P_0 + \rho g z$, and $e_v(\vec{x},t) = e'_v(\vec{x},t)P_0/(P_0 - \rho g z)$ with P_0 being the reference pressure of $1000mb$, ρ being the density of air, g the acceleration due to gravity, and z as the vertical coordinate.

Inclusion of pressure gradients deviates from other developments. The customary treatment is to ignore index gradients induced by local pressure gradients because

pressure equalizes nearly instantly upon advection. However, this ignores the pressure gradients which must be present in order to produce curvature of the flow. Before proceeding, it is important to address the impact of this inclusion of pressure on the assumed form of the structure function. There is a difficulty in that the application of Obukov's two-thirds law (19) in that he derived the law based on the assumption that it describes the local field of a passive additive. [52] As previously stated, to be considered a passive additive a quantity must not significantly affect the turbulent flow upon advection (passive), and its value must be conserved upon transport by the flow (additive). Generally, it is accepted that n can take on the form of a passive additive, if it is a expressed as a function of potential temperature, and specific humidity (or mixing ratio, potential vapor pressure, or some other conserved quantity) [12, 16, 32, 68]. As Obukov mentions, Tatarskii had already developed a statistically based structure function for the velocity perturbation field, which itself is not a passive additive, but also has a two-thirds scaling within the inertial subrange. Velocity perturbations are necessarily tied to localized non-hydrostatic pressure gradients by Newton's second law. Without an accelerating force, the velocity flow would not perturb. Because spatial variation in velocity must be proportional to spatial variation in pressure, it is therefore reasonable to assume that within the inertial subrange, pressure perturbations will also follow a two-thirds law.

An important consideration is whether this modification is necessary, based on the expected magnitudes of dP/dz and $\partial N/\partial P$. It turns out, that for the smallest eddies (less than $50cm$), typical pressure gradients are so slight as to be inconsequential. For the larger eddies, the gradients predicted by the Kolmogorov energy cascade, and a Lamb-Oseen vortex model are certainly of consequence. The degree which the structure function $D_n(r)$ depends on $D_P(r)$, limits the degree to which n can considered a passive additive. The Lamb-Oseen model predicts that, near the core

of larger eddies and at the wavelengths considered here, $D_n(r)$ depends on $D_P(r)$ to a similar degree as it depends on $D_\theta(r)$ and $D_{e_v}(r)$. While n is no longer a passive additive when its distribution is affected by pressure perturbations, the structure functions of velocity and pressure perturbations and passive additives have the same form. This presents a distinction, without a difference in application. Furthermore, inclusion of this pressure term has improved agreement of predicted turbulence with measurement.

It is straightforward to show that (25) is equivalent to that used by [2, 68] and many others under the assumption that the pressure and vapor pressure terms are negligible. Others provide expressions for maintaining the vapor pressure term as well [12, 16], but the only research which the author is aware of where the pressure term is maintained as it is here, is research based on this work [45]. In order to compare the methods described here to what is commonly done, estimates are made to using the temperature term alone as in [2], using temperature and vapor pressure (which can be accomplished using NWP data alone), and using all three terms (which requires radar data and the method in Section 2.4). It would be expected that better agreement with the $880nm$ scintillometer would be found if one were to use Ciddor's equation as the basis of the partial derivatives of N in the following method. The results will show that this is the case when two or three terms are used, but the RF N equation performed better when only temperature is considered.

An issue arises with (25) which is not present in (22): the sign of the terms in the sum. The partials of $N(T, P, e_v)$ and dP/dz always have the same sign, but the θ and e_v gradients may change sign. This may cause the T and e_v terms in (25) to sometimes reduce C_n^2, and at other times increase it. However, based on the physical model, one would expect that the magnitude of the total variation in n will be within

a range which is bounded by the three terms in (25). That is,

$$\left|\left|\frac{\partial n}{\partial T}\frac{d\theta}{dz}\right| + \left|\frac{\partial n}{\partial T}\frac{d\theta}{dz}\right| + \left|\frac{\partial n}{\partial T}\frac{d\theta}{dz}\right| - max\left(\left|\frac{\partial n}{\partial T}\frac{d\theta}{dz}\right|, \left|\frac{\partial n}{\partial T}\frac{d\theta}{dz}\right|, \left|\frac{\partial n}{\partial T}\frac{d\theta}{dz}\right|\right)\right| \leq \left|\frac{dn}{dz}\right| \leq \left|\frac{\partial n}{\partial T}\frac{d\theta}{dz}\right| + \left|\frac{\partial n}{\partial T}\frac{d\theta}{dz}\right| + \left|\frac{\partial n}{\partial T}\frac{d\theta}{dz}\right|. \quad (27)$$

For this reason, three adaptations of (25) are used here. The first is to use (25) as written. The second gives the maximum expected variation by summing the absolute value of each term in the expansion. That is,

$$C_n^2 = a^2\left(\frac{K_H}{K_M}\right)L_0^{\frac{4}{3}}\left(\left|\frac{\partial n}{\partial T}\frac{d\theta}{dz}\right| + \left|\frac{\partial n}{\partial P}\frac{dP}{dz}\right| + \left|\frac{\partial n}{\partial e_v}\frac{de_v}{dz}\right|\right)^2. \quad (28)$$

A third form is used as well based on the 2-norm distance in a space whose dimensions are the three terms in the expansion,

$$C_n^2 = a^2\left(\frac{K_H}{K_M}\right)L_0^{\frac{4}{3}}\left[\left(\frac{\partial n}{\partial T}\frac{d\theta}{dz}\right)^2 + \left(\frac{\partial n}{\partial P}\frac{dP}{dz}\right)^2 + \left(\frac{\partial n}{\partial e_v}\frac{de_v}{dz}\right)^2\right]. \quad (29)$$

For a majority of the measurements, (29) gave the best agreement between estimated and measured C_n^2. Unless otherwise noted, this form will be use in the remainder of this work.

As is customary, partials of refractivity, $N = (n-1)\times 10^6$, rather than refractive index n will be used to calculate C_n^2 in the remainder of the work. The results of using the more customary equation, (24), are used here, but (25),(28), and (29) are also evaluated based on the Ciddor refractivity equation, (57), which is known to more accurately predict refractivity in the visible and IR regime [13]. Comparisons of using *RF N* from (24) and *Ciddor's N* from the Ciddor equation, [13] are made. It is shown in the results that *Ciddor's N* provided much better agreement with the $880nm$ scintillometer C_n^2 than the RF N when estimating C_n^2 with (25), (28),

(29). Using *Ciddor N* typically reduces the RMSE by one-half or more. However, the temperature only estimates based on the conventional equation, (24), provide somewhat better agreement when applied to (22).

The quantity, $a^2 (K_H/K_M) L_0^{4/3}$, is found as described by Alliss and Felton [2]. As mentioned, the value of L_0 must be chosen, and this can have a significant impact on the value of C_n^2. In [2], the lower bounds of the Turbulent Kinetic Energy (TKE) used in their Mellor-Yamada-Janjic closure scheme [48] was modified, to bring C_n^2 down so that it better matched the data. The result of this lower bounds reduction is to reduce the size of L_0. As mentioned in Section 2.2, there is much disagreement in the correct value of L_0. In many cases, L_0 is chosen so that measurement and modeled data sets match well. [2, 34, 48, 78] Following conclusions of other authors, it is expected that actual value of L_0 depends on several factors involved in the PBL TKE budget. In this data, increasing L_0 causes the NWP based C_n^2 to more closely match the NEXRAD based C_n^2 data, and decreasing L_0 causes the NWP C_n^2 to more closely match the scintillometer data. Adjustments in L_0 could have been made for each data set in order to improved agreement in any particular method, but leaving L_0 fixed is believed to give the fairest representation of the performance of the methods used here. Using $L_0 = 100m$ appeared to give the best agreement for the standard, temperature only RFN method in all of the data sets presented here. This value is not only reasonable based on other observations of L_0 at altitudes of around $70m$, but it also favors the standard method for estimating C_n^2 in the RMSE and NBEC results. This way a persistent and significant improvement by one of the newly proposed methods can be attributed to the merits of the method, and not manipulation of L_0.

The partial derivatives $\partial N/\partial T$, $\partial N/\partial P'$, and $\partial N/\partial e_v'$ as well as mean gradients $d\theta/dz$ and de_v/dz are found from NWP data using the methods described in Sec-

tion 3.1. The dP/dz term is found using the method described in Section 2.4. While direct calculation of C_n^2 from these gradients and partial derivatives has been found to be the most straightforward method for estimating C_n^2, two other approaches were developed as well. The wavelength correction, and baselining method. These methods are also presented in this chapter, and their use may be preferable under certain circumstances.

2.4 Non-Hydrostatic Pressure Gradients

When mean potential temperature and vapor pressure gradients head to zero, C_n^2 values should likewise drop to zero according to (21). However, when observed gradients do go to zero, C_n^2 values in measured data do not drop as much as expected (For example, Figure 8). These small gradients create unrealistically small C_n^2 and thus errors when using the estimation scheme in Section 2.3 and sometimes numerical instability in the wavelength correction presented in Section 2.5. In order to address the issue, we consider here a method for estimating the non-hydrostatic pressure gradients generated by the circulation of turbulent eddies. Estimation of gradients using this method has produced consistent, measurable improvement in the agreement at both locations.

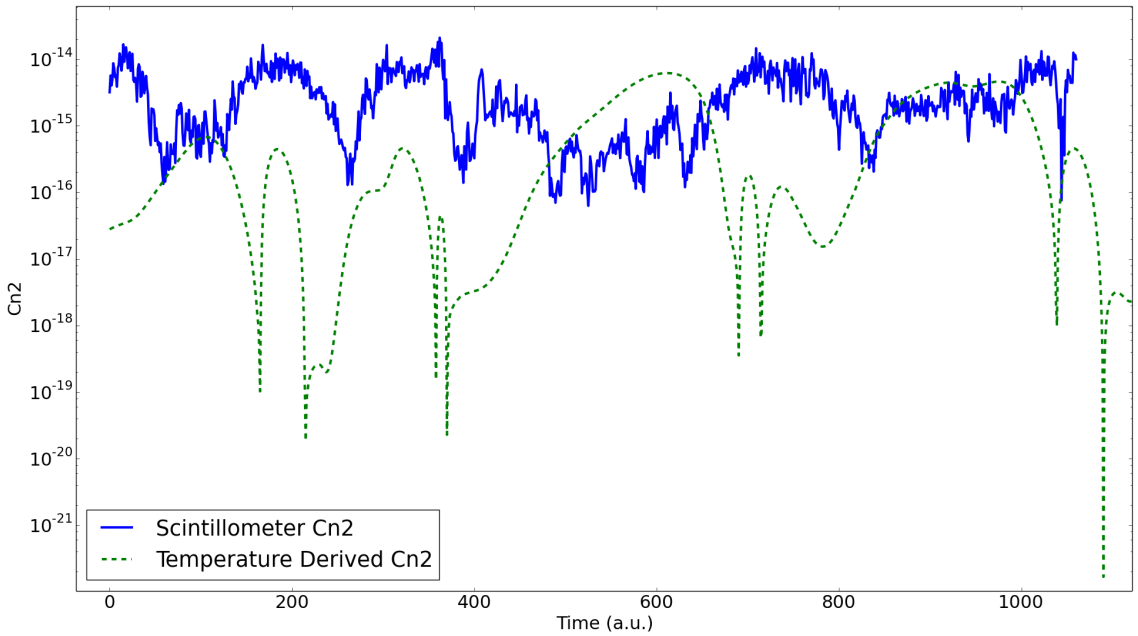

Figure 8. Scintillometer C_n^2 (solid blue line) taken from the Dayton, Ohio path on 21 to 26 July, 2014. Also, C_n^2 derived from NWP-based potential temperature gradients (dashed green line) for the same location and time period.

The existence of non-hydrostatic pressure gradients is predicted by the kinematics of eddy circulation. As with all rotational motion, air parcels must be continuously accelerated by some force, $\vec{F} = m\vec{a}$. In the case of a vortex within a fluid, this acceleration is created by a pressure gradient, which can be determined given a fluid density' ρ, tangential velocity, v, and radius of curvature, r. Here we assume that eddys quickly evolve to an irrotational form, and use the Lamb-Oseen vortex as a model. [61] In the Lamb−Oseen vortex,

$$v(r,t) = \frac{\Gamma}{2\pi r}\left[1 - exp\left(-\frac{r^2}{r_c^2(t)}\right)\right]. \tag{30}$$

Here Γ is the vortex circulation, and $r_c(t) = \sqrt{4\nu t}$ is the size of the vortex core, and ν is the viscosity.

From this model, we can compute the radial pressure gradient function,

$$\frac{dP}{dr}(r,t) = \rho\frac{v^2(r,t)}{r}. \tag{31}$$

In order to determine r_c, the mean eddy lifetime, τ_e as a function of eddy size must be determined. Tatarskii gives the rate of formation of the velocity fluctuations as $t^{-1} = v_l/l$ with l as the dimension of the disturbance (vortex size), $v_l \approx (\varepsilon l)^{1/3}$ as the characteristic velocity perturbation at length l, and ε as the rate of eddy energy dissipation into heat. Under steady state conditions, the eddy formation and dissipation rates must be the same. Since the mean lifetime of an eddy is the reciprocal of its dissipation rate, we use

$$\tau_e \approx l/v_l = \left(\frac{l^2}{\varepsilon}\right)^{1/3}. \tag{32}$$

This assumption allows r_c to be determined by eddy size, l. The circulation, Γ is then found as a function of eddy size based on eddy energy. The eddy energy is found by integrating over the eddy volume,

$$E(l) = \int_0^l \int_0^{2\pi} \int_0^{2l} \frac{\rho}{2} v(r,l)^2 r dr d\theta dz. \tag{33}$$

Here cylindrical coordinates are used, with the vortex cylinder length (in the z dimension) being equal to its diameter. Tatarskii gives the eddy energy as

$$E(l) = a\varepsilon^{2/3}\left(\frac{2\pi}{l}\right)^{-11/3}. \tag{34}$$

Equating (33) and (34) with (32) substituted into $v(r,\tau_e)$ from (30) and integrating

over θ and z gives

$$a\varepsilon^{\frac{2}{3}}\left(\frac{2\pi}{l}\right)^{-\frac{11}{3}} = \frac{\rho l\Gamma^2(l)}{2\pi}\int_0^l \frac{\left[1-exp\left(-\frac{r^2}{4\nu}\sqrt[3]{\frac{\varepsilon}{l^2}}\right)\right]^2}{r}dr. \tag{35}$$

Solving for $\Gamma(l)$ gives

$$\Gamma(l,\varepsilon) = \frac{\varepsilon^{\frac{1}{3}}\sqrt{a}\left(\frac{l}{2\pi}\right)^{\frac{4}{3}}}{\sqrt{\rho\int_0^l \frac{\left[1-exp\left(-\frac{r^2}{4\nu}\sqrt[3]{\frac{\varepsilon}{l^2}}\right)\right]^2}{r}dr}}. \tag{36}$$

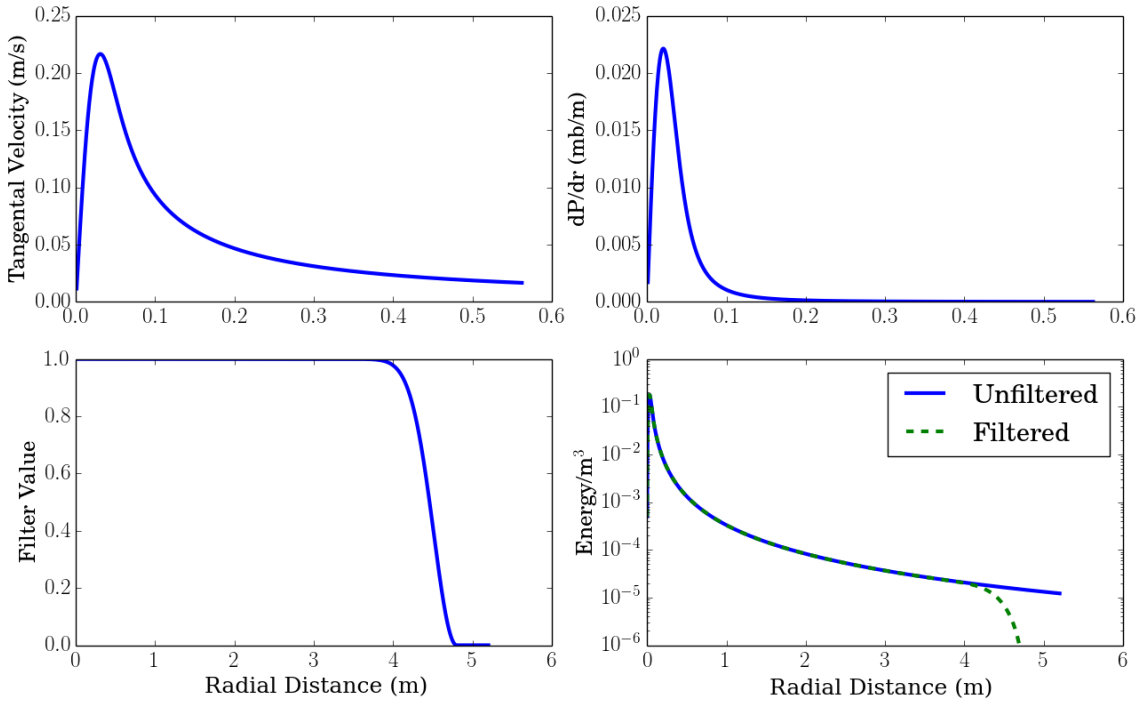

Figure 9. Top Left: Lamb−Oseen tangential velocity vs radial distance. Top Right: Pressure gradient vs radial distance. Bottom Right: Spatial filter vs radial distance as applied during integration of eddy energy. Bottom Left: Energy spectrum vs radial distance before and after applying the filter. All plots show values for a $4m$ eddy with $\varepsilon = 0.003m^2s^{-3}$ and an atmosphere at standard temperature and pressure. Some of the x-axis (radial distances) are truncated to less than the eddy's full $4m$ in order to show detail.

From (36) it can be seen that Γ depends, to first order, on $l^{4/3}$, and $\varepsilon^{1/3}$. The function $\Gamma(l, \varepsilon)$ is approximated numerically. During integration, a window function (Bottom left of Figure 9) is applied to force the eddy energy to zero near the 'edge' of the eddy. This filter represents fluid motions becoming uncorrelated with the eddy's vorticity at sufficient range from the eddy center and allows the numerical integral to converge. While numerical approximation of $\Gamma(\,\varepsilon)$ can be slow to compute, a fast and reasonable estimate can be calculated quickly based on the observation that $\Gamma(l, \varepsilon)$ is nearly linear in log-space of typical PBL eddy sizes and ε values. To produce the fast approximation, we define $\Gamma_0(l) = \Gamma(l, \varepsilon = 1.0)$. Taking the ratio $\Gamma(l, \varepsilon)/\Gamma_o(l)$ using (36) we find that

$$\Gamma(l, \varepsilon) \approx \Gamma_0(l)\varepsilon^{1/3}. \tag{37}$$

To approximate $\Gamma_0(l)$ we use a quadratic approximation

$$\Gamma_0(l) = exp\left[-0.80063 - 1.2822\frac{2\pi}{l} + 0.0047108\left(\frac{2\pi}{l}\right)^2\right]. \tag{38}$$

The quadratic approximation of $\Gamma_0(l)$ is correct to within $10^{-1.5}$ for eddies between $1cm$ and $100m$ (Figure 69).

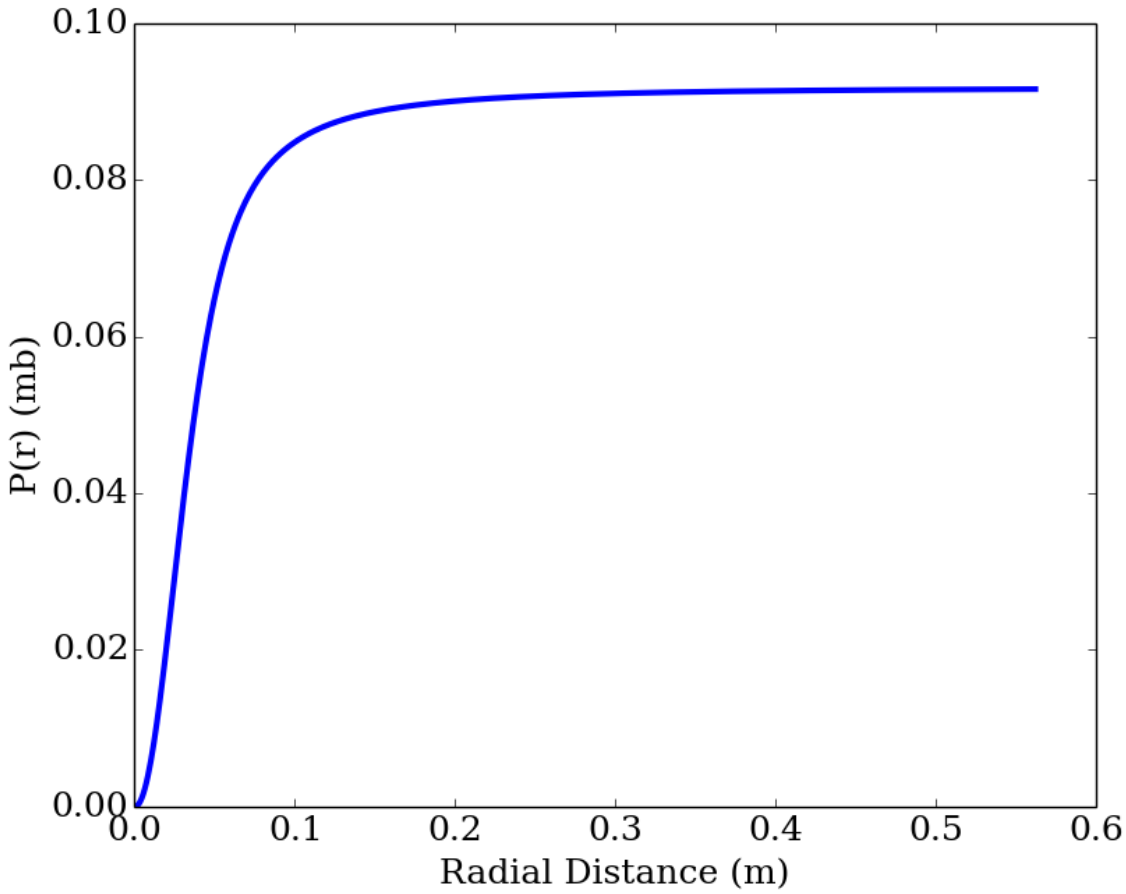

Figure 10. Pressure vs radial distance of $4m$ Lamb-Oseen vortex with $\varepsilon = 0.003m^2s^{-3}$ Pressure values are in millibars and signify deviations from the pressure at the center of the vortex.

Looking at the top right plot of Figure 9, it can be seen that the peak pressure gradient occurs at a radius of about 2.5 cm. This corresponds with a scattering body with diameter $D_s = 5cm$, which meets the Bragg condition for peak back-scattering. By integrating the dP/dr curve, the pressure structure itself can be found (Figure 10). This structure shows that most pressure variation (and thus pressure-related index variation) is confined to a region which is relatively narrow compared to the eddy size. If index perturbations were dependent on pressure perturbations alone, then the difference between the vortex size, D_v, and scattering body size, D_s, of this eddy

would be on the order of

$$\frac{D_s}{D_v} \approx 0.00625. \tag{39}$$

However, the size of the scattering portion of the eddy also depends on local temperature and water vapor perturbations. Using the same Lamb-Oseen velocity model, it is possible to consider how a uniform gradient would evolve under advection by a Lamb-Oseen vortex. Figure 11 shows the evolution of a gradient due to a Lamb-Oseen vortex over one mean eddy lifetime. Here, the core radius, r_c in (30), is left constant rather than varying with time. It is apparent that the parameter is spatially perturbed on scales much greater than that of the pressure (Figure 10), but still somewhat less than that of the total eddy size. Taking the scattering region from the Bottom-Right plot of Figure 11 to have a size of roughly $D_s = 0.5m$, the ratio of scatter to vortex size is

$$\frac{D_s}{D_v} = 0.0625. \tag{40}$$

This is still a large ratio considering the impact on the scaling of the energy spectrum based on measurement. Following the five-thirds law, this indicates that the spectrum scaling constant would be approximately 100 times too large! On the other hand, this does not create a significant change in scaling between C_n^2 measured by two different instruments as the ratio (40) does not change much for measurements taken throughout the inertial subrange. This is especially true for comparisons of C_n^2 measured by instruments like the large aperture scintillometers and NEXRAD radar, where the dominant scale for eddy interaction is about the same; around $5cm$ for both systems. Where this scaling may cause difficulty is in schemes which attempt to draw relationships between TKE and C_n^2.

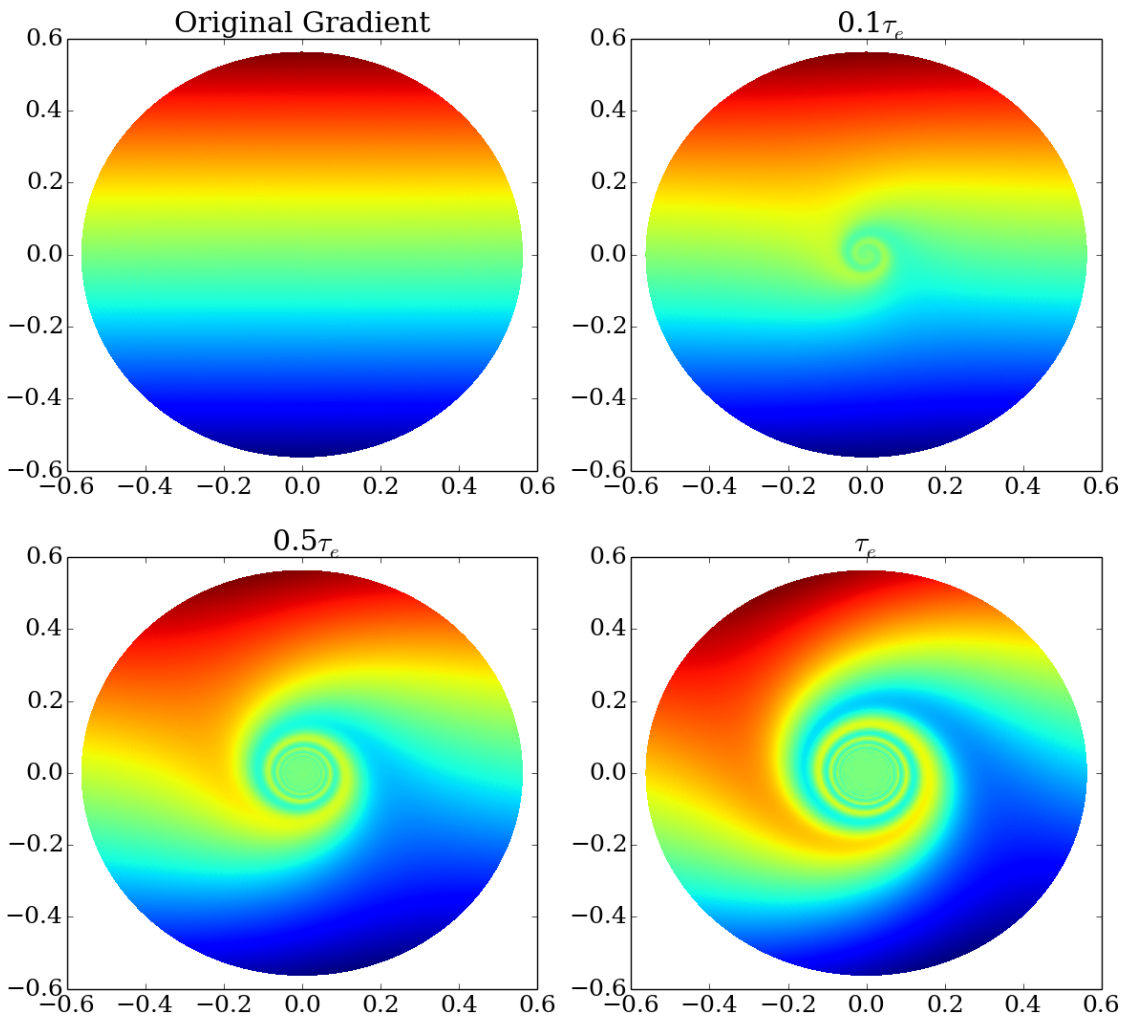

Figure 11. Plots show time evolution of gradient structure under advection by a Lamb-Oseen vortex with a $4m$ radius, thermal dissipation $\varepsilon = 0.003m^2s^{-3}$, atmospheric density of $\rho = 1.2041\ kg \cdot m^{-2}$, and kinematic viscosity $\nu = 1.5 \times 10^{-5}\ m^2s^{-1}$. Times are given above each plot relative to τ_e, the mean eddy lifetime. X and Y axis represent position, and plot color represents the passive additive value (arbitrary units).

2.5 Wavelength Correction

As described in Section 1.2, C_n^2 decorrelates quickly with small displacements in the centroid of a described volume, or time interval. Here the size of displacement is *small* when compared to the extent of the volume itself. In addition C_n^2, changes as

the wavelength, λ, of propagating radiation changes, even when measuring identical volumes. There is a difference between wavelength-based C_n^2 variation and spatial or temporal variation of C_n^2. Wavelength variation is not a chaotic process, and it depends on the response of n to T, P, and e_v at a particular wavelength. In principal, if C_T^2, C_P^2, $C_{e_v}^2$, and all the cross terms (C_{T,e_v}^2, C_{P,e_v}^2, and so on) are known, it is possible to determine the difference in C_n^2 at two different wavelengths with precision limited by measurement noise and the accuracy of the $n(T, P, e_v)$ relationship which is used. This section presents a method to estimate the wavelength dependent variation in C_n^2 based on $n(T, P, e_v)$ and passive additive gradients for θ, e_v and P.

The sensitivity of C_n^2 measurements to changes in λ can vary significantly with the wavelengths concerned and the measurement method [16,32,62,74]. For example, the Scintec scintillometer has relatively little λ dependence when used within path lengths recommended by the manufacturer. This λ independence comes about because the spectral weighting emphasizes eddies between 1 and $10cm$ while the first Fresnel zone size is less than $1cm$ [62]. However, over larger propagation paths, in the so-called 'deep turbulence' regime, chromatic dependence of C_n^2 can be seen [74]. In addition, measurements of C_n^2 taken with wavelengths in the RF, which are orders of magnitude larger than visible and IR wavelengths are expected to show significant differences. Because of these differences, a wavelength correction for C_n^2 was sought, and was the starting point of much of this research. The correction here is based on work that has been presented before in [9, 15, 19, 21]. As these previous works presented, the premise of the wavelength correction is that the index of refraction of the atmosphere depends jointly on temperature, pressure, and atmospheric composition, as well as the wavelength of the propagating wave. Under the assumption that the physical conditions are unaffected by the propagating wave, we look for a way to estimate C_n^2 measured at one wavelength from measurements taken at another wavelength (in this

case, estimating C_n^2 an $880nm$ based on C_n^2 measured at $10.7cm$).

To develop the wavelength correction, begin considering two monochromatic waves propagating through PBL turbulence. For wavelengths which do not experience strong resonant absorption (outside of the anomalous dispersion curve) $N = (n - 1) \times 10^6$ is predominantly a function of temperature, pressure, and the ratio of water vapor to dry air. Following the development of Tatarskii [67,68], we expect that there is space time function which describes the local distribution of each of these parameters, $T(\vec{x}, t)$, $P'(\vec{x}, t)$, and $e'_v(\vec{x}, t)$, respectively. As in Section 2.3, e'_v signifies vapor pressure, T is temperature, P' is pressure, and the prime indicates that values which include the effects of hydrostatic balance and turbulence induced perturbations. As is commonly done, T will be converted to potential temperature, which we will denote as $\theta = T\,(P_0/P)^{0.286}$. As we are not interested in the hydrostatic vertical variation of P' and e'_v, we will refer to non-hydrostatic deviations of these two quantities. That is, from here-on $P(\vec{x}, t) = P'(\vec{x}, t) - P_0 + \rho g z$, and $e_v(\vec{x}, t) = e'_v(\vec{x}, t)P_0/(P_0 - \rho g z)$ with P_0 being the reference pressure of $1000mb$, ρ being the density of air, g the acceleration due to gravity, and z as the vertical coordinate of $\vec{x}$. The expression for the non-hydrostatic vapor pressure comes from taking the potential vapor pressure with local pressure at hydrostatic balance. [16]

Within a region appropriate for Kolmogorov statistics to apply we would like to consider the structure function of index of refraction from the perspective of propagating radiation. In this region, the random fields $P(\vec{x}, t)$, $T(\vec{x}, t)$, and $e_v(\vec{x}, t)$ all have approximately stationary first increments. We make the customary simplification that the propagation time of electromagnetic waves is much shorter than time scales of the evolution of structure functions, so the flow is considered to be 'frozen' during propagation. If the field is locally homogenous and isotropic according to [67] within the region of interest, then we can define the index of refraction structure

function

$$D_n(r) = \left\langle [n(\vec{r} + \vec{x_1}) - n(\vec{x_1})]^2 \right\rangle . \tag{41}$$

It is then natural to consider, how would the structure functions at two different wavelengths, say $D_{n,10.7cm}(r)$ for $10.7cm$ radiation and $D_{n,880nm}(r)$ for $880nm$ radiation differ from one another within the same region. Using Obukov's two-thirds law [52] for the structure function of index of refraction in fully developed turbulence gives

$$D_n(r) = \begin{cases} C_n^2 r^{2/3} & l_0 \ll r \ll L_0 \\ C_n^2 l_0^{2/3} \left(\frac{r}{l_0}\right)^2 & r \ll l_0 \end{cases} \tag{42}$$

where l_0 and L_0 are the inner and outer scales of the inertial sub-range. Within the inertial subrange it is apparent that if $D_{n,10.7cm}(r) \neq D_{n,880nm}(r)$ then $C^2_{n,10.7cm} \neq C^2_{n,880nm}$. Therefore, we look for a method to relate the two structure function constants.

The wavelength correction is accomplished by expressing the ratio of the $C^2_{n,\lambda}$ values at each wavelength. Making use of Tatarskii's method (21), the ratio of C_n^2 values is related to the ratio of the vertical variations of n at each wavelength, dn_λ/dz,

$$\frac{C^2_{n,\lambda 1}}{C^2_{n,\lambda 2}} = \left(\frac{dn_{\lambda 1}/_{dz}}{dn_{\lambda 2}/dz} \right)^2 . \tag{43}$$

Here we have followed [16, 67] and assumed that the ratio of diffusion constants $K_{n,\lambda 1}/K_{n,\lambda 2}$ is approximately unity.

To find dn_λ/dz, a wavelength-appropriate empirical equation for refractivity, N, at each wavelength is used along with the local T, P, and e_v from weather forecast data. The equation is expected to have the form

$$N_\lambda = N(T, P, e_v : \lambda). \tag{44}$$

To find dn/dz we do a standard expansion of (44) in terms of its partials $\partial N/\partial T$, $\partial N/\partial P$, and $\partial N/\partial e_v$.

$$\frac{dN}{dz} = \frac{\partial N}{\partial P'}\frac{dP}{dz} + \frac{\partial N}{\partial T}\frac{d\theta}{dz} + \frac{\partial N}{\partial e'_v}\frac{de_v}{dz}. \tag{45}$$

This gives a wavelength correction

$$\frac{C^2_{n,\lambda 1}}{C^2_{n,\lambda 2}} = \left(\frac{\frac{\partial N_1}{\partial P'}\frac{dP}{dz} + \frac{\partial N_1}{\partial T}\frac{d\theta}{dz} + \frac{\partial N_1}{\partial e'_v}\frac{de_v}{dz}}{\frac{\partial N_2}{\partial P'}\frac{dP}{dz} + \frac{\partial N_2}{\partial T}\frac{d\theta}{dz} + \frac{\partial N_2}{\partial e'_v}\frac{de_v}{dz}} \right)^2. \tag{46}$$

As mentioned in Section 2.3, the terms in the sum of the wavelength correction, (46) are added using the 2-norm, resulting in a wavelength correction,

$$\frac{C^2_{n,\lambda 1}}{C^2_{n,\lambda 2}} = \frac{\left(\frac{\partial N_1}{\partial P'}\frac{dP}{dz}\right)^2 + \left(\frac{\partial N_1}{\partial T}\frac{d\theta}{dz}\right)^2 + \left(\frac{\partial N_1}{\partial e'_v}\frac{de_v}{dz}\right)^2}{\left(\frac{\partial N_2}{\partial P'}\frac{dP}{dz}\right)^2 + \left(\frac{\partial N_2}{\partial T}\frac{d\theta}{dz}\right)^2 + \left(\frac{\partial N_2}{\partial e'_v}\frac{de_v}{dz}\right)^2}. \tag{47}$$

This correction differs from previous work in that previous work had focused on ignoring the $\frac{dP}{dz}$ terms, and estimating the vertical gradients from NWP models [15,19,21], or by assuming that pressure and vapor pressure variation can be correlated to temperature variation [9]. Like previous methods, the gradients $\frac{dT}{dz}$ and $\frac{de_v}{dz}$ are estimated numerically from NWP models. A difficulty that arose in previous work was that vertical gradients of T and e_v (estimated using a first or second order differencing scheme) would often head to zero, making the ratio in (46) ill-conditioned. [15, 19, 21] As will be described in Section 3.1, gradients are now estimated using a third-order undetermined coefficient method, which reduces the occurrence of near-zero gradients.

The performance of the wavelength correction based on the number of terms will be investigated in this research. The correction using only the NWP-derived

potential-temperature gradient, $d\theta/dz$ is applied, along with one which uses both $d\theta/dz$ and the potential vapor pressure gradient, de_v/dz, and one which uses all three gradients $d\theta/dz$, de_v/dz, and dP/dz. As pressure gradients are actually radial in nature, following the turbulent flow's radius of curvature, they persist and are finite even when $d\theta/dz$ and de_v/dz go to zero. Because it prevents dN/dz from approaching zero, application of the correction with the pressure term removes the numerical instability from the wavelength correction (47).

Once all three gradients, dP/dz, $d\theta/dz$, and de_v/dz are determined, the next step is to evaluate the partial derivatives for each wavelength. For the radar, we use (24), restated here for convenience,

$$N = \frac{79}{T}\left(P + \frac{4800e_v}{T}\right). \tag{48}$$

Taking the partial derivative of (48) with respect to pressure, temperature and vapor pressure gives

$$\frac{\partial N}{\partial P} = \frac{79}{T}, \tag{49}$$

$$\frac{\partial N}{\partial T} = -\left(\frac{79P}{T^2} + \frac{2 \cdot 4800 \cdot 79e_v}{T^3}\right), \text{and} \tag{50}$$

$$\frac{\partial N}{\partial e_v} = \frac{4800 \cdot 79}{T^2} \tag{51}$$

A similar technique is applied below to Ciddor's equations. While this solution works well for wavelengths far from absorption lines, as λ approaches absorption features (like the $22GHz$ H_2O line), the wavelength dependence of N becomes apparent. In principal, it is possible to take the partial derivative of a more complete functional form of $N(T, P, e_v, \lambda)$, one which includes wavelength dependent absorption effects and how the absorption depends on pressure. [27] However, this approach quickly becomes complicated, especially when several absorption features are present at once.

An alternative approximate approach is used here which leverages existing codes like LEEDR or MODTRAN [5,22] which can accurately predict N with absorption effects included from extensive libraries of chemical species absorption spectra. Let N_C be the continuum refractivity predicted by an equation such as (48) or the Ciddor Equation. Let N be the refractivity which includes both the continuum effect and all relevant absorbing species in the atmosphere. As is shown in Section 7.1, an approximation can be made that

$$\frac{\partial N}{\partial x} \approx \frac{1}{N_C}\frac{\partial N_C}{\partial x}N. \tag{52}$$

This computation is much faster as N can be obtained from available software packages, and $\frac{1}{N_C}\frac{\partial N_C}{\partial x}$ can be found with by dividing (49), (50), and (51) by N_C. The resulting partial derivatives are:

$$\frac{\partial N}{\partial P} \approx \frac{NT}{4800e_v + PT}, \tag{53}$$

$$\frac{\partial N}{\partial e_v} \approx \frac{N4800}{4800e_v + PT}, \tag{54}$$

$$\frac{\partial N}{\partial T} \approx -\frac{N}{T}\frac{(9600e_v + PT)}{4800e_v + PT}. \tag{55}$$

For the 880 nm scintillometer, Ciddor's Equations must be used. Applying the same technique above begins with with, [13],

$$N = \rho_\alpha \frac{N_{\alpha s}}{\rho_{\alpha s}} + \rho_w \frac{N_{ws}}{\rho_{ws}}. \tag{56}$$

Where $N_{\alpha s}$ and N_{ws} are the wavelength-dependent reactivities of dry air and water vapor, respectively, under standard conditions; and $\rho_{\alpha s}$ and ρ_{ws} are the densities of dry air and water vapor under those conditions. The dependance of N on z is contained in the densities of dry air and water vapor in the air, ρ_α and ρ_w. Inserting

the expressions for the density of dry and and water vapor gives,

$$N = \frac{PM_\alpha}{ZRT}(1 - x_w)\frac{N_{\alpha s}}{\rho_{\alpha s}} + \frac{PM_w}{ZRT}x_w\frac{N_{ws}}{\rho_{ws}}. \tag{57}$$

Here, M_{alpha} is the molar mass of the dry component of the air, M_w is the molar mass of water vapor, x_w is the molar mixing ratio of water vapor to dry air, Z is the compressibility of moist air, R is the gas constant, and P is the pressure. As mentioned previously, this equation is simplified here to

$$N = \frac{P}{ZT}(A + x_w B). \tag{58}$$

Where A and B are wavelength dependent constants. As in the RF development above, the variation is put in terms of refractivity so that the base refractivity at a given wavelength, can be input from other models. The resulting equations for the partial derivatives of the Ciddor equations are

$$\frac{\partial N}{\partial P} \approx N\left(\frac{1}{P} - \frac{dZ}{dP}\frac{1}{Z},\right) \tag{59}$$

$$\frac{\partial N}{\partial e_v} \approx N\left[\left(1 - \frac{N_0}{N}\right)\frac{1}{x_w}, -\frac{dZ}{dx_w}\frac{1}{Z}\right]\frac{f}{P} \tag{60}$$

$$\frac{\partial N}{\partial T} \approx -N\left(\frac{1}{T} + \frac{dZ}{dT}\frac{1}{Z}\right). \tag{61}$$

In (60) N_0 is the index of refraction of the dry component of the air, and $f/P = dx_v/de_v$. Expressions for finding A, B, Z, dZ/dP, dZ/dT, and dZ/dx_v are taken from Ciddor's work with consideration being made for use of Pascals instead of millibars, and his slightly different definition of $N = (n-1)10^8$. Details of the Ciddor equations and constants, as well as the partial derivative terms are presented in Section 7.1.

2.6 Radar Baselining

The temporal and spatial resolution of NWP models is poor when compared to the radar, cell phone path, or the scintillometer. Despite these limitations, NWP based C_n^2 is often a good predictor of the low-frequency (variation over hours and days) behavior of C_n^2. NEXRAD can provide similar temporal resolution to the scintillometer, and has spatial resolution adequate to resolve C_n^2 structure along the cell phone, imaging, and scintillometer paths used here. However, as will be shown in Section 4.8 NEXRAD C_n^2 from the lowest elevation suffers from significant ground clutter, causing it to over-estimate C_n^2. Application of a noise correction by the following method will be referred to as *baselining*. The baselining technique attempts to use the NWP C_n^2 to correct the NEXRAD C_n^2 values by reducing NEXRAD C_n^2 values so that the mean C_n^2 reported by the NEXRAD matches that of the NWP C_n^2. This technique can also be applied to cell phone C_n^2 to allow it to estimate optical C_n^2.

Noise and clutter in the NEXRAD data may come from reflections off the ground, precipitation, aircraft, or wildlife. Regardless of the source of noise in radar C_n^2, if the noise is reasonably white and the clear air turbulence signals have a sufficient Signal to Noise Ratio (SNR), it may be possible to correct the radar C_n^2 with the baseline technique described here. Use of this technique provides an advantage over direct application of Tatarskii's method as it provides the opportunity to apply path-weighting functions to the corrected radar reflectivity. While path weighting was not applied to the Scintillometer comparison data, it was applied in the IDM comparison.

To make the baseline correction, NWP C_n^2 values are computed for each radar C_n^2 measurement. Then the the log of both the radar and NWP C_n^2 is low-pass filtered with a sliding mean. The difference between the filtered C_n^2 functions is then computed, and added to the unfiltered radar C_n^2,

$$C^2_{n,corrected} = C^2_{n,radar}(t) - C^2_{n,radar}(t) * f_M(t) + C^2_{n,NWP}(t) * f_M(t). \quad (62)$$

Here the $*$ symbol denotes discrete convolution, and $f_M(t)$ is the filter function which produces the M point sliding mean. Before correcting the data, precipitation signatures in the radar C_n^2 data, and periods of unrealistic NWP gradients are identified. This is done manually for each radar data set and discussed in more detail in Section 4.5 and Section 4.3. In about half the files (especially those which may have contained biological signatures), precipitation signatures were verified against ground observations, and compared well. The remaining C_n^2 data points from NWP and NEXRAD are then transformed into log-space and low-pass filtered as described above. The convolution is performed with a M-point wide rect function.

$$C^2_{n,Filtered}(m) = \frac{1}{M} rect\left(\frac{n}{M}\right) * C_n^2(n). \quad (63)$$

For comparison against scintillometer data, an $M = 10$ point filter was used. This produces a 50 to 90 minute (depending on NEXRAD scanning rate) 'sliding-average' of the log of both signals.

When generating C_n^2 data for the path weighting function for comparison with the IDM C_n^2 a similar baselining technique was used. First the unweighted path average was computed using (83), just is it was for scintillometer comparisons. Next, the baselining correction term was found for each radar measurement time, t, as

$$B_t = C^2_{n,NWP}(t) * f_M(t) - C^2_{n,radar}(t) * f_M(t). \quad (64)$$

The correction B_t is then applied to the C_n^2 value calculated for each bin along the path. These baselined C_n^2 values from the path were then used with the path weighting function to estimate IDM C_n^2.

2.7 Cell Phone Scintillation

Cell phones experience strong variation in Received Signal Strength Indicator (RSSI), which is related to the power received in the individual user's channel. As it is a periodic variation in power, the term *scintillation* will be used. However, the process by which scintillation occurs is different from that of optical systems. In optical systems, the power variance is the result of self interference of the arriving wavefront. Often modeled as a Gaussian, spherical, or planar wave-front, the wave is distorted via propagation though a media whose index of refraction is made inhomogeneous by turbulence. Upon arriving at the detector, the phase over the pupil plane is distorted from its expected, free-space propagation field. This aberration in phase results in beam wander and random focusing and defocusing in the image plane, hence variation in the received power.

Cell phones experience the same phase-front distortion, but cell phones have a sub-wavelength antenna, and no pupil, so the impact of phase-front distortion (which varies on time scales of seconds) on RSSI occurs through a different process. Cell phone RSSI variation depends jointly on manipulation of the channel's signal power by the *base station* and multipath fading. A base station is the collection of hardware at the cell phone transmitter which handles the RF signal processing and generation at the cell tower. RSSI variation due to manipulation of the signal by the base-station will appear as noise in cell phone C_n^2 measurements. Multipath fading is the result of EM field interference occurring at the receiver antenna, i.e., the superposition of many waves arriving from different paths. Cell phone scintillation is typically attributed to this multipath phenomenon, described later in this section. It will be shown that among other things, turbulence can contribute to power fading as well. Fading of cell phone received power is related to, but not the same as RSSI fading. [12] RSSI for the phones used here, is the power in the cell user's channel after extracting the

received signal. RSSI fading depends not only on the total received power, but also on how reliably the user can extract their carrier. If the spectral transfer function of the atmosphere is not flat in amplitude or linear in phase over the cell phone band, then the RSSI may vary in addition to signal power fading. This section presents an overview of cell phone technology and demonstrate how turbulence may create RSSI fading.

A cell phone network is defined as one created from many individual *cells* which are interconnected. Each cell is a roughly circular region within around $5km$ of a *base-station* [75]. Each base-station provides the transceiver for communicating with all users in a cell, and for routing their communications through the network. Modern cell phone networks use several different methods to address a common need: provide wide-area communications service to many users using a limited amount of bandwidth.

Because the performance of a user's communication channel is strongly limited by bandwidth, cell phone companies look to implement efficient methods to allow their bandwidth to be shared by all of their subscribers. There are four common ways to divide the available bandwidth among users: frequency division, spatial division, time division, and code division. [75] These four techniques are not exclusive. They are used in conjunction with one another in order to provide efficient bandwidth sharing. Frequency division involves breaking up the band of available frequencies into separate sub-bands. Each sub band thus has less bandwidth, and can transmit proportionally less information than the original band. Cell networks use frequency division among the cells so that each cell has a portion of the company's available spectrum. Providers can then subdivide the cell's band among the users, or for data, voice, and inter-cell communications. Networks also use spatial division to more efficiently re-use their spectral allotment. While adjacent cells generally use different

portions of the spectrum, distant cells can operate in the same band without interfering with each other. Time division works by having users take turns using the same band. This works well for common tasks like web-surfing, and voice communications where bandwidth demands are much less than a given channel provides. Code division, which is a spread-spectrum method, is less intuitive than time, space, or frequency division, but it is used in one form or another for modern cell networks (3G and on). In code division, a user's data is encoded with their unique key. Then, the encoded signals of all the users in the band are summed together to create the signal for transmission. Because of the nature of the keys, each user is able to pull their data out, and regard the data of the other users as noise. The encoding step causes the data of each user to actually require more bandwidth for transmission. However, this increased bandwidth cost is mitigated by allowing many users to transmit in the same band simultaneously. Because each user's data is spread out over a wider band, the technique is called spread-spectrum.

As previously mentioned, scintillation in the regime of RF communications is commonly attributed to *multipath* fading. Multipath is a wave-interference phenomenon due to waves following multiple paths from the Transmitter (Tx) to the Receiver (Rx). These paths are created due to reflections off objects in the environment. [12] This interference creates significant power fluctuations in both time and space. Because the length of the various propagation paths are different, signals originating from the cell base-station will arrive at the cell phone with path-dependent delays. While the delays and paths are not fixed in time, it will be assumed that the processes which vary path length occur on time scales which are slow enough so that the path is approximately static with respect to signal processing and propagation times. Under this quasi-static assumption, the analysis of propagation effects is simplified by the

ability to take the Fourier Transform of the received signal,

$$\tilde{S}(f) = \mathcal{F}\left\{s(t)\right\}, \tag{65}$$

where $\tilde{S}(f)$ is the frequency domain representation of the time domain signal received by the cell phone, $s(t)$, and $\mathcal{F}\{\cdot\}$ represents the Fourier Transform. The received signal can thus be represented as the sum of signals received after propagating along M_P paths plus noise, $\tilde{\mathcal{N}}(f)$,

$$\tilde{S}(f) = \tilde{\mathcal{N}}(f) + \sum_{k}^{M_P} \tilde{S}_k(f) \tag{66}$$

To find the total received multipath signal, the signal resulting from the k^{th} path, $\tilde{S}_k(f)$, which is make up of N_{SP} sub-paths must be found (Figure 12). To find $\tilde{S}_k(f)$,6 one could begin by finding the frequency domain transfer function, $\tilde{H}(f)$, [24] of the k^{th} path. The resulting phase and amplitude shift (in the frequency domain) of the received signal is then found by taking the product of the original signal component, $\tilde{S}_0(f)$, with $\tilde{H}_k(f)$. The transfer function of k^{th} path is, in turn, represented by the product of N_{SP} transfer functions for each of the N_{SP} sub-sections of the k^{th} path.

$$\tilde{S}_k(f) = \tilde{S}_0(f_0)\tilde{H}_k(f) = \tilde{S}_0(f) \prod_{j=1}^{N_{SP}} e^{i\pi} R_j \int_{C_j} \exp\left[\tilde{\gamma}(l,f)l\right] dl. \tag{67}$$

where the k^{th} path is made up of N_{SP} sub-paths as shown in Figure 12. The resulting signal component, $\tilde{S}_k(f)$, the original signal, $\tilde{S}_0(f)$, the location and frequency dependent propagation constant $\tilde{\gamma}(l,f)$ are complex quantities as indicated by the tilde, and each sub-path integral is performed over the path parameter l. The quantity $\sqrt{-1}$ is represented by i. Each subpath (except $j = 1$) is preceded by a reflection composed of a 180^o phase shift, a reflection coefficient, R_j, and possibly a Doppler shift. The

effects of the Doppler shift are omitted in (67), in order to simplify the integration. This omission does not significantly impact the calculation of turbulence effects on the propagating signal as index variation is essentially frequency independent for cell phone signals [12]. Each subpath creates an amplitude and phase variation which is represented by the path integral. The cumulative effects of index variation, scattering, and free-space path loss are combined into the location and frequency dependence of the propagation constant, $\tilde{\gamma}(l, f)$. The resulting signal component at the receiver would then be the sum of the signals received from all the possible paths plus the background noise

Actual calculation of the multipath effect is rarely tractable. However one can infer from the form of (67) and (66) how Turbulence may affect it. It is helpful to consider effects of varying time scales. On the time-scale of RF propagation (microseconds), turbulence will create a frozen field of spatially varying temperature and humidity which will affect the spatial dependence of $\tilde{\gamma}(l, f)$. This $\tilde{\gamma}(l, f)$ field will evolve on time scales associated with PBL turbulence, leading to fading on the orders of seconds to minutes. As described in Section 1.2, the index of refraction of the atmosphere is not a stationary process. Therefore, path-averaged index $\langle n \rangle$ is not expected to be fixed over time. Additionally, coherence lengths for PBL turbulence are typically around $0.1m$, so (for common PBL multipath path geometries) propagation paths would be expected to be incoherent over most of their length. The phasor which results after propagation through each subpath,

$$\tilde{\phi} = \int_{C_j} \exp\left[\tilde{\gamma}(l, f) l\right] dl, \tag{68}$$

is thus expected to vary as a non-stationary process with little to no correlation between individual paths. It is important, then, to consider how much of a change in the apparent path length (due to perturbations of n) is required to create a noticeable

change in $\tilde{\phi}$ after propagation.

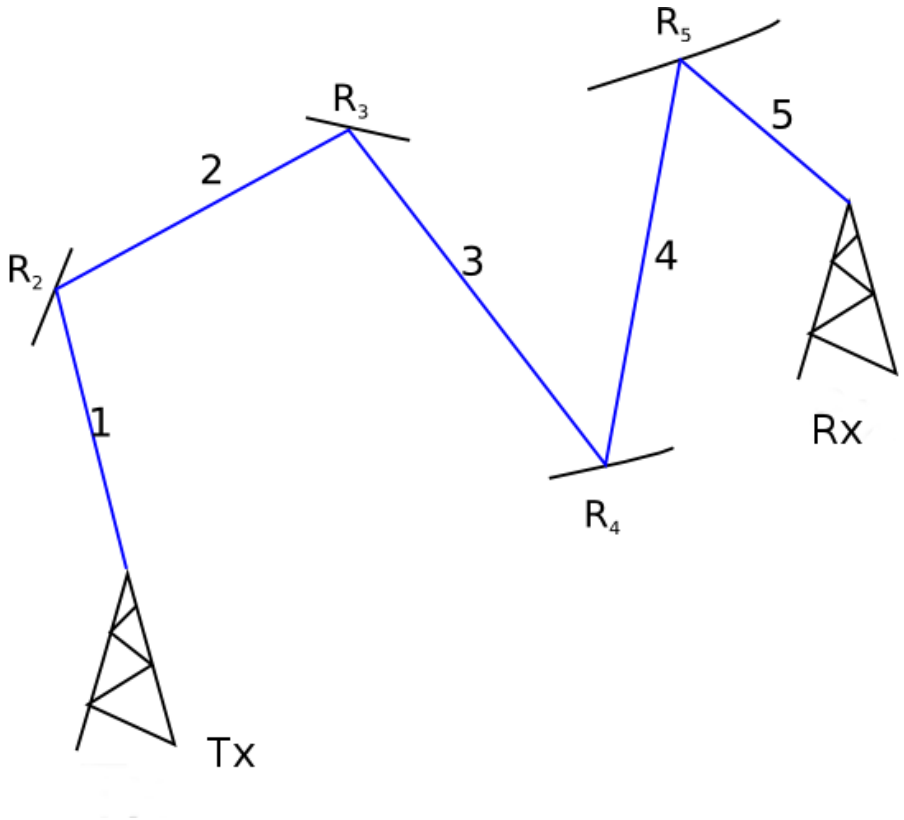

Figure 12. Illustration of a path where waves reflect multiple times before arriving at the receiver. The path is highlighted in blue and enumerated from 1-5. Objects are in black and the reflection surfaces are numbered as R_j.

For straight line propagation over distance r,

$$\tilde{\phi} = e^{inr\frac{2\pi}{\lambda}}. \tag{69}$$

The minimal variation in Δn required to shift the phase by π can be found by setting the exponent in (69) equal to π,

$$\Delta n = \frac{\lambda}{2r}. \tag{70}$$

As path distances are commonly several hundred meters to $5km$, and cell phone wavelengths are $16cm$, the required variation in n would need to be on the order of

$\Delta n \approx 0.0001$ for an $800m$ path (like those used to collect data for this work), or less for longer paths. As mentioned in Section 1.2, naturally occurring processes like $n(\vec{x}, t)$ have a self-similarity property where variation in a sliding average appears similar to variations on a smaller scale. This provides for a connection between C_n^2 and cell phone scintillation. NWP predicted variation in n over the course of 3 hours is typically $\Delta n \approx 0.00002$, just one-fifth the required Δn required to give a full phase shift of π over an $800m$ path. Assuming that path length variations due to turbulence are of a similar magnitude (via Kolmogorov's self-similarity hypothesis), it can be seen that index variation on cell paths can induce significant phase variation in each of the k paths, which is the requirement for cell phone scintillation to be tied to turbulent activity.

How is RSSI variation over time expected to relate to C_n^2? Consider a propagation environment where multipath effects are present. Say that the transmitter, receiver, and all reflectors on the k^{th} path remain stationary over the period of the evolution of turbulence (a minute). The j^{th} subpath from (67) would have an apparent path length, L_a, which depends on the index of refraction along the path. Assuming that dispersion is negligible, and turbulence will allow the structure of $n(\vec{x}, t)$ to evolve over the path, the path length at time t is

$$L_a(t) = \int_{C_j} n(l, t) dl. \tag{71}$$

The temporal structure function for path length can be found. For statistically homogeneous and isotropic turbulence,

$$D_{La}(\tau) = \left\langle [L_a(t) - L_a(t + \tau)]^2 \right\rangle. \tag{72}$$

Where t and τ are units of time. This gives the structure function for path length v

Substituting (71) for L_a gives

$$D_{La}(\tau) = \left\langle \left[\int_{C_j} n(l,t)dl - \int_{C_j} n(l,t+\tau)dl \right]^2 \right\rangle, \tag{73}$$

$$D_{La}(\tau) = \left\langle \left\{ \int_{C_j} [n(l,t) - n(l,t+\tau)]dl \right\}^2 \right\rangle. \tag{74}$$

This expression cannot be evaluated without knowledge of the integrand involved. However, the upper bounds of $D_{La}(\tau)$ can be determined using the Cauchy-Schwarz inequality. Let $f(l) = [n(l,t) - n(l,t+\tau)]$, and $g(l) = 1$, by CS,

$$\left[\int_C f(l)g(l)ds \right]^2 \leq \int_C f^2(l)ds \int_C g^2(l)ds, \tag{75}$$

$$D_{La}(\tau) \leq L \int_C \left\langle [n(l,t) - n(l,t+\tau)]^2 \right\rangle ds, \tag{76}$$

$$D_{La}(\tau) \leq L \int_C D_n(\tau)ds = L^2 D_n(\tau). \tag{77}$$

This shows that the temporal structure function of path length can be considerably larger than the index of refraction temporal structure function, with the constant of proportionality growing up to the path length squared. This is, of course, an upper bound. While the lower bounds is zero, this would imply that the path length does not change over time via (72), which is not physically observed.

So it becomes apparent, that the structure function for path length will be a scaled version of the index of refraction structure function along the path. As variation in the apparent path lengths in a multipath environment will lead to signal fading, we expect that the RSSI structure function (in time) will closely follow the temporal path length structure functions. This leads to a very important question concerning the relationship between the index of refraction temporal structure function and the path-length structure functions. Unfortunately, no satisfactory theory exists linking the spatial, $D_n(\rho)$ and temporal $D_n(\tau)$ structure functions of atmospheric parameters

like C_n^2 [16]. Taylor's frozen flow does provide a short term relationship between the temporal and spatial structure functions via the mean wind, but does not extend to long time periods or large areas. There is some evidence that on certain time scales $D_n(\tau)$ does follow a two-thirds law, similar to $D_n(\rho)$. Despite this, it is possible to use the radar to measure $D_n(\tau)$ along the primary (direct) propagation path from the cell tower, to the phone. In addition $D_{RSSI}(\tau)$ can be measured via the cell phone. If the path scaling happens to be fairly constant (and possibly proportional to L^2 or L), then we would expect that there would be a correspondence between $D_{RSSI}(\tau)$ and $D_n(\tau)$. In previous research it was shown that cell phone scintillation does correlate well with C_n^2 time series from NEXRAD [8]. Furthermore, the strength of the correlation depended on the temporal width of the window used to calculate the scintillation index for the cell phone.

In addition to the index variation, mechanical turbulence production (wind blowing on trees, signs, buildings and the like) will change the propagation environment by moving reflecting and scattering structures. This changes the actual integration path, reflection coefficients, and may vary the Doppler shifts along the path. Longer-term diurnal variation in the PBL vertical temperature and pressure gradients will also affect fading as path bending causes changes to the path geometry. In addition, the reflection coefficients for surfaces can change as dew, frost, precipitation, and evaporation change surface composition. While these long-term variations are not caused by turbulence, the production of PBL turbulence is related to them, so there may be additional turbulence information due to these fading processes.

For signals with small bandwidth (quasi-monochromatic), the fading of the signal will approximately follow the fading of the center frequency. However, for wider-bandwidth signals, the phase and intensity fading may not be constant across the band. In this case, the shift of phase and amplitude of components within the band

could cause increased fading in the RSSI as described below.

Code division can be implemented using time-domain or frequency-domain encoding. For the phones used in this research, the cell network uses codes which are orthogonal in the time domain. The decoding step involves a correlation of the total received signal with a copy of the original signal. If we allow $s(t)$ and $\tilde{S}(f)$ to be the time and frequency domain representations of the received signals and $s_0(t)$ and $\tilde{S}_0(f)$ to be the corresponding original signals, then the correlation of the received signal to the original can be found using the convolution theorem,

$$\mathcal{F}^{-1}\left\{(s_0 \star s)\,[n]\right\} = \mathcal{F}^{-1}\left\{\sum_{m=-\infty}^{\infty} \bar{s_0}[m]s[m+n]\right\} = \overline{\mathcal{F}^{-1}\{s\}}\mathcal{F}^{-1}\{s_0\}. \tag{78}$$

Here $\mathcal{F}^{-1}$ indicates an inverse Fourier Transform and the over-bar indicates a complex conjugate. Because of the correlation, phase and amplitude variation within the band can show up as RSSI power loss. If we let $\tilde{H}[f]$ be the discretized representation of path fading effects outlined in (67) and (66) and $\tilde{S}'[f]$ be the received signal without those effects so $\tilde{S}[f] = \tilde{S}'[f]\tilde{H}[f]$, then we can see that the resulting RSSI depends on the frequency domain product of $\overline{S_0}[f], S'[f]$ and $H[f]$. Assuming that RSSI is the maximum correlation value, it can be expressed as

$$RSSI = max\left(\mathcal{F}^{-1}\{\overline{S}_0[f]S'[f]H[f]\}\right) \tag{79}$$

While the actual phase and amplitude variation within the band may still be slight, the effect on the maximum correlation strength (RSSI) may be significant. This could increase the σ_{RSSI} beyond the σ_I expected from C_n^2 alone. The additional variation observed in cell phone scintillation may be due, in part, to the correlation process described here.

To compare cell-based C_n^2 with measurement, the scintillation index is used. The

scintillation index is defined as [12, 32]

$$\sigma_I^2 = \frac{\langle I^2 \rangle - \langle I \rangle^2}{\langle I \rangle^2}. \tag{80}$$

Here σ_I^2 is the scintillation index, and I is received signal intensity in dBm which is approximated with RSSI. This index is then assumed to be proportional to the Rytov variance and the Rytov variance was then used to calculate C_n^2 using

$$\sigma_I^2 \approx \sigma_1^2 = 1.23 C_n^2 k^{7/6} x^{11/6} \tag{81}$$

This result was developed for the optical process where scintillation comes from self-interference of the primary wave with secondary waves generated by scattering off index of refraction inhomogeneities. This effect only produces a minor fading in cell phones compared to the multipath fading. Use of (81) is not appropriate for cell phone scintillation. There is no reason to believe that the path length dependence for multipath fading will be $x^{11/6}$, and the Rytov approximation is based on an expansion of the multiple scattering function in the assumption of approximately forward scattering, which is not what is seen with multipath fading. However, as a new form has not been developed, (81) is used, as it was in [8]. Using the new method for calculating (80) presented in Section 3.3, resulted in C_n^2 values which were the same order of magnitude as predictions made by using the RF $N(T, P, e_v)$ equation.

III. Instrumentation

3.1 Numerical Weather Prediction

NWP provides a convenient source of atmospheric data for turbulence studies and is used in both current and past research [1, 2, 30, 33, 47, 48]. NWP uses finite-differencing methods to solve a many coupled differential equation (the models) at points on a geometric grid. Operational forecasts incorporate several different models together with each model predicting different physical processes which affect the energy and chemistry state of the atmosphere. The result of these coupled processes is a chaotic system of differential equations whose accuracy degrades over time due to increased sensitivity of the solution on initial conditions. Observation of this effect by E. N. Lorenz lead to his famous paper, *Deterministic Nonperiodic Flow.* [43] Chaotic systems are those for which small changes in the initial conditions create large variations in the outcome after a sufficient number of steps [30, 33]. In order to increase the time over which a forecast is accurate, one can increase the precision of the initial measurement state, or increase the length of time between steps in the model. Increasing the time step size is not without cost as the spatial resolution is limited by the time-step size. The grid size must be large enough that air parcels cannot advect across an entire grid within one time step. This is due to the computational stability requirement known as the Courant-Friedrichs-Levy (CFL) stability criterion. If the CFL criterion is violated, then the solution will experience unrealistic exponential growth. Operational forecasts strike a balance between having a small enough grid to be able to resolve weather systems, and having a large enough time step to be accurate for a useful time into the future. [30] Four grid-points from the Global Forecast System (GFS) 0.5^o grid are shown in Figure 13.

Figure 13. United States Great Lakes region depicting the $7km$ UD to VA hospital path is depicted as a yellow line with small green markers at each end. WPAFB is marked with the yellow pin. The four large teal markers show the four closest 0.5^o GFS grid points. The KILN radar location is depicted in the lower right quadrant by a red target. Teal lines indicate county boarders, while grey lines are state boarders. Image copyright owned by ©Google 2015

Because PBL turbulence requires such a small grid (centimeter scale) to resolve the inertial subrange, the period over which such a forecast could be expected to be accurate is very short, on the order of seconds to minutes (depending on the velocities and models involved). It is readily apparent that direct computation of PBL turbulence via NWP is impractical. In order to predict the evolution in an area of interest such as the Dayton scintillometer path, which is almost $7km$ long, one might choose a $1 \times 1 \times 8km$ grid. For this region, a $0.5cm$ grid would require initialization of atmospheric parameters for 64×10^{16} points. As a comparison, the operational GFS forecast uses less than 21×10^6 points. As direct computation over a

grid of this scale is impractical with current computer capabilities, this work follows other modern techniques which use NWP data to estimate large-scale variations, and infer turbulence parameters from these. [1, 2, 47, 78]

The two forecasts used here are the GFS and Rapid Refresh (RAP) models. Both models use a pressure coordinate system. The RAP model uses a sigma-pressure coordinate [72], where the base pressure level is defined as ground level, and vertical positions are defined based on a normalized ratio between the ground pressure, and pressure at the top of the forecast domain. This forecast did a better job describing gradients near the surface for the Albuquerque site (See Section 4.3). The GFS model uses a hybrid pressure coordinate system. There are fixed pressure levels in the upper atmosphere, a sigma pressure system near the surface, and a mixed sigma/constant pressure coordinate in the mid-atmosphere. [63] In pressure coordinate models, the vertical spacing in meters AGL varies with weather conditions and height. Typically, spacing in the lower PBL for both models ranges around 190 to 275m, with 220m being typical at the height of the centers of the scintillometer paths.

The horizontal spacing of GFS is 0.5^o, which is 43km spacing in the East-West direction and 56km in the North-South direction at latitude 40^o. RAP uses a 13km grid. As grid points do not coincide with measurement locations, interpolation methods are used to determine parameters and gradients. GFS forecasts have a three hour time resolution, and are updated every 6 hours. RAP forecasts are updated every hour. Because both of these are much slower than the radar sampling rate, data are interpolated in time as well. There are a total of 5 parameters which must be estimated at the path location. All three of the partial derivatives, $\partial N/\partial P'$, $\partial N/\partial T$, and$\partial N/\partial e'_v$ and the gradients $d\theta/dz$ and de_v/dz. Recall that P' and e'_v are pressure and vapor pressure including the effect of hydrostatic balance while e_v is the potential vapor pressure, defined as $e_v(\vec{x}, t) = e'_v(\vec{x}, t)P_0/(P_0 - \rho gz)$ in Section 2.3.

Before any interpolation, the available parameters are used to calculate θ and e_v at each NWP grid point. Both the GFS and RAP forecasts are then interpolated vertically to the path height AGL. Because the ground height differs at each latitude and longitude used in the grid, the first step is to convert the heights of the forecast grid to z, height AGL. Then interpolation is done in each vertical column using a cubic spline fit of the data to the point z_0, the height AGL of the path center. A spline fit was chosen to interpolate to z_0 for each column. An example fit is shown in the left plot of Figure 14.

Initially gradients were approximated using first and second order differencing and nearest-neighbor interpolation to z_0. However, this often produced gradients near-zero, which led to numerical instability when using (46) or (47) before the pressure term was added. A partial fix involved employing a higher-order technique for estimation of gradients. While several options exist (the right plot of Figure 14 shows four possible approaches), the method of finite differencing with undetermined coefficients was chosen, as is described in Appendix 7.2. Using this method to estimate the derivatives did reduce the occurrence of numerical instability, but adding the non-hydrostatic pressure gradient term is what actually addressed the incorrect underlying physical assumption.

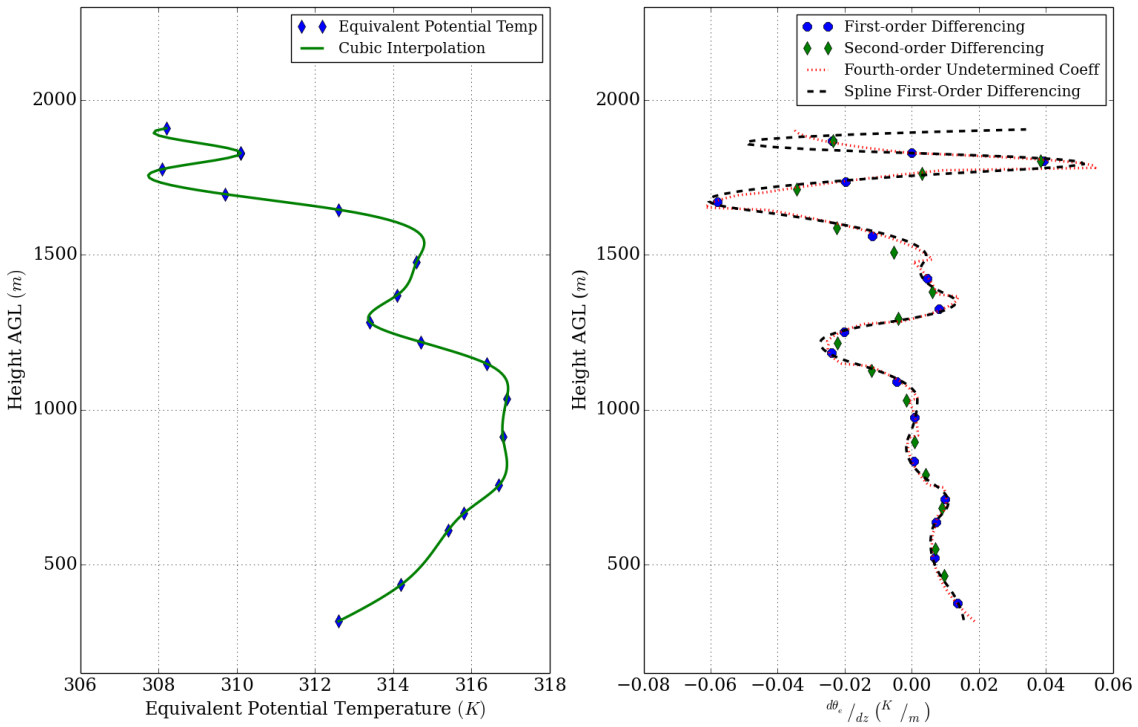

Figure 14. The left plot shows equivalent potential temperature vs Height AGL from RAOB launched 12 November 2015 at 1200 EST in Wilmington Ohio (blue diamonds), and the cubic spline interpolation used to extrapolate NWP data to the path height. The right plot shows four methods of approximating derivatives of the RAOB data on the left. The blue circles use a first-order differencing approach, and the green diamonds use a second-order approach. The red-dashed line uses the 3^{rd} order undetermined coefficient approach. The black dotted line is the derivative obtained from the spline fit.

Once NWP data have been vertically interpolated to z_0, and the required gradients $d\theta/dz$ and de_v/dz have been found at z_0, the z_0 values are then interpolated in latitude and longitude. Here there is a difference in how the RAP data at Albuquerque, and the GFS Dayton data are handled. At Albuquerque, the only interpolation method that gave results which matched well with RAOB data was the nearest-neighbor method. This is likely due to the large vertical variation in ground level around Albuquerque. The GFS data around the Dayton site was interpolated using a spline.

The first interpolation was to the latitude of the path, and the second interpolation was to the path longitude.

In addition to the spatial interpolation, the NWP data are temporally interpolated to match the forecast times. Here a linear interpolation is used.

After interpolation, the atmospheric parameters are processed by LEEDR [22] to determine the refractivity N at each wavelength. These refractivity values are then used to find the partial derivatives $\partial N/\partial P'$, $\partial N/\partial T$, and $\partial N/\partial e'_v$ using (59),(61), and (60) respectively for IR-visible applications or (53), (55), and (54) for RF. Once these partials and gradients were obtained, they could be used in the various methods for estimating C_n^2

In order to facilitate extraction of forecast data, several programs have been written. The first is a GUI which makes setting options for the various programs easier. There is a separate extraction routing for the RAP and GFS forecasts. This approach was chosen because of the significant differences in how the forecasts are gridded. These programs also perform all of the spatial interpolation, and gradient extraction. They are threaded applications written in C, but still require several minutes to over an hour to complete, depending on the number of forecasts and grid points involved. The GFS versions can also locate and download data for a time period automatically. There are Python scripts for interpolating the output data in time to match the radar file times. The python script also formats the data in a way that is easily ingested by MATLAB®. Matlab scripts automate the use of LEEDR to extract N and the partials $\partial N/\partial P'$, $\partial N/\partial T$, and$\partial N/\partial e'_v$. Python scripts are used to employ the methods included here, plotting, and performance calculations.

3.2 NEXt-generation RADar

There are excellent texts devoted to weather radar [16, 59]. This section presents selected topics from the books on radar theory which is pertinent to this research. The NEXRAD WSR-88D radars used here are klystron based mono-static radars operating at $\lambda = 10.7cm$ with a $750kW$ peak power and $1.56kW$ average power output. The receiver bandwidth is $0.795MHz$ with $1.57\mu s$ and $4.57\mu s$ pulse widths available, depending on the mode. [16, 42] Resolution has been improved using super-resolution processing techniques, [51, 70, 71] and newer radar (all data used here except for the 2010 KILN data) shows range gates at $250m$, with a 1^o beamwidth. Newer radars also provide dual polarization information which may be used for scatterer classification. The extent of radar coverage for weather detection is depicted in Figure 15.

The NEXRAD wavelength is chosen to be close enough to the $22GHz$ water resonance so that interaction with water allows the the radar to detect hydrometers, but not so much that the range is limited by absorption. While the range for precipitation detection is well over 400 km, it has been observed that clear-air turbulence detection is limited to around $150km$ under ideal conditions (strong TKE, temperature gradients, and vapor pressure gradients) and under 30 km under poor conditions (dry winter air) with 50 to $60km$ being a typical maximum range.

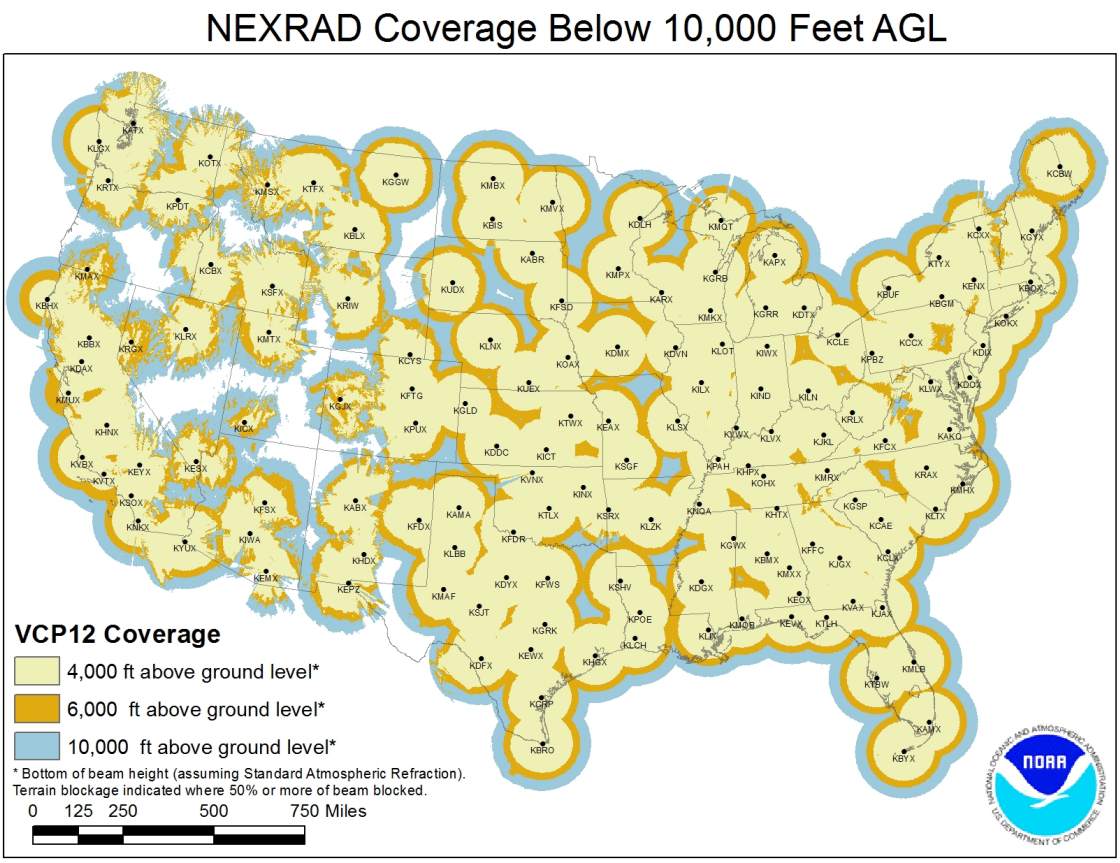

Figure 15. Map of NEXRAD coverage over the continental United States.

Three components returned by the radar and used in this research are the reflectivity, Doppler, and Doppler spectrum width. Reflectivity is recorded in decibel reflectivity factor dBZ, which has units of ${}^{mm^6}/_{m^3}$ and relates the actual volume reflectivity to its meteorological properties. The Doppler measurement returns the integrated radial (directed away from the radar) velocity of all scatterers within the measurement volume. The Doppler spectrum width is a measure of how spread out the returned velocities are within a volume. A narrow spectral width indicates that scatterers within a volume have similar radial velocity components, while a wide spectral width indicates that scatterers are not moving with uniform radial velocities. [16, 59]

To improve the accuracy of the dBZ recorded by the radar, preprocessing techniques are applied to remove ground clutter from the radar return. In order to identify ground clutter the radar preprocessor attempts to remove returns which are near zero-Doppler and have a low spectral width. Unfortunately, this technique can filter out some energy from true meteorological events, like straight-line winds. Depending on the weather, the cost of increased ground clutter may be acceptable if it improves detection of specific phenomena. For this reason, the radar can be run in several Volume Coverage Pattern (VCP) modes which vary in their optimization. Some emphasize convection monitoring, while others detect low-level precipitation, or attempt to reduce the effects of range folding. Based on observations in the data used here, it appears that both noise and sensitivity of NEXRAD C_n^2 measurements varies with the selected mode. In addition to Doppler filtering, clutter maps for each radar site are used to help reduce the chance of false identification. Despite the filtering and based on the results in Section 4.4, it appears that the data used here still not only contain ground clutter, but ground clutter is the primary contributor of noise.

NEXRAD radar files are compressed and made available online by the National Oceanic and Atmospheric Administration (NOAA). [50] Radar files are organized based on a hierarchy of objects. Details of the radar structures are available on NASA's TRMM RSL website. [49] On the top level are several different types of measurements called *radar volume*s. For this work, the reflectivity, Doppler, and Doppler Spectrum Width volumes were used. Each Volume is then broken up in vertically stacked rings called *radar sweep*s (Figure 18). The sweeps are then broken up in the azimuthal direction into *radar ray*s. Each ray is then subdivided by range increments into *bin*s. In Figure 16, a portion of the lowest elevation sweep from the Wilmington, Ohio NEXRAD station (KILN) NEXRAD is depicted showing reflectivity of the bins and rays of a clear air return. An illustration of a 3-D sweep quadrant is presented

in Figure 17.

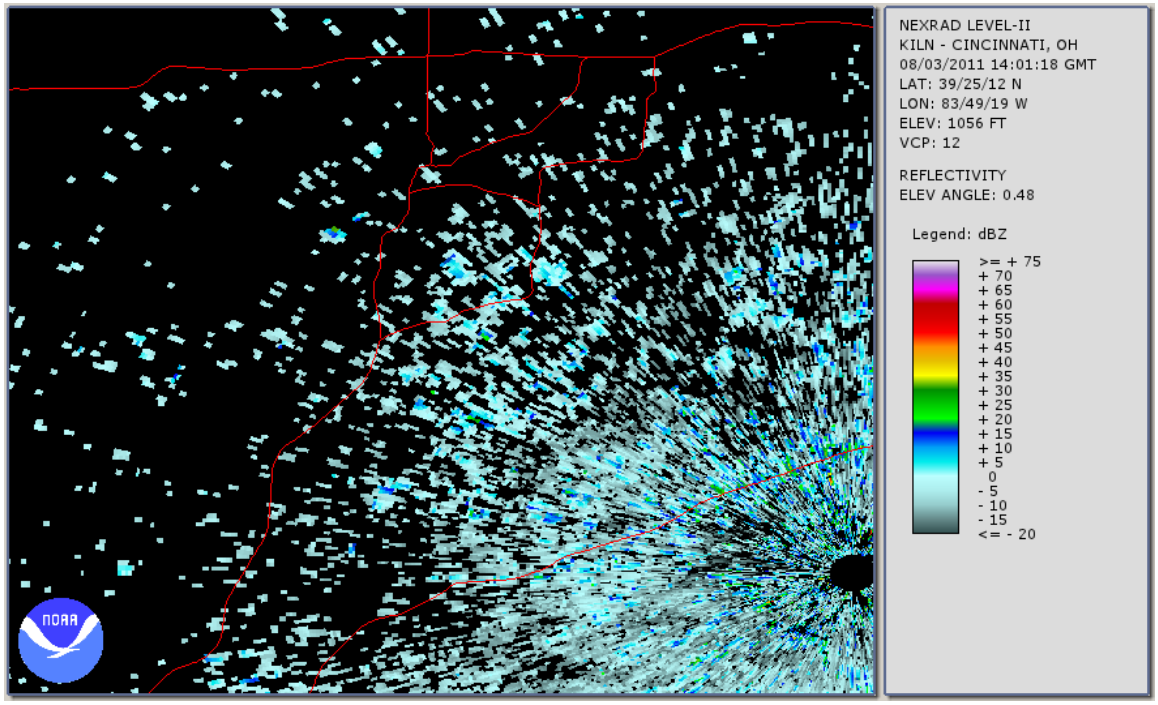

Figure 16. Wilmington NEXRAD Radar image showing clear air returns from the Miami Valley region. The red lines are major highways in the area. I-70 heads East to West along the upper the top of the image. I-75 is the left-most North to South Highway. I-71 heads from South-East (Cincinnati) to North-West (Columbus) along the lower right of the figure. Also depicted are I-675, US-35, and State-Route 4 in and around Dayton, Ohio.

Radar images do not have standard spacings for the sweeps, rays, and bins. NEXRAD radars have several different coverage patterns which are used to optimize the radar for the current weather conditions. Turbulence detection is most effective in one of the two clear-air modes. In these modes, radar sensitivity is maximized at a cost of increasing the interval between measurements. Clear-air reflections are still visible in precipitation modes, but at reduced range. Of course, turbulence echos are not visible in areas with precipitation, but it's quite common for there to be precipitation far from the turbulence measurement site (recall that the radar range is over

$400km$) which causes the radar to be in one of its precipitation modes.

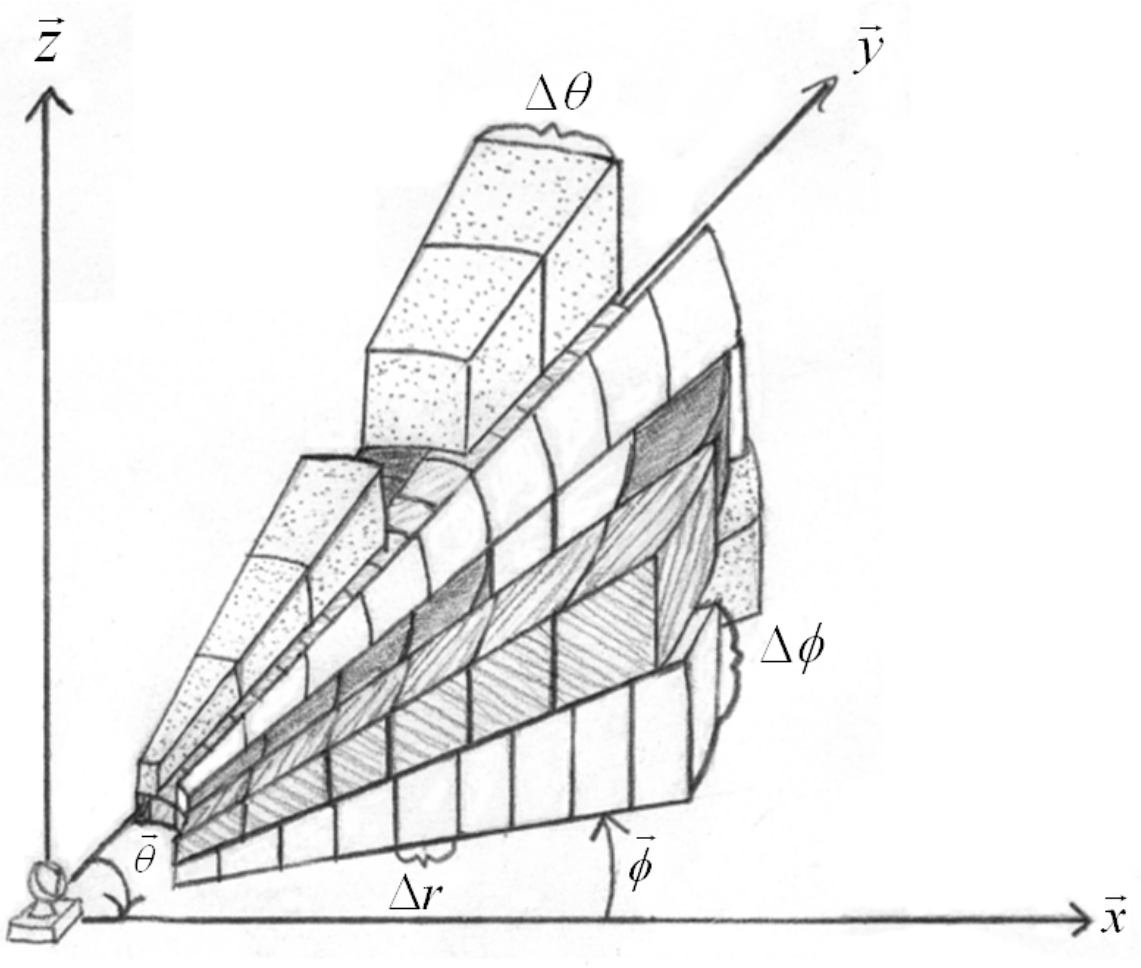

Figure 17. A quadrant of a NEXRAD measurement *volume*. The volume is divided by elevation angle into *sweeps*. Each sweep is subdivided by azimuthal angle into *rays*. Each ray is subdivided by range into individual *bins*. The spacing of sweeps, rays, and bins is irregular, and there are many structures which are 'empty', having no data.

Automated extraction of radar data is made difficult by the variable nature of the radar scan geometry. [8, 10, 49] Each volume that is opened has information about the number of sweeps, and their spacing. Each sweep, when opened has information about the number of rays, and their spacing. The number of rays can be different in every sweep within a single file. Bins are similar to rays and sweeps in that each ray

may have different bin spacing, with different initial distances, and different numbers of bins. Furthermore, there are missing bins, rays, sweeps and volumes, and some of the bins contain data, but the data are corrupted. In order to prevent software crashes, it is important to check each element and make sure that it is not empty before trying to access the data. The data must all be checked for bad values as well. The program written for this research opens radar files, determines their geometry, and determines which bins coincide with a desired path.

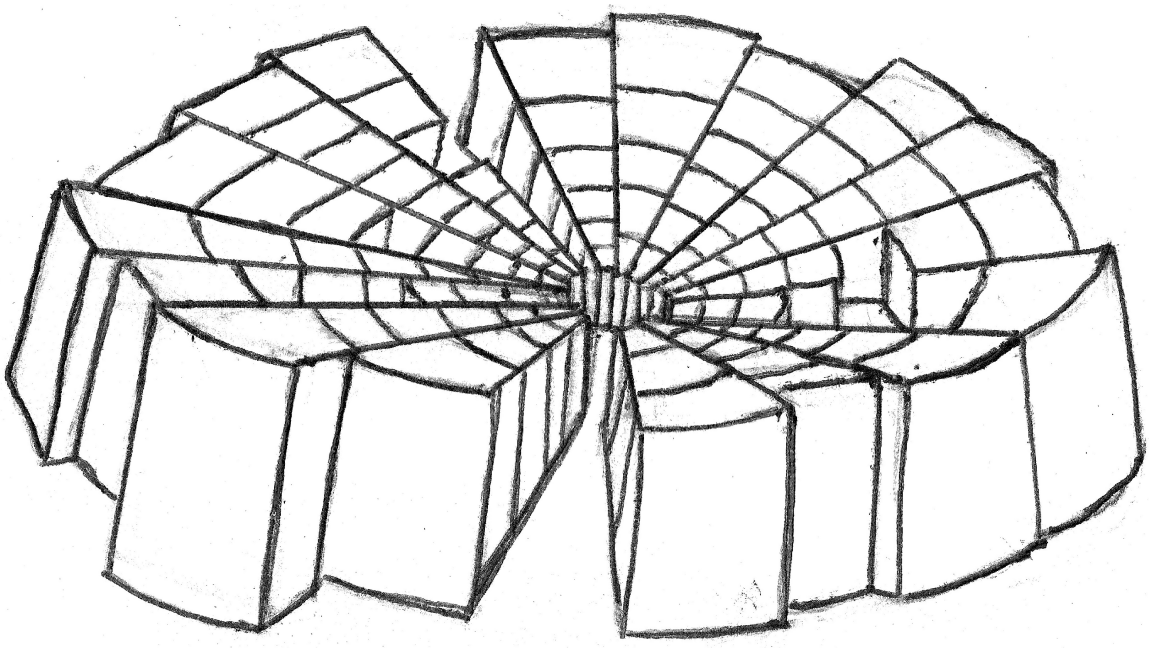

Figure 18. Illustration of a weather radar sweep. The azimuthal divisions of the sweeps are rays, and the radial divisions of the rays are bins. In each radar sweep it is possible for rays or bins to be missing. Also the spacing and number of bins varies from ray to ray, the spacing and number of rays varies from sweep to sweep.

The most straightforward method for using radar to measure turbulence is done by relating the clear-air mode (no precipitation) reflectivity measurement of the radar to the intensity of the turbulence. Simply put, stronger turbulence creates stronger returns to the radar. A quantified estimation of this relationship is given in [16,19,21],

$$C_n^2 = 2.63\pi^5\lambda^{-11/3}\,|K_w|\,\frac{10^{dBZ/10}}{1000^6}. \tag{82}$$

Following Doviak's convention, λ is the wavelength, K_w is the complex index of refraction for water, and dBZ is the reflectivity.

The first adaptation from radar to scintillometer measurements is a correspondence between the region being measured by the scintillometer to the radar measurement volume. This correspondence has been presented in previous work [10] and will be summarized here. The optical system propagates along a straight, narrow path which passes through, or just below, several of the 3-D bins that make up a radar measurement volume, as in Figure 19.

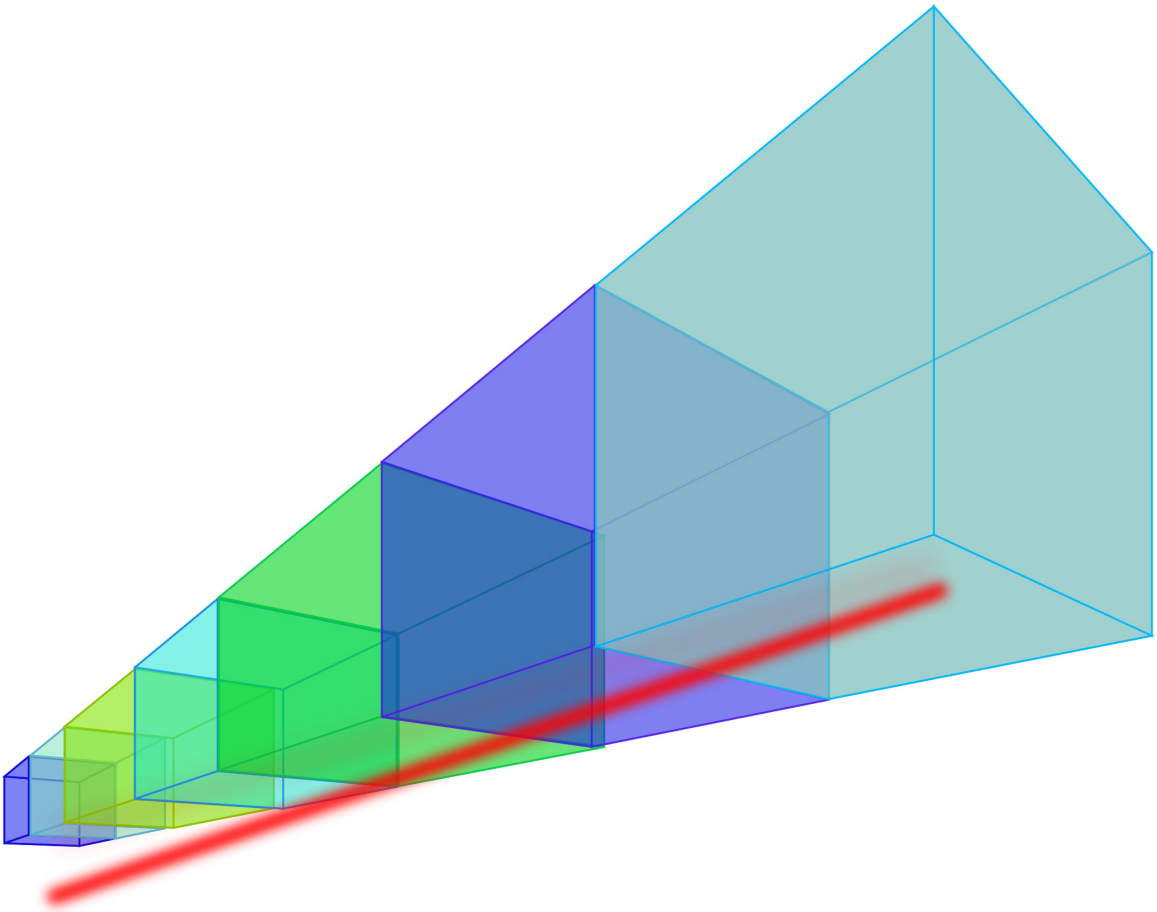

Figure 19. A scintillometer path (red beam) passing under 3-D radar measurement bins.

Due to variations in the NEXRAD volume geometry, the mapping of radar data to the scintillometer path must be recomputed for each radar measurement. [8, 49] The mapping is accomplished by first determining which radar data bins the scintillometer path passes through. If the bottom of the lowest radar sweep is above the scintillometer path (as pictured in Figure 19) then the bins which are closest to the scitillometer path are used. A weighted average of the measured reflectivity values is then computed for the bins that the scintillometer path passes through. The contributions of the reflectivity measurements to the average are weighted by the proportional length of the path within each measurement bin, l_i, via

$$\langle dBZ \rangle = 10 \log_{10} \left(\frac{\sum_i l_i Z_i}{\sum_i l_i} \right). \tag{83}$$

Here l_i is the length of the path within the i^{th} bin, and R_i is the reflectivity of the i^{th} bin. Because clear air returns are weak, paths often have bins with no measurable reflectivity. The contributions of 'empty' bins are removed from the path average. Once this path-averaged reflectivity, dBZ, is obtained, it is then used to compute the radar C_n^2 for the path via (82).

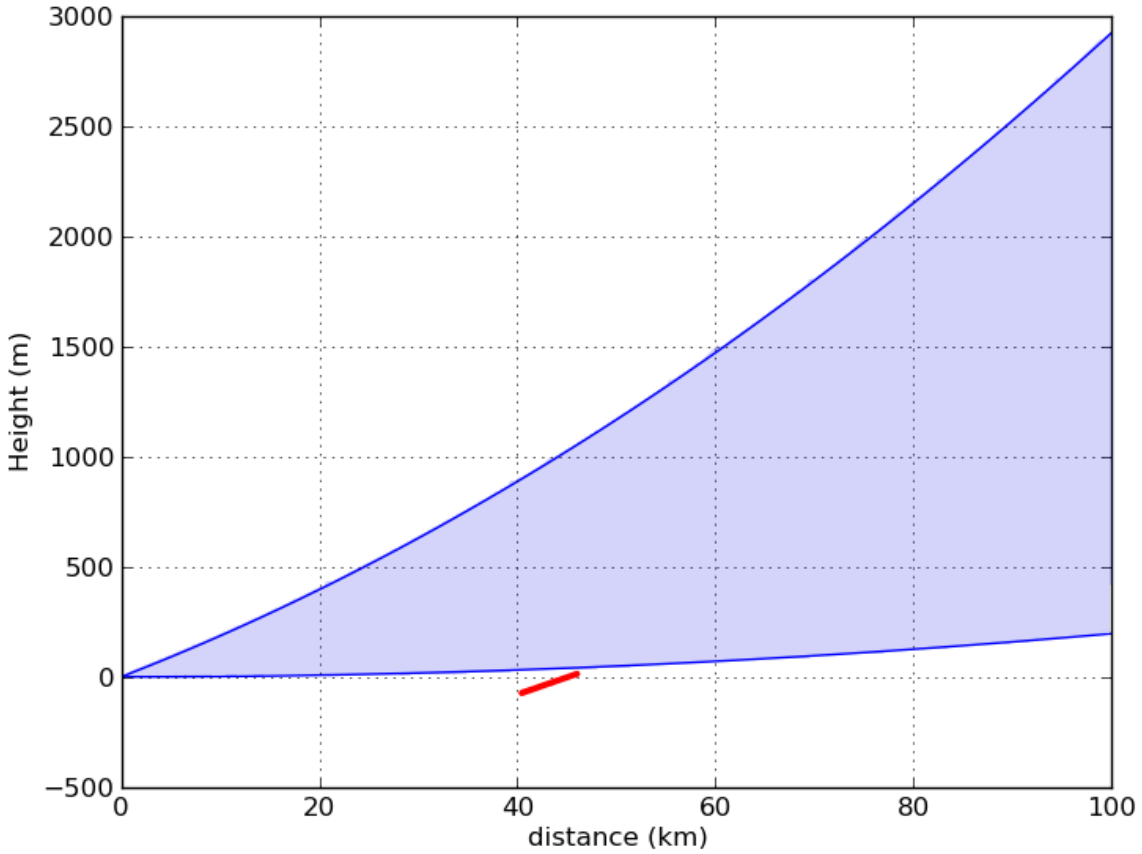

Figure 20. Radar main beam height vs. distance using the four-thirds assumption (blue). The upper line is for 1^o of elevation and the lower is for horizontal propagation. The short red line indicates the Dayton scintillometer path after accounting for elevation. Horizontal distances are in kilometers and vertical distances are in meters.

In addition to the path average, the individual bin data, geometry, and the portion of the path contained in the bin are recorded. Measurements of wind velocity and spectrum width are also collected in the same manner, with both path averages and bin by bin data being returned. The path averaged data are used for comparison to the scintillometer and cell phone measurements, and the bin by bin data are used for the IDM technique.

The extraction of NEXRAD data is accomplished using purpose written C code which employ's NASA's RSL. [49] It was noted that radar files are sometimes corrupted and can cause the RSL library to crash, so a Python script was written to open all files once with the RSL before processing, and delete any files which cause the RSL to crash. Extraction times are generally shorter than NWP extraction, but threaded extraction still takes about 5 to 30 minutes to complete. Radar data must be acquired before downloading.

3.3 Cell Phone Data Collection and Processing

Cell phones have a variety of sensors whose data are available through prewritten implementations of the Android® operating system. The advantage of using existing Java methods to access data (should be) convenience, fast development, and platform independence via standardization. The difficulty is that data collection methods will depend on how these methods are implemented. For this work, the cell signal characteristics, time, and phone location are recorded. It would have been preferred to be able to query the device state on a regular basis, say every 30 seconds. However, the Android Operating System (OS) is not structured in a way that is conducive to this approach.

For mobile devices, security and power consumption are both significant device performance concerns. To address these, the OS of Android devices implements a

broadcast-listener model for on-board sensors. In this model, applications do not request data from devices. Instead, applications can request that the OS activate the sensor upon opening, and then the application implements a listener for the sensor. Once activated, the sensor will broadcast its state periodically (*when* a particular sensor chooses to broadcast is sensor and device specific). Any applications which have an active listener for that particular sensor will then receive the data the sensor chose to broadcast. For the phone-state sensor (which gives signal power information), it will broadcast whenever it notices a change in the RSSI of either the voice, or data channel. It also appears to broadcast based on other parameter changes, as some data were collected when neither the voice nor the data RSSI changed. The position sensor (GPS) also broadcasts based on a state-change basis, when there is a change in location. From a data recording standpoint, this broadcast-listener model has the advantage of reducing the amount of data needed to represent the device state variation over time. However, the irregularity of the data sampling rate makes implementation of many common statistical analysis tools more difficult than it would be with evenly spaced sampling times.

Data collected here are available from three different paths. The first is the same path used in [8] and is pictured in Figure 21. This path is $623m$ in length. The second path used is longer and does not have a direct line of sight to the tower. It is $1.77km$ in length. The third path is $621m$ long, and has a direct line of sight to the tower.

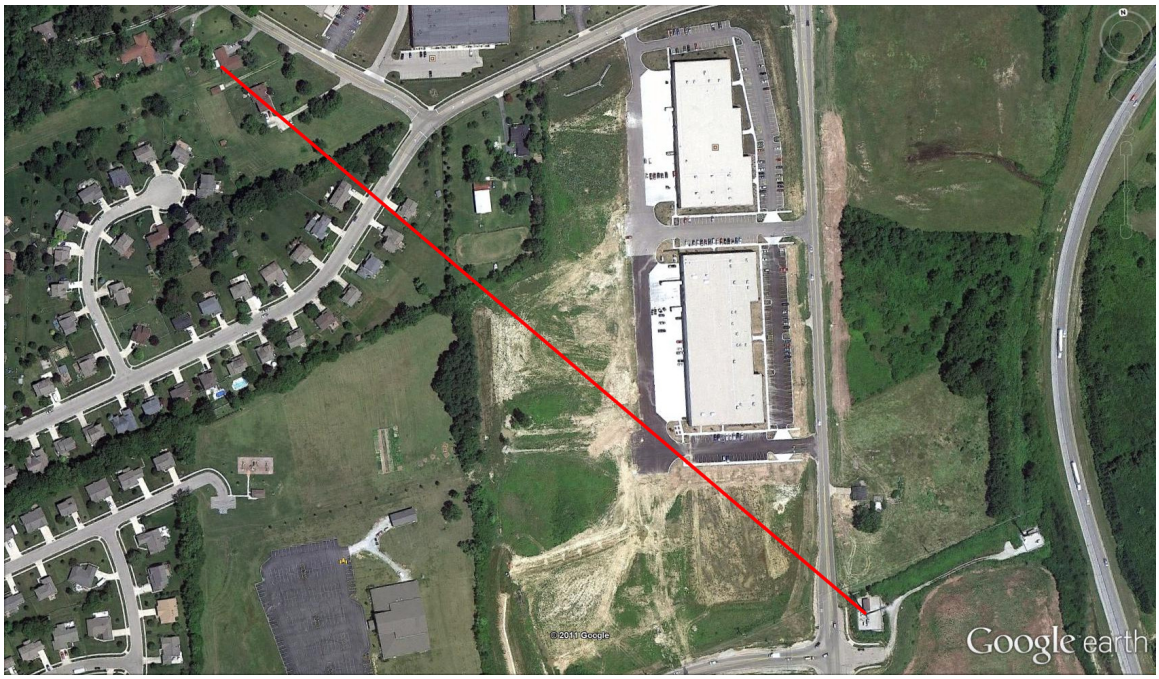

Figure 21. Satellite image of Transmitter to Receiver path for the first cell phone data collection location. The path length is $623m$. The distance from the KILN radar (not shown) is $42km$. Image copyright owned by ©Google 2015.

The phones used here report RSSI for two signals: voice and data. Both of these channels require a method for sharing the available bandwidth among the users. The carriers in this case, Sprint® and Verizon®, use a bandwidth division scheme known as Code Division Multiple Access (CDMA). While one might expect that the two channels (voice and data) from a single handset would show similar RSSI variation, this was not the case. While these signals showed high correlation when comparing long term (many hours) data, they often showed poor short term (several minutes) correlation. This correlation behavior was seen for both RSSI and C_n^2 values. Furthermore, two identical model phones were used at times but in close proximity, and would also show dissimilar behavior.

This disagreement is not unexpected because both the base station and phone are constantly adjusting the signal power through processing and hardware gain mecha-

nisms. Since there is no available information about these processes, they appeared as considerable noise in the signal power measurements. Furthermore, each channel has a different spectral signature. The two channels used different carrier center frequencies. The combination of using separate bands and each channel's unique spectral signatures could cause differing interference effects from the same environment.

The logging software uses program functions provided in the Android SDK. This allowed for reasonable development times, but also limited the functionality of the device. It would have been preferred to record the RSSI on a set time interval, perhaps every second, or half second. A good method for doing this was not found. Instead, the application opens a log, and records an entry every time the position or RSSI changes. For this reason the records are not evenly distributed. Some time periods have over 100 changes in a minute, others have less than one change every five minutes. Furthermore, the phone would sometimes close the log without notice, or stop taking measurements for extended periods of time. This lead to very few long-period measurements. Despite these issues, 42 data sets of reasonable length (4 hours or more) were recorded. In the recordings, the base station location, and local time is provided along with the power levels of both channels, and the phone's Global Positioning System (GPS) location. This provided sufficient information to calculate σ_I^2, and from it estimate C_n^2. Attempts were made to avoid moving the phone while measurements were taken. This was easiest to accomplish at night, which is why many of the logs begin in the evening and end in the morning.

The original RSSI logging application code was lost due to a hard-drive crash. A new version of the application has been developed which appears to be more stable. Two phones of the same model were retired from their duties as phones, and now are dedicated measurement devices. The measurement timing issue still persists, but continuous measurements are now available from periods on the order of weeks rather

than hours.

Previously, data were interpolated to an evenly sampled space before processing. [8] This solved some implementation problems, but created others. Because the space between broadcast events varied from seconds to hours, it was quite possible that there would be zero variation in RSSI within a period. These zero (or near-zero) variances led to numerical instability in some algorithms, and unrealistic drops in apparent C_n^2 which needed to be filtered out. The RSSI interpolation step has been removed from initial data processing in this work. Instead of having a fixed time window, means and variances are computed for variable sample spaces directly (as described below). The variance and mean RSSI values used in (80) are calculated using the approach presented here. This approach was shown to provide more appropriate C_n^2 values than those obtained in previous work.

The new method used to calculate the RSSI mean and variance overcomes numerical stability issues which arise from variable sample spacing. To arrive at the new method, make the assumption that there exists a function which describes the true RSSI over time, $RSSI'(t)$. This function is sampled at discrete times. The sampling time itself is an increasing function, $t_{i+1} \geq t_i \; \forall \; t$ with variable spacing drawn for the set of natural numbers. That is, $t_{i+1} = t_i + \tau_i$ with $t \in \mathbb{Z}$ and $\tau \in \mathbb{N} \triangleq \{0, 1, 2, 3, \ldots\}$. The distribution of τ is not known, and comparison to a Poisson fit shows that the observed data exhibits a more narrow peak and fat tail than Poisson distributed data (Figure 22).

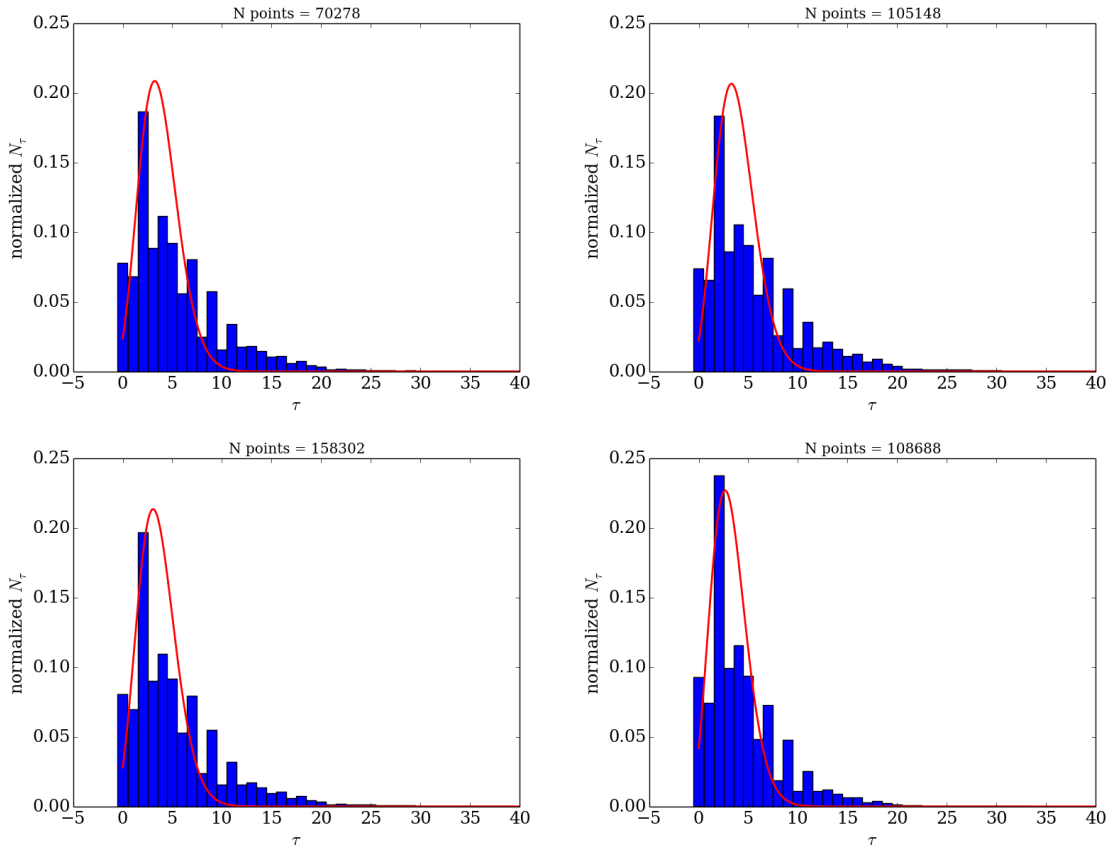

Figure 22. Four distributions of τ, the temporal spacing (in seconds) between cell phone RSSI samples. Blue bars indicate the histogram of relative number of samples (times $> 40s$ were omitted from the histogram, maximum observed $\tau = 200s$). The red line indicates a Poisson process curve fit to the histogram data. Plots are drawn from different months of the year. Clockwise from top left the corresponding months are March, May, July, and September.

Regardless of the underlying distribution of τ, it is necessary to find an acceptable means of estimating the mean RSSI over time, $\langle RSSI'(t) \rangle$ and the square of its first moment $\sigma^2_{RSSI'}$ from the discretely sampled data, $RSSI(t_i) = RSSI'(t_i) + \mathcal{N}_i$ where $\mathcal{N}_i$ is noise it the i^{th} sample and $t_i \in t_0, t_1, t_2, \ldots, t_{M-1} \subset \mathbb{Z}$ are the M sample times with a maximum resolution of one second. Because the underlying function $RSSI'(t)$ is unknown outside of the sample points, any attempt to estimate the

moments of $RSSI'(t)$ from the samples $RSSI(t_i)$ will have to make assumptions about the behavior of $RSSI'(t)$ between points. Here an assumption is chosen which leads to a numerically stable method for estimating $\langle RSSI'(t)\rangle$, and $\sigma^2_{RSSI'}$.

Assuming that $RSSI'(t)$ is an integrable function, $\langle RSSI'(t)\rangle$ over a given interval is defined as,

$$\langle RSSI'(t)\rangle = \frac{1}{T}\int_{t_0=0}^{t_M=T} RSSI'(t)dt = \frac{1}{T}\sum_{i=0}^{M-1}\int_{t_i}^{t_{i+1}} RSSI'(t)dt. \tag{84}$$

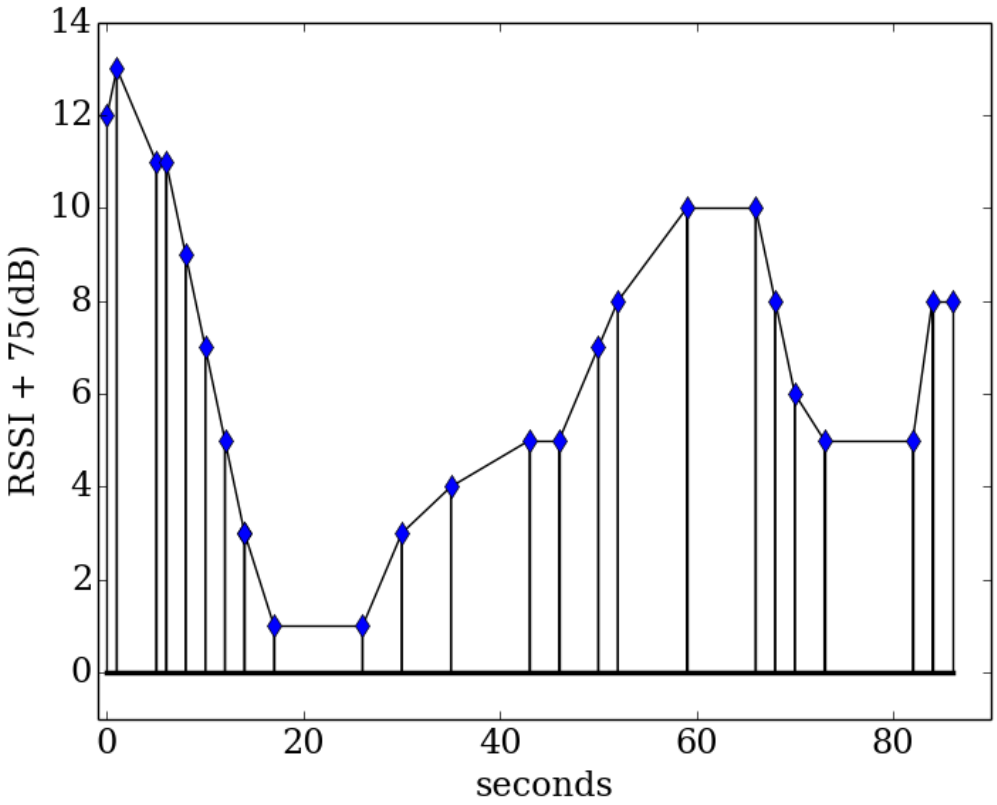

Figure 23. Cell phone voice RSSI samples vs time. Blue triangles represent the sampled points, and the solid black lines depict the piecewise trapezoidal function used to approximate the unknown $RSSI'(t)$ function. RSSI values have been increased by $75dB$ so that integrating trapezoids are easier to depict.

It is then assumed that the integrals between sample points can be approximated using a piecewise integration of trapezoidal functions (Figures 23 and 24),

$$\frac{1}{T}\sum_{i=0}^{M-1}\int_{t_i}^{t_{i+1}} RSSI'(t)dt \approx \frac{1}{T}\sum_{i=0}^{M-1}\int_{t_i}^{t_{i+1}} RSSI(t_i) + t\frac{\Delta RSSI}{\Delta t}dt. \tag{85}$$

Here $\Delta RSSI = RSSI(t_{i+1}) - RSSI(t_i)$ and $\Delta t = t_{i+1} - t_i$. So long as $RSSI'(t)$ is of bounded variation, the RHS of (85) will approach the LHS in the limit that the largest interval $\tau \to 0$ via the standard convergence of a Riemann sum to a Riemann integral.

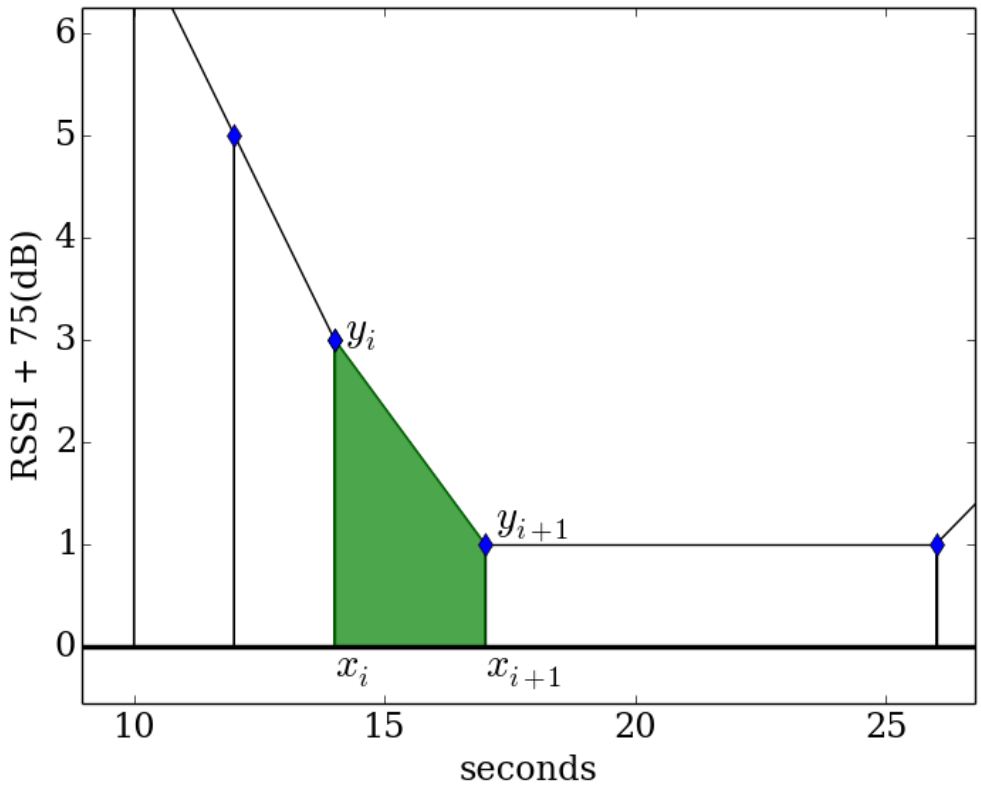

Figure 24. Close up of the i^{th} polygon to be integrated (shaded green). Datum points (blue triangles) are taken from the data originally shown in Figure 23.

It may be possible to test to see if there is reason to believe this trapezoid approx-

imation is flawed. Begin by finding the mean over the entire data set using just the first and last point and the trapezoidal hypothesis. Then, add one of the data points back in and recompute the mean. Add another point, and recompute the mean again, and so on until all available m-point intervals are used to compute the mean. If the mean value shows a tendency converge, then although there is no proof that convergence would continue if the missing unsampled portions of the RSSI'(t) function were added to the integration, there would be no reason to believe that convergence would not happen.

This section shows how the mean and variance of a piecewise-trapezoidal function

$$f(x) = \begin{cases} y_0 + (x - x_0)\frac{\Delta x_0}{\Delta y_0} & \text{if } 0 \leq x < x_1 \\ y_1 + (x - x_1)\frac{\Delta x_1}{\Delta y_1} & \text{if } x_1 \leq x < x_2 \\ \vdots & \vdots \\ y_i + (x - x_i)\frac{\Delta x_i}{\Delta y_i} & \text{if } x_i \leq x < x_{i+1} \\ \vdots & \vdots \\ y_{M-1} + (x - x_{M-1})\frac{\Delta x_{M-1}}{\Delta y_{M-1}} & \text{if } x_{M-1} \leq x < x_M \end{cases} \tag{86}$$

with $\Delta x_i = x_{i+1} - x_i$, and $\Delta y_i = y_{i+1} - y_i$ can be computed when the integer-sized intervals are irregular. The area of each trapezoid can be broken into a rectangular and triangular part for which it is obvious that,

$$A_i = \int_0^{\Delta x_i} f(x)dx = y_i \Delta x_i + \frac{1}{2}\Delta x_i \Delta y_i. \tag{87}$$

Here A_i is the area under the i^{th} trapezoid. By factoring out the Δx term, expressing

it explicitly, and combining y_i terms A_i becomes

$$A_i = \frac{1}{2}(x_{i+1} - x_i)(y_i + y_{i+1}). \tag{88}$$

The difference in x values may suffer catastrophic cancellation. To avoid this when applying the method to cell phone data, leave all times as integer seconds, and define $t_0 = 0$. For time periods used here (days to months) values will remain small enough to avoid any numerical instability. To find $\langle RSSI \rangle$ substitute (88) into (85) to get,

$$\langle RSSI \rangle = \frac{1}{2T} \sum_{i=0}^{M-1} (t_{i+1} - t_i)(RSSI_{i+1} + RSSI_i). \tag{89}$$

Finding the squared-variance for the trapezoidal function $f(x)$ is done in a similar manner. Begin with the piecewise defined variance assuming a uniform (over time) PDF,

$$\sigma_f^2 = \frac{1}{T} \sum_{i=0}^{M-1} \int_0^{\Delta x_i} \left(f(x) - \langle f(x) \rangle\right)^2 dx. \tag{90}$$

For a zero-mean trapezoidal function $g(x) = f(x) - \langle f(x) \rangle$ with samples at x_i with value $\eta_i = y_i - \langle f(x) \rangle$, the squared variance can be found from the area under $g^2(x)$,

$$S_i = \int_0^{\Delta x_i} g^2(x) dx = \int_0^{\Delta x_i} \left(\eta_i + x \frac{\Delta \eta_i}{\Delta x_i}\right)^2 dx. \tag{91}$$

Here $\Delta \eta_i = \eta_{i+1} - \eta_i$. Evaluating the square gives

$$S_i = \int_0^{\Delta x_i} \eta_i^2 + 2x \frac{\eta_i \Delta \eta_i}{\Delta x_i} + x^2 \left(\frac{\Delta \eta_i}{\Delta x_i}\right)^2 dx. \tag{92}$$

On integration (92) becomes

$$S_i = \Delta x_i \left[\eta_i^2 + \eta_i \Delta \eta_i + \frac{1}{3} \Delta \eta_i^2\right]. \tag{93}$$

Substitution of (93) into (90) gives

$$\sigma_f^2 = \frac{1}{\sum_{i=0}^{M-1} \Delta x_i} \sum_{i=0}^{M-1} \Delta x_i \left[\eta_i^2 + \eta_i \Delta\eta_i + \frac{1}{3}\Delta\eta_i^2 \right]. \tag{94}$$

Using the same numerical considerations as in (89), will not necessarily be stable. The factor $\Delta\eta_i^2/3$ could be ill conditioned, and the sum within brackets could also suffer from catastrophic cancellation. In practice, values of η_i typically vary from -10 to 10 with integer steps when working in the dB space. Numerical stability becomes an issue in linear space. Just as Rytov variance for optical scintillation is computed in log-space, RSSI variance calculated using (94) will be done in log space where numerical stability is not a concern.

While a higher-order polynomials could be used as the integrating function (for example, the popular Simpson's Rule could be adapted to the irregularly-spaced data), the computational cost of using these methods (for this data) is not justified by the relatively small reduction in error. The weights of the integrating polynomial must be found for each interval because the spacing is irregular. Furthermore, the data occasionally has $\Delta x_i = 0$, so direct application of methods to find the polynomial constants will result in division by zero. In order to use a higher-order method, the data would have to be filtered to remove all $\Delta x_i = 0$ points, then the constants of integration could be found for each sub-interval. By comparison, the trapezoidal method presented here requires no computation of polynomial weights, and handles $\Delta x_i = 0$ without instability so long as $\sum_{i=0}^{M-1} \Delta x_i > 0$ which holds true for the cell data and $M > 1$.

Once $\langle RSSI \rangle$ and σ_{RSSI}^2 are found, the scintillation index can be found using a

modified, but equivalent form of (80)

$$\sigma_I^2 = \frac{\sigma_{RSSI}^2}{\langle RSSI \rangle^2}. \tag{95}$$

To find C_n^2, σ_I^2 is used in (81). In order to find C_n^2 over time, which can then be compared to NWP and NEXRAD based C_n^2, a fixed $M = 100$ sliding window is used. Because of the irregularity of τ, the temporal width of this window will also vary. The arithmetic mean of the sampling times is used to represent the time of each C_n^2 measurement, $\langle t \rangle = \frac{1}{M} \sum_{i=0}^{M-1} t_i$.

IV. Measurement Noise, Uncertainty, and Clutter

As there are several methods for determining C_n^2, it is important to consider how clutter, noise, and uncertainty play into each component system individually and when brought together into an integrated system. The impact of these on the systems described herein is a limit on performance quantified by the metrics presented in Section 2.1. Unfortunately, quantification of significant clutter, noise, and uncertainty was not available for the input data used herein. So, while these impacts can be studied qualitatively, it is not possible to determine if a particular method is performing within expected bounds. Measurements of structure function constants can vary by more than an order of magnitude in just one minute, or by points which are only a few meters apart. Because variation is over orders of magnitude, plots and comparisons are done in common log space.

When one considers the resolution scales of the data sources involved, it becomes apparent that high frequency variation may only be captured in a statistical sense, and we look for agreement in the low-frequency data components. A valid question centers around how important are the differences in time scale. That is, how much error would be expected if measurements are not simultaneous? With respect to the RMSE error criteria, it is possible to estimate the best-case scenario. That is, if the data were correct, but sampled at a much lower rate (as the NWP and NEXRAD data are), or if data have a temporal uncertainty (as the NEXRAD data have), what would the RMSE be? To find this, scintillometer data are down-sampled via nearest-neighbor interpolation to the radar and scintillometer time-stamps. The down-sampled forms are then up-sampled to the scintillometer data rate using the same linear interpolation which is used with the estimates, and the RMSE is computed. This gives an estimate of the best-case scenario for estimation.

The first two sections here describe both scintillometer and the IDM methodology

from a confidence standpoint. Next, confidence issues in the NWP data are presented, followed by general considerations for the NEXRAD radar. Then, several sections address various possible sources for noise in the NEXRAD data. Finally, cell phone scintillation uncertainty and noise are discussed.

4.1 Scintillometer Error and Uncertainty

Both scintillometers used for comparison are large-aperture scintillometers. These are standard tools for measuring C_n^2 along paths which vary from a few hundred meters to about 10 km. The scintillometer used at the Dayton location is a Scintec BLS2000 [62]. Like other large aperture scintillometers, the BLS2000 integrates C_n^2 over the path with a stronger weighting toward the path center and turbulence near either end of the path having a negligible effect. The scintillometer has a spectral weighting function which peaks around $3cm$ for the conditions of the Dayton path, which is close in scale to the $5cm$ peak spectral weighting of the NEXRAD. Scintillometers do suffer from saturation effects as well as a measurement floor. The effective range of measurements depends on the system which is used, its configuration, and the path length. For the Dayton path, the scintillometer is effective for $4 \times 10^{-17} \leq C_n^2 \leq 6 \times 10^{-13}$. In the data used here, C_n^2 typically peaks at 1×10^{-14} during the day, with a few occasions reaching up to 3×10^{-14}. Most days, the lower bounds of C_n^2 is 10^{-16} or greater. There are a few instances when the lower bound reaches down to 4×10^{-17}, and many periods when there was no recorded C_n^2. Some of the missing data may be due to C_n^2 being too low to detect. This effect is exacerbated in the winter and during storms. The reason being that the window used for the scintillometer receiver blocks a substantial portion of the IR energy. A replacement window of IR-transparent glass was used, but was not water or air-tight. In cases of poor weather, data collection was intermittent.

There are large fluctuations in the scintillometer C_n^2. For this reason, low-pass filtering is often applied to get a smoother measurement. The Albuquerque scintillometer uses a slightly shorter path, but the spectral and path weightings are similar to that of the Dayton path. While the effective bounds for the Albuquerque site are slightly different from those of the Dayton site, they are sufficient for the measurements taken.

4.2 Image Derived C_n^2 Uncertainty

The IDM technique has been accepted for presentation at the 2016 IEEE Aerospace conference [4]. While this technique is not part of the research presented here, the radar data were used to compare against the IDM results. As the technique is new, the available data cover only a short period of about 1 day. As has been seen in comparison with scintillometer data, it is quite possible for there to be significant disagreement on a given day. Difficulties were exacerbated by cloud cover, and storms within the radar coverage area which kept the radar from operating in clear-air mode. Without more data, no definite conclusions can be made. That being said, generating the comparison NWP/NEXRAD C_n^2 data met with its own challenges with respect to creating suitable data for use in the path weighting functions of the IDM.

The path weighting function, $w(l)$, for the IDM technique varies depending on the size and spacing of the objects in the image which are used in the IDM technique. Ideally, the continuous C_n^2 profile over the path would be available, and the resulting measured C_n^2 would be found from

$$\left\langle C_n^2 \right\rangle = \int_0^L w(l) C_n^2(l) dl. \tag{96}$$

In practice this is not possible to evaluate (96) properly, because there are often several

bins with no measurable reflectivity (Figure 25). For a constant-valued weighting function, this is not an issue, as missing data can be handled using (83). For a non-constant path-weighting function, the missing data will introduce errors, regardless of how the data are handled. In fact, even in cases where the radar provides complete data for the path, errors will be introduced. This is because the radar reflectivity is based on the volume-weighting function of the radar beam itself. In general, the volume weighting function of the radar is not expected to give the same $\langle C_n^2 \rangle$ as the path weighting function, (96), passing through the volume.

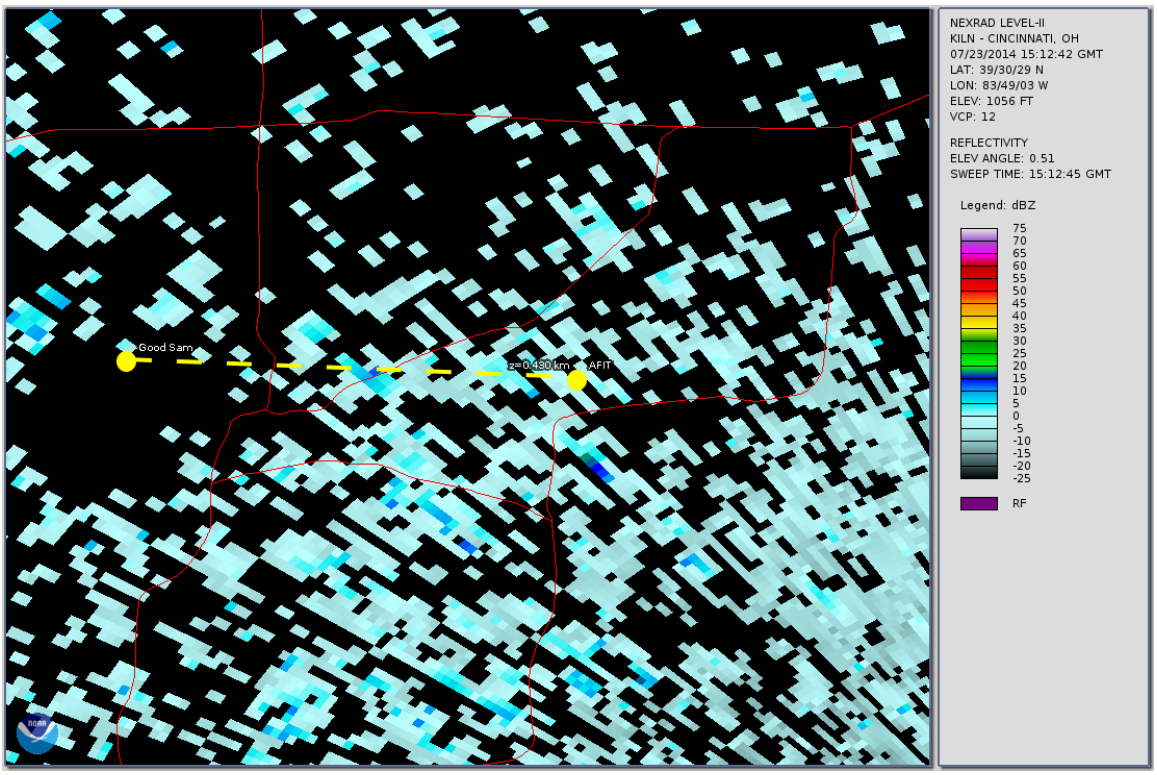

Figure 25. NEXRAD radar image showing the IDM path in yellow drawn over reflectivity bins from 23 July 2014. The radar time-stamp is 1512 GMT, or (local time) 1112 EDT. The Good Samaritan Hospital is located on the West (left) end of the path, and the camera is located at AFIT on the East end of the path. Black areas indicate bins with no measurable reflectivity. Image generated using the NOAA WCT viewer.

The differences in weighting between the radar and IDM technique exist, but little

can be done to account for them. On the other hand, there are several methods for handling missing data in the path weighting function. The first, is to substitute data for the missing sections. The substituted values are, of course, some form of a guess about what the actual value of C_n^2 is within the bin. Common guesses could include interpolating from existing data, using a rule of thumb value, using a mean value from NWP, or setting data to a default value. All of these methods introduce error into the measurement. In some cases, the error may be slight. In others the guessed value may dominate the remaining measured data when determining $\langle C_n^2 \rangle$. The impact of guesses will depend on which data are being substituted, $w(l)$, what values are chosen to substitute, and how closely the guess approximated the actual C_n^2.

Another option was used in [4]. The path weighting function was re-normalized, so that it only included the valid data. Here $0 \leq l < 1$ is a parameter of the path length. The path's location is defined by $\vec{x}(l)$ and $C_n^2(\vec{x}(l)$ gives the radar reflectivity at point $\vec{x}$ as the value of the bin $\vec{x}$ is within. If we define a function which represents where valid NEXRAD data are present within the path as

$$v(l) = \begin{cases} 1, & \text{bin contianing } \vec{x}(l) \text{ has data} \\ 0, & \text{otherwise} \end{cases}, \tag{97}$$

then the path weighting function can be renormalized via

$$\langle C_n^2 \rangle = \frac{\int_0^1 w(l)v(l)C_n^2\left[\vec{x}(l)\right] dl}{\int_0^1 w(l)v(l)dl}. \tag{98}$$

This choice does not introduce incorrect data, but does improperly weight existing data. Despite the fact that the weightings are no longer correct, the proportionality is maintained between existing data.

The turbulence eddy size most strongly weighted by this method has not been

established yet, but is expected to be larger than the telescope aperture, but smaller than the outer scale of turbulence. Because this technique is based on tilts, the first derivative of the phases, it is expected to be able to overcome saturation issues which are encountered for intensity based scintillometery.

4.3 Uncertainty in NWP

As mentioned in Section 1.5 NWP has spatial and temporal resolution which is very coarse when compared to PBL turbulence. Keep in mind that turbulence advects with the mean wind, and it is not uncommon for scintillometer C_n^2 to change by half an order of magnitude from minute to minute. For a $5kn$ wind, this would indicate that C_n^2 can vary significantly over just $150m$. Compare this to the GFS forecast, which was used in much of this work. GFS has a 0.5^o resolution in both longitude and latitude. This results in a grid spacing which is much larger than the propagation paths which are compared to (Figure 13). Like other NWP models, the vertical resolution of the GFS grid is much finer than horizontal resolution. The GFS forecast uses a pressure coordinate, and levels are spaced $25mb$ apart from $1000mb$ to $800mb$. This corresponds to about $220m$ of separation in the lower PBL (where the scintillometer paths are located). Grid spacing necessary to resolve the structure of turbulence would need to be finer than the typical inner scale, $1.0cm$. Their coarse spacing precludes using GFS (or other NWP models) to determine the perturbation structure of the lower atmosphere. Instead, NWP is used to obtain gradients of the mean (slowly varying) atmospheric parameters, which can be used with Tatarskii's method, (23), to estimate structure function constants.

These gradients are not without uncertainty. Forecast models are numerical solutions for several coupled partial differential equations. As such, they must be initialized with boundary conditions which match real-world conditions over the grid.

A combination of previous forecast output and available observation data is used to generate the initial conditions. Both sources have uncertainty and noise, which is carried forward into each realization of the model. No attempts were made to account for this uncertainty in the NWP data. As a partial mitigation, the most recent NWP model was used for each data time. This means that for GFS, the +0 and +3 hour forecast data were used when available. At times, a forecast would not be available, or the available version would be corrupted. In this case the most recent available forecast is used. For example, the data for hours 1200 and 1500 normally come from the 1200 forecast at the +0 hour and +3 hour time steps. If the 1200 forecast is not available, then both the 1200 and 1500 data must be found from a previous forecast. In order to get the 1200 and 1500 data, then the 0600, would be used with its +6 hour and +9 hour steps. If the 0600 hour forecast is not available, then the 0000 hour forecast would be used with the +12 and +15 hour forecast, and so on. This minimizes the impact of the stepwise increase in forecast uncertainty.

The bounds of accuracy required for the NWP forecasts is determined, by comparing error in C_n^2 by deviations in temperature to the error expected to be induced by the low temporal resolution (hours) of the forecast compared to the scintillometer (1 minute). This comparison shows how large the error in NWP gradients (their data which are used to estimate C_n^2) must be to be as large as the smallest possible error induced by resampling. It turned out that the $\langle RMSE \rangle$, averaged in log space over all 12 months of data for the KILN data, is 0.3286. Based on how the gradients are used in (21), the NWP gradients would need to be off, on average, by a factor of 1.5 in order to be as large as the smallest possible resampling error. That is

$$0.7 < \frac{x_{est}}{x_0} < 1.5 \tag{99}$$

where x_{est} is the NWP value and x_0 is the true value. Comparison with RAwindsonde

OBservation (RAOB) data shows that this condition is satisfied for GFS forecasts.

The resampling $\langle RMSE \rangle$ for Albuquerque was higher at 0.4120. However, there were also significant systematic errors in gradients obtained from the RAP forecast, which was used to obtain gradients for the Albuquerque estimates. The source of these systematic errors could not be identified. Instead, a scaling factor (typically $^1/_{20}$) was applied to RAP-derived gradients in order to minimize the error between these forecasts and available RAOB data. To determine the scaling factor, RAOB gradients were compared to RAP gradients at several times through each month. Then the mean scaling was applied to all the RAP data that month. The magnitude of the scaling varied from month to month, and affected both the temperature and pressure gradients. This systematic error was also seen when RAP was used to compute gradients for the Dayton data. Note that GFS gradients did not appear to have this issue and were used for all included Dayton NWP data.

The RAP was chosen because of its fine resolution in latitude and longitude. Initially the GFS was used to process the Albuquerque data. However, it was noted that NWP predictions of C_n^2 were poor compared to those of Dayton. After searching for a cause, it was discovered that the root issue was the NWP interpolation scheme used. As written, the NWP code uses a grid of 16 points to do a cubic spline interpolation in latitude and longitude to the path location. This method was originally developed for the vertical interpolation. The method was extended to use as horizontal interpolation. The issue when applied to Albuquerque is that the ground height at the Albuquerque site is much higher than the ground height at some of the included nearby GFS grid points. Because of the significant vertical variation, estimates of temperature, pressure, humidity and their gradients were found to be incorrect. The RAP forecast was chosen as it has much finer resolution. However, the RAP processing algorithm also had to be simplified to use nearest neighbor for its horizontal

interpolation. It turns out that the closest GFS point is about $^1/_2$ the distance of the closest RAP point to the Albuquerque path location. Unfortunately, gradients from this GFS forecast site did not match well with RAOB data either. GFS temperature values for this site (at pressures just above ground level) did not show the trends or structure of RAOB data. After accounting for the systematic errors in the vertical gradients, RAP data did the best job matching observed atmospheric conditions at the Albuquerque site. For this reason, RAP data were used for Albuquerque.

In addition to raw NWP inaccuracies, there may be errors in some of the standard parametrization used for Tatarskii's method (23). This was noted when comparing the IDM technique. The value of C_n^2 determined was significantly lower than measured during periods of a stable PBL. It was discovered in this data that the ratio of the eddy diffusivity of heat to the eddy diffusivity of momentum, $^{K_H}/_{K_M}$, determined from the Kondo equation [38] became quite small during stable conditions. The quantity $^{K_H}/_{K_M}$ is used the relate the flux Richardson number, R_f, which is the ratio of the buoyant production to mechanical (shear) production terms in the TKE budget equation

$$R_f = \frac{\text{Buoyant Production}}{\text{Shear Production}}, \tag{100}$$

to the measurable Bulk Richardson number, R_i through the relation

$$R_f \approx \frac{K_H}{K_M} R_i. \tag{101}$$

The approximation is due to the use of first-order closure to handle ever expanding perturbation terms. Kondo's equation is an empirical fit of the ratio $^{K_H}/_{K_M}$ to R_i

and is defined as [38]

$$\frac{K_H}{K_M} = \begin{cases} \frac{1}{7R_i} & R_i > 1 \\ \left(6.837R_i + \frac{1}{1+6.837Ri}\right)^{-1} & 0.01 \leq R_i \leq 1 \cdot \\ 1 & R_i < 0.01 \end{cases} \tag{102}$$

The determination of R_i and ${}^{K_H}/_{K_M}$ relies on temperature and wind shear from NWP. However, NWP are often unable to accurately predict the formation and impact of clouds on local temperature structure. It has been noted that Temperature based C_n^2 estimates tend to be noticeably larger than scintillometer measured C_n^2 under cloudy or overcast conditions. For example, Figure 26 shows estimates and scintillometer data from April 20-30 of 2013. Comparison with local weather observations showed that skies were overcast with the exception of two periods. The first clear to partly-cloudy period ran from the latter part of the 20^{th} through the first half of the 23^{rd}, and the second ran from the 25^{th} through the end of the 27^{th}. While at appears that C_n^2 estimates still do well for a few hours after clouds first arrive, the correspondence between sky-cover, and C_n^2 over-estimation is apparent. In the results, Section 5.1, the increased error during the months July-September for the Dayton estimates is observed to be due to this phenomenon.

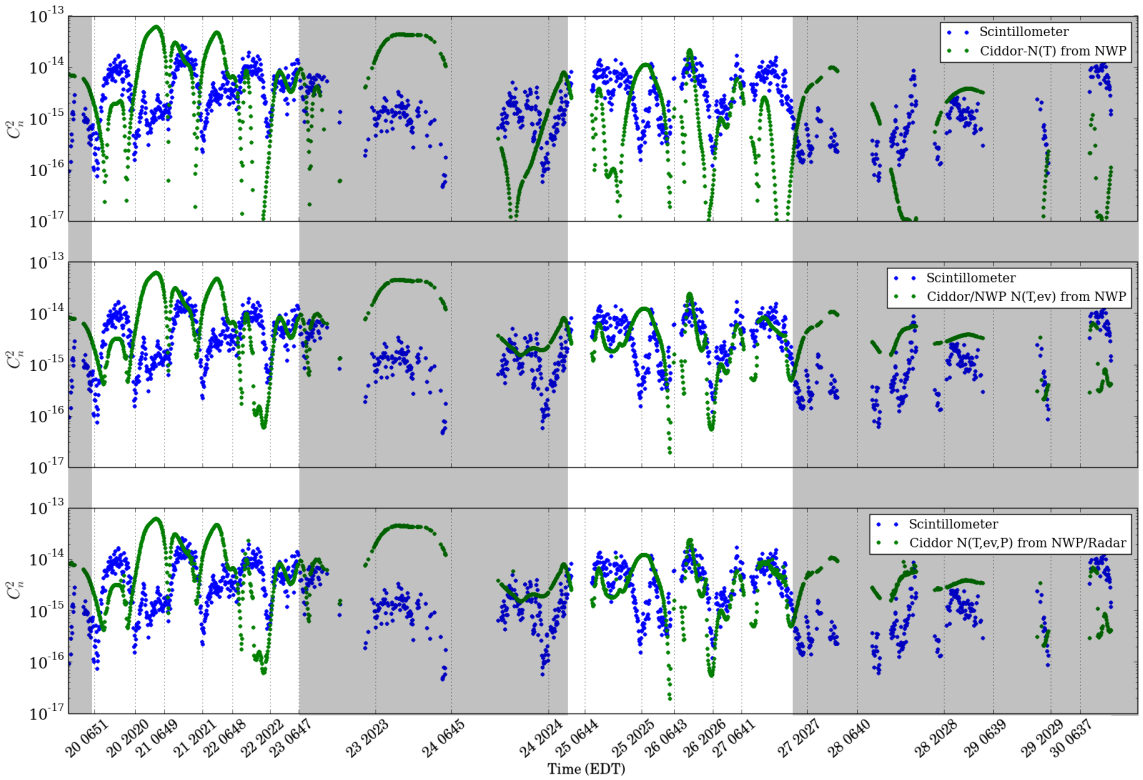

Figure 26. Estimated C_n^2 and scintillometer C_n^2 vs time from the Dayton site taken 20-30 April, 2013. Scintillometer data are blue dots in all three plots. Green dots are estimates made using Ciddor's equation using only temperature (top), using temperature and vapor pressure (middle), and using temperature, vapor pressure, and non-hydrostatic pressure gradients (bottom). Shaded areas indicate periods of overcast skies and x-axis ticks occur at local sunrise and sunset.

There are two NWP gradients which could be causing the increase in NWP-estimated C_n^2; potential temperature and wind velocity. The magnitude of the squared potential temperature gradient $\left(\frac{d\theta}{dz}\right)^2$ is proportional to C_n^2. Clouds during the daytime reduce the large instability which is commonly present due to solar heating of the surface. At night, clouds reduce the stability by reducing radiative losses at the surface. In both cases, they significantly reduce the magnitude of $\frac{d\theta}{dz}$. If NWP is not properly capturing these radiative processes, then it could be over-estimating C_n^2 because of overestimation of $\frac{d\theta}{dz}$.

The possible cause of decreased C_n^2 in the IDM comparison could be large R_i and thus low $\frac{K_H}{K_M}$. R_i is defined as

$$R_i = \frac{\frac{g}{\theta_v}\frac{d\theta_v}{dz}}{\left(\frac{dU}{dz}\right)^2 + \left(\frac{dV}{dz}\right)^2}. \tag{103}$$

Here g is the acceleration due to gravity, θ_v is the virtual potential temperature, U and V are the zonal and meridional components of the wind. R_i is thus proportional to $\frac{d\theta}{dz}$ and inversely proportional to squared wind shear, $\left(\frac{dU}{dz}\right)^2 + \left(\frac{dV}{dz}\right)^2$. NWP overestimation of $\frac{d\theta}{dz}$ or underestimation of the shear would cause R_i to be too large and $\frac{K_H}{K_M}$ based on the Kondo equation and C_n^2 to be underestimated. A consistent underlying cause of these discrepancies during cloudy periods has not been found. And there are several cloudy periods where NWP based C_n^2 estimates appear to be fine. However, periods of severe overestimation and underestimation have thus far been associated with cloudy periods.

The RAP forecast would often return potential temperature and vapor-pressure gradients which were well over an order of magnitude larger than those seen on the GFS and RAOB data. It was also noted that these abnormally large gradients led to large errors in C_n^2 estimates. For this reason, a step was added to the processing where data were removed from comparisons when gradients exceeded 20 times the typical gradient values. That is when gradients of θ or e_v reach magnitudes of 0.06 $^{units}/_{meter}$, the corresponding data were removed from the comparisons. This step was done manually, in a similar manner to identification of precipitation in the NEXRAD data, or missing scintillometer data. Figure 27 shows an example of filtering the e_v gradient from Albuquerque data. Red regions correspond to periods which will be removed from comparison.

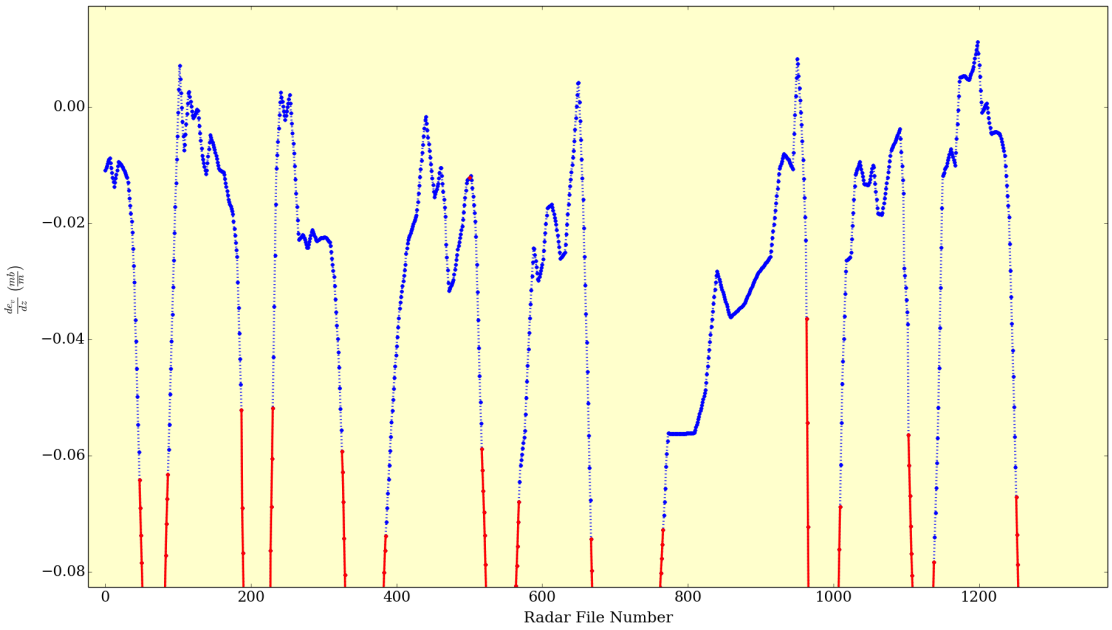

Figure 27. NWP gradients, de_v/dz in mb/m vs NEXRAD file number. The red regions show an example of manually filtered NWP gradients, which were rejected as being unrealistically low.

4.4 Radar Data Inconsistancies

Radar C_n^2 is derived from reflectivity measurements under the assumption that reflected energy is due to scattering of index gradients created by turbulent eddies within the inertial subrange. Reflections from any other sources is considered to be noise and could artificially increase the radar C_n^2, and mask turbulence-induced Doppler-spectrum width. This section and the four following sections present an investigation of the impact of possible clutter and noise sources.

The first source to consider is hydrometers. These could be clouds or precipitation in the data. Rain events are typically easy to identify as they produce abrupt increases in reflectivity with typical increases being 1-3 orders of magnitude. These events can also be cross checked by comparing to ground observations, examining the radar

volume coverage pattern, and the radar's wide-area reflection pattern. In the presence of hydrometer noise, C_n^2 measurements from the radar are considered unreliable.

Another source of noise is reflections off biological or man-made objects in the atmosphere. NEXRAD radar reflectivity is often used to study both insects, migratory birds, and bats. [23, 31, 53] While these reflections are certainly present, it has long been known that index gradients also contribute to the total scattering in a given volume of air. [26] Before proceeding, it is important to consider whether the NEXRAD measurements used herein are trustworthy measurements of clear air turbulence, or if clear-air reflectivity is dominated by ground clutter, insects, birds and aircraft. While scattering cross sections for various biological and man-made structures are fairly well known, volume scattering requires populations densities, which are more difficult to determine. [16, 23, 26] Based on the findings here, we believe that the majority of the data used includes some echoes from insects, birds, and ground reflections, but with the exception of ground clutter, these signals do not dominate turbulence returns in most of the data. To show this, we look to see how strongly mean radar reflectivity follows population dynamics. We will show that radar reflectivity and C_n^2 do not correlate well with known population dynamics, and that aircraft are not likely to be present in most of the C_n^2 data sets. One exception is a cell phone path which is 2 km from a civilian airport.

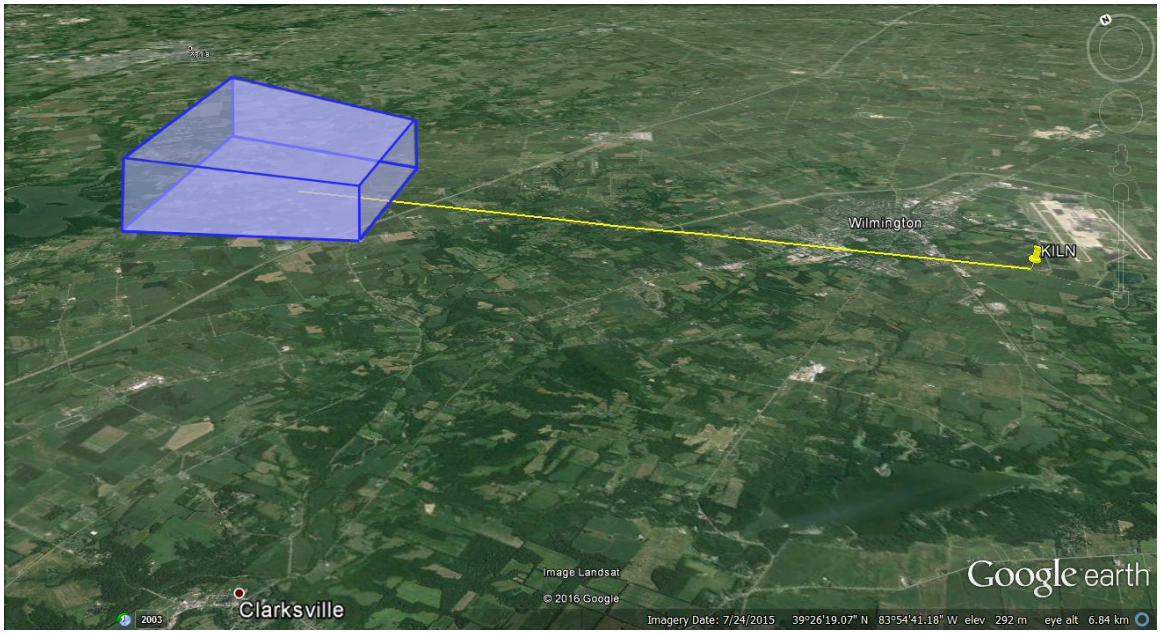

Figure 28. Image of Southwest Ohio showing the KILN radar and the location of the measurement volume used in this study. The distance from the radar to the center of the volume is $14.5km$**.**

In Section 4.9 some of the geometric considerations pertaining to NEXRAD use are presented. In order to investigate geometric effects and other noise sources, a volumetric representation of C_n^2 in the PBL is used. NEXRAD radar can resolve C_n^2 structure if measurements are taken at a radial distance of about $14km$ (Figure 28). At this range, the width of radar bins is around $250m$. Range gating is typically $250m$ as well, so the bins are approximately symmetric at this range (Figure 29). This means that the first four elevations (nominally centered at 0.5^o,1.5^o,2.5^o,and 3.5^o) of clear-air VCP will fill a typical daytime PBL. Here measurements are taken with an azimuthal range of 8^o, a radial range of $3km$, and elevation range of 4^o. These dimensions provide a $2 \times 3 \times 1km$ volume of C_n^2 measurements.

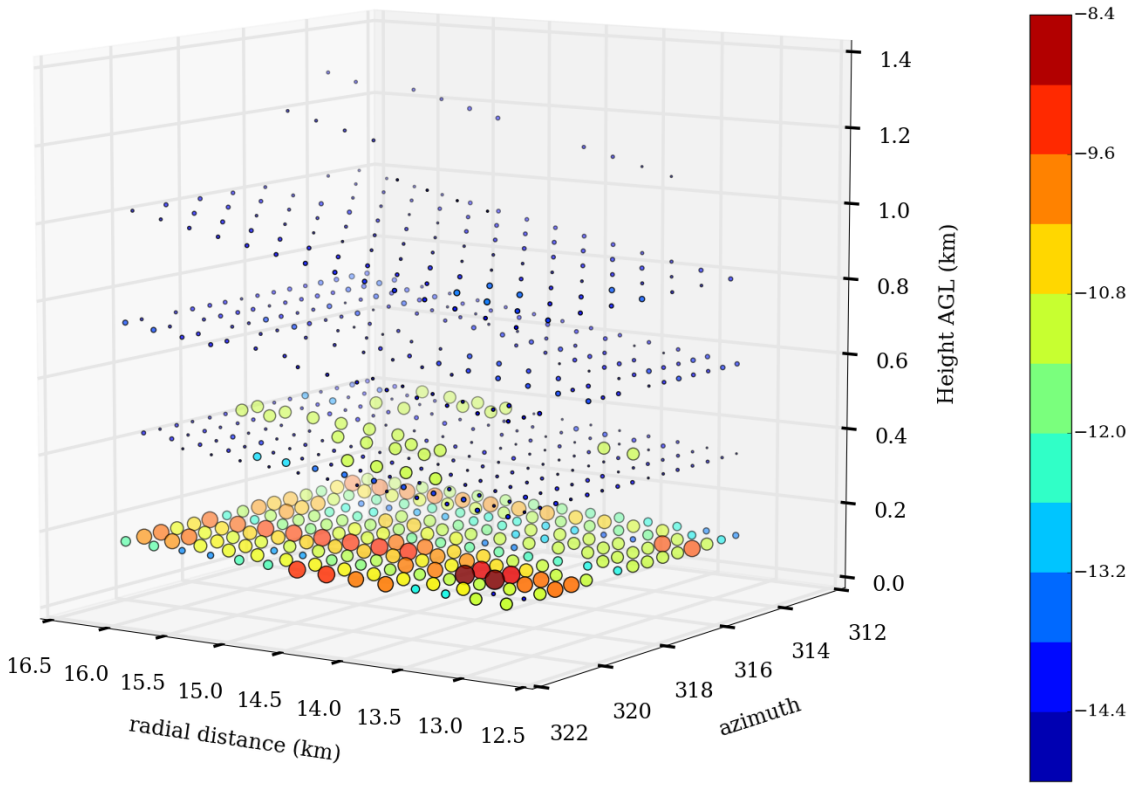

Figure 29. Single volumetric C_n^2 measurement taken by the KILN radar on 27 November, 2013 at 0656 EST. Each sphere represents a measurement of C_n^2 (arbitrary scale) with the color and sphere size being proportional to $Log_{10}(C_n^2)$. The x-axis corresponds to the bearing from North. The y-axis corresponds to radial distance from the radar, and the z-axis corresponds to the vertical height of the beam. Terrain under the volume includes Ceaser's Creek state park and surrounding farmland.

This volumetric measurement technique was used to investigate clutter (addressed in the next section), and the vertical structure of C_n^2 in the PBL. While each volume provides valuable information by itself. It is also important to view how the volume will evolve over time. In order to show vertical structure over time, the radial and azimuthal dimensions are collapsed down for each volume in a time series. The bin data are then re-plotted as C_n^2 vs height vs time. An example data set is presented in Figure 31. Because of the beam elevation, the height of each bin increases with

radius. This causes the higher elevation rays to show more vertical diversity than lower elevations. A 2-D representation of collapsing measurements in the radial dimension is shown in Figure 30.

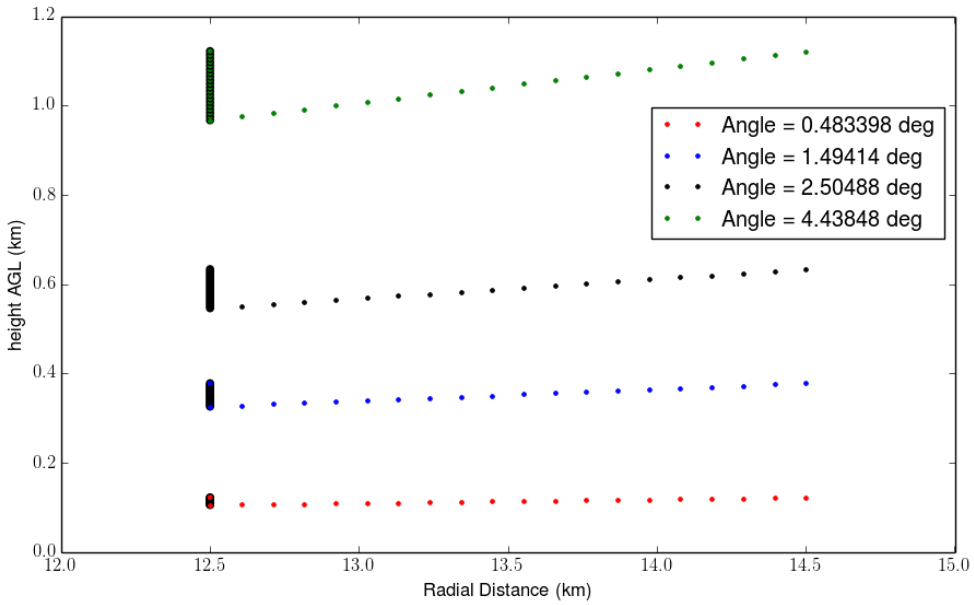

Figure 30. Height above ground level (AGL) vs radial distance for four elevation angles reported by KILN radar in clear-air mode. Each color represents a different elevation angle. The outlined circles to the left are the resulting heights after collapsing measurements down in the radial dimension as done when converting from the volumetric C_n^2 measurements to the C_n^2 vs height vs time representation in Figures 31 and 32.

As is shown in this Figure 31, variation in C_n^2 measurements within the lowest portion of the PBL is quite large. This large variation in the lowest elevation has been seen in all plots of this type. Daytime C_n^2 generally decreases with height up to about $800m$ then increases slightly near the top of the PBL. Nocturnal C_n^2 also decrease with height. However, while the mean decreases with height, nocturnal C_n^2 often shows a wide range of C_n^2 throughout the nocturnal boundary layer (up to approximately $600m$ in Figure 32), while daytime PBL values tend to show a wide

range only in the lowest elevation. The top of the nocturnal boundary layer can be seen by the significant drop in C_n^2. Additionally, the dusk quiescent period can be seen in Figure 31 between 1937 and 2131. In Figure 32 there did not appear to be a dusk quiescence, while in 33 the dawn and dusk quiescent periods are quite visible. Ground observations at sunset showed that skies were clear and a steady wind of about $6kn$ ($3.1^m/_s$) was present on 1 May, and on 21 July skies were also clear with a variable $3kn$ ($1.5^m/_s$) wind. It may be that biological echoes (Section 4.6) are artificially elevating clear air reflectivity in the May data. Conditions on 9 February were also clear, with light winds.

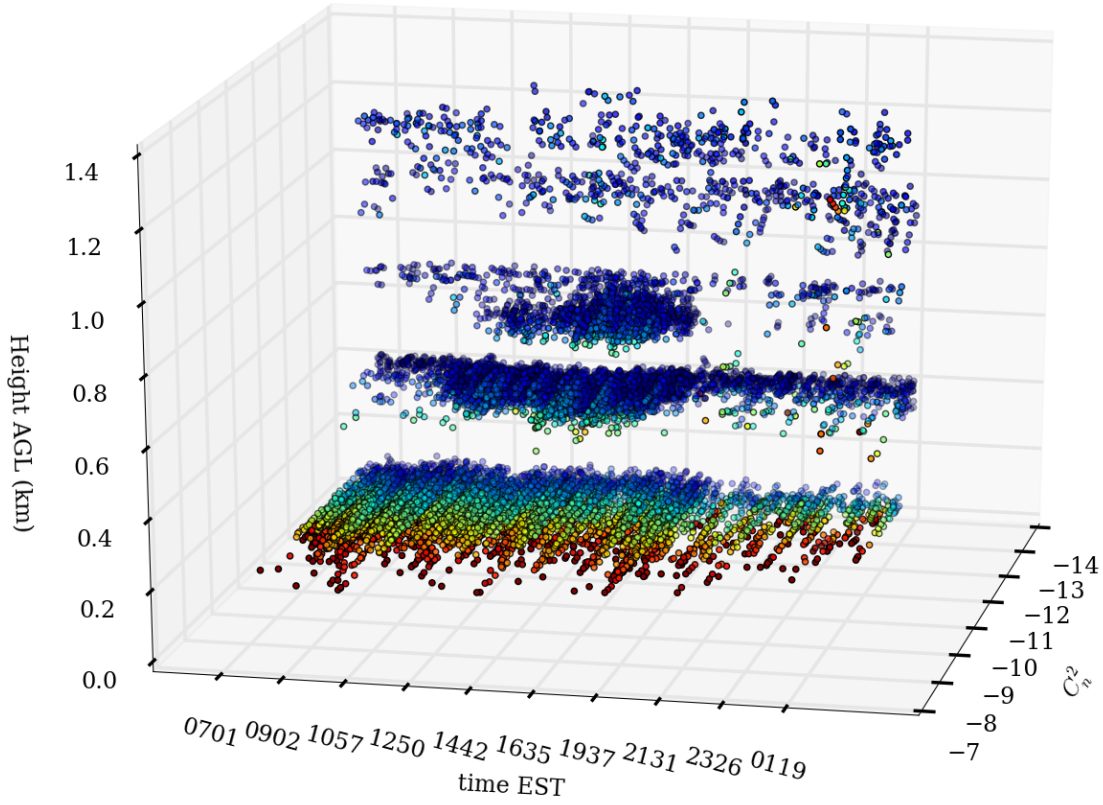

Figure 31. Vertical C_n^2 vs time from the KILN radar measured on 9-10 February, 2013 when migratory birds were not expected to be present. Each sphere corresponds to one measurement from the volume described in Figure 29. The y-axis corresponds to the local time (EST) when the measurement was taken. The x-axis position and sphere color correspond to $Log_{10}(C_n^2)$, and the vertical axis corresponds to the vertical height of the center of each measurement. Local sunrise occurred at 0734 EST and sunset occurred at 1805 EST.

Near the scintillometer path, there is not sufficient spatial resolution in the radar data to estimate the vertical structure of C_n^2. Attempts were made to scale radar C_n^2 by fitting vertical scaling measured close to the radar to a quadratic polynomial, and then applying this equation to scale radar C_n^2 from the center of the beam height to the scintillometer path height. In a majority of cases, this decreased measurement accuracy. Another attempt was made to create a climatological scaling. Quadratic

fits of the vertical variation of C_n^2 were generated for all radar files within a month. Then the mean of each parameter was calculated for the parameter ensemble from each month. While these monthly parameter means did show seasonal dependence, and variation with location, applying the scaling to measured data did not provide any measurable improvement in agreement.

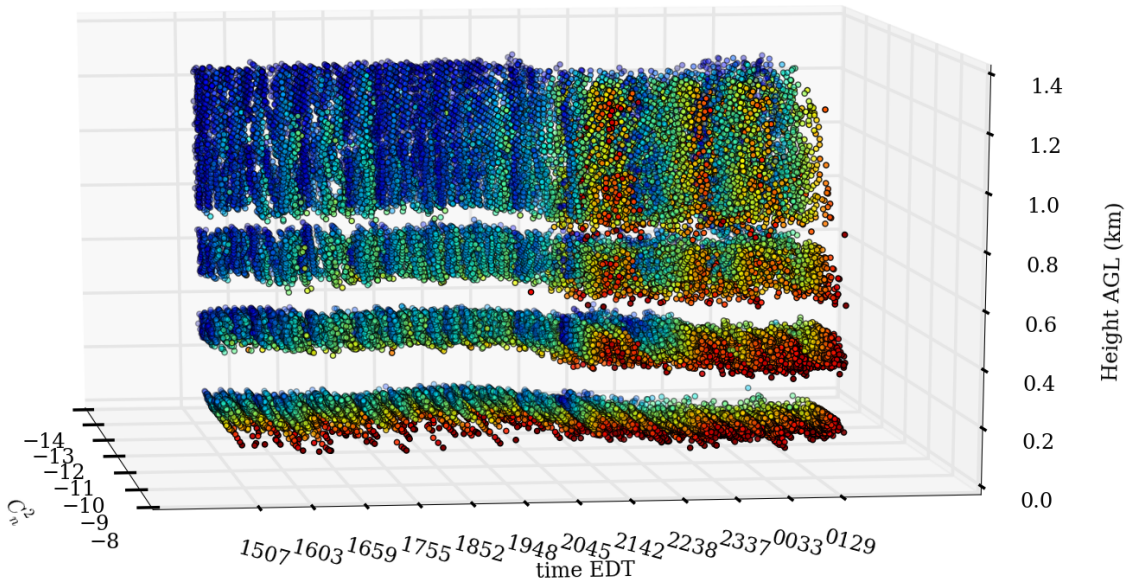

Figure 32. Vertical C_n^2 vs time from the KILN radar measured on 1-2 May 2013, when migratory birds are expected to be present. Each sphere corresponds to one measurement from the volume described in Figure 29. The y-axis corresponds to the local time (EDT). The x-axis position and sphere color correspond to $Log_{10}(C_n^2)$, and the vertical axis corresponds to the vertical height of the center of each measurement. Local sunset occurred at 2031 EDT.

Part of the reason that application of the scaling did not help for the data used herein may be the distance of the scintillometer path from the radar. At the distances used here, the radar integrates measurements over most of the boundary layer. Since the lower PBL returns a wide spread of values, even though sensitivity may be 3 to $4dB$ below the maximum of the radar main beam gain, C_n^2 near the bottom of the

boundary layer commonly shows values which range from those of the upper PBL to about 3 orders of magnitude above values in the upper PBL. Based on (10), the 3 to $4dB$ drop in sensitivity of the beam at the scintillometer path height would not overcome the large increase in C_n^2 seen at the bottom of the PBL. Assuming that variation at the Dayton path is similar to variation seen in these volumetric measurements, it would be expected that the radar C_n^2 is dominated by the larger C_n^2 values in the lower PBL.

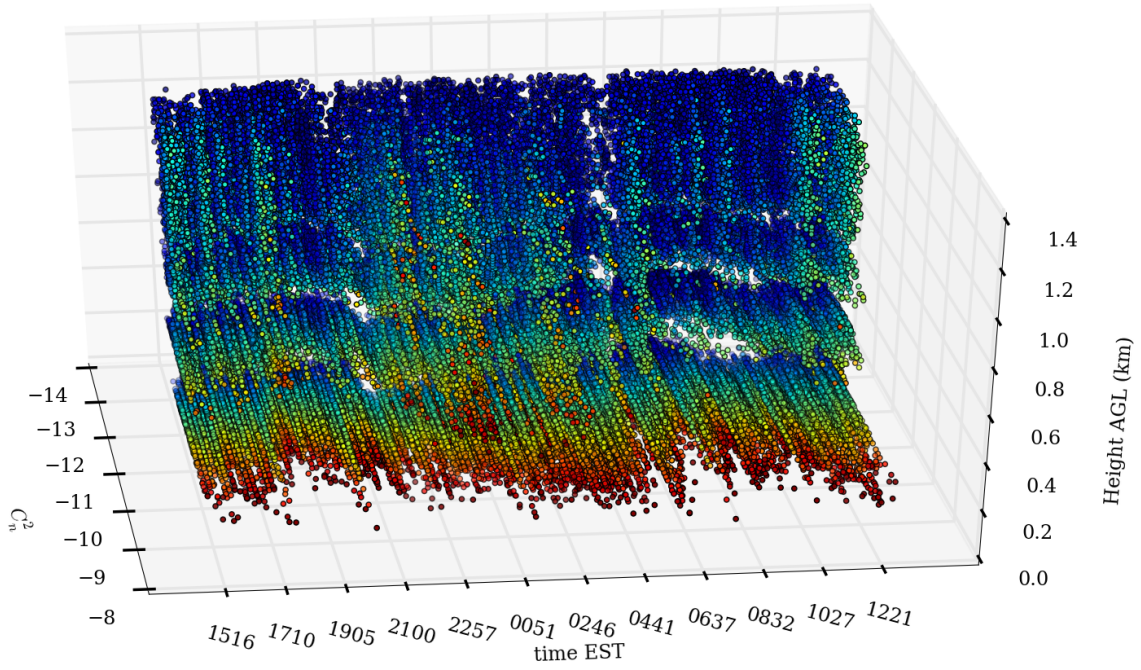

Figure 33. Vertical C_n^2 vs time from the KILN radar measured on 21-22 July 2014, when birds are expected to be present. Each sphere corresponds to one measurement from the volume described in Figure 29. The y-axis corresponds to the local time (EDT). The x-axis position and sphere color correspond to $Log_{10}(C_n^2)$, and the vertical axis corresponds to the vertical height of the center of each measurement. Local sunset occurred at 2057 EDT and sunrise occurred at 0626.

Another difference between the scintillometer and radar measurements is the weighting of C_n^2 along the path. The scintillometer, like the radar, averages C_n^2

along the path, but the weighting function of the scintillometer is strongest in the center. [62] On the other hand, the radar reflectivity is averaged evenly along the path. Applying the scintillometer weighting to the radar path is possible, but has not been investigated in this work.

The next section will discuss how hydrometer noise is handled. After this, Section 4.6 will explore the impact of biological signals from birds and insects. Bats are not investigated per se, but as they are of a similar size to birds, it is assumed that their contribution will have a similar impact. Following this, Section 4.7 will discuss if and where aircraft may have an impact. Finally, in Section 4.8 the impact of ground clutter will be presented.

4.5 Precipitation

Precipitation affects turbulence, and all measurement methods. Fortunately, it's easy to see with the radar, and shows up as large increases in reflectivity, and proportionally large increases in reflectivity based C_n^2. It is assumed that detection of turbulence echoes in the presence of precipitation is not possible for NEXRAD. For this reason precipitation events are identified as in Figure 34 and data from these periods are ignored in the RMSE and NBEC calculations.

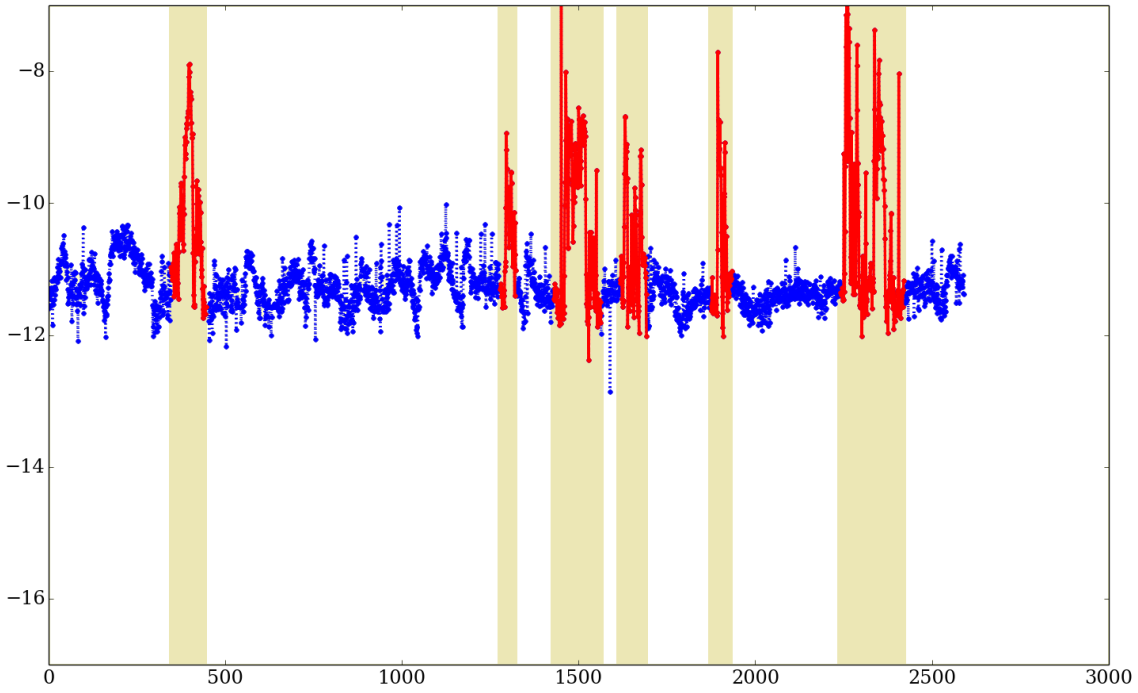

Figure 34. Radar C_n^2 vs radar file number (in chronological order). Portions of the plot in blue indicate points that will be maintained. Portions of the plot in red with a shaded background are identified as precipitation events, and will be omitted from the results.

Before writing a program to allow the user to interactively select points to omit, more straightforward approaches were attempted. Initially, a filter was put in place based on the NEXRAD VCP. However, this was a poor choice, as there are many periods when the radar is in a precipitation mode but the air in and around the region of interest is clear. For example, Figure 35 shows the VCP in the middle plot and the path-averaged reflectivity in the bottom plot (on a file by file basis). It is apparent that during much of the 10 day period the KILN radar is in VCP 12, a precipitation mode. However, precipitation is only evident in a few hours worth of data. This makes sense when one considers the difference in area between the Dayton scintillometer path, and the radar coverage area.

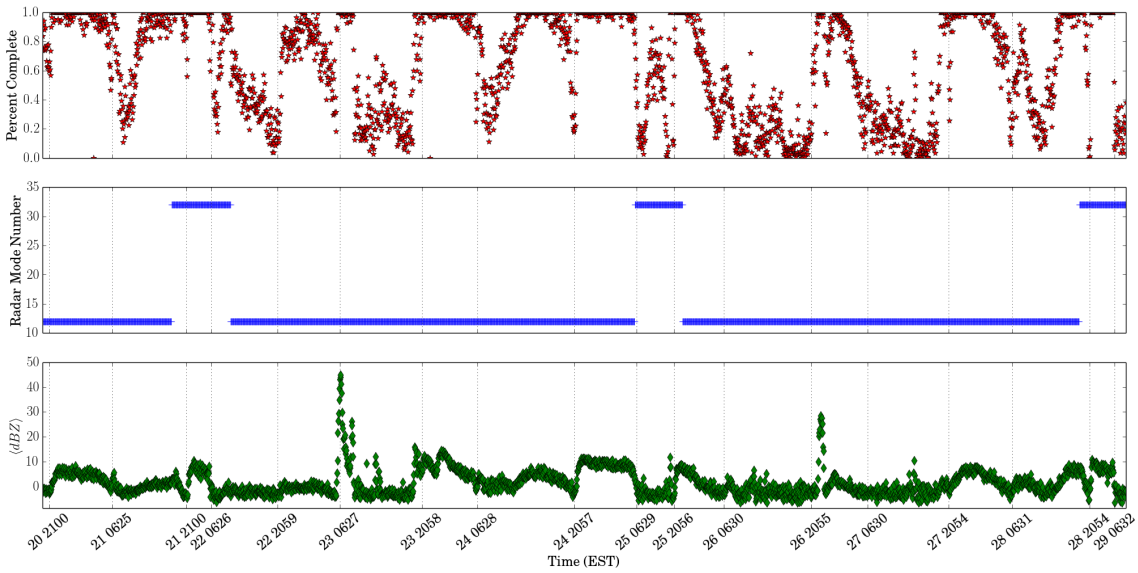

Figure 35. Top: Completeness of NEXRAD data vs radar file number for data bins along the Dayton Scintillometer path. Middle: Radar volume coverage pattern (VCP) vs radar file number. Mode 12 is a precipitation mode, and mode 32 is a clear air mode. Bottom: Path-averaged reflectivity ($\langle dBZ \rangle$) vs radar file number. Note that while the NEXRAD spend much of the 10-day period in precipitation mode, there are only three precipitation events. The first occurs between files 700-750, the next from files 1860-1890, and a small event can be seen from 2100-2010. Data are taken from 20-30 July, 2014.

4.6 Birds, Bats, and Bugs

NEXRAD radars have become a popular tool for studying bird populations [23,53]. For this work, it is worth understanding sources of reflected energy in radar echoes, so that it can be determined when, if at all, turbulence-based echoes are present and significant contributors. A first step in estimating the influence of birds, is to estimate the number of birds required to reflect the amount of energy seen in radar returns. Radar reflectivity is measured $dBZ = 10log_{10}(Z)$, which gives a measure of how many drops of water are present in a given volume. Z has units of mm^6/m^3 which can be

converted to $\eta = {}^{\sigma}/_{m^3}$ the radar-cross-section per unit volume using [16]

$$\eta = \frac{\pi^5}{\lambda^4} |K_w|^2 Z. \tag{104}$$

Here $\lambda = 0.107\ m$ is the radar wavelength and K_w is the complex index of refraction of water $|K_w|^2 \approx 0.929285$. Doviak lists the scattering cross section of small birds to be $\sigma_b = 10^{-3} m^2$, and larger birds (sea gull) at $\sigma_B = 10^{-2} m^2$. To determine the population density, say of small birds, ρ_b required to give an equivalent reflectivity,

$$\rho_b = \frac{\eta}{\sigma_b} = \frac{\pi^5}{\lambda^4 \sigma_b} |K_w|^2 Z. \tag{105}$$

Taking the common log of both sides gives

$$\log_{10}(\rho_b) = \log_{10}\left(\frac{\pi^5 |K_w|^2}{\lambda^4 \sigma_b}\right) + \log_{10}(Z) \approx 9.3364 + \frac{dBZ}{10}. \tag{106}$$

Because Z is in mm^6/m^3 while σ_b and λ are in m^2 and m, respectively, Z must be converted to m^6/m^3. This gives the population as a function of dBZ as

$$\log_{10}(\rho_b) = 9.3364 - 18 + \frac{dBZ}{10}. \tag{107}$$

To find the number of birds per radar bin in the radar volumes like Figure 29, multiply by the bin volume ($V_{bin} \approx 250 \times 250 \times 250\ m^3$). This gives the number of birds n_b per bin,

$$\log_{10}\left(\frac{n_b}{bin}\right) \approx 9.37 - 18 + \frac{dBZ}{10} + log_{10}(V_{bin}) = \frac{dBZ}{10} - 1.4698. \tag{108}$$

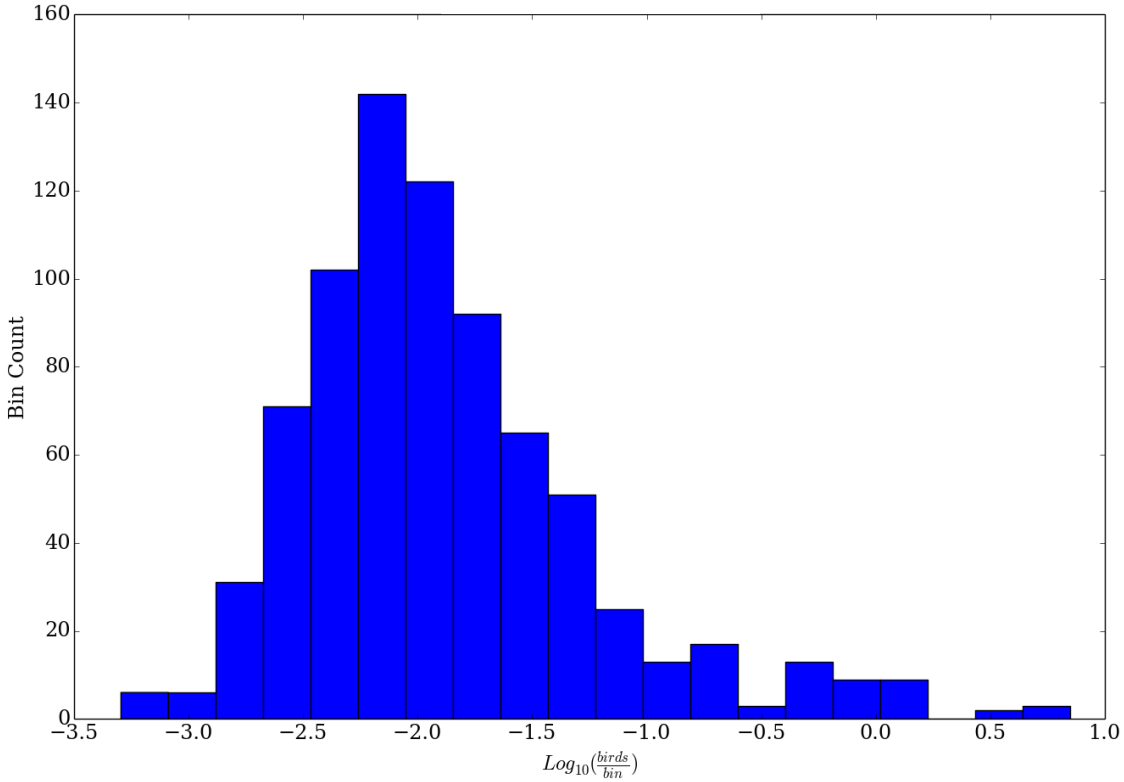

Figure 36. Histogram of the number of birds per bin required to give the refracted energy recorded in the afternoon by the KILN NEXRAD radar on 21 July 2014 at 1632 EDT. The total number of birds is found by adding up the number of birds in all the bins with at least 1 bird per bin.

Using this method, the required bird population per bin was calculated for an afternoon and evening volume in July. Histograms of the resulting bird populations are presented in Figures 36 and 37. Note that most bins have less than 1 bird per bin in both plots. The maximum total number of birds present, N_{birds}, (listed at the top of the figure) is found by adding up the number of birds required to create the received energy in each of the M bins. The number of birds is truncated the nearest whole bird before summation,

$$N_{birds} = \sum_{i=1}^{M} floor(n_{b,i}). \tag{109}$$

The first notable fact is that the number of birds shown is not at all unreasonable for mid July. The volume involved covers an area of about $9km^2$ up to a height of about $1.2km$. This is actually an upper bound for the number of (small) birds, the actual population is likely much smaller.

Assuming that this volume represents typical ornithological population, it can also be used to estimate how much energy reflected from the whole volume is expected to be due to birds. To do so, compare the total scattering cross section of the volume to the scattering cross section of the maximum number of birds present, N_{birds}. For the data used in Figures 36 and 37, birds account for 75% and 47% of the total scattering cross section, respectively. Attributing this much scattered energy to birds is likely an overstatement, but puts a limit on the expected ornithological contribution.

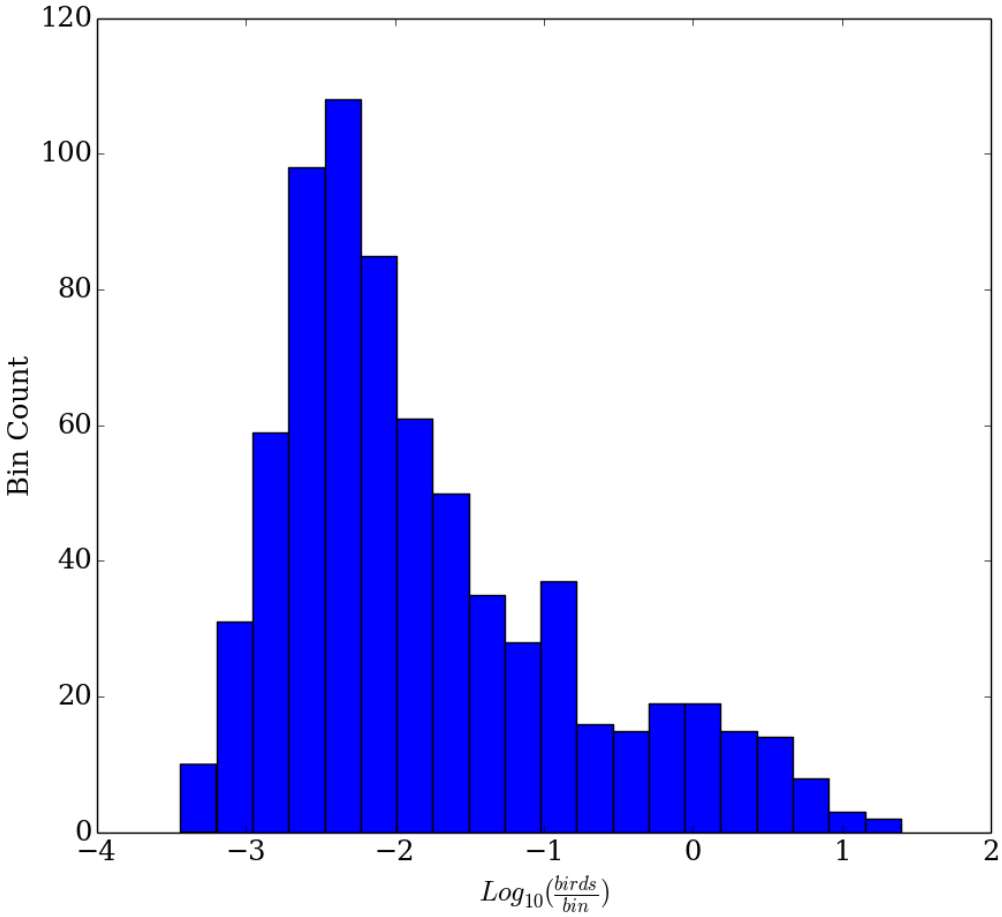

Figure 37. Histogram of the number of birds per bin required to give the refracted energy recorded in the evening by the KILN NEXRAD radar on 21 July 2014 at 0343 EDT. The total number of birds is found by adding up the number of birds in all the bins with at least 1 bird per bin.

To see how the maximum number of birds varies over time, the technique used to create Figures 36 and 37 is carried out for 300 NEXRAD volumes, representing approximately 24 hours. The resulting maximum possible number of birds, N_{birds}, and percent of the cross section which could have been attributed to N_{birds} birds is presented in Figure 38. The mean percent is about 37% of the total cross section. This presents an upper bound on the typical portion of energy reflected in a volume

which could be due to avian sources. Similar statistics from December (31%), and May (42%) show that the maximum percent cross section attributable to birds is consistently under 50% of the total scattered energy. Based on these values, birds could be important in determining reflected energy, but they will not be able to mask other scattering processes. The remainder of this section looks to see how well bird populations correlate with returned energy.

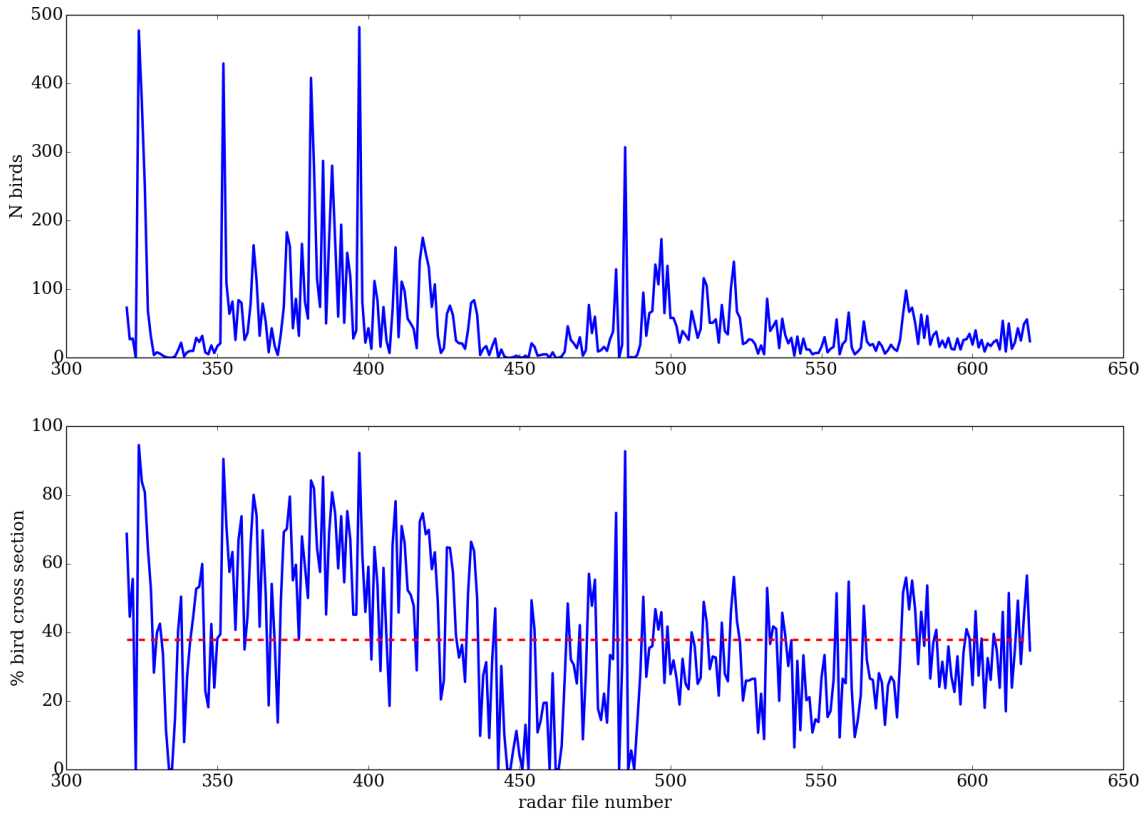

Figure 38. Top: Maximum possible number of birds present, N_{birds}, per NEXRAD volume measurement. Bottom: Percent of total measured scattering cross-section of the NEXRAD volume which would be due to N_{birds} birds (solid blue line) and the mean percent taken over all 300 volumes (red dashed line). Data are taken from 22 July at 0528 EDT until 23 July at 0514 EDT.

For birds, the monthly mean ornithological populations, and mean clear-air C_n^2 values will be compared. As many population statistics are based on radar studies,

a non-radar source was sought for comparison. Monthly aircraft bird strike rates from the Smithsonian Institute were obtained for four different states, Ohio, New Mexico, Kansas, and Tennessee. The bird strike rates (strikes per one million flights) are assumed to be proportional to local bird populations and are compared to the monthly average C_n^2 values (omitting precipitation events) from NWS NEXRADs in those states, KILN, KABX (Albuquerque), KICT (Wichita), and KNQA (Memphis). Bird strike numbers were divided by the number of commercial flights per month, to give the number of strikes per one million flights. While the Smithsonian has been collecting bird strike data since the 1960's (reports are mandatory for all commercial and military aircraft), only data from 2000-2014 were used here. [64, 73] Ohio and New Mexico were chosen because they correspond to the scintillometer measurement locations used in this research. Tennessee was chosen because Memphis is in a primary migration path for many North American birds, and Kansas was chosen because scintillometer and radar data were already available from the CASES 99 campaign. It turned out that the site used in CASES 99 [58] was too far from the KICT radar site to effectively measure turbulence, so those data are only used in this portion of the research.

Table 1. Pearson r and p correlation values for mean C_n^2 vs bird strike rates for four states. Correlations are taken over all 12 months, and over 7 months from May to October (when migratory birds are present [53]).

	Ohio	New Mexico	Tennessee	Kansas
12 Month r	0.660	0.721	0.870	0.904
12 Month p	0.020	0.008	2.4e-4	5.5e-5
7 Month r	0.305	-0.020	0.469	0.645
7 Month p	0.506	0.965	0.288	0.118

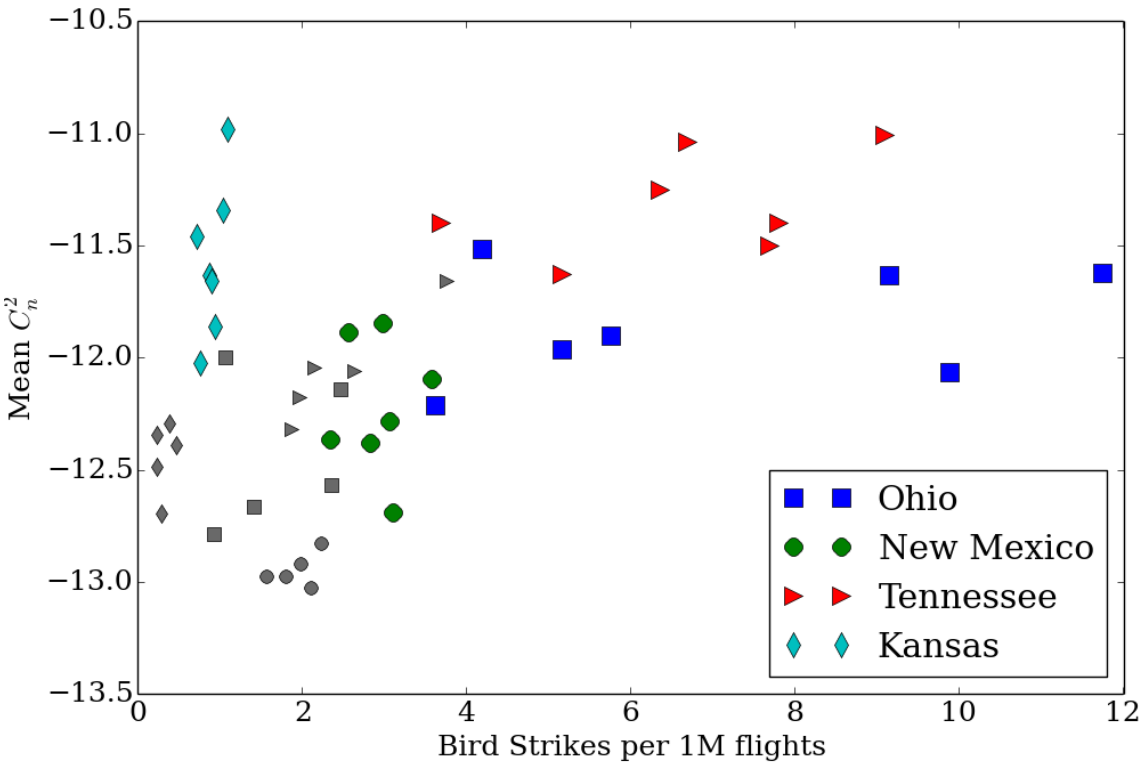

Figure 39. Mean C_n^2 vs bird strike rates (per 1M flights) for Ohio, New Mexico, Tennessee, and Kansas. The larger colored markers are for the months April-October, when migratory birds are generally present in these states. Smaller grey markers are for winter months.

Figure 39 and Table 1 show the correlations from all four sites, and Figure 40 has the annual rates and mean C_n^2 for Dayton and Albuquerque plotted together. Bird strike rates and reflectivity are both low in the winter months for all sites. The 12

month correlations between bird strike rates and radar reflectivity are high, but this is expected as bird population, bird flight time, and radar reflectivity all respond to the same seasonal stimulus. Low values from the radar are expected due to the relatively dry air and reduced foliage reducing the clear-air and ground reflectivity for the radar. Low values for birds are also expected due to fewer birds being present, and flying less during colder months with shorter days. It would be expected, that if birds are predominant contributors to clear air reflectivity, then the correlations between reflectivity and bird strikes should be strongest when many birds are present. However, from spring to fall, the correlation between the strike rates and average C_n^2 does not show a meaningful positive correlation for any of the sites (Table 1) except for Kansas. However, even in the Kansas data there is an 11% probability that 7 samples from a uniform distribution would correlate (or anti-correlate) at least as well as 0.645. Furthermore, the mean C_n^2 values are highest in Kansas, where bird strike rates are smallest, and while Ohio has the highest bird strike rates, its peak C_n^2 is the second smallest. These correlation results show that bird populations do not correlate with radar reflectivity. This lack of correlation shows that avian echoes cannot be significant sources of scattered energy in the majority of NEXRAD dBZ measurements.

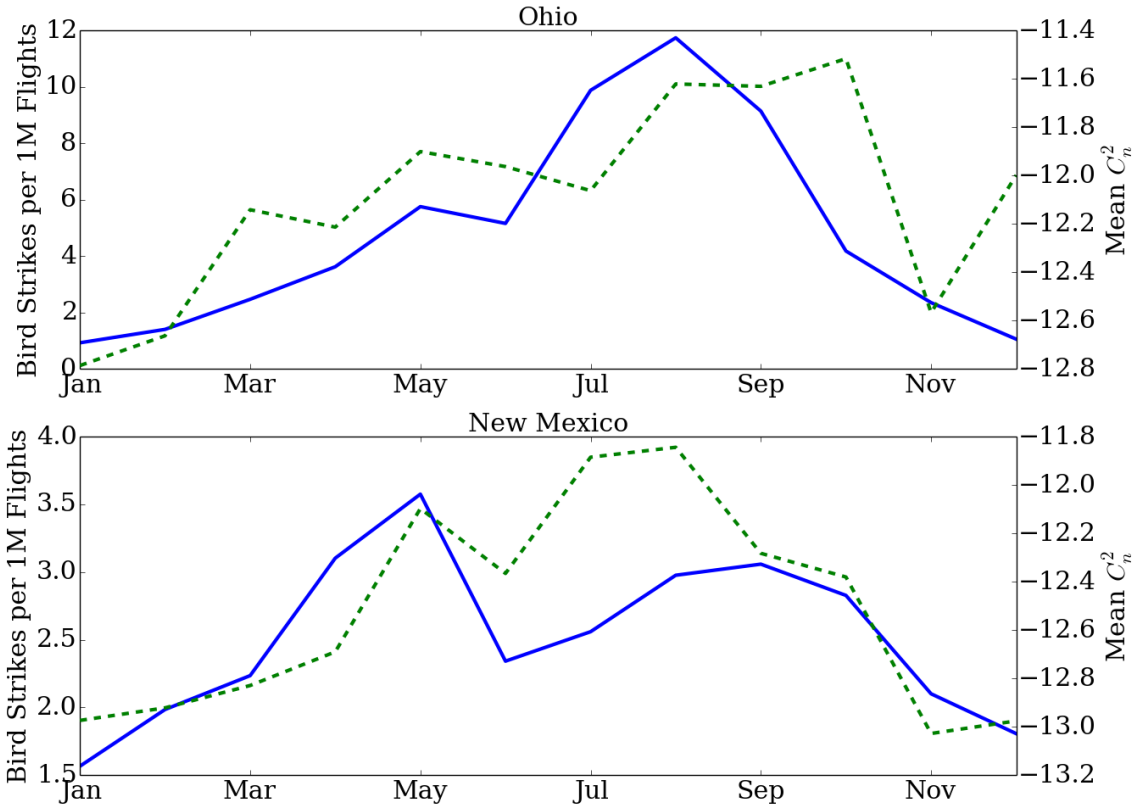

Figure 40. Mean bird strike rates (per 1M flights, solid blue) and mean C_n^2 (dashed green) vs month for Ohio (Top) and New Mexico (Bottom).

Another commonly cited ornithological occurrence is that of the large increase in radar reflectivity covering wide areas after sunset during the spring and fall [23, 53]. This bloom of reflectivity was also noted in summer and winter months (albeit to a lesser degree from mid-November through February) in both the Dayton and Albuquerque data (other data was not investigated). It is certainly expected that nocturnal birds are contributing some of the reflected energy present in this bloom effect. The nocturnal bloom is most pronounced during the spring and fall, when migrating birds are present. However, presence of the bloom throughout the year indicates that migrating birds are not solely responsible for these increased nocturnal reflections.

In the Ohio data, there appears to be a strong correlation to the the extent of the night-time reflection and the local flora. The reflection rates stay strong from mid-March until early November. While this period begins weeks before the majority of migratory birds appear, and ends several weeks after they have passed, it does correspond with the seasonal growth and loss of vegetation especially the leaves on local deciduous trees.

In the Albuquerque data, the night-time radar reflectivity is also weaker in the winter and shows a spatial correlation between vegetation reflected energy. Largely arid regions in the north-west and those shadowed by land features often offer fewer reflections (Figure 42). While the correlation to vegetation could also be caused by fewer biological signatures being present (due to habitat), the depressed signals over shadowed but habitable areas indicates that ground reflections are providing a significant portion of the returned energy. As will be shown in Section 4.8, investigations of higher elevation sweeps support this hypothesis, as reflected energy from higher elevations, but taken at the same height above ground level (by changing the radial distance from the radar) systematically show weaker returns by about 15 to 20dBZ. These greater returns from the lowest radar sweep are expected if ground clutter is a significant source of reflected energy, but not if the increased reflections are primarily avian, insect, or aircraft reflections.

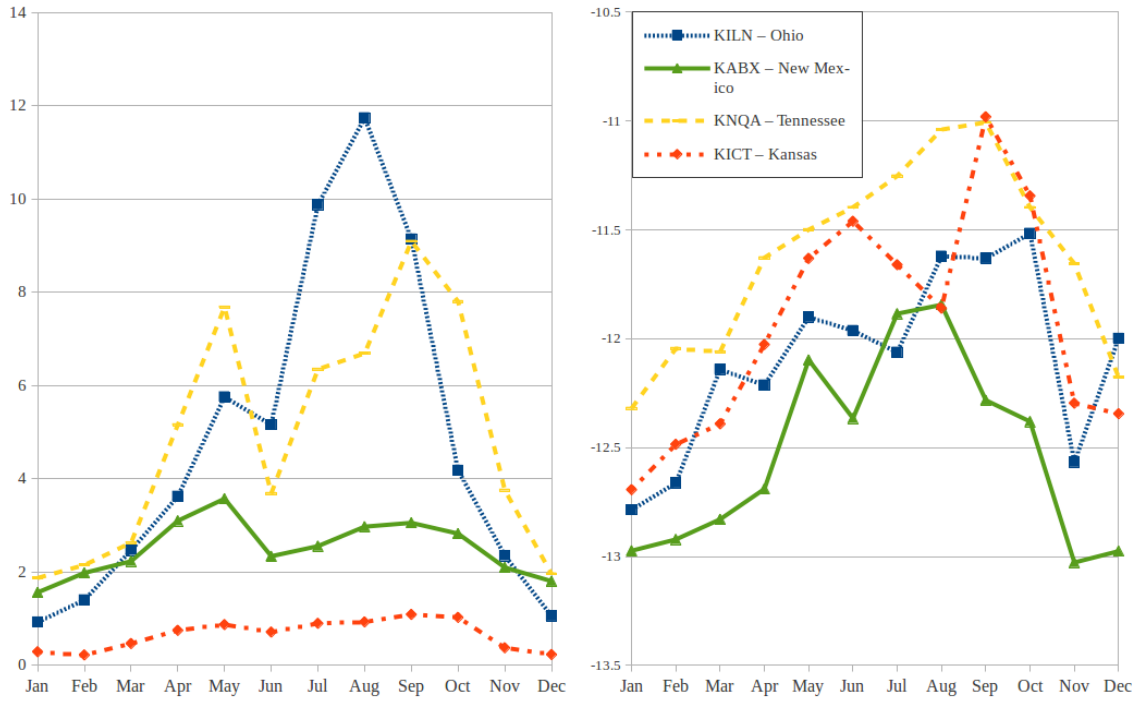

Figure 41. Left: Bird strikes per 1M flights vs month of the year. Data are taken from 2000-2014 for four different states. Right: Mean C_n^2 for four locations by month of the year.

Ground reflections will also increase at night when increased refractive bending lowers the radar main beam so that more of it intersects the ground, which is believed to be the dominant cause of the bloom effect currently being attributed to bird migration. A final observation which indicates that avian echoes are less significant than ground clutter is that the most significant change in mean C_n^2 from Figure 41 is a large drop that occurs from October to November in the Wichita, Dayton, and Albuquerque data, and from November to December in the Memphis data. These drops correspond to the loss of foliage in the fall for their respective sites. While these drops in mean C_n^2 do coincide with the largest month to month drop in bird strikes for Kansas and New Mexico, the C_n^2 drop occurs one month after the greatest drop in bird strikes in those respective states (Figure 41).

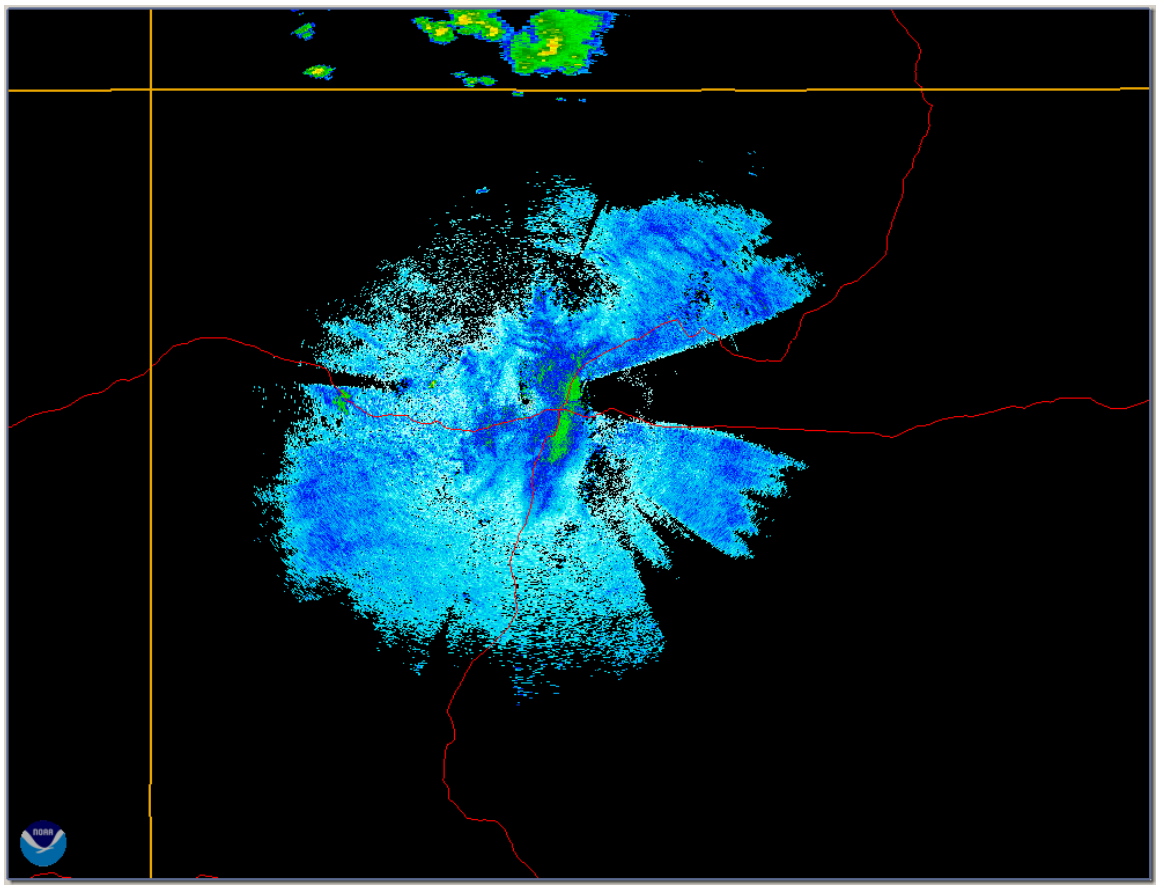

Figure 42. Radar reflectivity image from the KABX radar near Albuquerque, New Mexico. Color indicates dBZ, red lines are interstate highways, and gold lines are state borders. The area North and West of Albuquerque shows intermittent reflectivity often seen over terrain with low back-scatter in the North East, or in the shadow of land-forms (East and North). Image generated using NOAA WCT-Viewer.

Insects may also be important contributors to scattering within a clear-air volume. Insect activity varies diurnally and seasonally with species. [7,55] The activity of flying insects is sensitive to local climate with activity closely related to daily temperature and winds. Insect seasonal populations also depend on climate and habitat [6, 7]. While no local seasonal insect population data could be found for comparison, the clear-air reflectivity of the radar often follows a diurnal pattern of increase throughout the day until near sunset when reflectivity drops off significantly before increasing

again at night and falling off again at dawn. While insect activity generally increases with temperature, it is also negatively affected by wind speed. Based on these behaviors, we would expect that flying insect activity would peak later in the day and early evening when temperatures are still high, and winds are generally weaker. Then the activity would slowly decrease through the evening as temperatures decrease, and winds increase. This pattern does not match the typical reflectivity behavior, so it is expected that insects are contributing scatterers, not dominant scatterers. [6,7,55] Furthermore, as many airborne insects generally move with the wind, their signatures are expected to help track the magnitude of the Doppler velocity spread, σ_v which is required for the optical C_n^2 estimate method described below. So while they may artificially increase the measured C_n^2, these scatterers may be beneficial to this technique by more strongly weighting turbulence induced velocity spread over other influences like aircraft, birds, and ground clutter.

Based on these findings it is assumed that biological contributions (here we are not including foliage in with biological contributions), while present, do not dominate returned energy values and can be ignored. While this will cause occasional errors, especially during peak migratory seasons, these errors are accepted because it is not feasible to manually search for avian and aircraft echos in the radar files (around 300 to 400 per day of data, with over 250 days represented here). In addition to the cost of searching such a large volume of data, the beam size is relatively large at both paths, making positive identification of these clutter sources uncertain.

4.7 Aircraft

If birds are significant contributors, then aircraft would also be significant noise sources when present. At both scintillometer sites, the measurement volumes are in the lowest elevation with a beamwidth of approximately $900m$. While the sites for

the PBL-structure volumes and cell phone data collection are near several civilian airfields, the volumes for the turbulence paths are near the edges of class C airspace for the Dayton and Albuquerque international airports, without being aligned with runways. For these reasons, it is believed that aircraft will rarely be present in the scintillometer measurement volume.

It may be that aircraft are present in radar data taken from the cell phone paths, or for the PBL-structure volumes as there are several civilian airports nearby. The end portion of the cell phone path is $1.86km$ from the Dayton-Wright Brothers Airport. This may lead to aircraft echoes contaminating some of the retrieved comparison radar data, but this is expected to be rare. This expectation is based on the fact that the radar samples around 720 radial and 8 or more vertical rays in its 5-10 minute cycle. During peak periods (weekends), the airport traffic rarely exceeds one flight every 5 to 10 minutes. Considering that the portion of the approach which coincides with bins used by the cell phone path encompasses only one ray (Figure 43), it is quite unlikely to have aircraft noise in the radar return.

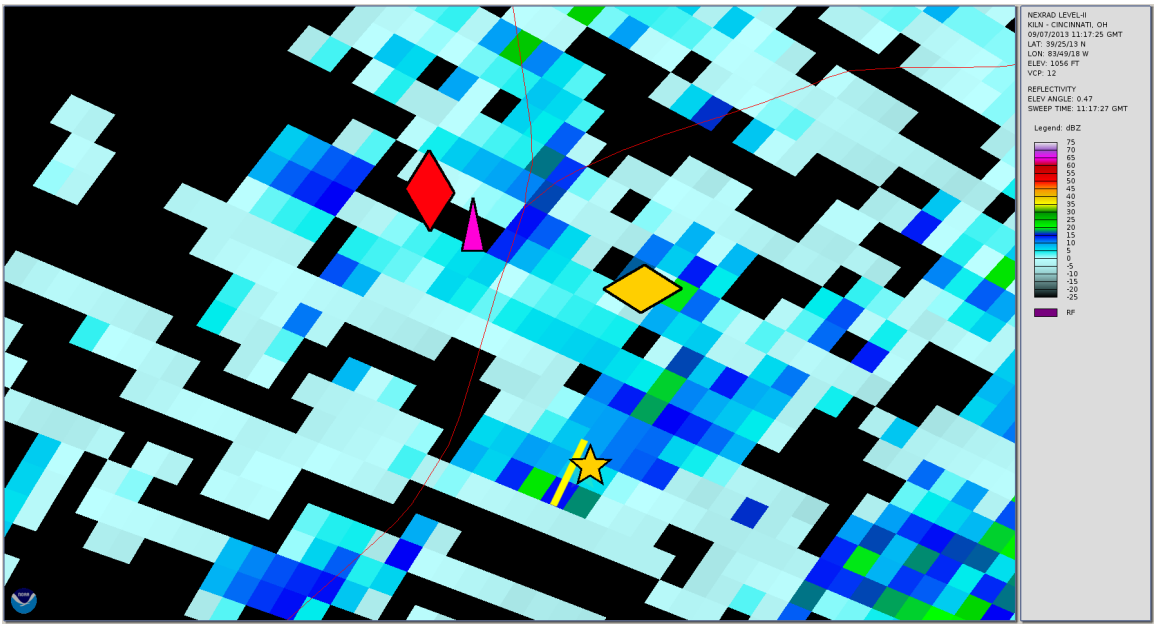

Figure 43. Radar Image of the region where cell phone paths 1 and 2 were located. Bin color indicates radar reflectivity. The vertical red diamond is the first receiver location. the horizontal yellow diamond is the second receiver location. The cell phone tower's location is represented by a magenta triangle, and the nearby airport is indicated with a yellow star, and strip with the approximate runway location. Bin radial spacing is 250m and azimuthal spacing is 0.5^o, or about 350m.

4.8 Ground Clutter

Ground clutter appears to be present in much of the NEXRAD radar data. As the ground clutter can affect both the reflectivity and Doppler information used here, it's important to attempt to understand how much of the energy received by the radar is ground clutter.

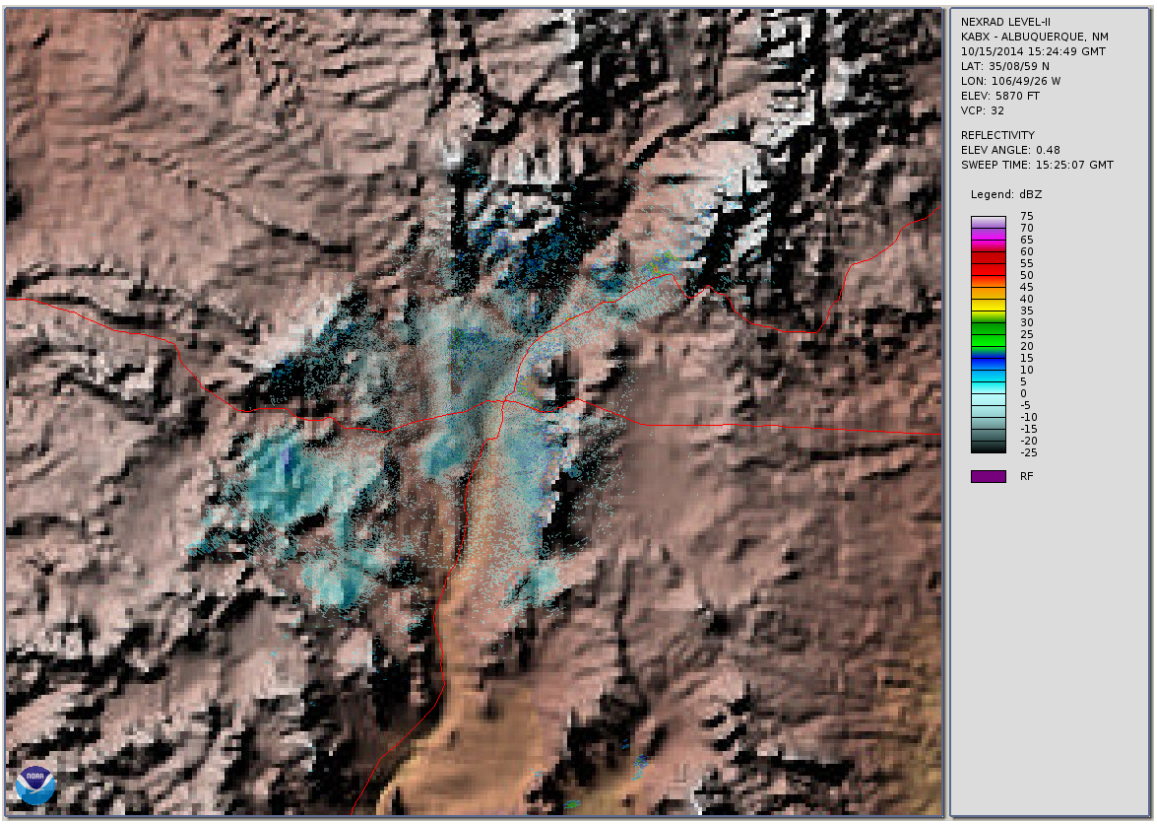

Figure 44. NEXRAD reflectivity in dBZ from the Albuquerque radar taken on 15 October 2014 at 1524 GMT. Reflectivity is overlaid above a topographic image to show how reflectivity from the lowest elevation closely follows terrain features. Like all NEXRAD data used here, these data have been processed to remove ground clutter. Image generated using NOAA WCT-Viewer.

The radar data used here are Level II data [16, 49] which have been preprocessed to remove ground clutter. This is accomplished by two techniques, a zero Doppler filter and ground clutter map. Of course, this does not remove all ground reflections as surface features like trees, structures, bodies of water, vehicles can show non-zero Doppler reflections, and the amount of reflected energy from the ground will change based on variations in surface conditions and the degree to which the radar beam is refracted down into the surface. Furthermore the finite bandwith of the system will cause some of the zero-Doppler energy to spread into sidebands. Ground returns

can be seen in that average reflectivity increases in regions where the radar beam significantly intersects the ground, and increased Doppler spread along roads and in urban areas where many moving, man-made structures are present. The ground maps may also artificially reduce dBZ. In cases where dBZ is fairly constant over a large area, ground features can sometimes appear as reduced reflectivity (Figure 45).

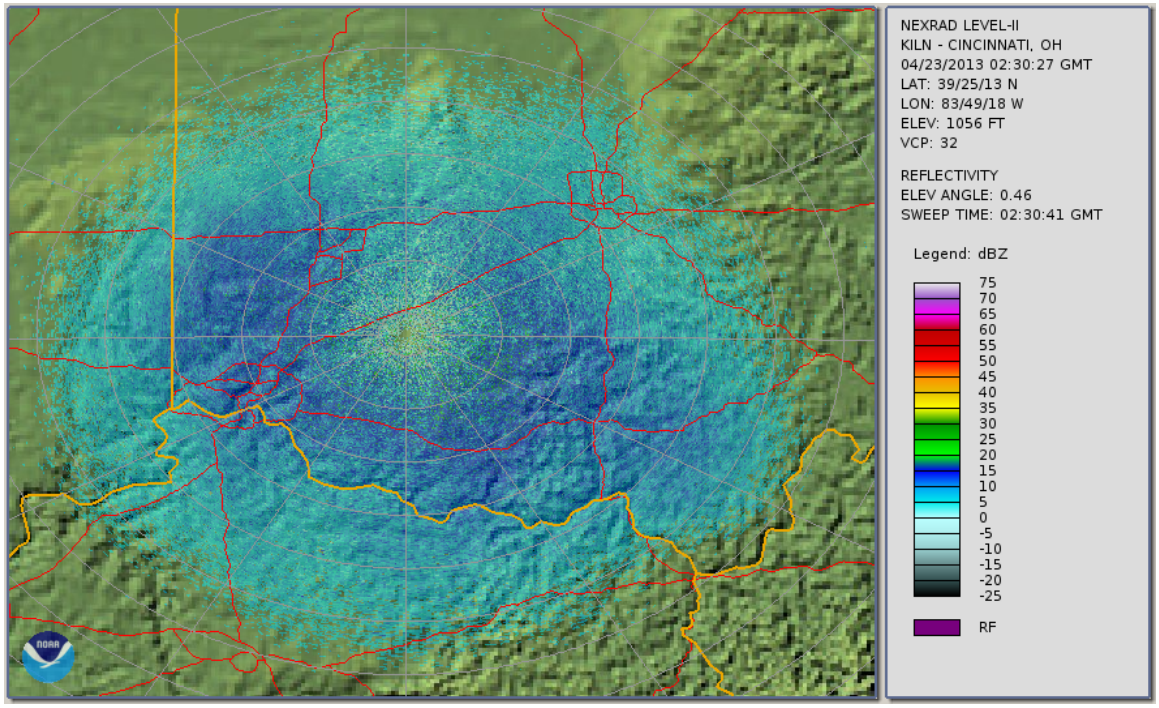

Figure 45. NEXRAD reflectivity in dBZ from the Wilmington, Ohio radar taken on 23 May 2013 at 0230 GMT. Reflectivity is overlaid above a topographic image to show how the ground clutter map may reduce reflectivity. Note the elevated land feature north of the radar shows reduced reflectivity compared to surrounding regions. This area consistently shows a drop in dBZ, which may be due to the ground clutter map. Image generated using NOAA WCT-Viewer.

As in Figure 44, ground clutter shows up as increased reflectivity in regions where the radar beam significantly intersects the ground, and increased Doppler and Doppler spread along roads and in urban areas where many moving, man-made structures are present. Ground reflections will also increase at night when increased refractive

bending lowers the radar main beam so that more of it intersects the ground. As noted in Section 4.6, the most significant change in seasonal $\langle C_n^2 \rangle$ is a large drop that occurs from October to November in the Wichita, Dayton, and Albuquerque data, and from November to December in the Memphis data (Figure 41). These drops correspond to the loss of foliage in the fall for their respective sites.

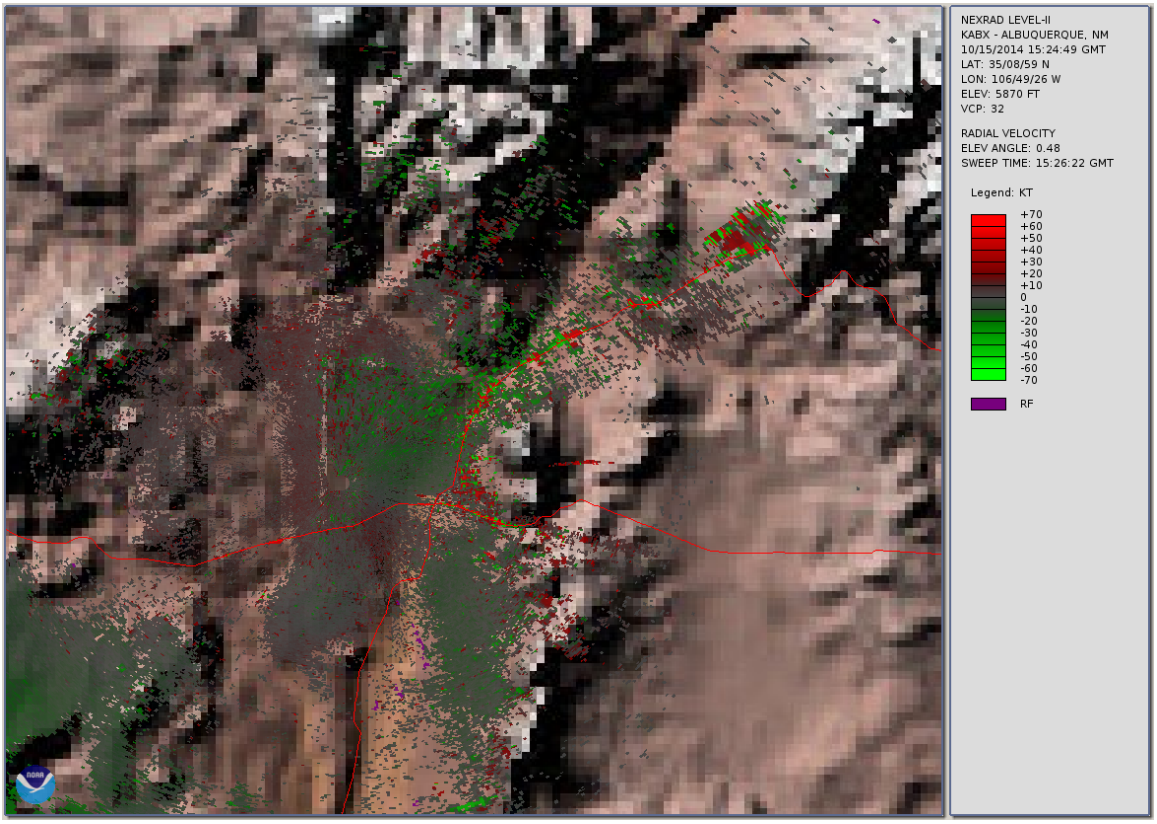

Figure 46. Doppler velocity from the lowest elevation of the Albuquerque, New Mexico radar taken 15 October 2014 at 1524 UTC overlaid upon a USGS topographic colormap. The red lines indicate US Interstate highways 40 and 25 intersecting at Albuquerque, New Mexico, with Santa Fe in the upper right portion of the map. This image shows the typical increased Doppler over roads and urban areas. Image generated using NOAA WCT-Viewer.

Ground returns also show Doppler behavior which indicates echos from man-made surface features. For example, when roads align so that traffic moves radially,

there may be significantly increased Doppler reflections from traffic. For example, in Figure 46, nearby highways, and urban areas show significantly increased Doppler. Figure 47 shows that these effects are not universal, but also depend on land form. Note that in the region North-East of the radar, there is a portion of highway I-71 which shows persistent elevated Doppler. However, the portion of the I-71 which is west of the radar shows few signs of elevated Doppler. The land to the West slopes away from the radar.

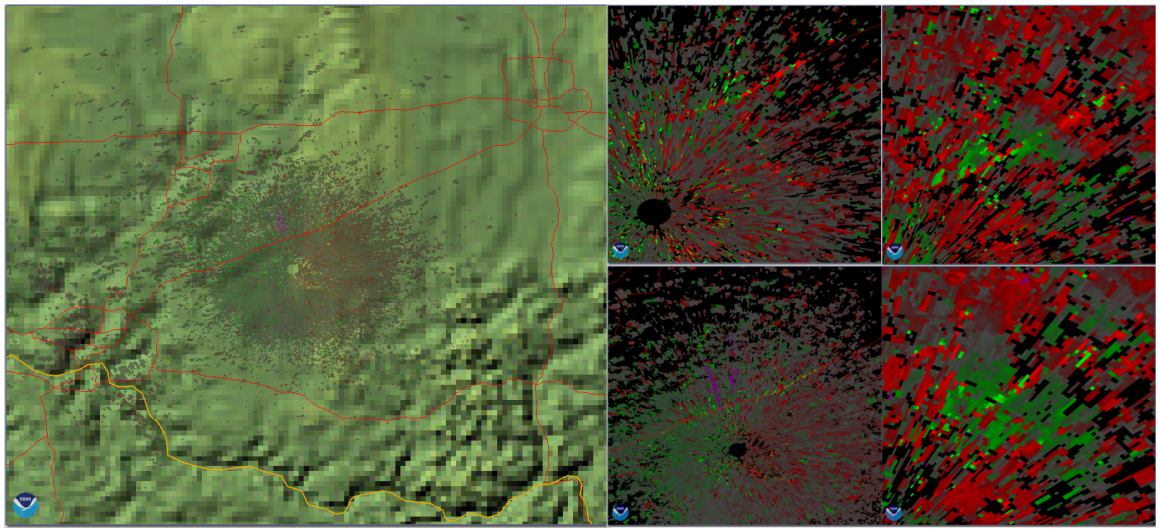

Figure 47. Doppler velocity from the lowest elevation of the KILN radar taken 7 September 2013 at various times. Left: overlaid upon a USGS topographic colormap. The red lines indicates US Interstate highways between Cincinnati (lower left), Dayton (upper left), and Columbus (upper right), Ohio. Note that all images show increased Doppler on the portion of highway I-71 which has a grade facing toward the radar, and is oriented radially with the radar. Right 4 plots show the region of I-71 where vehicle reflections create persistent high-Doppler returns. Images generated using NOAA WCT-Viewer.

Comparisons of radar measurements from similar altitudes, can also show the magnitude of ground reflections. As the first elevation beam is centered at 0.5^o, and the second is typically around 1.5^o, it is possible to look at samples from similar

heights AGL, and see how they compare. For example, the lowest beam elevation typically shows clear air returns which are about 15 to 20dBZ higher than other elevations (Figure 48). This increase in dBZ at lower elevations is only greatest between the lowest and second lowest elevation angles. The range of clear air returns is also greatest in the lowest beam and decreases as the beam elevation increases. From mid-spring to mid-fall, ranges of well over 100km are often seen for the lowest elevation. In cases of strong refraction, the reflectivity pattern may seem to invert compared to what would be expected based on terrain. That is, areas sloping toward the radar may show reduced reflectivity. This may be due to the ground-clutter map filter as shown in Figure 45.

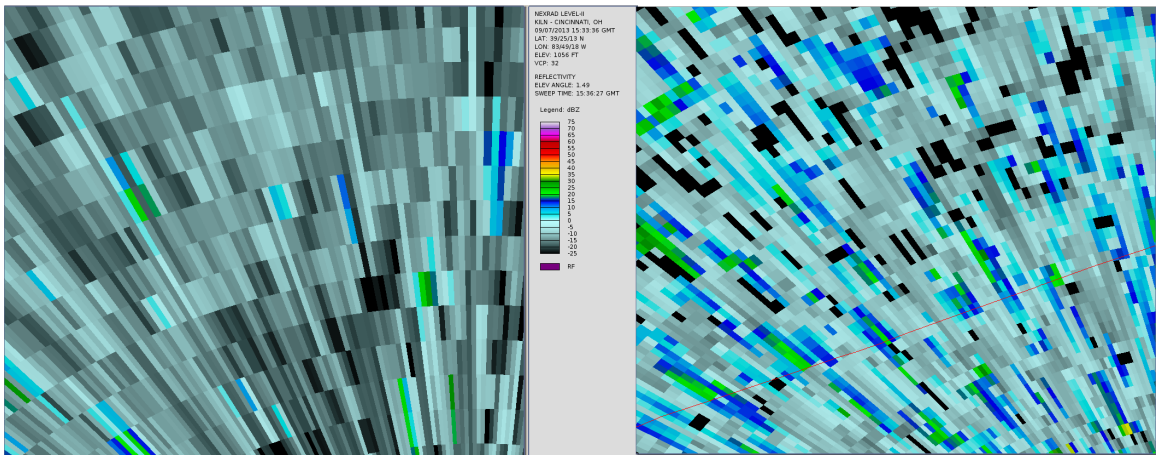

Figure 48. NEXRAD reflectivity in dBZ from the Wilmington Ohio radar. Both images are of data from the same file, 07 September 2013 at 1533 UTC. Left: Reflectivity taken from the second elevation, 1.49^o. Ranges are chosen so that the beam height is 0.6km in the lower right hand corner and extends up to 1.6km at the upper left hand corner. Right: Reflectivity from the lowest elevation, 0.48^o. Beam height varies from 0.6km in the lower right corner to 1.6km in the upper left corner. While the ranges are different, the height represented is the same in both images. The lower elevation plot on the right shows considerably higher dBZ because of ground clutter. Image generated using NOAA WCT-Viewer.

In 2014, an attempt was made to correct radar data based on the amount of path bending predicted by NWP. The results of the initial study are presented in Section 7.3. While these results were promising at the time, it turned out that the correction technique did not extend well to new locations, and different times of the year. These initial results are included in the Appendix as they illustrate the correlation between the amount of radar beam refraction (how strongly the atmospheric temperature, pressure, and vapor pressure gradients bend the beam down to the Earth) and the amount of elevated reflectivity seen in NEXRAD C_n^2 vs scintillometer C_n^2. The hypothesis that ground clutter elevates NEXRAD C_n^2 also explains why results do not transfer well to other locations and times of year. Ground reflections depend on several factors including the land use, vegetation, structures, and motion of surface features. For this reason, the amount of elevated C_n^2 measurement is expected to correlate with the amount of path bending. The path bending estimate is not enough, in and of itself, to compensate for clutter. A further failing of this method may be due to overstatement of the role of ground clutter. By attempting to attribute the bulk of the additional energy to the 'beam height' several other important processes are missed. The appendix has an explanation of the details of this correction, which was dubbed the *stability correction*.

4.9 Geometric and Location Considerations

Ideally, the Numerical Weather Prediction (NWP), radar, cell phone, IDM, and scintillometer data would represent the same location, at the same time. In practice this is not possible. With respect to time, there is a significant uncertainty in when the radar data were collected. Each NEXRAD radar file has a time-stamp, but it takes several minutes to complete the sweep. So while the file time-stamp is used as the time that the radar took its measurement, it will typically be several minutes after

the true moment when the measurement was taken. Several minutes is a long time scale for turbulence measurements as scintillometer C_n^2 can vary by over an order of magnitude within this time. There is no correction for this timing issue in the data presented here. NWP data are even more problematic in that their temporal resolution is either 1 or 3 hours (depending on the forecast used). Regardless of the interpolation method used to estimate parameter values between existing data points, RMSE will be increased as higher frequency variation is not captured.

The lowest radar beam from the Wilmington, Ohio NEXRAD station (KILN) typically extends from 0^o (horizontal) to 1^o in elevation. Using the four-thirds assumption, and accounting for differences in elevation, it can be seen (Figure 20) that the scintillometer path is just below the lowest beam. For this path, the error between the flat Earth and four-thirds [16] approximations varies along the path from about $40m$ to $46m$. The KILN beam is almost a kilometer wide when it passes above the Dayton path, and the scintillometer path would be just under -$3dB$ from the beam max. The Albuquerque path is closer to the radar and at a similar height AGL, and would typically fall within the $3dB$ bounds which defines the main lobe.

In addition to the temporal differences between NWP, radar, and scintillometer data, there are significant spatial differences as well. The GFS data are spatially interpolated to the center of the scintillometer path. RAP data are not interpolated, rather, values from the nearest neighboring site are used. While the Albuquerque scintillometer path is within the 1^o radar beamwidth of the Albuquerque, New Mexico NEXRAD station (KABX), the main lobe ($3dB$ beamwidth) also intersects the ground at this site. The Dayton scintillometer passes a few meters under the 1^o KILN beam, but is clear of the ground. The clear air returns from the NEXRADs are a weighted integral of all scattering bodies within the radar volume [16]. Therefore, even for simultaneous measurements, it is feasible that the radar would measure sig-

nificantly different turbulence values than the scintillometer, even though the return contains some energy scattered from the same eddies that the scintillometer measures.

As discussed in Section 4.1, C_n^2 can vary significantly over distances much less than the differences between site locations, and much smaller than NEXRAD bins. Geometric differences will thus be a limiting factor in how well measurements agree.

4.10 Cell Phone Uncertainty

Cell phone data are affected by both environmental processes which introduce noise and system limitations. While little is offered here in terms of quantification of noise, a description of expected processes is provided. First, the multipath environment will be presented, followed by a discussion of path bending and Fresnel zone issues. Next, the impact of using uncooperative transmitters will be discussed. Finally, the device limitations will be noted.

From an environmental standpoint, any processes which affects the RSSI, will appear as noise in the estimated C_n^2. As described in Section 2.7, the RF propagation environment typically allows for several different propagation paths which provide a significant portion of the received signal. This is quite different from optical systems like scintillometers where it is usually safe to assume that all energy arrives via the direct propagation path. While multipath fading may help improve cell phone turbulence sensitivity, it also provides a significant noise source. Changes in both dielectric and reflection structures in the environment, as well as small changes in the device orientation and position can create significant RSSI variation. While the devices were stationary most during data collection, the surrounding environment is quite dynamic. It is expected that a portion of signal variation is due to non-turbulent environmental processes which change the multipath propagation environment.

In addition to multipath effects, variation in the amount of obscuration of the

Fresnel zones can affect total received power. If obscuration varies with time, then RSSI effects could depend on the dynamics of which zones are obscured, and to what degree. The first Fresnel zone is at least partially obscured at the second site. For all sites, the cell phone path would be expected to follow the same four-thirds path bending as the NEXRAD (which is at a similar wavelength). A question becomes whether variation in the path bending via variation in dn/dz could be a significant contributor to scintillation. For path 2, the path distance is $1.78km$. The total deflection from a straight path using the four-thirds path radius is about $7cm$. As the first Fresnel zone has an $8.6m$ radius, the number of blocked zones is not expected to vary enough for fading from Fresnel zone blocking to be important. While longer paths would see more deflection, the Fresnel zone also grows. So, up to the typical $5km$ range for cell towers, variation in path bending is not expected to be significant.

This is not to say that variation in dn/dz does not affect RSSI. Based on the four-thirds assumption, the end of the path does deflect by nearly half a wavelength. The coefficient of variation of $d\langle n\rangle/dz$ is approximately 15%. Assuming that the standard deviation of deflection is proportional to 15% of the total deflection, then it would be expected that standard variation in beam deflection is less than $\lambda/10$. Similar displacement of the device would typically produce minor fading. For this particular path, variation in the vertical gradient of the index of refraction (including hydrostatic and adiabatic variation) is not expected to be a significant noise source when compared to multipath fading from other variations of scattering bodies in the propagation environment. At $5km$, the standard deviation of deflection could be over $7cm \approx \lambda/2$. At this range, typical variations in the vertical gradient of refraction would be a significant noise source. An important question then becomes one of time scale. What is the temporal structure function of path deflection? Slow variations can be predicted by NWP, but this method is insufficient to determine the fast changes

of $d\langle n\rangle/dz$. The IDM technique may help estimate these as the total deflection of the hospital image can be used to determine the magnitude of path deflection.

In addition to fading from environmental processes, the cell phone transmitter itself dynamically varies the signal power received [8, 75]. The power requirements to maintain service can vary significantly between subscribers within a cell. A user who is outdoors and fairly close to the tower with an unobstructed view, would be able to accept a much lower broadcast signal power than users who are inside of buildings, far from the tower, or in regions shadowed by terrain. There is only a finite amount of signal power available to the cell phone transmitter and this signal power must be shared by all users. In order to provide the best service to all users, the cell phone base-station actively varies the portion of the total available power in each user's channel. As the transmitters are uncooperative, there is no way no normalize RSSI to account for redistribution of power from the transmitter. Therefore, the transmitter will induce an unknown amount of noise, based on user activity within the cell, into cell phone C_n^2 measurements.

Like all instruments, the cell phone is limited in resolution, accuracy, and by system noise. The system resolution is $1dB$ of RSSI and temporally limited to 1 second. Accuracy is not well documented for any of the sensors. The GPS accuracy appears to be reasonably good with position correct to within several meters. RSSI is not a calibrated measure (even though it is sometimes listed in dBm). Generally, the phones typically measure from -90 to -60 dB, which is a reasonable value for actual power in units of dBm. In practice, poor calibration does not matter for cell phone operation as it's the relative change in RSSI which is important. Using (95) emphasizes relative variation instead of actual values. There will still be a constant offset due to the accuracy of the spacing of the dB scale. However, the baselining method will account for this systematic error along with other noise sources which

are suitably white. The resolution is a limiting factor. Some of the high-frequency variation is certainly not captured due to the low RSSI resolution. This may prevent the cell phone from being sensitive to small C_n^2 variations. Quantification of this limitation would be difficult without knowing more about the multipath environment, the device, and cell base station induced C_n^2 noise.

V. Results

Several methods for measuring and estimating C_n^2 have been compared. The majority of the results presented in this chapter will focus on using NWP and NEXRAD to estimate C_n^2 as measured by a scintillometer. The next section will compare how well the methods presented here estimate C_n^2 at both scintillometer sites. Following this is a section describing the results of applying the Lamb-Oseen model to turbulent eddy structure. The next section presents a short synopsis of the IDM technique results, and the final section presents examples of Cell phone C_n^2 computed using the techniques of Section 3.3.

An important fact to consider when comparing these results, is that most C_n^2 estimation schemes contain at least one "coefficient of ignorance." For all of the methods based on Tatarskii's formula, (23), this coefficient is often L_0. In the following charts, L_0 could be manipulated to change some of the results. For instance, the *RF* $N(T)$ always has a lower RMSE than *Ciddor* $N(T)$ because $\partial N/\partial T$ is larger when the *RF* equation is used. As the primary contributor to RMSE is underestimation of C_n^2, it's natural that the *RF* $N(T)$ would, on average, be closer. However, as one increases L_0 a point will be reached where most of the error is overestimation, and *Ciddor* $N(T)$ will be the better choice. For this reason, L_0 was set to a fixed value, $L_0 = 100m$, at both locations. This value was chosen early on (when working with the standard form of Tatarskii's method), as it appeared to reduce the overall RMSE at each site. This value is left fixed because there is not a general consensus as to the proper value for L_0, and it is not the focus of this work to explore the appropriate choice for L_0. In fact, many authors adjust this value (or another parameter which affects L_0) in order to show that their theory matches data. Choosing a value that works well for the standard, temperature only, method unfairly weights results against the newer methods proposed here. This will help to strengthen the significance of any results

which favor these new methods.

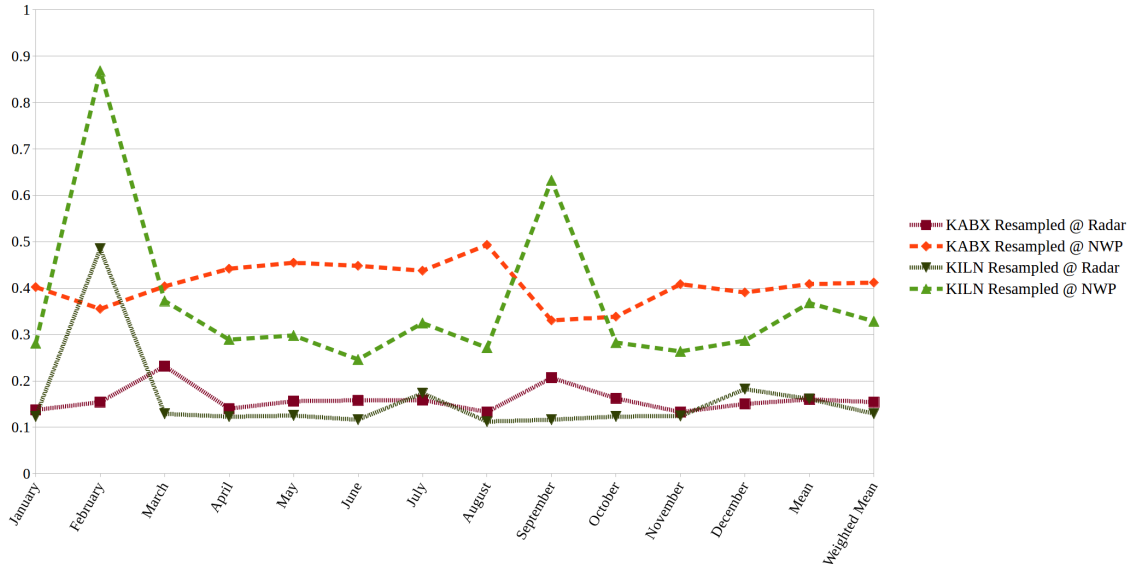

Figure 49. Scintillometer resampling RMSE for the Dayton, Ohio (green KILN) and Albuquerque, New Mexico (red KABX) sites by month of the year. RMSE is found by downsampling to the NEXRAD and NWP data times using a sliding average, then upsampling back to the scintillometer rates. The RMSE here shows what will be considered the best possible RMSE. The weighted and unweighted $\langle RMSE \rangle$ over the year is presented on the left end of the plot.

For much of the monthly data, there is not a meaningful 'error bar' to show significance. If all input measurement errors and uncertainty were known, it may have been possible to find an approximation of the induced error. However, because measurement error and NWP uncertainty are not available, error estimation is not possible. Floating point error and error from incorrect assumptions about the eddy structure (which there is nothing to compare with) are present, but operations are typically well conditioned, and a better eddy structure model to compare against is not known to the author.

As mentioned in Chapter IV, the scintillometer data are resampled to the NEXRAD and NWP times, then these data are compared to the original scintillometer data us-

ing the RMSE and NBEC metrics. Figure 49 shows these resampled RMSE values along with the 12 month mean RMSE and the weighted mean RMSE. As expected, the faster NEXRAD sampling produces less RMSE than the slower NWP sampling. Because the partial derivatives $\partial N/\partial T$, $\partial N/\partial P'$, and $\partial N/\partial e'_v$ and the gradients $d\theta/dz$ and de_v/dz are all based on NWP, it is realistic to expect that the best possible RMSE performance will be similar to the 0.3 to 0.4 $langle$RMSE$\rangle$ shown for resampling to the NWP rates.

5.1 NWP and NEXRAD vs Scintillometer

Before showing the results of the new methods presented here, an example of C_n^2 taken from radar reflectivity using the standard method, (10) compared to scintillometer measured C_n^2 is presented in Figure 50. The data used here are from the Dayton path, and were taken in October of 2011. The similarity between NEXRAD and scintillometer C_n^2 variation is apparent, especially in the first half of the plot (there were clouds and rain present after the 11^{th}). An atypical pattern of higher nocturnal C_n^2 is present in both sets of data. The elevated nocturnal C_n^2 is more apparent in the radar data, but its simultaneous occurrence in the scintillometer data (which are not generally sensitive to birds) implies that the cause is (at least partially) due to a process which is increasing C_n^2. As the radar is much more sensitive to water vapor processes than the scintillometer, the additional radar increase may indicate that the increase involves the moisture gradient.

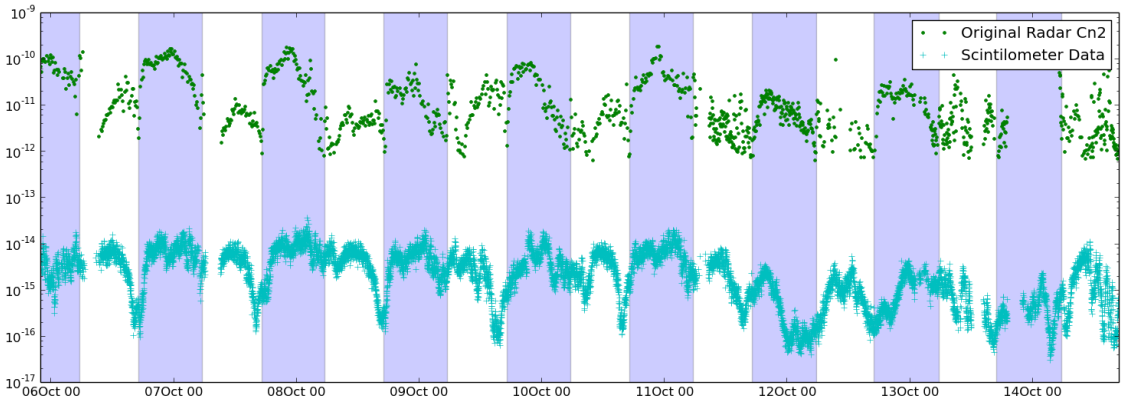

Figure 50. C_n^2 **vs time from the UD scintillometer (teal) and NEXRAD radar (green dots) using the method of Doviak [16]. Dark bands indicate nighttime.**

The impetus for development of the methods presented here comes from data like those in Figure 50. The RMSE in Figure 50 is somewhere around 3-4, and the methods used here typically reduce this RMSE significantly, with many of the months showing an RMSE of 1.5 to 2 times the best case RMSE. In the results presented here, reference will be made to the methods presented at the end of Section 2.1, which are restated here for convenience.

1. **RF** $N(T)$ Using Tatarskii's method (25), with dN/dT based on RF N in, (24), $d\theta/dz$ obtained from NWP, and ignoring other terms. This is a common method for estimating C_n^2.

2. **Ciddor** $N(T)$ Using Tatarskii's method (25), with dN/dT based on Ciddor's N in, (57), $d\theta/dz$ obtained from NWP, and ignoring other terms.

3. **RF** $N(T, e_v)$ Using Tatarskii's method (25), with dN/dT and dN/de_v' based on the RF N in, (24), $d\theta/dz$, and $de_v dz$ obtained from NWP, and ignoring the dP/dz term. This method is sometimes seen when estimating C_n^2, especially in the RF regime.

4. **Ciddor** $N(T, e_v)$ Using Tatarskii's method (25), with dN/dT and dN/de'_v based on Ciddor's N in, (57), $d\theta/dz$, and de_v/dz obtained from NWP, and ignoring the dP/dz term.

5. **RF** $N(T, e_v, P)$ Using Tatarskii's method (25), with dN/dT, dN/de'_v, and dN/dP' based on the RF N in, (24), $d\theta/dz$, and de_v/dz obtained from NWP, and dP/dz determined from radar Doppler spectrum width, as described in Section 2.4.

6. **Ciddor** $N(T, e_v, P)$ Using Tatarskii's method (25), with dN/dT, dN/de'_v, and dN/dP' based on Ciddor's N in, (57), $d\theta/dz$, and de_v/dz obtained from NWP, and dP/dz determined from radar Doppler spectrum width, as described in Section 2.4.

7. **RF** $N(T, e_v) + WC(T, e_v)$ Here the *RF* $N(T, e_v)$ estimate is corrected using the wavelength correction (46) using RF N for the numerator partial derivatives, and Ciddor's N for the denominator, but with the pressure terms neglected.

8. **RF** $N(T, e_v, P) + WC(T, e_v, P)$ Here the *RF* $N(T, e_v, P)$ estimate is corrected using the wavelength correction (46) using RF N for the numerator partial derivatives, and Ciddor's N for the denominator, and using all 3 terms.

The results of some of these methods are identical to numerical precision. Specifically *Ciddor* $N(T, e_v)$ and *RF* $N(T, e_v) + WC(T, e_v)$ provide identical results as do the *Ciddor* $N(T, e_v, P)$ and *RF* $N(T, e_v, P) + WC(T, e_v, P)$ methods. In addition, the baselined versions of these method pairs are equivalent. While all of these methods are presented in the tabular RMSE, and NBEC plots, other portions of this section will omit redundant results.

Not all months had the same availability of data. The amount of useful comparisons depends on the availability of scintillometer data and favorable weather con-

ditions for the NEXRAD and NWP data. The total number of points are counted based on the number of NEXRAD files which are used in the comparison. After rejecting files with precipitation, no corresponding scintillometer data, or excessive NWP gradients, the remaining points are included in the RMSE and NBEC results. In some cases, mean RMSE ($\langle RMSE \rangle$), are reported in addition to the RMSE for each month. These means are found by averaging over the 12 month period at each location. The unweighted mean is found from

$$\langle x \rangle = \frac{1}{12} \sum_{i=1}^{12} x_i. \tag{110}$$

In addition to the unweighted mean, a mean is also calculated with weights based on the number of points in each month per

$$\langle x \rangle = \frac{1}{N} \sum_{i=1}^{12} n_i x_i. \tag{111}$$

Here n_i is the number of points in the i^{th} month and N is the total number of points. Both of means are reported because the each add a different emphasis based on climate and time of the year. As data availability are partially dependent on weather conditions, the weighted average will emphasize performance in seasons when more data are available, while the unweighted mean emphasizes year round performance. The number of point shown in Figure 51 indicates that the weighted mean emphasize data from late Summer and Spring.

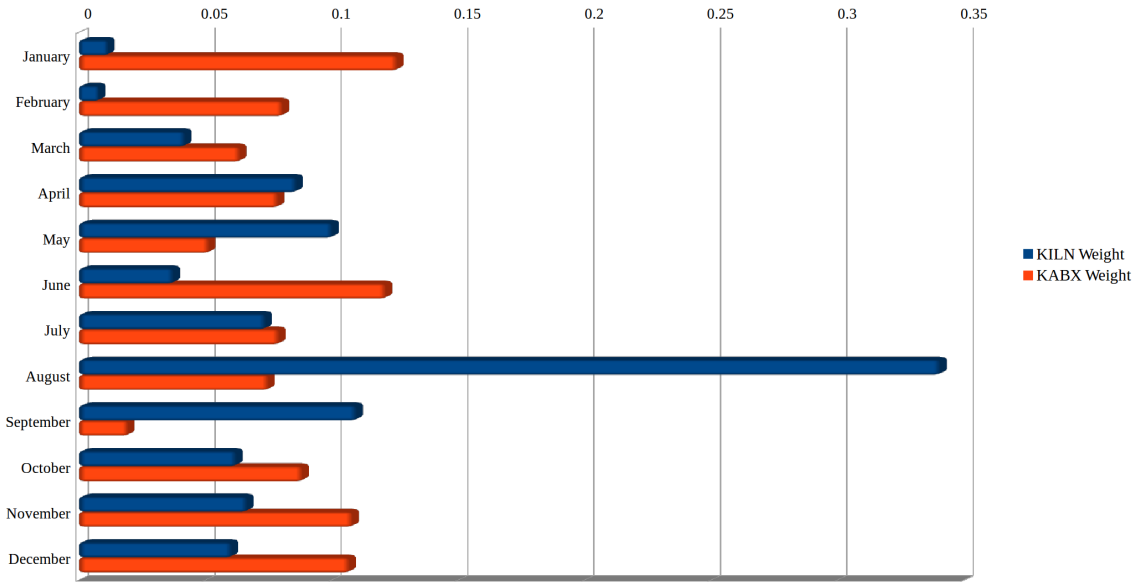

Figure 51. Monthly weights for the Albuquerque and Dayton data sets. Each weight is found from n_i/N where n_i is the number of data points used for comparisons in the i^{th} month, and N is the total number of points used from each location.

As shown in Figures 52 and 53, the temperature-only estimates, *RF* $N(T)$ and *Ciddor* $N(T)$ performed similarly at both sites, with *RF* $N(T)$ being slightly better in all months except for November, December and March at the Dayton site. The August data from Albuquerque (Figure 52) were taken over a period which was often overcast with several thunderstorms and rainy periods. It is not known if this is the reason for significantly higher error in the August estimates.

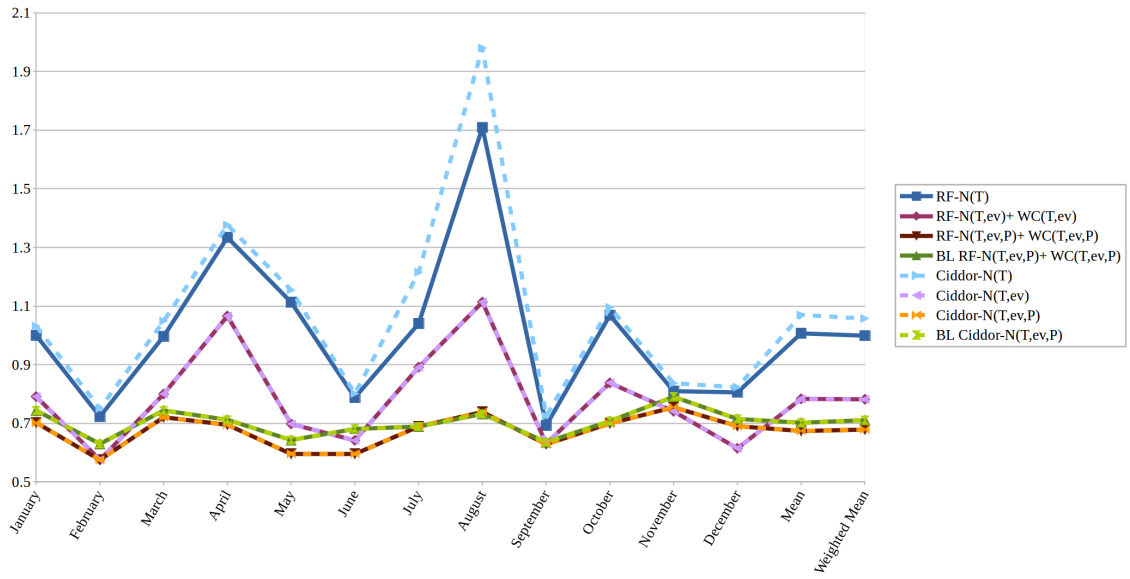

Figure 52. Mean RMSE between estimated C_n^2 and scintillometer measured C_n^2 vs month of the year for the Albuquerque, New Mexico site. Both the *Ciddor* based results (dashed lines) and *RF* results (solid lines) are pictured. Results using the wavelength correction are identical to their corresponding *Ciddor* based results. That is, the RMSE of *RF* $N(T, E_v)$ + $WC(T, e_v)$ is identical to *Ciddor* $N(T, E_v)$, *RF* $N(T, E_v, P)$ + $WC(T, e_v, P)$ is identical to *Ciddor* $N(T, E_v, P)$, and the baselined versions *BL RF* $N(T, E_v, P)$ + $WC(T, e_v, P)$ is identical to *BL Ciddor* $N(T, E_v, P)$. In this case, dP/dz was derived using a fixed eddy size of $0.67m$ for the scintillometer eddy size.

Figures 52 and 53 show that adding vapor pressure and pressure terms generally reduce the RMSE. While improvement from adding pressure is noticeable at the Albuquerque site (Figure 52), it is less pronounced at the Dayton site (Figures 53 and 54). Figure 54 shows the results at the Dayton site without the temperature only methods, so that the effects of adding pressure are more apparent. The improvement in RMSE at the Albuquerque site from inclusion of e_v (Figure 55) may be less pronounced because Albuquerque is a significantly drier climate than Dayton. By comparing C_n^2 vs time from some of these months, it's possible to see when the additional vapor pressure and pressure terms become important to calculating C_n^2.

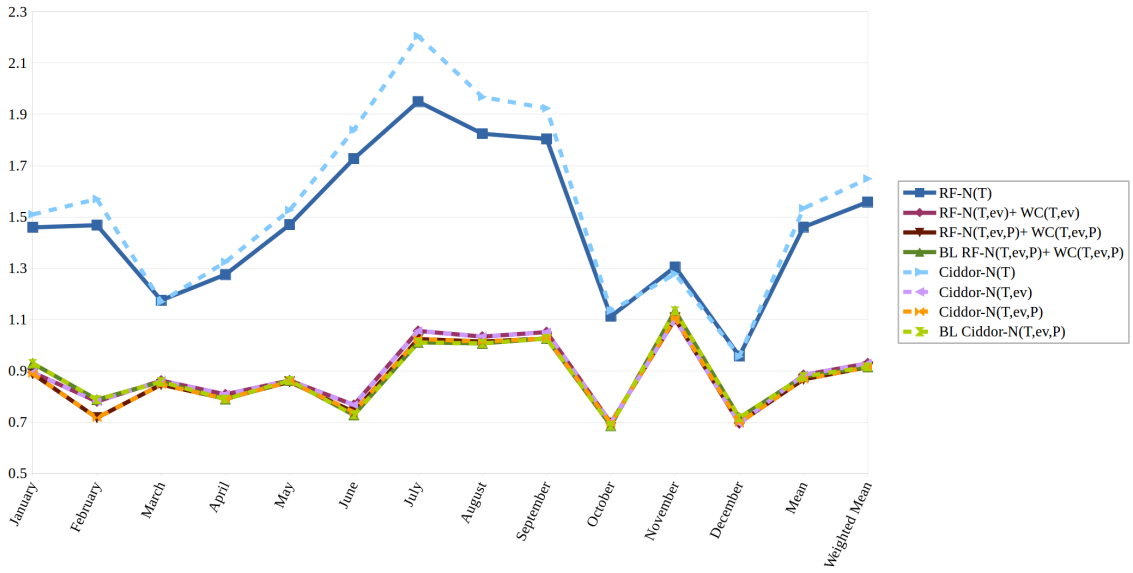

Figure 53. Mean RMSE between estimated C_n^2 and scintillometer measured C_n^2 vs month of the year for the Dayton, Ohio site. Both the *Ciddor* based results (dashed lines) and *RF* results (solid lines) are pictured. Results using the wavelength correction are identical to their corresponding *Ciddor* based results. That is, the RMSE of *RF* $N(T, E_v)$ + $WC(T, e_v)$ is identical to *Ciddor* $N(T, E_v)$, *RF* $N(T, E_v, P)$ + $WC(T, e_v, P)$ is identical to *Ciddor* $N(T, E_v, P)$, and the baselined versions *BL RF* $N(T, E_v, P)$ + $WC(T, e_v, P)$ is identical to *BL Ciddor* $N(T, E_v, P)$. In this case, dP/dz was derived using a fixed eddy size of $1.0m$ for the scintillometer eddy size.

Figure 58 shows scintillometer C_n^2 along with six methods for estimating C_n^2. As is typical at both locations, the *RF* N estimates (in the left column) becomes progressively worse but the *Ciddor* N estimates become progressively better as e_v and P terms are added. Adding the e_v term reduced the RMSE when compared to temperature only methods in all 24 months of data. However, the pressure correction only improved estimates in 19 of the 24 months.

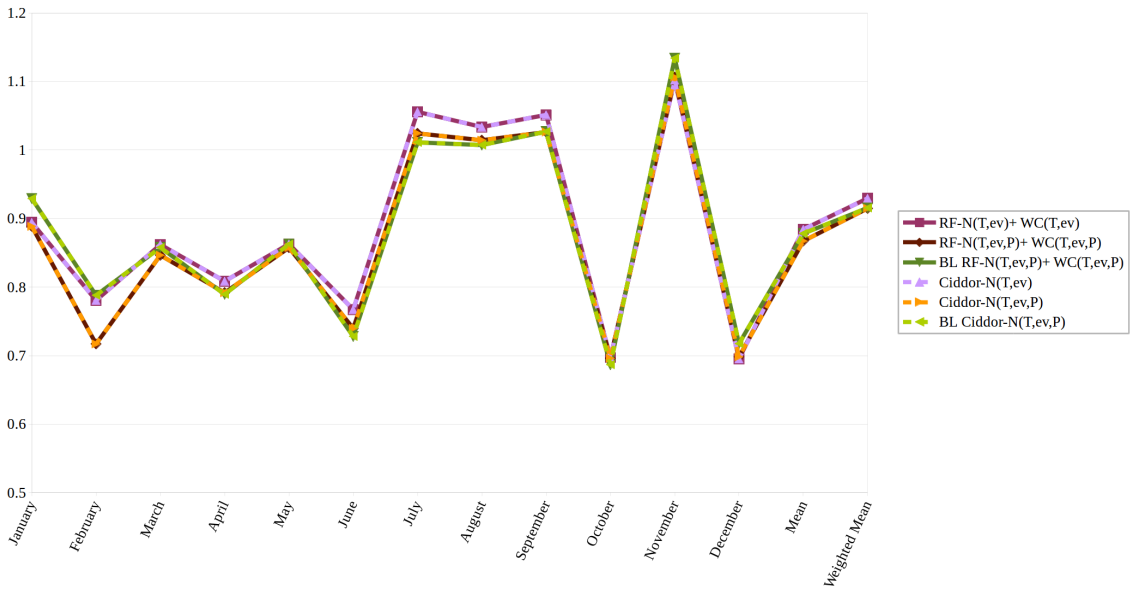

Figure 54. Data from Figure 53, without the temperature only methods. Mean RMSE between estimated C_n^2 and scintillometer measured C_n^2 vs month of the year for the Dayton, Ohio site. Both the *Ciddor* based results (dashed lines) and *RF* results (solid lines) are pictured. Results using the wavelength correction are identical to their corresponding *Ciddor* based results. That is, the RMSE of *RF* $N(T, E_v)$ + $WC(T, e_v)$ is identical to *Ciddor* $N(T, E_v)$ and *RF* $N(T, E_v, P)$ + $WC(T, e_v, P)$ is identical to *Ciddor* $N(T, E_v, P)$. In this case, dP/dz was derived using a fixed eddy size of 1.0 m for the scintillometer eddy size.

At the Albuquerque site, the pressure correction degraded the RMSE in November, and December. The pressure correction also slightly degraded the November and December RMSE at the Dayton site. Figure 55 shows the difference in RMSE for estimated C_n^2 generated using *Ciddor* $N(T, e_v)$ versus *Ciddor* $N(T, E_v, P)$, Improvement $= RMSE_{T,e_v} - RMSE_{T,e_v,P}$. It is apparent that pressure plays a greater role in both improving and degrading the RMSE in the Albuquerque data. The cause of greater improvement in the Albuquerque data is unclear. It could be due to differences in the two NWP sources, or in the site itself.

In comparisons from both locations, periods of significant persistent C_n^2 overesti-

mation by the NWP based estimates were noted. The overestimation in these periods appears to be due to unrealistically large temperature and vapor pressure gradient magnitudes. While both sites show similar mean gradients there is much greater variation in the RAP gradients than in the GFS gradients. Typically there are several periods in each month when the gradients become unrealistically large. Data are not compared for times, i, when the forecasts provide gradients, $d\phi/dz$ whose magnitude is more than an order of magnitude greater than the mean gradient magnitude,

$$\left|\frac{d\phi_i}{dz}\right| > 20 \times \left\langle \left|\frac{d\phi}{dz}\right| \right\rangle . \tag{112}$$

If unrealistically low $d\theta/dz$ and de_v/dz at the Albuquerque site are more common, then the pressure term would provide a more significant correction. In cases where the gradients are too large, the pressure term will tend to increase error. Without an additional source of gradient data, it is not possible to be certain if the NWP data (or the interpolation and gradient estimation schemes) are at fault, or if there is a site specific reason (possibly humidity) for increased effect of the pressure term on C_n^2 RMSE at the Albuquerque site. Comparisons with RAOB data were performed at both sites. GFS gradients compared well with RAOB measurements, but RAP gradients did not. RAOB data were used to scale RAP gradients so that they matched RAOB data.

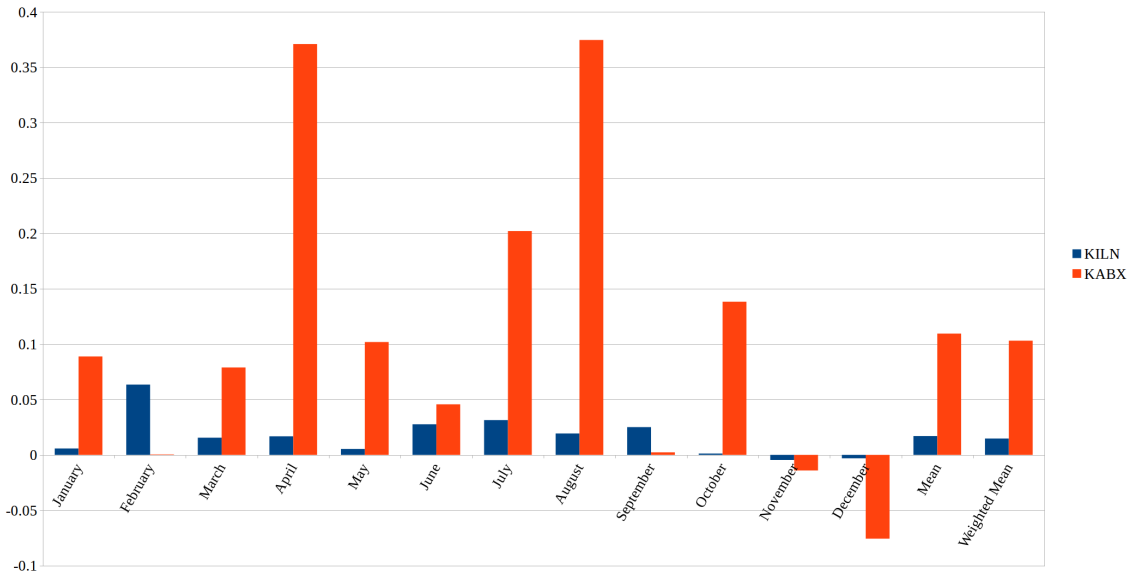

Figure 55. Improvement (reduction) in RMSE from adding the pressure term by month for the Albuquerque and Dayton Data sets.

Considering the improvement from using either *Ciddor* $N(T, e_v)$ or *RF* $N(T, e_v)$ + $WC(T, e_v)$, the ⟨RMSE⟩ decreases by between 0.217 and 0.629 from estimates using temperature alone (Table 2). In linear space, this corresponds to 39% and 77% reduction in RMSE.

Compared to the *Ciddor* $N(T, e_v)$ method, including the P term adds additional, but less pronounced reduction in RMSE. In Albuquerque, the pressure correction reduced the *Ciddor* $N(T, e_v)$ RMSE by 0.10, or 21% in linear space. In Dayton, the pressure difference reduced RMSE by 0.0147, corresponding to only a 3% reduction in linear RMSE. While the Albuquerque improvement seems significant, the improvement at the Dayton site appears to be nominal.

When working with the IDM technique, it was discovered that the estimation of K_H/K_M used in Tatarskii's method provided unrealistically low values under certain conditions. While this will be explored more in Section 5.3, the corrective factor found there was applied to a few of the months of the KILN data; July, August, September

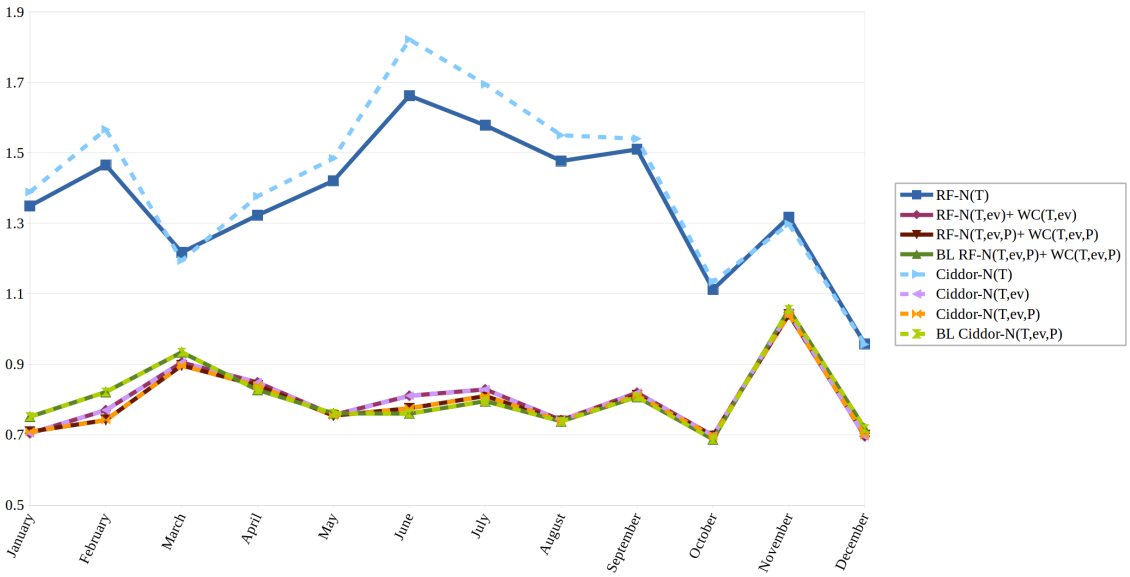

Figure 56. Dayton (KILN) RMSE by month for 8 different C_n^2 estimation methods. The months of July, August, September, and November had their Bulk-Richardson number R_i modified by $R_i' = \sqrt[3]{R_i}$ before calculation of K_H/K_M via the Kondo equation, (102).

and November. While there was little change in the November results, the July-September results were improved substantially (compare Figure 53 and Figure 56).

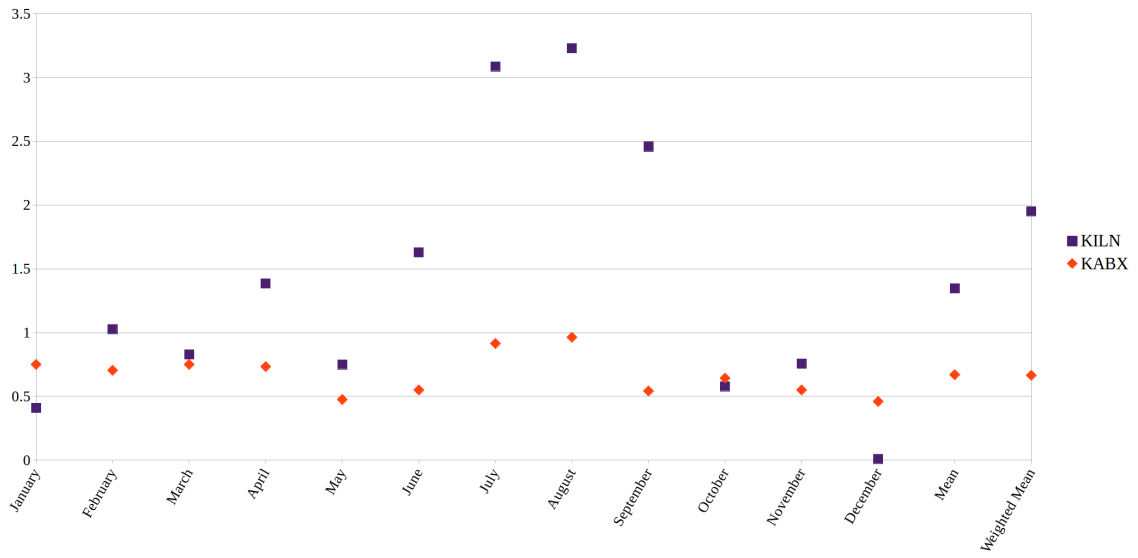

Figure 57. Eddy size (in meters) which gave the best improvement in RMSE when going from *Ciddor* $N(T, e_v)$ to *Ciddor* $N(T, e_v, P)$ vs time of the year for both the Albuquerque, New Mexico (KABX) and Dayton, Ohio (KILN) sites.

As part of the pressure correction, the proper eddy size must be selected. At one stage, the eddy size was allowed to vary, and the size that produced the lowest RMSE was used. The sizes from each month are presented in Figure 57. It can be seen that the months which had unusually small K_H/K_M, July-September at the Dayton (KILN) site, also benefited from larger eddy sizes. With these sizes, the improvement by adding the pressure term was 0.0512 RMSE or 12.5% at the Dayton site and 0.135 RMSE or 36.6% at the Albuquerque (KILN) site. In the remainder of the results, the Albuquerque eddy size was fixed at $0.67m$, and the Dayton eddy size was fixed at $1.0m$. The eddy size directly impacts the magnitude of the pressure term. A more effective method for determining the eddy size may yield better results. One approach may be to use the local air viscosity and density to find an eddy size which produces an appropriately sized scatterer. In the case of the scintillometer, $3cm$. In addition to eddy size, Doppler spectrum width, which is used to determine ε, has a

large impact on the magnitude of the pressure term. Doppler spectrum width data from NEXRAD vary over several orders of magnitude, and are often incomplete. A method which can more accurately estimate ε, combined with a proper selection of the eddy size may show more improvement in RMSE than is shown here.

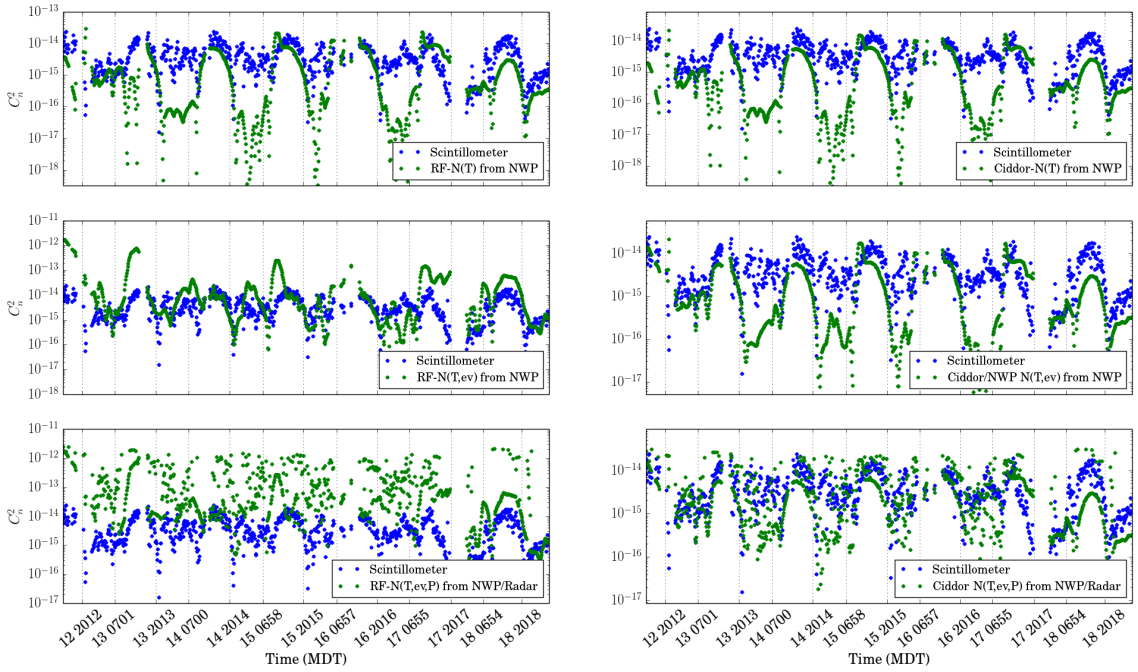

Figure 58. Plots show C_n^2 vs time (day and hour) with axis ticks at local sunrise and sunset. Blue dots are C_n^2 values measured by scintillometer at the Albuquerque site and interpolated to the radar file measurement times. Green dots are estimates of C_n^2 created using the *RF N* in the left column and *Ciddor's N* equation in the right column. The top row estimates C_n^2 using potential temperature gradients alone. The middle row adds potential vapor pressure gradients to the estimation, and the bottom row adds the non-hydrostatic pressure gradients to the estimation. Blue dots are scintillometer based C_n^2 measurements. Data are from 12-20 April 2013.

While the inclusion of the pressure term helps some, the greater benefit can be seen from using the *Ciddor N* to estimate C_n^2 instead of *RF N*. This is an important result as most authors are still using the *RF N*, and tweaking coefficients to make it work with visible/IR data. The comparisons here show that *Ciddor N* provides significantly better fidelity for predicting C_n^2 of an $880nm$ scintillometer than *RF N*. The inclusion of e_v alone does much to improve RMSE and the range of conditions

Table 2. RMSE vs method for data taken from each site. The Dayton and Albuquerque data each include data from all 12 months. The Dayton data uses 15,571 datum points, and the Albuquerque data uses 12,357 datum points.

Method	Dayton	Albuquerque
Re-Sample Scintillometer Data	0.2889	0.4119
RF $N(T)$	1.558	0.9989
Ciddor $N(T)$	1.649	1.057
RF $N(T, e_v)$	1.335	1.241
Ciddor $N(T, e_v)$ & *RF* $N(T, e_v)$ + $WC(T, e_v)$	0.9295	0.7817
RF $N(T, e_v, P)$	1.380	2.123
Ciddor $N(T, e_v, P)$ & *RF* $N(T, e_v, P)$ + $WC(T, e_v, P)$	0.9147	0.6786
BL Ciddor $N(T, e_v, P)$ & *BL RF* $N(T, e_v, P)$ + $WC(T, e_v, P)$	0.9155	0.7106

under which Tatarskii's method is applicable. Before, it may have been necessary to omit data when dT/dz drops below a certain threshold, but using Ciddor's equation with e_v and P terms allows for Tatarskii's method continue to provide good estimates.

The RMSE metric shows that *Ciddor* $N(T, e_v, P)$ provides the best possible estimate, on average. There are some months when *Ciddor* $N(T, e_v)$ and the baselined corrections do better, but the lowest $\langle$RMSE$\rangle$, averaged over all months is *Ciddor* $N(T, e_v, P)$ in both locations. While this method provides the lowest RMSE, on average it is does not necessarily provide the best estimate most often.

The NBEC test adds a criteria which is different from the RMSE test. Th RMSE is independent of the other tests involved, but the NBEC is highly dependent on which other tests are involved. The NBEC results are presented based on two forms of the NBEC comparison. Figures 59 and 60 both show the results of comparing the *Ciddor* $N(T, e_v, P)$ method to all other methods. The *Ciddor* $N(T, e_v, P)$ method was

chosen as it was one of the best performing methods based on the RMSE metric. In these charts the NBEC is computed, then 50% is subtracted from the result. Because these are two-test comparisons, if the *Ciddor* $N(T, e_v, P)$ method provides a closer estimate about 50% of the time, then it is of similar goodness as the method it is being compared against and will show a value near zero on the chart. Increasingly positive NBEC−50 indicates that *Ciddor* $N(T, e_v, P)$ is the increasingly better method, and the more negative the result, shows that *Ciddor* $N(T, e_v, P)$ is a proportionally worse method. When two methods are the same within ±1% the result bar is omitted from the chart.

In both Figures 59 and 60, it is interesting that the *Ciddor* $N(T, e_v)$ method often has a better NBEC than *Ciddor* $N(T, e_v, P)$, even though its RMSE was generally worse. At both sites the *Ciddor* $N(T, e_v)$ had a better 2-method NBEC in 7 months. The Dayton site showed that *Ciddor* $N(T, e_v)$ was better than *Ciddor* $N(T, e_v, P)$ in March-June, then again in October-December. Albuquerque showed *Ciddor* $N(T, e_v)$ performing better than *Ciddor* $N(T, e_v, P)$ in February, May, June and September-December. *Ciddor* $N(T)$ also outperformed *Ciddor* $N(T, e_v, P)$ at times. *Ciddor* $N(T)$ had a better NBEC than *Ciddor* $N(T, e_v, P)$ in 5 months at Dayton (March, May, and November-December) and in 6 months at Albuquerque (May, June, and September-December). However, the *Ciddor* $N(T, e_v, P)$ performed better than *RF* $N(T)$ in all months expect June at the Albuquerque site, where *RF* $N(T)$ was marginally better. Figure 61 from the Dayton site, shows that *RF* $N(T)$ is better than *Ciddor* $N(T)$ in only 7 months, even though its RMSE is better than that of *Ciddor* $N(T)$ in 10 of the months.

Similarities in performance of the methods becomes more apparent when NBEC−50 scores are averaged over all 12 months. Figures 62 and 63 show these averages with equal weighting in the average given to each month. Error bars indicate the sample

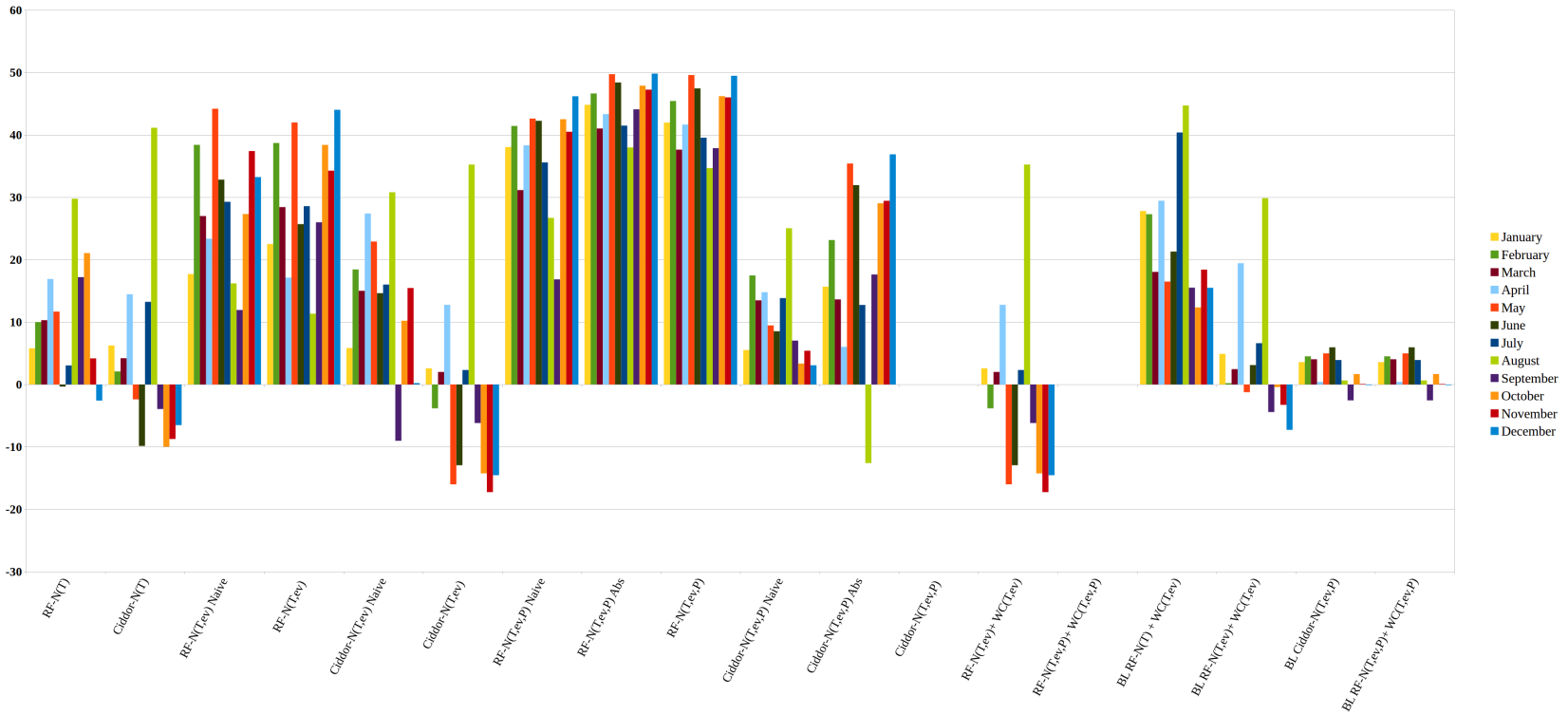

Figure 59. 2-Method NBEC-50 for the *Ciddor* $N(T, e_v, P)$ based C_n^2 estimate vs comparison method for each month of the year at the Albuquerque (KABX) site. Colored bars represent the two-method NBEC-50 for the *Ciddor* $N(T, e_v, P)$ method. Positive values indicate that *Ciddor* $N(T, e_v, P)$ provided a closer C_n^2 estimate more often than the comparison method. Each color represents the month of the year which is being compared.

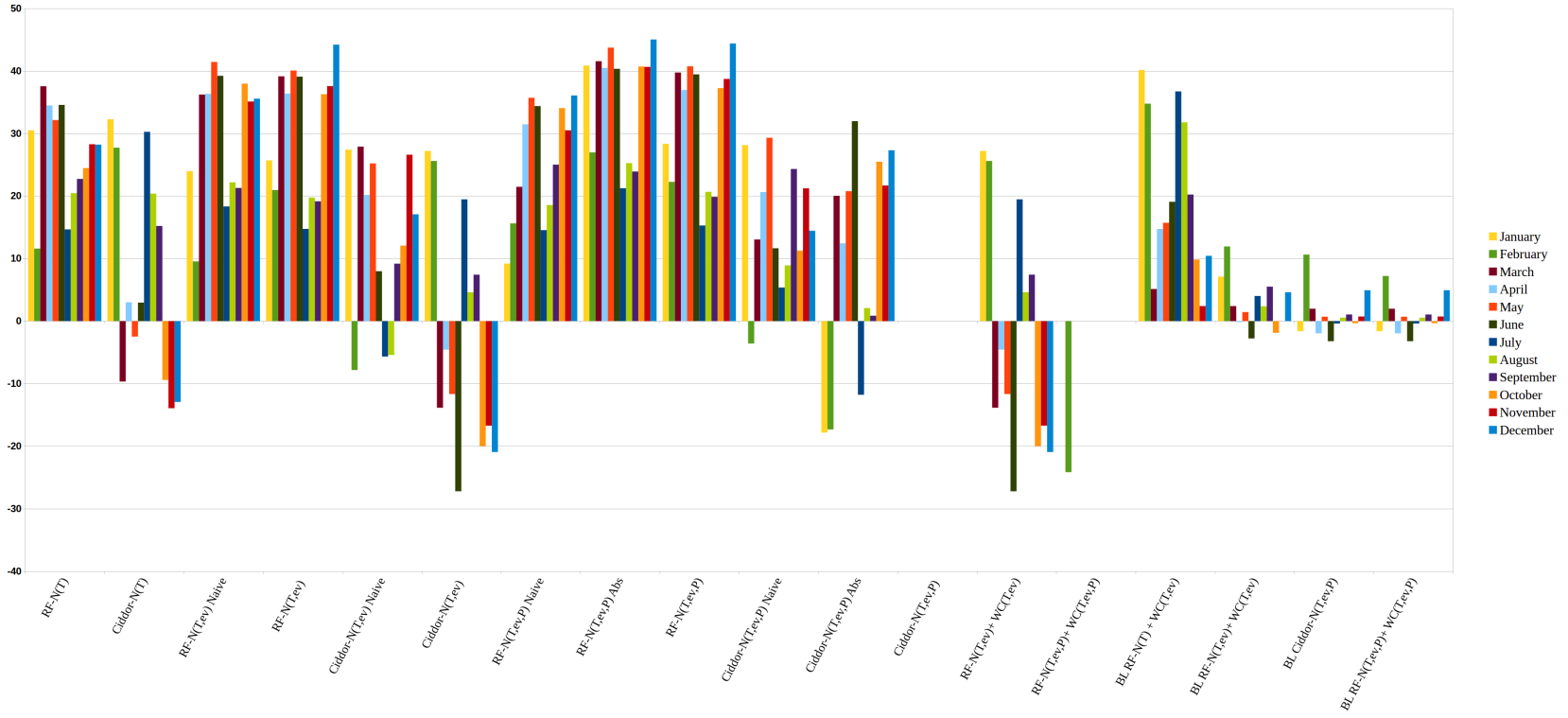

Figure 60. 2-Method NBEC-50 for the *Ciddor* $N(T, e_v, P)$ based C_n^2 estimate vs comparison method for each month of the year at the Dayton (KILN) site. Colored bars represent the two-method NBEC-50 for the *Ciddor* $N(T, e_v, P)$ method. Positive values indicate that *Ciddor* $N(T, e_v, P)$ provided a closer C_n^2 estimate more often than the comparison method. Each color represents the month of the year which is being compared.

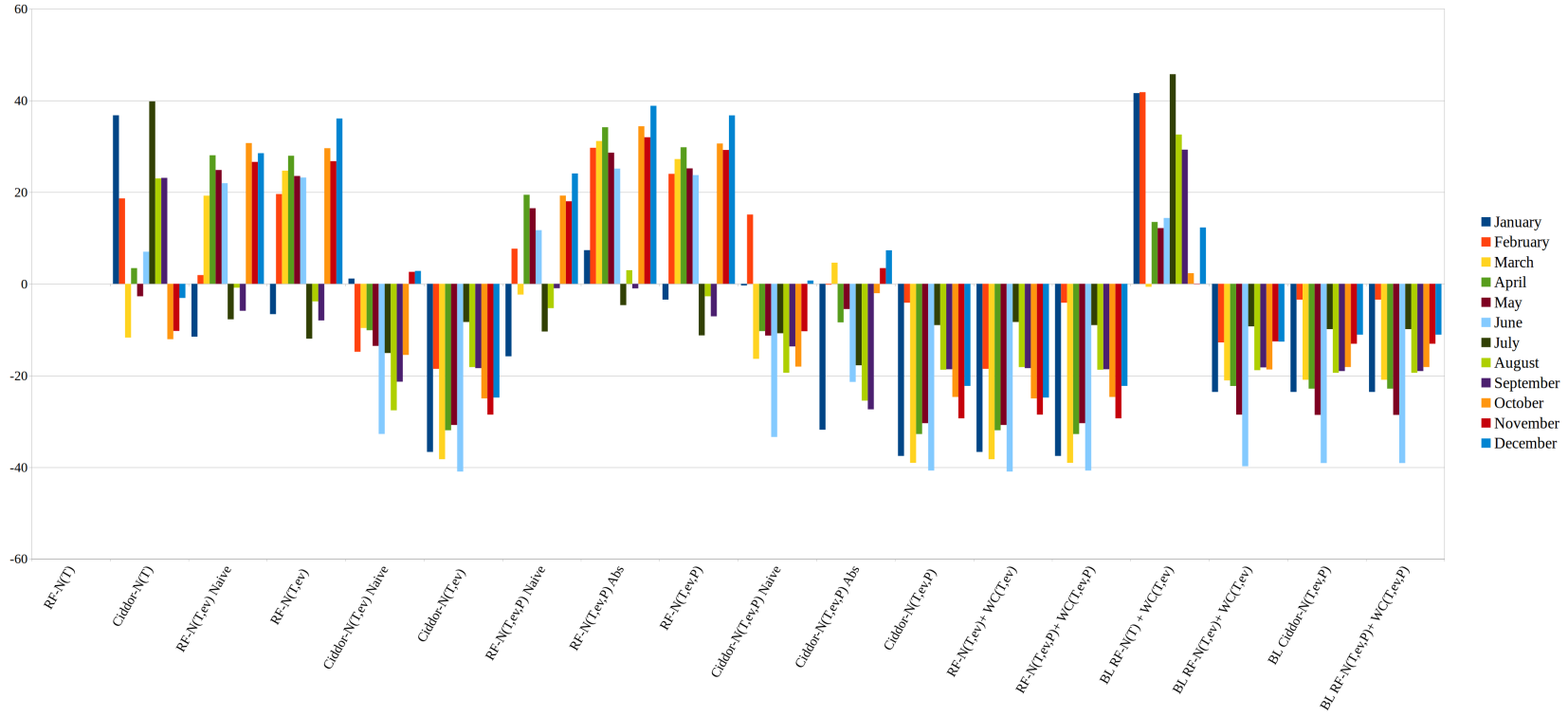

Figure 61. 2-Method NBEC-50 for the *RF* $N(T)$ based C_n^2 estimate vs comparison method for each month of the year at the Dayton (KILN) site. Colored bars represent the two-method NBEC-50 for the *RF* $N(T)$ method. Positive values indicate that *RF* $N(T)$ provided a closer C_n^2 estimate more often than the comparison method. Each color represents the month of the year which is being compared.

standard deviation, and a method will be considered significantly bettor or worse, when the error bars are entirely above or below the NBEC = 0 line, respectively. While there are some differences in the two locations, it can be seen that the *Ciddor* methods outperform the *RF* methods when additional variables are added in, but *RF* $N(T)$ does perform better than *Ciddor* $N(T)$. When comparing the various *Ciddor* or $RF + WC$ techniques which use T and e_v to those which include T, e_v, and P or the baselining techniques, there does not appear to be a significant improvement between the different methods. For most methods, use of the Pythagorean sum as in (29) appears to do significantly better than the Naive form, (25) or the form which uses the maximum variation, (28).

In addition to the 2-method NBEC, a 6-method NBEC was performed which included both temperature only methods, *RF* $N(T)$ and *Ciddor* $N(T)$, non baselined methods *Ciddor* $N(T, e_v)$ and *Ciddor* $N(T, e_v, P)$, and baselined *Ciddor* $N(T, e_v, P)$ and baselined *RF* $N(T, e_v) + WC(T, e_v)$. Recall that baselined *BL RF* $N(T, e_v) + WC(T, e_v)$ and baselined *Ciddor* $N(T, e_v)$ are completely equivalent in terms of their results.

It is apparent that although *Ciddor* $N(T)$ had the worst RMSE scores, it ends up having the best NBEC scores. Based on this and the RMSE results, it appears that *Ciddor* $N(T)$ does well for a good portion of the estimates, but when it does miss, it tends to miss by a lot. While *Ciddor* $N(T, e_v)$ did better in the 2-method NBEC comparisons, it is shown to be less ideal when compared to several methods at once. Based on the averages on the right side of the figures, it appears that NBEC scores for *Ciddor* $N(T, e_v, P)$ and the baselined *Ciddor* $N(T, e_v, P)$ are nearly identical, and overlap the better performing methods. This is a very important result to consider when looking at methods with combined inputs. If the temperature gradients are overestimated, for any reason, even if the other gradient terms are correct, they will

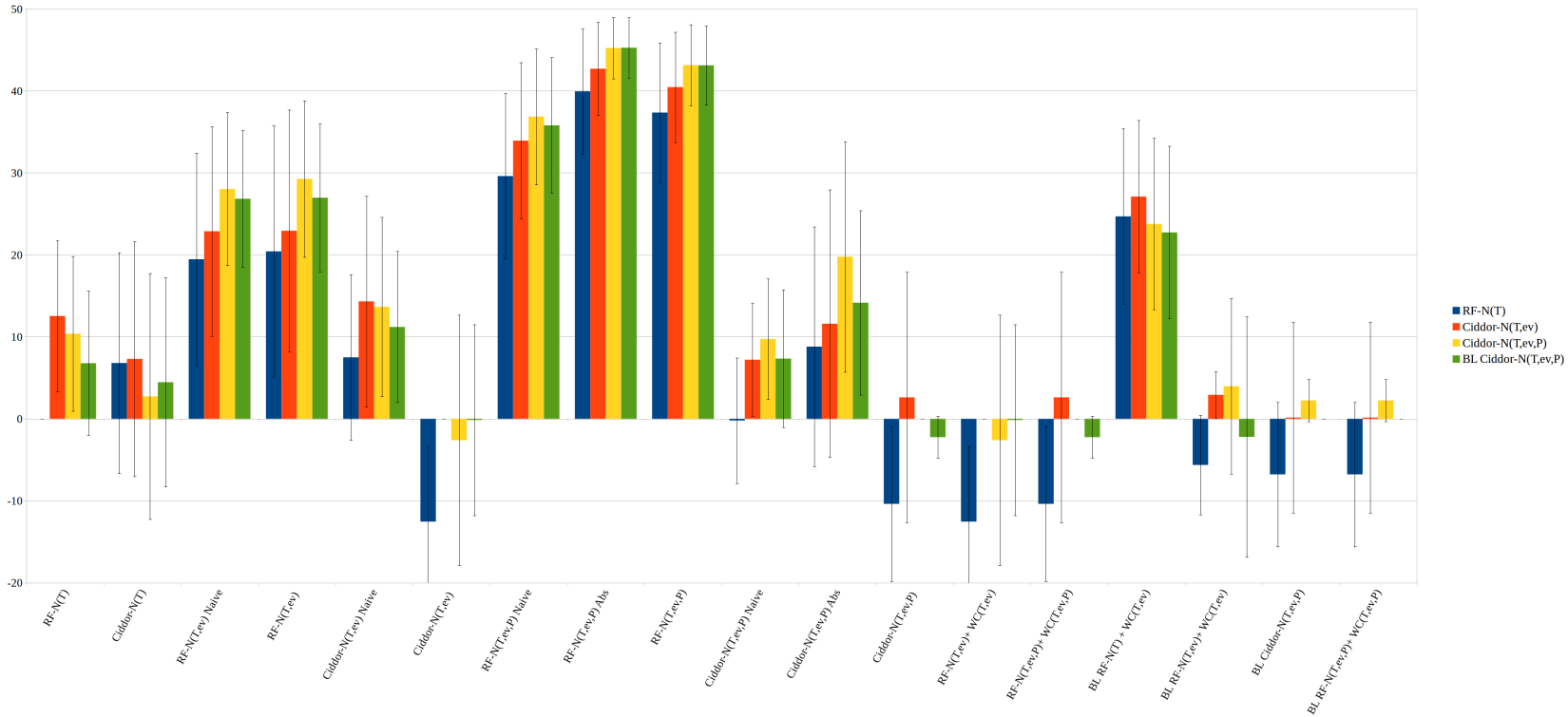

Figure 62. Albuquerque (KABX) Mean 2-Method Normalized Best Error Count −50 for four methods compared to 16 NWP/NEXRAD methods. Mean is taken over all 12 months, with equal weighting given to each month in the mean.

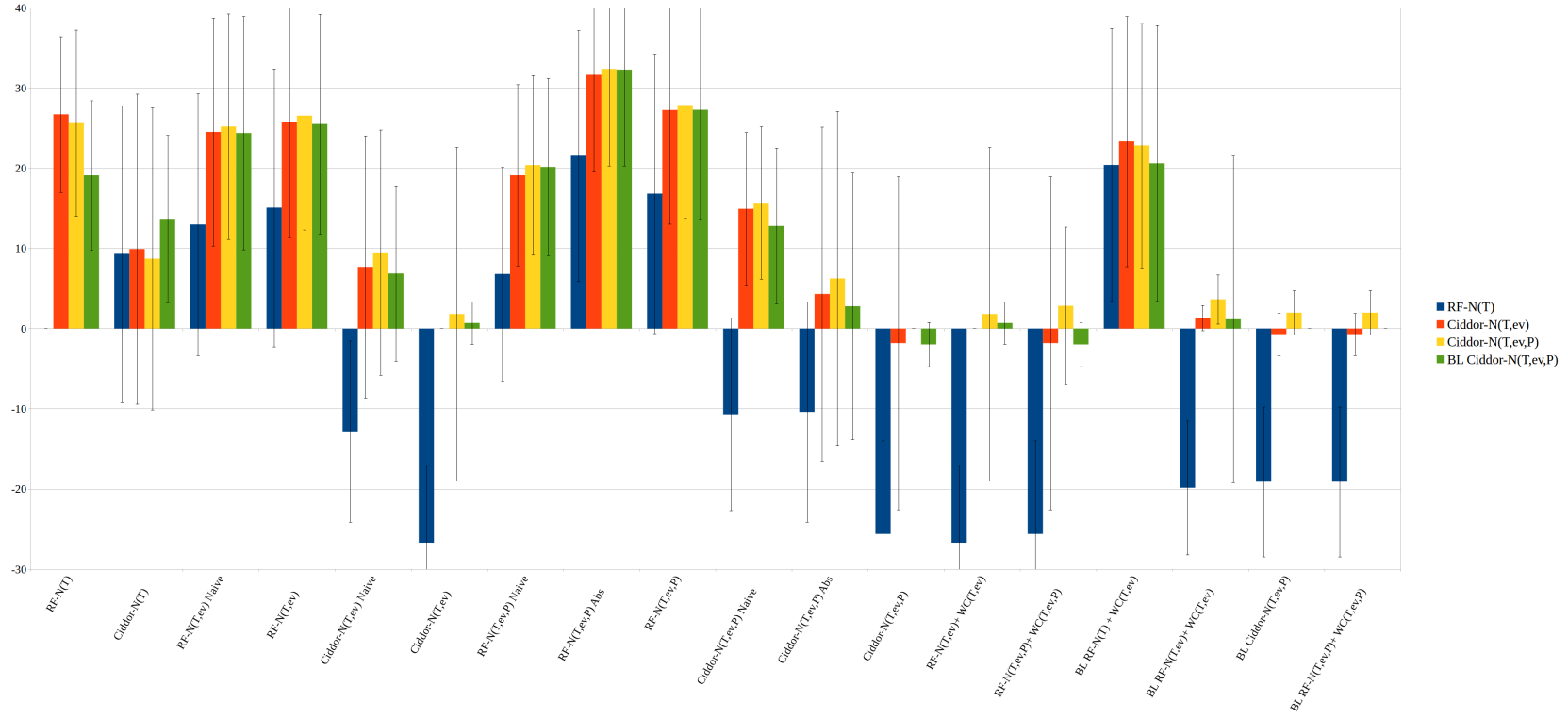

Figure 63. Dayton (KILN) Mean 2-Method Normalized Best Error Count -50 for four methods compared to 16 NWP/NEXRAD methods. Mean is taken over all 12 months, with equal weighting given to each month in the mean.

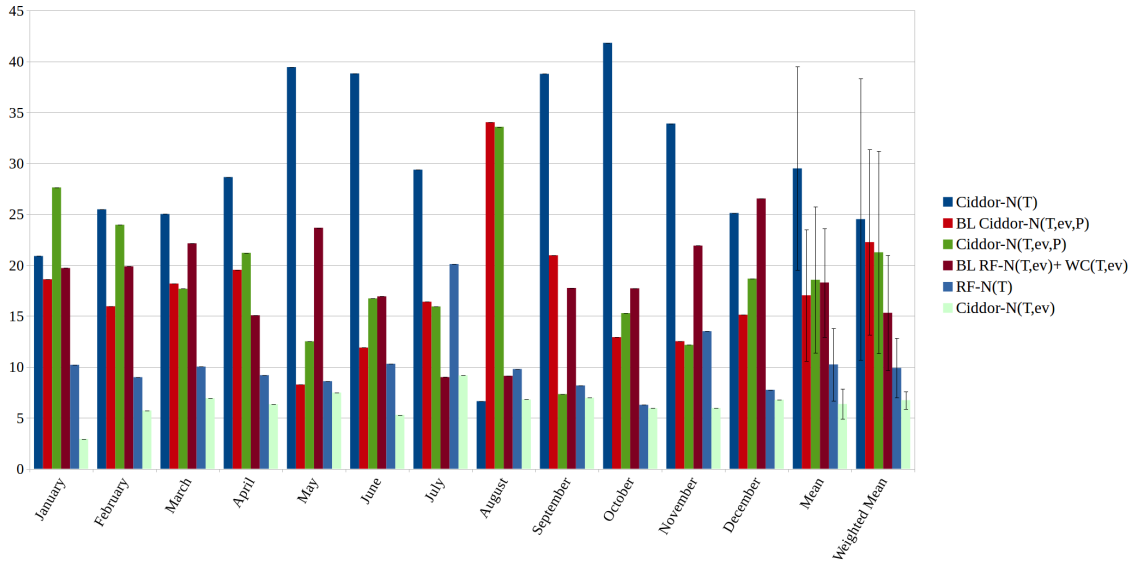

Figure 64. Albuquerque (KABX) 6-Method Normalized Best Error Count for each month of the year, the 12-month mean, and 12-month mean weighted by number of data points in each month. Error bars indicate the 12-month sample standard deviation.

appear to be incorrect in these metrics because they will tend to push the result further from its true value. It may be that the *Ciddor* $N(T, e_v)$ tends to do well because it tends to slightly overestimate the scintillometer C_n^2, so added pressure terms will only serve to degrade the term. However, if the overestimation is typically slight, then reducing L_0 may end up more strongly favoring *Ciddor* $N(T, e_v, P)$

As alluded to before, the NBEC can be affected by choice of L_0. In a similar way, it is also affected by shortcomings of NWP used here for the Tatarskii method. It is not uncommon for this method to show strong over-estimation or underestimation of C_n^2 during extended periods. As the e_v and P terms increase the C_n^2 estimate their NBEC score will be affected by any tendency of Tatarskii's method to underestimate or overestimate C_n^2.

Over-estimation was noted in the Noise section (Figure 26), and this sort of pattern is also noted in other data. For example Figure 66 shows a portion of the Dayton data from several days in March. In this data, there are periods where the temperature

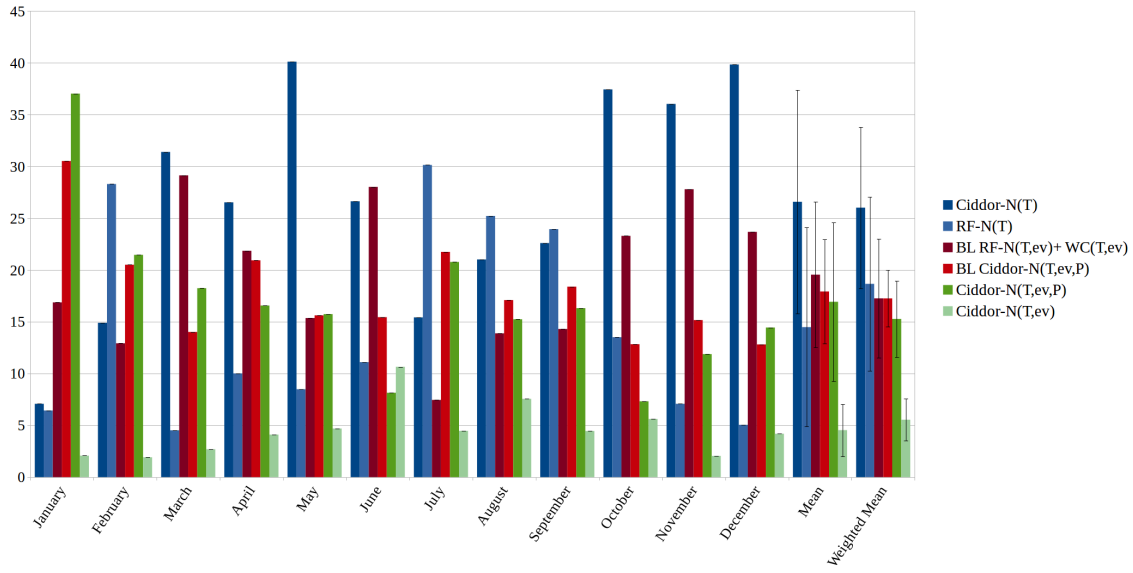

Figure 65. Dayton (KILN) 6-Method Normalized Best Error Count for each month of the year, the 12-month mean, and 12-month mean weighted by number of data points in each month. Error bars indicate the 12-month sample standard deviation.

method overestimates C_n^2. While the e_v and P terms do little to modify C_n^2 in these periods, because they increase C_n^2, they will have degraded NBEC scores. Their RMSE improvement is not significantly effected, because the RMSE at these points is nearly the same as the temperature-only method RMSE. These elevated estimates appear to be driven by large values of $d\theta/dz$ taken from NWP data. It is supposed that the NWP data may not be reliable at these times. Because no method for identifying when these NWP are unreliable is presented, these data are left in the results. The drops in C_n^2 when $d\theta/dz$ goes to zero are significantly improved by adding the additional terms, which is why the RMSE scores still show that the e_v and P terms are helpful.

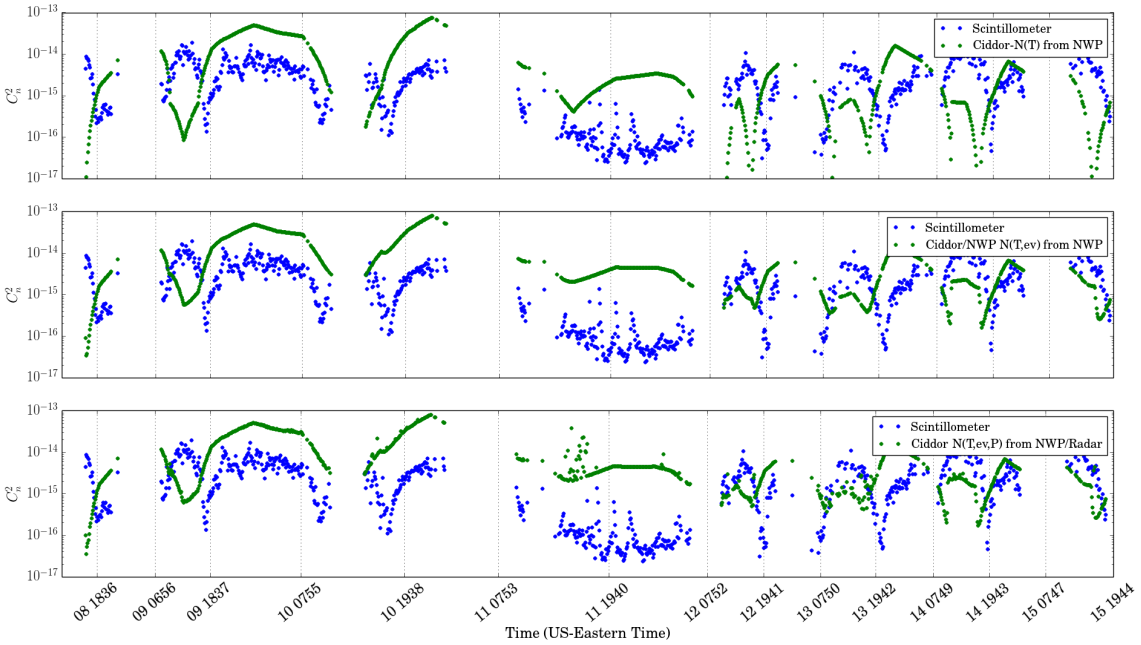

Figure 66. C_n^2 **vs time (axis ticks indicate sunrise and sunset) from March 2013. Blue dots indicate scintillometer data from the Dayton site, and green dots are estimates created using NEXRAD and NWP data and the *Ciddor*** $N(T)$ **(top), *Ciddor*** $N(T, e_v)$ **(middle), and *Ciddor*** $N(T, e_v, P)$ **(bottom) methods.**

Under-estimation due to periods when $d\theta/dz$ goes to zero is an expected consequence of the flawed assumption that e_v ad P are safely ignored in determining C_n^2 for visible to IR systems. However, there are periods when strong underestimation arises, and is not improved by adding the e_v and P terms. This is noted in the scintillometer, and IDM technique data. It appears that the ratio K_H/K_M used in (25),

$$C_n^2 = a^2 \left(\frac{K_H}{K_M}\right) L_0^{\frac{4}{3}} \left(\frac{\partial n}{\partial T}\frac{d\theta}{dz} + \frac{\partial n}{\partial P}\frac{dP}{dz} + \frac{\partial n}{\partial e_v}\frac{de_v}{dz}\right)^2, \tag{113}$$

which is determined using the Kondo equation, (102) from the Bulk-Richardson number, R_i [38, 48] can become quite small when NWP predicted wind gradients dU/dz, and dV/dz become small. Small gradients force R_i to become quite large, and in turn decrease K_H/K_M. It is apparent from (113) that regardless of which terms of

the $\frac{dn}{dz} \approx \frac{\partial n}{\partial T}\frac{d\theta}{dz} + \frac{\partial n}{\partial P'}\frac{dP}{dz} + \frac{\partial n}{\partial e'_v}\frac{de_v}{dz}$ expansion are maintained, a small K_H/K_M value can force the entire C_n^2 estimate to be small. An ad-hoc fix of taking the cube root of the NWP-based Richardson number, $R'_i = \sqrt[3]{R_i}$, before using the Kondo equation to compute K_H/K_M showed much better agreement in both the July-September Dayton scintillometer and IDM comparisons. This correction is only suggests that the K_H/K_M estimates from these data may be incorrect. The cube root modification is not used in the actual RMSE and NBEC data, but it does suggest that RMSE results may be improved by including more accurate gradients.

5.2 Non-Hydrostatic Pressure Gradient Results

This section presents the eddy structure, pressure gradients, and numerical results of applying the Lamb-Oseen model as described in Section 2.4. Based on the shape of the pressure gradient structure (Figure 67) the majority of pressure based scattering is confined to a small and narrow region near the center of the eddy. Depending on the kinematic viscosity, ν, and the energy dissipation rate, ε, an eddy with a size between $2m$ to $10m$ will provide a pressure gradient peak at a radius of $2.5cm$, corresponding to a scattering body size of approximately $5cm$, the dominant Bragg scattering size for NEXRAD radar.

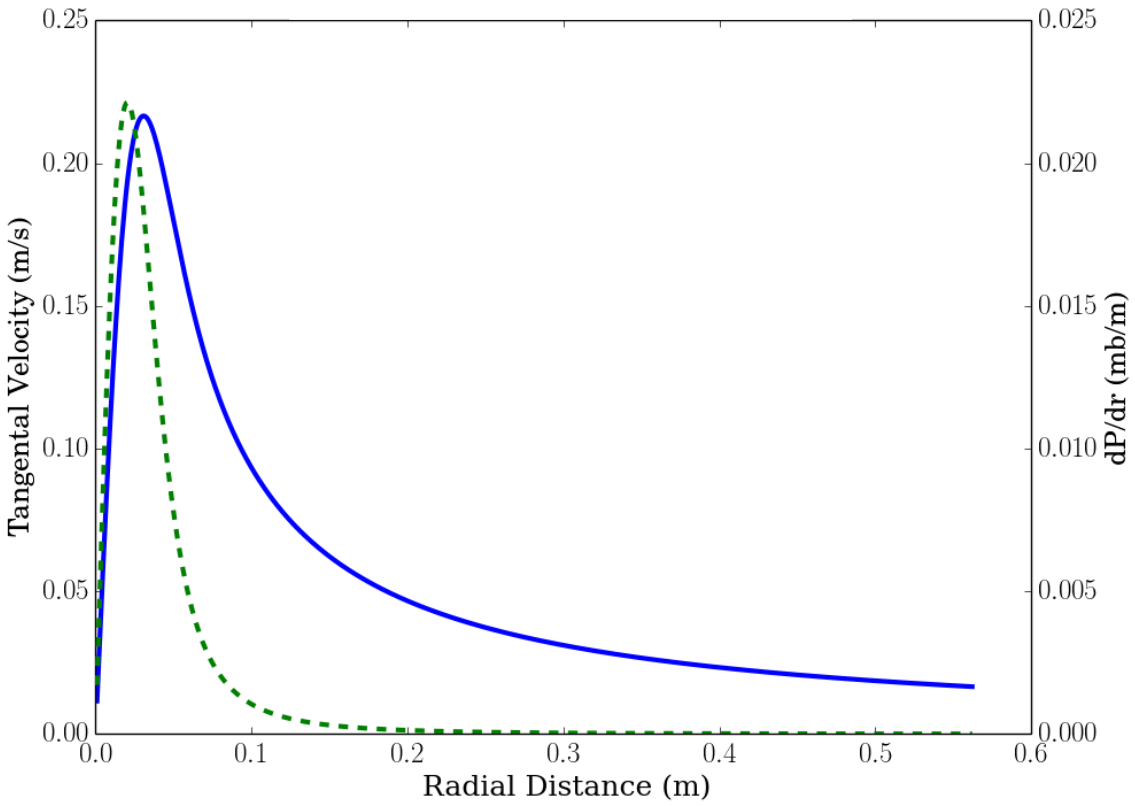

Figure 67. Radial eddy structure derived from the Lamb−Oseen vortex model for a $4m$ eddy with $\varepsilon = 0.008(m^2 s^{-3})$. The solid blue line and left axis show tangential velocity vs r. The dashed green line and right axis show the pressure gradient vs r. Note that the peak of the pressure gradient curve is at a radius of approximately $1/4$ the radar wavelength.

The magnitude of the peak of the pressure gradient depends strongly on ε. Values of ε are calculated from the Doppler spectrum width, σ_v, measured by the NEXRAD radar (Figure 68). [16] The relationship between σ_v and ε depends on the geometry of the radar bin. The width of the radar beam increases with radial distance, but the radial spacing is constant. Thus, the radar bins appear long and skinny near the radar, and like a wide but thin shell far from the radar. Doviak and Zrnik [16] give $\varepsilon(\sigma_v)$ based on a first order expansion of the hyper geometric function with respect

to the aspect ratio $r^2\sigma_\theta^2/\sigma_r^2$,

$$\varepsilon \approx \left[\frac{\sigma_v^3}{\sigma_r(1.35a)^{3/5}}\right]\left(\frac{11}{15}+\frac{14}{15}\frac{r^2\sigma_\theta^2}{\sigma_r^2}\right)^{-3/2}, \tag{114}$$

where σ_r is the range gate spacing of the radar, σ_θ is the radar beamwidth, and a is a universal constant as in (21). In the data used here, the value of ε varies from $10^{-5} < \varepsilon < 10$, leading to pressure gradients which may vary over 5 orders of magnitude. The value $dP/dz = 0.03\ mb/m$ in Table 3 is common for eddies between $5m$ to $10m$ and an ε of about 0.01, which also create scattering widths of around $5cm$.

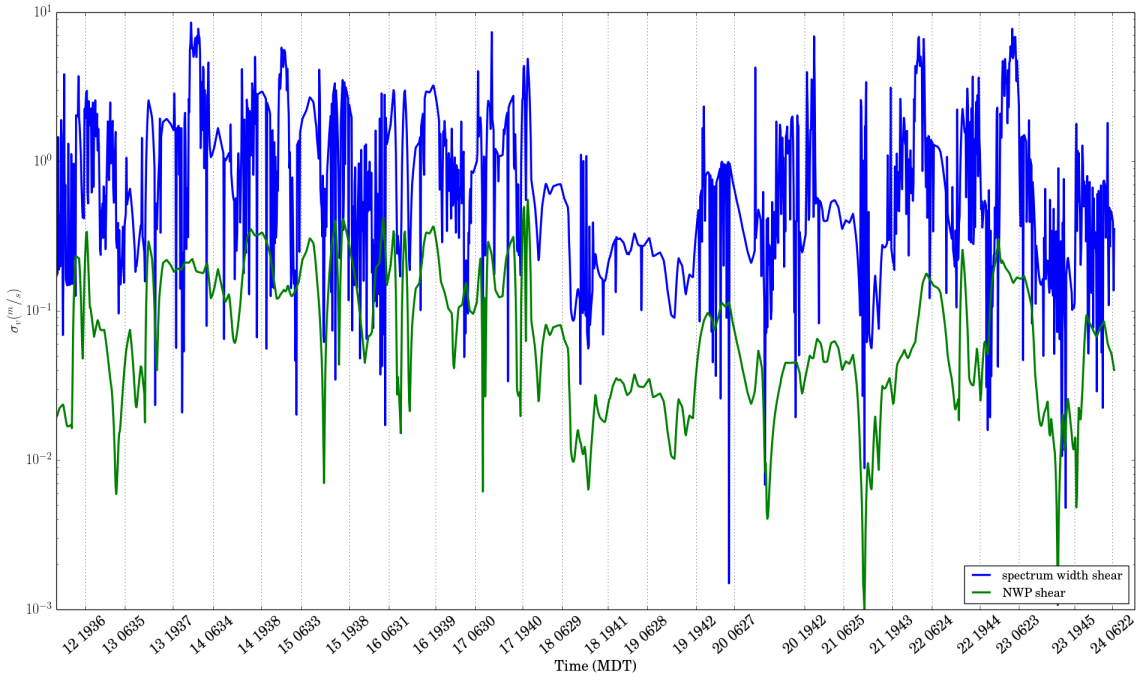

Figure 68. Wind shear vs time (day and time listed) from April 2013 at the Albuquerque site. The green line shows NWP (RAP) based wind shear and the blue line shows NEXRAD Doppler-Spectrum width shear. Portions of the NEXRAD wind shear which do not have measurable data are filled in with NWP shear (the smooth sections of the blue curve).

Table 3. Partial derivatives of refractivity and vertical gradients taken from Dayton, Ohio and Albuquerque, New Mexico. Values are number-of-point-weighted means of the absolute values of the respective quantities. All pressures are in millibars, potential temperatures in Kelvin, potential vapor pressures in millibars, and distances are in millimeters unless otherwise noted.

λ	$\partial N/\partial P$	$\partial N/\partial T$	$\partial N/\partial e_v$	dP/dz	$d\theta/dz$	de_v/dz
Dayton						
10.7 cm	0.2430	1.231	4.039	24.86	5.370	4.736
880 nm	0.2776	0.9443	0.5035	2.813	5.370	4.736
Albuquerque						
10.7 cm	0.2716	0.9368	4.601	43.41	3.314	3.147
880 nm	0.2790	0.7625	0.4934	2.775	3.314	3.147

NEXRAD spectrum width are often incomplete. In order to provide continuous data, NWP shear are used to fill in the missing data as shown in Figure 68. As NEXRAD spectrum width are typically much larger than NWP shear, the NWP shear is adjusted so that its mean matches the mean of the NEXRAD shear. Even though the NEXRAD shear is assumed to be the correct magnitude, it is not known which data source should actually be trusted more when estimating shear.

Calculation of circulation for the Lamb-Oseen model, Γ, requires numerical integration of the denominator in (36). Because this integration is performed several thousand times for each data set, a faster method was sought as described is Section 2.4. The difference between the estimated circulation and the circulation calculated via numerical integration is presented in Figure 69. The dependence on ε is negligible for values encountered in this work. The error as a function of l stays under 2% throughout the inertial subrange, which is considered acceptable as it is significantly less than other error sources in this work.

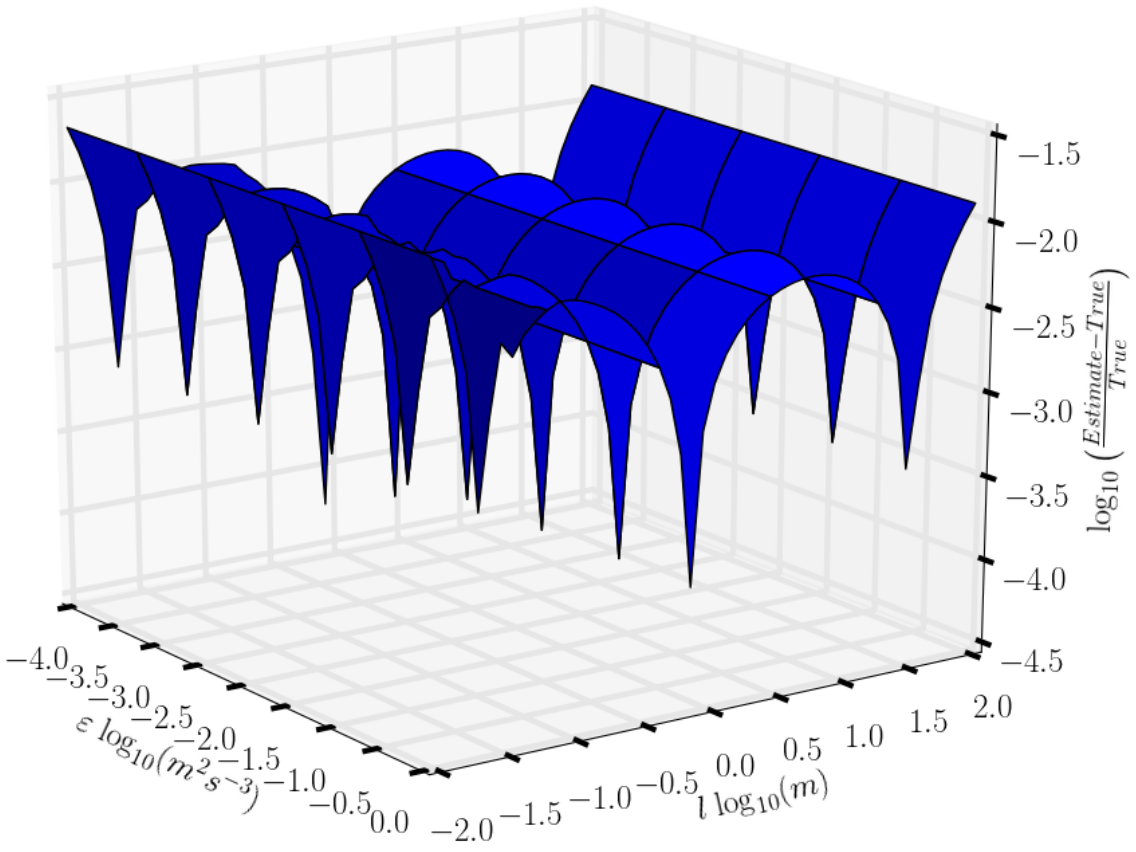

Figure 69. Relative Error between $\Gamma(l,\varepsilon)$ calculated using (36) and $\Gamma(l,\varepsilon)$ from the approximation (37) and (38) vs eddy size, l, and dissipation, ε. All axis are common logarithm.

The improvement in RMSE from adding pressure terms varies from negligible to moderate. The limitations from other noise and error sources make it difficult to determine the significance of the pressure results. If the eddy velocity and pressure structures do bear some resemblance to the models presented here, then there will be little change for conclusions in most previous work with the exception of methods which relate eddy scattering size to eddy energy. This includes the development of Doviak which gives ε from spectrum width. Doviak assumes that $5cm$ eddies are the primary scatterers contributing to the spectral width. However, the Lamb-Oseen model predicts that they are in fact several meter eddies which have $5cm$ scattering

cores. This could indicate that his development, used here, is over-estimating eddy energy.

5.3 Image Differential Motion

The results of the IDM method are to be presented at the 2016 IEEE Aerospace Conference. The IDM data currently comprises only one day, and the technique does not work well during day to night transitions. The path is about $10km$ further from the radar than the Albuquerque or Dayton scintillometer sites. Because of this increased distance, the radar data appeared to be more sparse on this day (Figure 25) which made path weighting more difficult. The IDM weighting is not uniform, so incomplete data create errors as discussed in Section 4.9. Additionally, the original estimates (center plot in Figure 70) severely underestimated C_n^2 at the beginning and end of the day. Investigation of this discrepancy led to the realization that the Bulk-Richardson number, R_i, which is used to calculate the ratio K_H/K_M used in (25) was quite small due to very low vertical wind gradients. Based on an examination of the correlation between the R_i and the differences between IDM based C_n^2 and estimated C_n^2 a cube root modification,

$$R_i' = \sqrt[3]{R_i}, \tag{115}$$

was applied to the original R_i values. While ad-hoc, this correction greatly improved agreement (bottom plot in Figure 70).

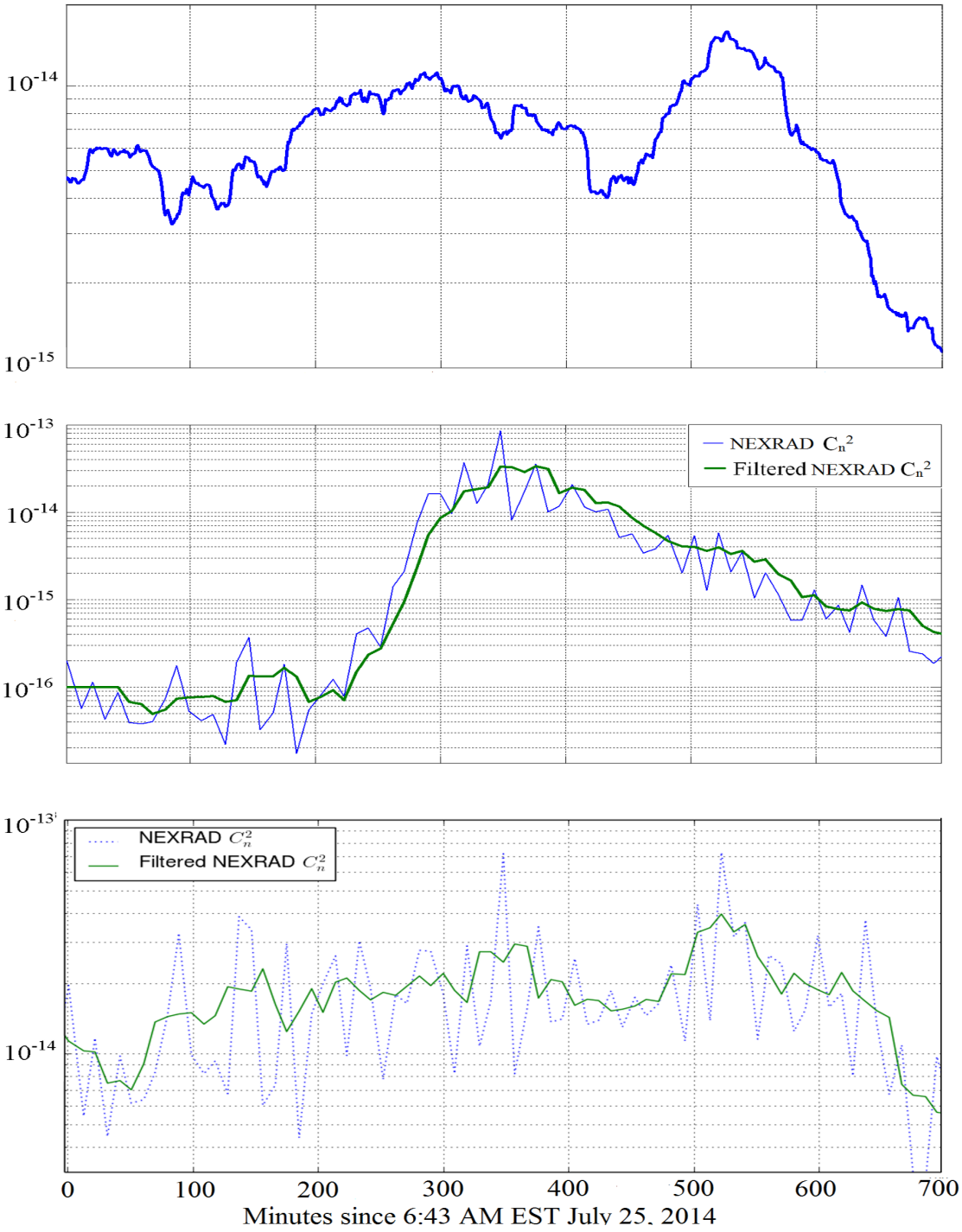

Figure 70. C_n^2 **vs time from three different methods. The IDM technique (top),** ***BL Ciddor*** $N(T, E_v, P)$ **estimates with IDM path weighting applied (middle), and** ***BL Ciddor*** $N(T, E_v, P)$ **estimates where NWP-based** R_i **is modified by the cube-root method,** $R_i' = \sqrt[3]{R_i}$**. All data are taken from 23 July 2014 at the AFIT to Good Samaritan Hospital path. Figures taken from [4].**

In addition to providing comparisons, this data provided an example of how baselining can be important to estimation of C_n^2. The techniques which use NWP do not provide sub-path resolution, so the path weighting cannot be applied. While the NWP method which uses spectral width to estimate wind shear could be used, the spectral width data tend to be much more sparse than reflectivity data. Even though the baselining does not always show significant improvement over the non-baselined methods, its utility becomes apparent in cases like this, where it can provide significantly higher temporal and spatial resolution.

5.4 Cell Phone and Radar

Cell phone data have been collected from three different locations, and several years are available for processing. Using the scintillation calculation method presented in Section 3.3, C_n^2 values are found which are similar in magnitude to radar reflectivity based C_n^2. Figure 71 shows C_n^2 calculated from a 100 point sliding mean. The raw cell phone data are depicted in Figure 73.

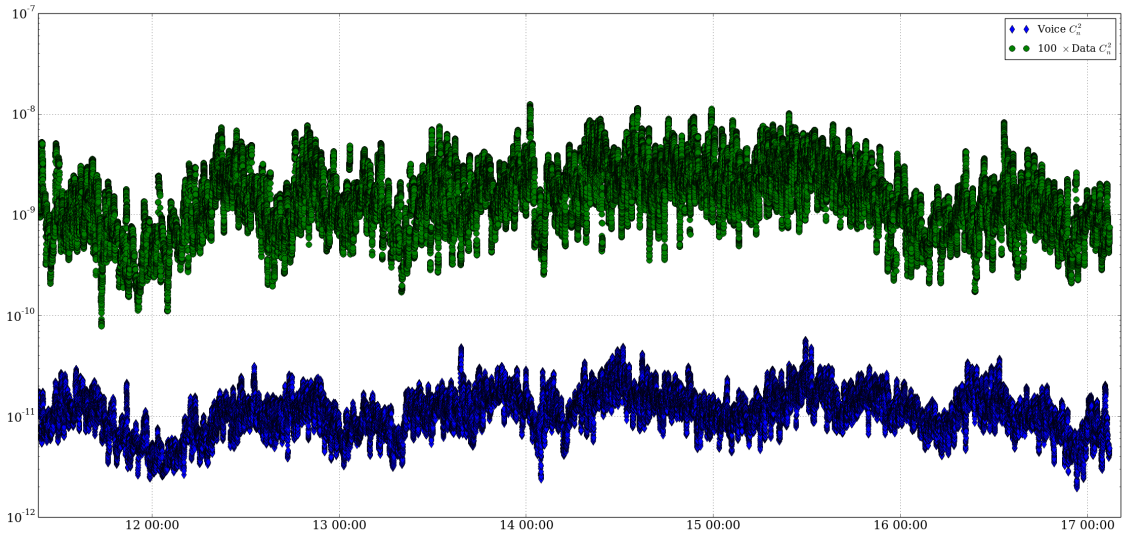

Figure 71. C_n^2 **vs time calculated based on 6 days of power scintillation in cell phone voice and data channels. Data were taken from the second cell phone data path, operating on the Sprint® network. Data** C_n^2 **are multiplied by 100 in order to provide separation on the plot.**

The magnitude of C_n^2 seen in Figure 72 is closer to NEXRAD C_n^2 than those found in [8]. In fact, they are the same magnitude as the RF $N(T, e_v, P)$ estimates shown in Figures 58 and 74. Unlike the lower resolution NEXRAD data, the temporal resolution of cell phone C_n^2 is similar to that of a scintillometer. The data used in Figure 71 covers 494,999 seconds with 108,588 points, which gives an average interval of about $4.5s$. This particular path is $750m$ in length, which is slightly coarser spatial resolution than the NEXRAD provides. These data values have not been compared to NEXRAD data.

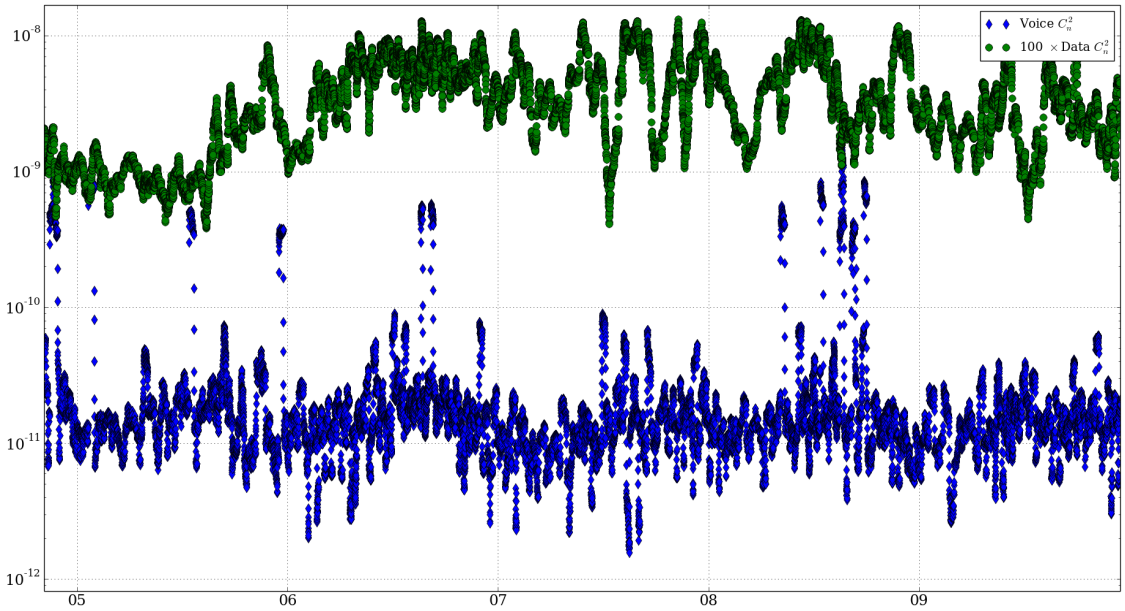

Figure 72. C_n^2 **vs time calculated based on 5 days of scintillation in cell phone voice and data power. Data were taken from the third cell phone path, operating on the Verizon® network. Data** C_n^2 **are multiplied by 100 in order to provide separation on the plot.**

Data from the third location have similar properties (Figure 72), despite coming from a different location, using a different network and hardware. One hardware issue encountered was that the RSSI for the data channel were about $60dB$ higher than those of the voice channel, and RSSI recordings by other devices. This increase in RSSI, creates an increase in C_n^2. For the plot in Figure 72, $60dB$ were subtracted from the data channel RSSI before processing. While complete data from June are common for both the NEXRAD and scintillometer, November data become more sparse. Cell phone scintillation is measurable throughout the year. It is unknown if noise is a greater factor at times when NEXRAD turbulence detection is difficult.

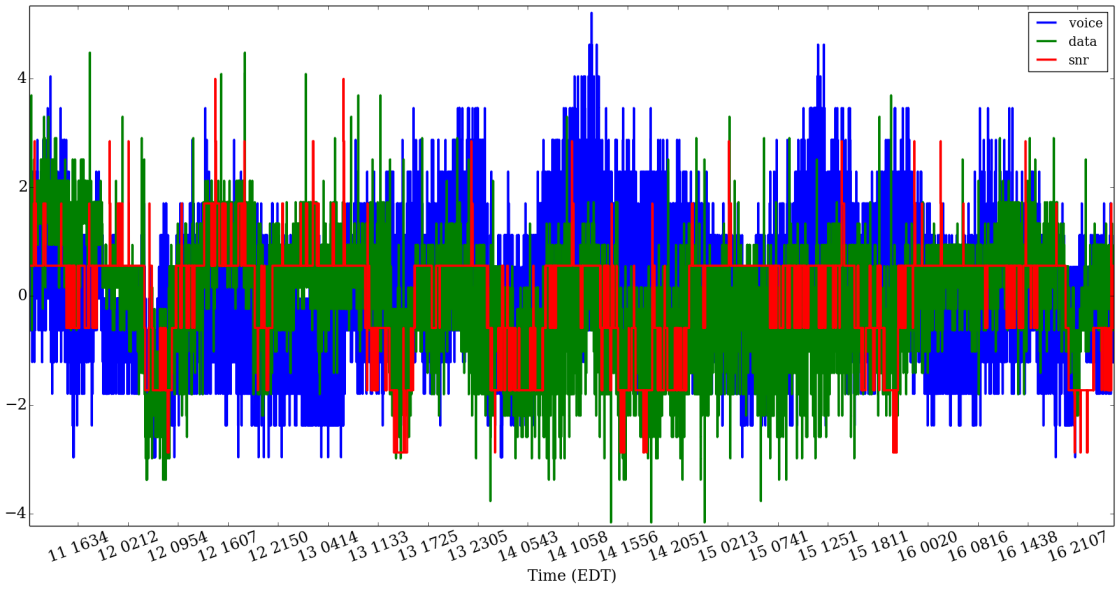

Figure 73. RSSI and SNR vs time recorded for both the voice and data channels from 11-17 June, 2015.

The distribution of time intervals suggests that the RSSI variation process is not Poisson distributed. Figure 22 shows four distributions (blue histograms) of time intervals, τ in seconds, from four different data sets. While the distributions appear similar, they are significantly more peaked, and have fatter tails than the Poisson distribution fits (in red). The distribution plots are truncated at $\tau = 40$, but the actual τ ranged up to several hundred seconds. The non-Poisson distributions are expected, as turbulence-induced RSSI variations are not independent events. Examination of other histograms has shown a consistent distribution of τ.

No comparisons have been made between cell phone C_n^2 and NEXRAD C_n^2. Previous work has shown that there is a significant correlation between the radar and cell phone C_n^2, and C_n^2 processed using the new technique (and the reasonable -60dBm $\langle RSSI \rangle$ values) gives C_n^2 magnitudes similar to those predicted by NWP and RF (N, e_v, P) using the baselining or wavelength correction technique, it should thus be possible to estimate scintillomoter C_n^2 from the cell phone.

5.5 Which Gradients are Important Where

The impact of adding variables ties in closely with the difference between using *Ciddor N* vs *RF N*. It was seen in plots like those in Figure 74, that adding variables caused the *Ciddor N* results to more accurately predict what the $880nm$ scintillometer would measure, and using *RF N* caused the results to head toward what the radar (and cell phones) measure for C_n^2. It is quite apparent that RMSE is improved significantly when adding vapor pressure, when using the appropriate equation. The pressure term also helps, but its improvement is less significant.

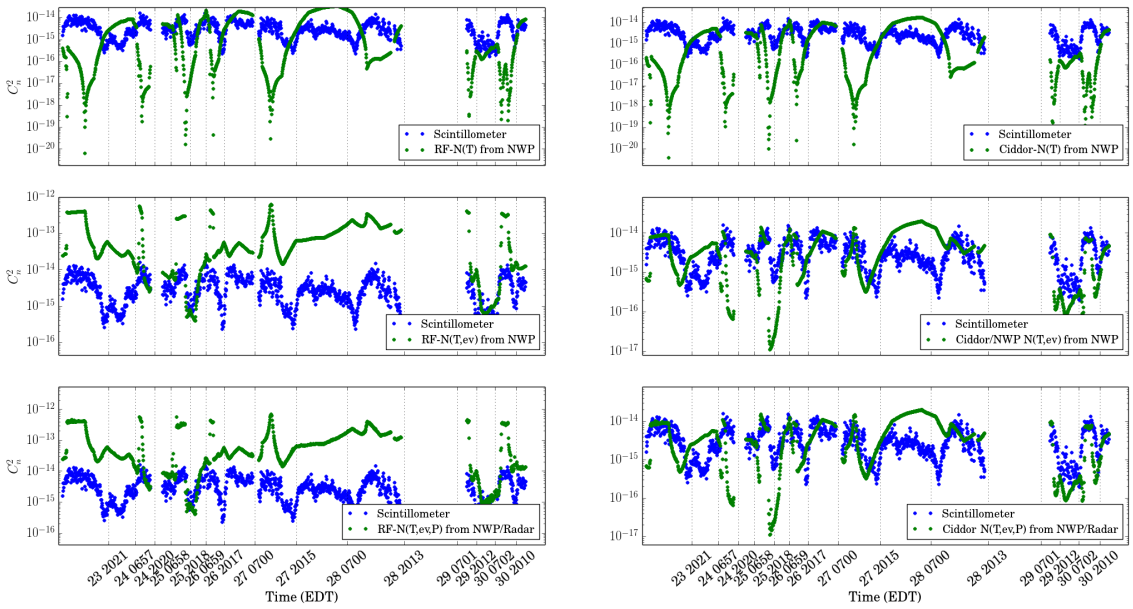

Figure 74. Plots show C_n^2 vs time (x-axis ticks are at sunrise and sunset times). Blue dots are C_n^2 values measured by the scintillometer, and green dots are C_n^2 estimates created using the *RF N* in the left column and *Ciddor's N* equation in the right column. The top row estimates C_n^2 using potential temperature gradients alone. The middle row adds potential vapor pressure gradients to the estimation, and the bottom row adds the non-hydrostatic pressure gradients to the estimation. Blue dots are scintillometer based C_n^2 measurements. Data are from 23-31 August 2013 at the Dayton site.

Looking at what happens to radar estimates, we see that pressure is more significant in Albuquerque. This is expected based on the Lamb-Oseen circulation relationship (36). Note that Γ is inversely proportional to the square root of density.

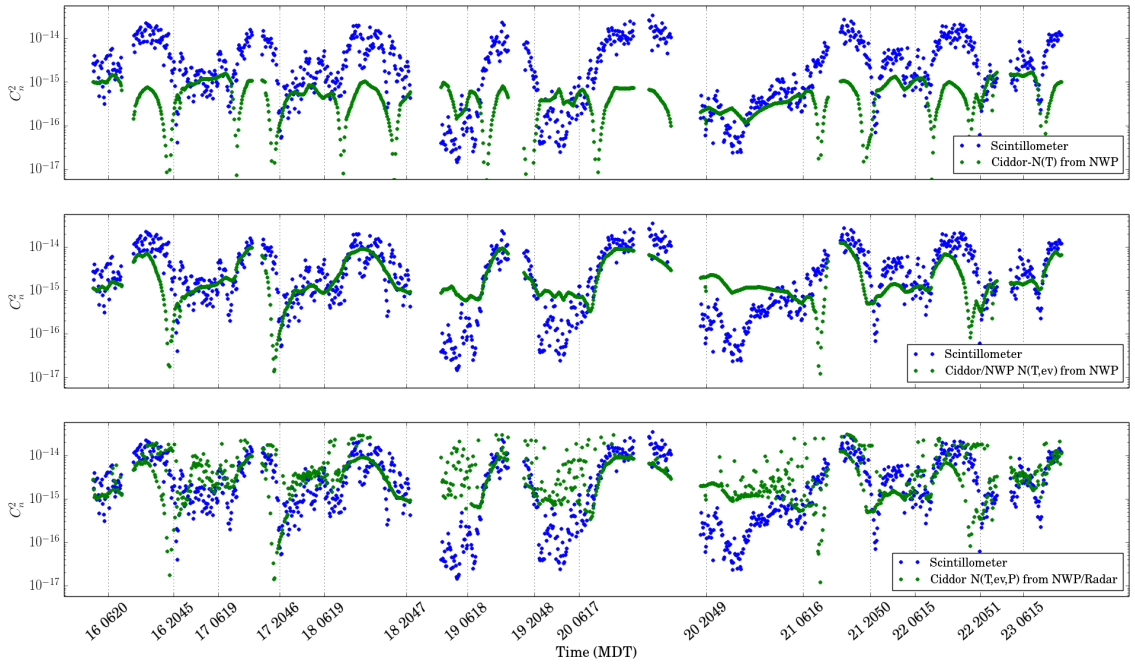

Figure 75. C_n^2 **vs time from the Albuquerque scintillometer (blue dots) and three NWP/NEXRAD estimation schemes (green dots). Data are taken from 16-22 May, 2013. Times depicted on the axis are local sunrise and sunset. Note that temperature only estimates (top) tend to over-estimate** C_n^2 **at night. Clear skies to scattered clouds were present on the first day, and the beginning of the second day. Then, conditions were mostly cloudy to cloudy through the** 19^{th}**. The** 20^{th} **was partly cloudy and the** 21^{st} **and** 22^{nd} **were partly cloudy to clear.**

Therefore, the lower density air at the Albuquerque site is expected to have a greater index gradient for the same amount of rotational energy.

There are times when the additional terms worsened agreement, especially when temperature gradients are so strong that they cause all the C_n^2 estimates to be too high. The data used here have not been compared with other sources to verify that the temperature gradients are especially high, but it has been noted that this effect seems to occur when NWP estimates gradients under cloudy to overcast skies, especially at night. Figure 75 shows estimates using all three methods from May 2013 at the Albuquerque site. It can be seen that NWP-based predictions do not always capture the lower C_n^2 values present at night. This could also be due to poor estimates of vertical wind shear or temperature gradients by the NWP model. It has

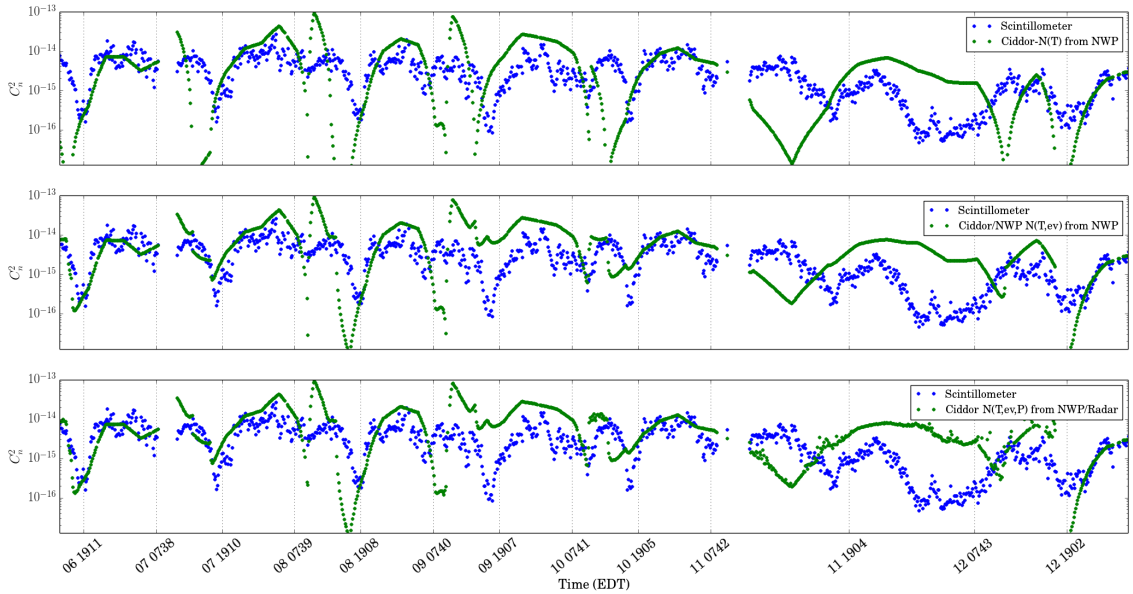

Figure 76. C_n^2 **vs time from the Dayton scintillometer (blue dots) and three NWP/NEXRAD estimation schemes (green dots). Data are taken from 6-12 October, 2011. Note that estimates tend to follow** C_n^2 **well on the first three days, which saw clear skies. On October** 9^{th} **skies became mostly-cloudy to overcast.**

been noted that cloudy conditions seem to correlate with this problem. For example, Figure 76 shows data from the Dayton site in October. The first three days were largely clear, with some periods of partly cloudy skies. On 8 October, skies became mostly cloudy. The estimation schemes appear to do a better job on the first three days, and experience overestimation errors on the latter days.

It is apparent from these plots that there are issues with the NWP data during cloudy periods. A solution is not provided here, but it is noted that while the additional terms make the estimate worse, during these periods, it's only by a small amount compared to the error in temperature measurement. However, in periods when the temperature measurement is close, or strongly underestimates C_n^2, the additional terms can provide significant improvement.

5.6 Does Baselining Help?

Baselining is an interesting subject because the results did not provide improvement as expected. Based on the RMSE test, baselining helped as much as hurt agreement. NBEC was also inconclusive, as improvement from baselining, on average, was within the error-bars of other methods using the same input variables In either case, the change in overall RMSE or NBEC induced by baselining was minor. For estimation of scintillometer paths, the baselining appears to have been an extraneous step. It was expected that the higher temporal resolution would have improved RMSE. It certainly looks like the baselined data has behavior which is similar to the scintillometer (Figure 77).

Consideration of the time uncertainty problem reveals a reason why the baselining method may not perform well as implemented here. As described in Section 4.4, the radar file timestamps indicate a time near when radar measurements are taken, but the actual moment when a volume of air is measured by the radar is uncertain to within a time on the order of the radar cycle time, 5 to 10 minutes. It is apparent from the scintillometer data, that C_n^2 can vary significantly over this period. Until the radar measurement time can be more accurately determined, the timing uncertainty will limit the agreement of measured data.

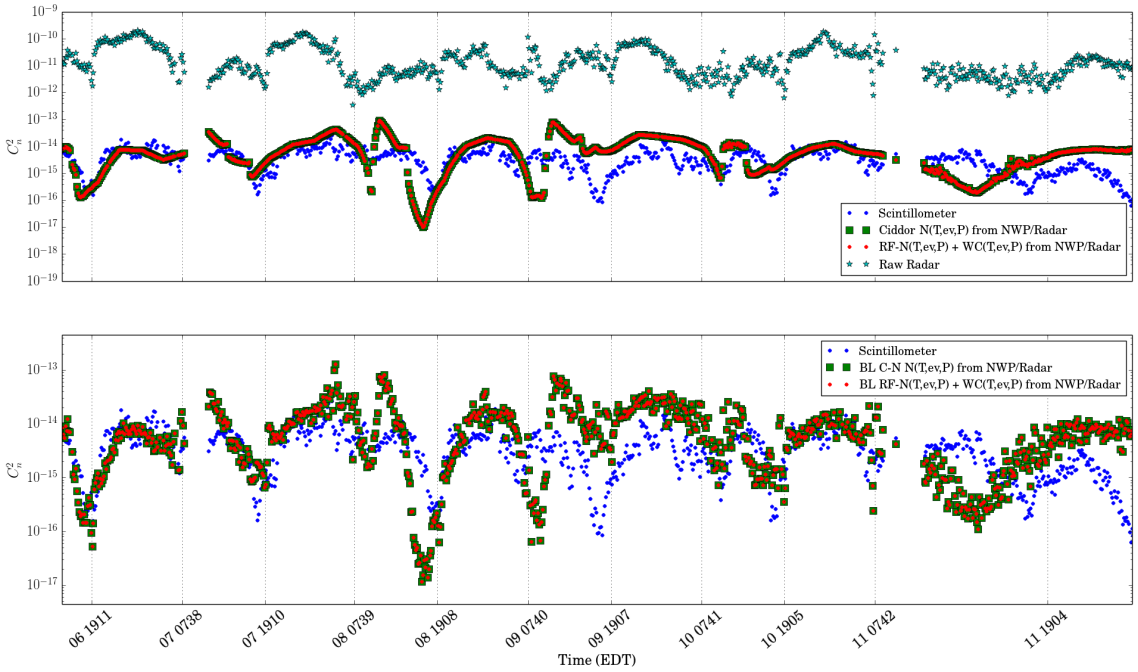

Figure 77. C_n^2 **vs time from 6-11 October 2011 at the Dayton site. The blue dots are** C_n^2 **measured by the scintillometer, and the teal stars are the row radar** C_n^2**. The red dots and green squares in the top plot are estimates of** C_n^2 **made using *Ciddor*** $N(T, e_v, P)$ **and *RF*** $N(T, e_v)$ $+$ $WC(T, e_v)$**, respectively. In the lower plots, the original radar** C_n^2 **from the top-plot is then baselined to the *Ciddor*** $N(T, e_v, P)$ **and *RF*** $N(T, e_v)$ $+$ $WC(T, e_v)$ **estimates.**

The baseline technique does find utility for applications like the IDM technique. Here, the improved radar spatial resolution allowed for approximate path weighting to be applied. The temporal uncertainty still exists. In this case, there is also measurement error introduced from having to chose a method to handle the incomplete radar data in the path weighting. Application of the IDM to a path closer to the radar, where more bins are available may alleviate this somewhat.

The baseline technique also provides a method for cell phone based C_n^2 to be converted. While the cell phone does not directly measure wind speed, a correction can be made to *Ciddor* $N(T, e_v)$, which showed good performance for the radar. This

would allow the high temporal resolution of the cell phone to be used immediately. It may be possible to predict the pressure gradients from NWP as well. This was recently shown to be possible using a non-hydrostatic model in [45]. Additionally, NEXRAD can be used as described here, with the cell phone providing a higher temporal resolution of C_n^2 variation. Cross-correlation techniques with cell phone data may also allow for the radar time to be more accurately determined.

VI. Conclusions and Future Work

6.1 Conclusions

This research has developed the first method which allows for accurate estimation of visible/IR C_n^2 remotely, passively, and in a volumetric sense with useful spatial and temporal resolution. In addition to the technical contributions which follow, this presents a new capability for DE, imaging, and optical communications system development. The research here can be applied directly to available radar, NWP, and cell phone systems, or used to develop more capable systems based on the limitations of current systems which were identified in this work.

Several new contributions have arisen from this work. The most well-established and significant contribution is demonstrating that Ciddor's equation *should* be used as the refractivity model when calculating C_n^2 via Tatarskii's method. Closely related to this contribution, is demonstration that under many conditions, IR C_n^2 does not depend on temperature perturbations alone. Based on these contributions, an improved wavelength correction has been developed along with several methods which can combine freely available NEXRAD and NWP data into volumetric C_n^2 measurements, and a way ahead for using emitters of opportunity to measure C_n^2. The final contribution is the investigation into non-hydrostatic pressure gradients and a suggested model for these pressure perturbations.

Inclusion of additional terms does not agree well with observations when RF reflectivity models are used. This supports the conventional approach of only considering temperature perturbations when estimating C_n^2 for the visible and IR regime. Use of *Ciddor* $N(T)$ when determining C_n^2 likewise produces poorer results than *RF* $N(T)$. It is only when additional terms are included and Ciddor's equations are applied that agreement begins to improve. *Ciddor* $N(T, e_v)$ provides a significant reduction

of RMSE, and improved NBEC. Generally the RMSE in log space was cut in half, which justifies using *Ciddor* $N(T, e_v)$ (or one of the other, similarly performing methods) over *RF* $N(T)$.

As can be seen from the data, the vapor pressure and pressure term can be safely ignored when temperature gradients are large. Because use of *Ciddor* $N(T, e_v)$ or *Ciddor* $N(T, e_v, P)$ does not significantly change C_n^2 predicted by the conventional *RF* $N(T)$ when $\frac{d\theta}{dz}$ is large, these results do not refute earlier other works which often show good agreement using *RF* $N(T)$ under these conditions. What the pressure and vapor pressure terms provide is a reasonable explanation of why observed C_n^2 does not drop as much as the temperature-only models predict. The data here shows that predicted behavior matches observations much better when e_v and P terms are included, and the Ciddor equation is used.

While several methods were developed and compared here, the choice of which to use and when can be inferred by the RMSE and NBEC results. Some of the methods used here produced identical results. Using *Ciddor* $N(T, e_v, P)$ is equivalent to using *RF* $N(T, e_v, P)$ + $WC(T, e_v, P)$. Likewise, the results from using *Ciddor* $N(T, e_v)$ were identical to results from *RF* $N(T, e_v)$ + $WC(T, e_v)$. Other techniques, like baselining did not produce significant differences in RMSE or NBEC. However, other qualities of these methods may make them more desirable in particular circumstances.

While the wavelength correction of C_n^2 derived from NEXRAD-measured clear-air reflections was the original impetus for this research, it turns out that using Ciddor's equation with all three terms is a more straightforward approach to estimating optical C_n^2. There are still instances where this correction would be important. NWP forecast, and measurement devices are often more accurate with respect to temperature than other quantities like vapor-pressure. Using a multi-wavelength approach, it would be possible to determine factors like the ratio of C_T^2 to the humidity based $C_{e_v}^2$ and the

cross-term C^2_{T,e_v}. As NWP can more accurately predict C^2_T, the ratio could be used with multi-wavelength C^2_n to estimate the $C^2_{e_v}$ and C^2_{T,e_v} terms.

NWP based C^2_n estimates can be made without NEXRAD or cell phone inputs. However, NWP-based estimates will be limited in resolution. The radar is a useful as a tool as its Doppler spectrum width measurements allow for calculation of the non-hydrostatic pressure gradients, dP/dz, which improves the resolution of the pressure term. Through baselining, the NEXRAD or cell phone can also provide a high temporal and spatial resolution C^2_n. As the baselining methods are shown to be as good as or better than using the NWP based methods, they provide an opportunity to conduct studies such as the path-weighting comparisons from the IDM technique, which are not possible with the coarse NWP data. The baseline technique met with mixed results. While it generally improved measurements in the Dayton data, it degraded measurements by a similar amount in the Albuquerque data. Because of the terrain geometry at the Albuquerque site, the amount of surface clutter is likely to be higher than at the Dayton site. This may cause the "clear air" reflections to be less correlated with turbulent activity at Albuquerque.

The pressure perturbation contributions was found by bringing together existing models of refractivity, the Lamb-Oseen vortex, and Tatarskii's method. The need to include pressure perturbations matches well with physical theory, past, and current observations. It is known that real vortices quickly evolve toward an irrotational form in the absence of forcing mechanisms, so use of the Lamb-Oseen model is appropriate for well-developed turbulence. While the existence of non-hydrostatic perturbations is on solid footing, the results are inconclusive with respect to the appropriateness of the Lamb-Oseen model and the pressure perturbations it predicts. While the pressure term did improve RMSE overall, the improvement is negligible in some cases, and moderate at best. There are several reasons, outside of the model validity, as

to why the improvement is not greater. These include the fact that the pressure term is often only a small adjustment in the presence of typical temperature and vapor pressure gradients. Additionally, the characteristic eddy size which was used may be incorrect. Incorrect or noisy eddy energy measurements could reduce the effectiveness of the pressure term. NWP gradient overestimation in either $d\theta/dz$ or de_v/dz and improper choice of L_0 can also degrade the effectiveness of the pressure term as described at the end of Section 5.2. Previous measurements have shown that the pressure term is negligible. [17, 25, 27] However, measured evidence of pressure perturbations have been conducted near the surface where the Lamb-Oseen model predicts that perturbations would be inconsequential (due to the maximum vortex size being limited to the height AGL). Where the scintillometer paths took their measurements (60 to $70m$ above the surface), there was plenty of room for larger eddies to form. For this reason the pressure term could take on full value unlike pressure perturbations measured closer to the surface. Furthermore, the Lamb-Oseen model predicts that the pressure term is negligible throughout most of the eddy, with only a relatively small volume possessing a significant pressure gradient, so the mean perturbation would in fact be negligible. In addition, the modifications of the velocity structure for a three-dimensional vortex have not been explored here. While support for the pressure term is weak, there is no evidence that the term should be rejected. The gradient magnitudes and resulting index perturbations are not unreasonably large, and the eddy velocity structure provides an explanation why the ε calculated from Doppler spectrum width may be too large.

The radial distance of both sites causes the radar to integrate over a shell which is approximately $900 \times 900 \times 250m$. This spatial averaging of a space well outside the correlation length of PBL turbulence is expected to contribute much more to C_n^2 disparity than the path weighting inaccuracy. While the C_n^2 data volumes show that

the lower portion of the PBL shows significantly stronger C_n^2, it is the opinion of this author that these values are inflated largely due to ground clutter, and to a lesser degree biological scatterers. While this provides significant noise in the reflectivity magnitude measurement, the noise impact on Doppler and Doppler spectrum width is harder to determine. It is possible that the spectrum width is not as negatively affected because many of the surface motions are driven by winds, which are tied to turbulent eddy motion. On the other hand, many surface objects (especially those which have non-zero Doppler and will thus pass through some of the ground-clutter filtering) move under their own volition, or in response which does not correlate with velocities of the turbulent flow. Further research, comparing returns from upper elevations would be useful for determining how much of an effect surface clutter has on Doppler and Doppler spectrum width measurements.

6.2 Future Work

There are many questions which this work leaves unanswered. Based on what was found here, there are many avenues which should be explored. For the sake of clarity, these are presented in an enumerated list.

1. The wavelength correction needs to be tested against multi-wavelength data. Dr. Voronsov at UD has done several tests using multiple wavelengths both on the UD path and at Hawaii [74]. It should now be possible to compare his results with predictions made by the wavelength correction and NWP.

2. The methods used here did not apply a proper path weighting to the radar C_n^2 estimates for the scintillometers. Two options include a proportional weighting approach like that used in [4]. This weight would be based on the scintillometer path weighting function. A more crude approach which avoids the difficulty in

applying a path weighting in the presence of missing data, would be to use the even path weighting, but only measure over a portion of the middle of the path.

3. An interesting study would be to investigate how the Bragg condition would change for continuous index gradients like in the Lamb-Oseen model vs the index step function (i.e. a sphere of material with a constant index which is different from its surrounding media). This work, like other contemporary research, assumes that each eddy scatters as if it were a sphere of homogeneous material placed within an environment with a different index of refraction. Does scattering based on a more realistic, smoothly varying index still predict that the dominant back-scattering size is $\lambda/2$?

4. Rytov's expansion, which was developed for optical scintillation due to turbulence is used for conversion of cell phone scintillation. However, it has not been verified if this is an appropriate approach. A comparison should be made between Rytov's development and the cell phone multipath scattering effect to determine what, if any, changes should be made to the development.

5. Doviak's volume-weighted scattering function for determining C_n^2 from dBZ (10) is based on the assumption that the eddy size equals the scattering size. However, the Lamb-Oseen model predicts that the scattering size is much less than the eddy size. Does the relationship in (10) need adjusted to account for the fact that the dominant scatterers may come from larger eddies than previously thought? A similar question may be asked for the relationship between Doppler spectrum width and eddy energy dissipation rate, (34).

6. The cell phone gives both the magnitude of RSSI variation, and when the variation occurs. As the time between variation carries information about the process, is there a way to use both forms of information? Is there additional

information which can be gained beyond C_n^2?

7. Is there a correlation between overcast skies and C_n^2 overestimation? It has been observed that NWP based C_n^2 estimates do not agree with scintillometer measurements during periods of strongly overcast skies or precipitation.

8. The NEXRAD radar returns cross-polarization data, which can be used for hydrometer identification. It is often used for identification of bio-clutter (birds), but bird presence is based on reflectivity which does not correlate well with populations. Is it possible to use cross-polarization to differentiate between bio-clutter, ground-clutter, and turbulence?

9. Can the radar demonstrate the Taylor Frozen Flow Hypothesis? Try taking the radar image, and processing parallel paths from the area around the scintillometer path, taking into account the mean wind. Do we see that paths at a certain time in the past correlate better? Maybe this is because the radar is measuring t minutes before the scintillometer.

10. It is apparent that if the Lamb-Oseen velocity structure is even approximately accurate, that the size of the vortex may be much greater than the size of the region of strong gradients which interact with propagating waves. The scale ratio is on the order of 100 to 1000 for eddies investigated here. While this does not significantly affect comparisons between measurements of C_n^2 and C_θ^2, and other structure-function constants, it does suggest that further research into relationships between these and TKE or ε measurements (and estimates) should be carried out.

11. The baselining function uses time averaging. While this is good, time-space averaging, where the total reflectivity in a large area over a long time is compared to NWP may be more appropriate. It would be interesting to rework the radar

extraction to provide a volume-averaged C_n^2 along with the path-based C_n^2. The volume average can then be baselined to the NWP C_n^2, and the baseline results applied to the bins along the path. Because the radar would be averaging over a volume similar to the NWP grid size, this baseline approach may be the more appropriate form.

12. An important question about path deflection becomes one of time scale. What is the temporal structure function of path deflection? Slow variations can be predicted by NWP, but what of the fast changes? The IDM technique can help estimate these as the total deflection of the hospital image can be used to determine the magnitude of path deflection. Knowing this can help understand how important short-term path deflection may be to cell phone scintillation.

VII. Appendix

7.1 Ciddor Equation Constants

Ciddor's equations were originally intended to estimate refractivity defined as $N_C = (n-1)\times 10^8$, which makes it two orders of magnitude larger than the convention used here, $N = (n-1)\times 10^6$. In addition, Ciddor uses units of Pascals for pressure instead of millibars (used throughout the remainder of this work). In this section, these differences will be addressed. As presented in Section 2.2, Ciddor's method for finding refractivity can be cast into the form:

$$N = \frac{p}{ZT}\left(A + Bx_w\right) \tag{116}$$

where A and B are wavelength-dependent constants, p is pressure in Pascals (used by Ciddor instead of millibars which are denoted P), Z is the compressibility of moist air, T is temperature in Kelvin, and x_w is the molar ratio of water vapor to dry air. In order to use the wavelength correction, or to estimate C_n^2 from atmospheric gradients we wish to know how to find the partial derivatives, $\partial N/\partial P$, $\partial N/\partial T$, and $\partial N/\partial e_v$. These partial are given in terms of N:

$$\begin{aligned}
\frac{\partial N}{\partial P} &= N(T,P,e_v) f_P(N,P,e_v),\\
\frac{\partial N}{\partial T} &= N(T,P,e_v) f_T(N,P,e_v),\\
\frac{\partial N}{\partial e_v} &= N(T,P,e_v) f_{e_v}(N,P,e_v).
\end{aligned}$$

This serves two purposes. First, the scaling factors f_P, f_T and f_{e_v} are all unitless, so the varying definitions of N are handled automatically. Second, the impact of absorption lines can be approximately included with minimal effort as follows. In-

clusion of absorption features could be done explicitly using techniques described by Hill et al [27]. This technique requires some work to implement, however, as relevant absorption species must be known for a given wavelength, and the absorption specra data for all relevant species would need to be included in the calculation. Fortunately, modern software packages like LEEDR [22] exist which automatically handle these steps and can be used to compute $N(\langle T\rangle, \langle P\rangle, \langle e_v\rangle, \lambda, x_1, x_2, x_3, \ldots)$, the refractivity at a given wavelength, λ, using local environmental conditions (x_i is the molar mixing ratio of the i^{th} atmospheric constituent which has a significant contribution to N). The approximation used here is based on the difference between the continuum refractivity, N_C, say form Ciddor's equation, and the actual refractivity, N, which includes the impact of absorption lines,

$$N = N_C + \sum_i N_i. \tag{117}$$

The corresponding partial of N with respect to parameter β is,

$$\frac{\partial N}{\partial \beta} = \frac{\partial N_C}{\partial \beta} + \sum_i \frac{\partial N_i}{\partial \beta}. \tag{118}$$

Using Ciddor's equation, the scaling factor $f_{C,\beta}$ can be found,

$$f_{C,\beta} = \frac{1}{N_C}\frac{\partial N_C}{\partial \beta}. \tag{119}$$

When the true refractivity is known, the approximate partial as found from

$$\frac{\partial N}{\partial \beta} \approx N f_{C,\beta}. \tag{120}$$

The difference between the true partial, and this estimate is then

$$\frac{\partial N}{\partial \beta} - N f_{C,\beta} = \frac{\partial N_C}{\partial \beta} + \sum_i \frac{\partial N_i}{\partial \beta} - \left(N_C + \sum_i N_i \right) \frac{1}{N_C} \frac{\partial N_C}{\partial \beta}. \tag{121}$$

Combining summation terms on the RHS and canceling the $\frac{\partial N_C}{\partial \beta}$ terms leaves

$$\frac{\partial N}{\partial \beta} - N f_{C,\beta} = \sum_i N_i \left(\frac{1}{N_i} \frac{\partial N_i}{\partial \beta} - \frac{1}{N_C} \frac{\partial N_C}{\partial \beta} \right). \tag{122}$$

Away from absorption lines, N_i depends to first order on concentration just like N_C. For temperatures and pressures encountered in the lower atmosphere, and for wavelengths far from absorption lines,

$$\partial N_i \partial \beta - \frac{1}{N_C} \frac{\partial N_C}{\partial \beta} \ll \frac{\partial N_C}{\partial \beta} \tag{123}$$

for both temperature, pressure, and vapor pressure. In these same regimes $N_i \ll N_C$ so the relative error induced by (120) is quite low. The error of the approximation in (120) can become significant in in regions of strong anomalous absorption. On the other hand, this technique is not expected to be applied in these regimes, as systems of interest are usually designed to operate away from absorption features. It is also sufficient to consider only first order variation of atmospheric quantities. The first order Taylor-Series expansion of N with respect to the atmospheric variables is

$$N(T + \Delta T, P + \Delta P, e_v, \Delta e_v) = N(T, P, e_v) + \frac{\partial N}{\partial T} \Delta T + \frac{\partial N}{\partial P} \Delta P + \frac{\partial N}{\partial e_v} \Delta e_v + C. \tag{124}$$

For turbulence induced variations of T, P, e_v atmospheric deviations are quite small compared to their mean value, amounting to changes of less than $^1/_{1000}$ over distances of a meter. Because the partials, $\partial N/\partial T$, $\partial N/\partial P$, and $\partial N/\partial e_v$ are also small (typically between 1 and 10) compared to the typical values of $N \approx 250$, this

approximation holds well for most wavelengths.

In the following equations, there are two forms of temperature. Upper case T indicates temperature measured in Kelvin, and lower case t indicates temperature in degrees Centigrade. In Section 2.5 three expressions for finding the partials are given,

$$\frac{\partial N}{\partial p} = \frac{N_0}{p} - \frac{N}{Z}\frac{dZ}{dp} \tag{125}$$

$$\frac{\partial N}{\partial e_v} = N\left[\left(1 - \frac{N_0}{N}\right)\frac{1}{x_w} - \frac{dZ}{dx_w}\frac{1}{Z}\right]\frac{f}{p} \tag{126}$$

$$\frac{\partial N}{\partial T} = -N\left(\frac{1}{T} + \frac{dZ}{dT}\frac{1}{Z}\right). \tag{127}$$

Here again, p is pressure in Pascals (causing the pressure units of (125) to also be Pascals) and the rest of this work uses millibars. In order to account for this, the chain rule is used

$$\frac{\partial N}{\partial P} = \frac{\partial N}{\partial p}\frac{dp}{dP} = \frac{\partial N}{\partial P}100. \tag{128}$$

The derivatives of compressibility with respect to pressure are

$$\frac{dZ}{dp} = \frac{p}{T^2}(d + ex_w^2) + \frac{Z-1}{p}, \tag{129}$$

$$\frac{dZ}{dT} = \frac{1 - Z - \left(\frac{p}{T}\right)^2(d + ex_w^2)}{T} - \frac{p}{T}\left[a_1 + 2a_2 + x_w(b_1 + c_1x_w)\right], \tag{130}$$

$$\frac{dZ}{dx_w} = \frac{P}{T^2}\left\{2ePx_w - T\left[b_0 + b_1t + 2x_w(c_0 + c_2t)\right]\right\}. \tag{131}$$

The term f/P is given by

$$\frac{f}{p} = \frac{\alpha + \beta p + \gamma t^2}{p}. \tag{132}$$

The compressibility of moist air is given by

$$Z = 1 - \frac{P}{T}\left[a_0 + a_1t + a_2t^2 + (b_0 + b_1t)x_w + (c_0 + c_1t)x_w^2\right] + \left(\frac{P}{T}\right)^2(d + ex_w^2). \tag{133}$$

Which make use of the following constants:

a_0	a_1	a_2
$1.58123 \times 10^{-6} KPa^{-1}$	$-2.9331 \times 10^{-8} Pa^{-1}$	$1.1043 \times 10^{-10} K^{-1} Pa^{-1}$
b_0	b_1	c_0
$5.707 \times 10^{-6} KPa^{-1}$	$-2.051 \times 10^{-8} Pa^{-1}$	$1.9898 \times 10^{-4} KPa^{-1}$
c_1	d	e
$-2.376 \times 10^{-6} Pa^{-1}$	$1.83 \times 10^{-11} K^2 Pa^{-2}$	$-0.765 \times 10^{-8} K^2 Pa^{-2}$

7.2 Higher Order Numerical Differencing

The method of undetermined coefficients presented here as based on the Air Force Institute of Technology (AFIT) Math 674 Numerical Analysis for Scientific Computing course notes.

This approach is based on the more general method of undetermined coefficients which can be used to find higher order derivatives, or (as in this case) higher order approximations of lower-order derivatives. In this case, a third order approximation of the first derivative. Starting with a function , $f(x)$, which has been sampled at several points, x_1, x_2, x_3, x_4, the goal is to have a solution of the form

$$f'(x) = a_1 f(x_1) + a_2 f(x_2) + a_3 f(x_3) + a_4 f(x_4) + O(h^4). \tag{134}$$

Here the spacing between sample points is not constant, so h will be the largest interval between points. A Taylor series expansion of $f(x_i)$ can be taken around x for each of the x_i

$$f(x_i) = f(x) + (x_i - x) f'(x) + \frac{(x_i - x)^2}{2} f''(x) + \frac{(x_i - x)^3}{6} f'''(x) + O((x_i - x)^4). \tag{135}$$

This form has the desired value $f'(x)$ in it. Applying (134) to each expansion of

$f(x_1), f(x_2), f(x_4), f(x_3)$, and grouping by constant terms gives

$$\begin{aligned} f'(x) =& a_1 f(x) & +a_2 f(x) & & +a_3 f(x) & & +a_4 f(x) + \\ & a_1 f'(x) h_1 & +a_2 f'(x) h_2 & & +a_3 f'(x) h_3 & & +a_4 f'(x) h_4 + \\ & a_1 f''(x) \frac{h_1^2}{2} & +a_2 f''(x) \frac{h_2^2}{2} & & +a_3 f''(x) \frac{h_3^2}{2} & & +a_4 f''(x) \frac{h_4^2}{2} + \\ & a_1 f'''(x) \frac{h_1^3}{6} & +a_2 f'''(x) \frac{h_2^3}{6} & & +a_3 f'''(x) \frac{h_3^3}{6} & & +a_4 f'''(x) \frac{h_4^3}{6} + O(h^4). \end{aligned} \tag{136}$$

Here $h_i = x - x_i$. (136) will be satisfied if all the rows but the second sum to zero. This can be expressed as a linear equation,

$$\begin{bmatrix} 1 & 1 & 1 & 1 \\ h_1 & h_2 & h_3 & h_4 \\ \frac{h_1^2}{2} & \frac{h_2^2}{2} & \frac{h_3^2}{2} & \frac{h_4^2}{2} \\ \frac{h_1^3}{6} & \frac{h_2^3}{6} & \frac{h_3^3}{6} & \frac{h_4^3}{6} \end{bmatrix} \begin{bmatrix} a_1 \\ a_2 \\ a_3 \\ a_4 \end{bmatrix} = \begin{bmatrix} 0 \\ 1 \\ 0 \\ 0 \end{bmatrix} \tag{137}$$

Which gives the coefficients for (134).

7.3 The Stability Correction

In 2014, an attempt was made to correct the difference between the radar C_n^2 and scintillometer C_n^2 based on the amount of refractive bending in the beam, and the wavelength correction. In practice, this method worked, but is not useful because the corrective parameters (described later) are highly dependent on the location and time of year. The work and reasoning is presented here, as the section does highlight the importance of ground clutter as a noise source.

In the remainder of this section, unless otherwise noted, C_n^2 will refer to the $\log_{10} C_n^2$ value obtained from NEXRAD reflectivity using (10). This is done to clean up notation. The difference between the wavelength corrected radar C_n^2 and the

scintillometer C_n^2 is $\Delta C_{n,1}^2 = C_{n,scint}^2 - C_{n,radar}^2$. All differences as in ΔC_n^2 are differences between the $\log_{10} C_n^2$ values. Data used here are from 6-10 October, 2013.

A relationship was sought between the difference in NEXRAD and Scintillometer data and the atmospheric parameters, dn/dz and dT/dz. dT/dz is approximated from finite differences in T from the GFS forecast. To calculate dn/dz, a modified form of (45) was used,

$$\frac{dn}{dz} = \frac{dT}{dz}\left(\frac{\partial n}{\partial T} + \frac{\partial n}{\partial P'}\frac{dP'}{dT} + \frac{\partial n}{\partial e_v'}\frac{de_v'}{dT}\right). \tag{138}$$

The different terms used in this form are presented in [9]. The advantage of this form is that it allows for the wavelength correction to be applied without having to know any of the local gradients, only the local T, P', and e_v'. The disadvantage is that the assumption that deviations of pressure and vapor pressure correlate to temperature variation is likely to be a poor one. It should be noted that this is no longer the preferred method for finding refractive bending as it is still primarily temperature based, and ignores contributions from P' and e_v'. A better method is to use the partial derivatives as calculated by LEEDR, and the vertical gradients of P', e_v' and T. Note that for refractive bending, hydrostatic and adiabatic effects are included because the total refraction of the beam is desired. The omission of dP'/dz is not expected to impact these results as the variation in dn/dz is important, and the vertical pressure gradient is dominated by the essentially constant hydrostatic balance gradient. Omission of de_v'/dz may have impacted the data presented here somewhat.

ΔC_n^2 and dn/dz are both shown in Figure 78. In order to help with the statistical comparisons, all the values are centered around 0 and normalized. This allows dn/dz to be directly related to the radar beam height. Positive values indicate sub-refraction (the radar beam is higher than normal), and negative values indicate super-refraction

(the radar beam is lower than normal).

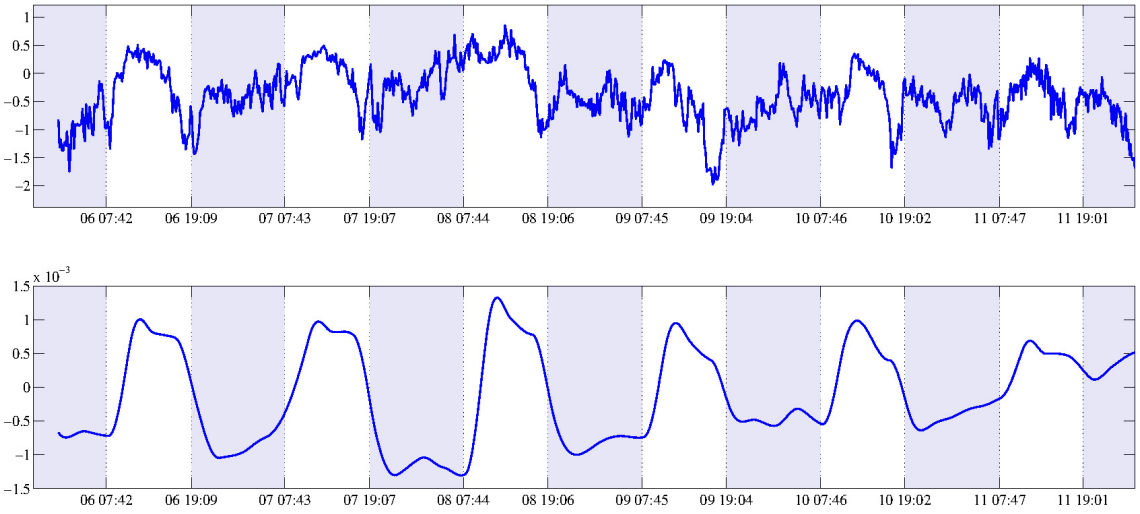

Figure 78. Comparison of $\Delta C_n^2 = C_{n,scint}^2 - C_{n,radar}^2$ (Top) and the zero-mean stability parameter: $dn/dz - \langle dn/dz \rangle$ (Bottom) vs local time. The mean was removed to aid in visualizing whether the beam is refracted down more than normal (< 0) or if it is refracted up more than normal (> 0).

The similarity noted between ΔC_n^2 and dn/dz led to development of the stability correction. As shown below, this correction would also attempt to use dT/dz to provide further correction. Meteorological *stability* refers to the deviation of the vertical temperature gradient from neutral buoyancy. In a stable atmosphere, the temperature drops slowly with height (or increases in some cases) so that an air parcel which is displaced up cools adiabatically, becomes cooler than the surrounding air, and sinks back down. In an unstable atmosphere, the temperature drops quickly with height so when an air parcel is displaced up, it remains warmer than the surrounding air despite the cooling due to expansion. Because it is warmer, buoyant forces accelerate the air parcel in the upward direction. Since stability depends on the same factors as the gradient terms dn/dz and dT/dz, the method of adjusting radar C_n^2 based on these gradients was named a *stability correction*. This correlation raises questions

about why each of the gradients affect noise in the radar. Two possible mechanisms are ground clutter, which is directly dependent on dn/dz and turbulence production via PBL dynamics which are dependent on the atmospheric stability.

Correcting the radar C_n^2 measurements was attempted with three functions based on the behavior of dn/dz and dT/dz. After correction, the scintillometer C_n^2 was estimated well (to logarithmic accuracy). While an physical explanation could be made for the first two corrections, the third was based on observed residual differences. In the end, these fits are specific to this data set, and attempts to use these corrections on data taken at other times or locations met with poor results. For this reason, these methods were abandoned.

The stability correction was developed after examining corrections derived from several atmospheric variables: index of refraction, humidity, wind speed, pressure and temperature. It was seen that while all of these parameters correlated with $\Delta C_{n,1}^2$ to some degree, the greatest agreement came when correcting $\Delta C_{n,1}^2$ based on dn/dz, dT/dz, and the time rate of change of dn/dz. By plotting $\Delta C_{n,1}^2$ as a function of dn/dz a quadratic dependance could be seen (Figure 79).

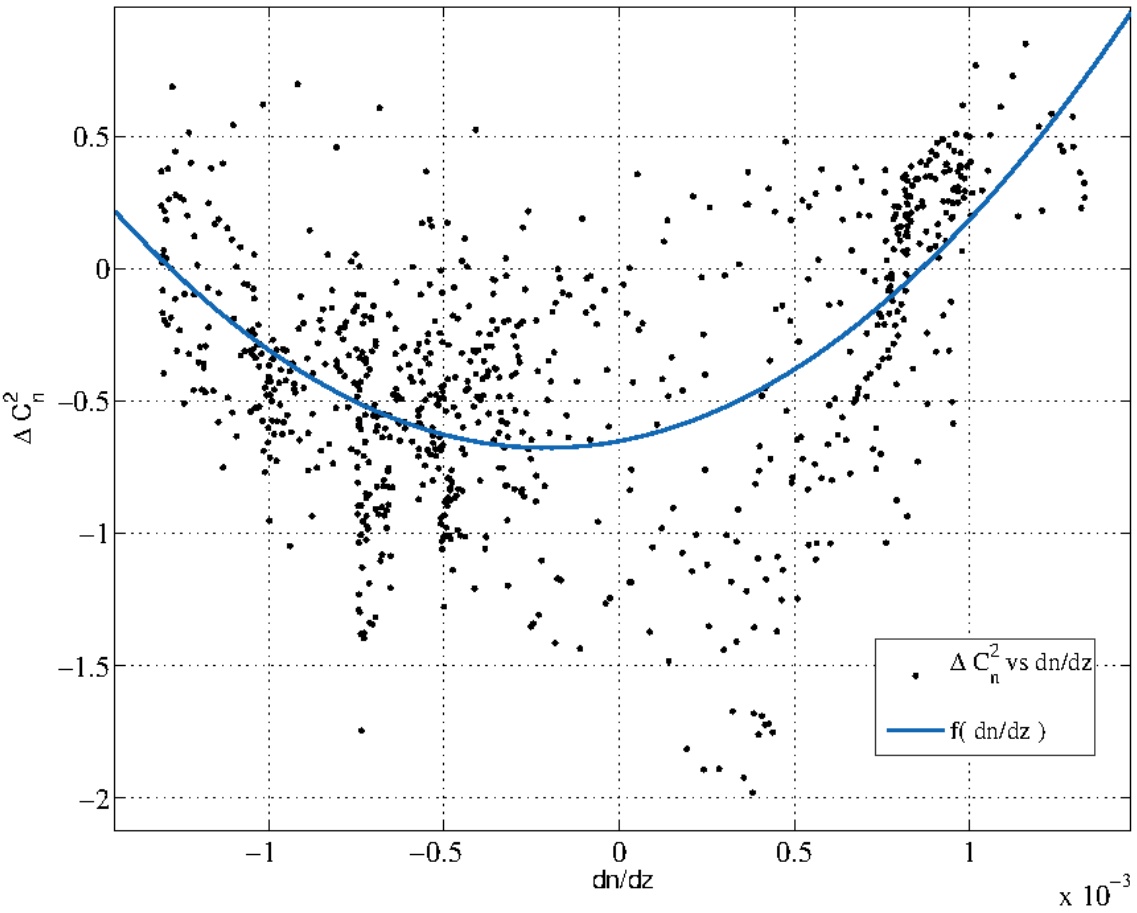

Figure 79. Scatter plot of $\Delta C_{n,1}^2$ as a function of dn/dz. As dn/dz increases, the beam is expected to go higher. Note that most of the time, the radar is over-estimating the turbulence ($\Delta C_{n,1}^2 < 0$) unless the beam is relatively high.

Further improvement can be found by then computing a new

$$\Delta C_{n,2}^2 = \Delta C_{n,1}^2 - VGC_1 \left(\frac{dn}{dz} \right) \tag{139}$$

where $VGC_1(dn/dz)$ is the 1^{st} Vertical Gradient Correction (VGC) based on dn/dz. The next correction, VGC_2 was found by comparing $\Delta C_{n,2}^2$ to dn/dz's time rate of change, $d/dt(dn/dz) \equiv d\dot{n}/dz$. Plotting this ΔC_n^2 as a a function of $d\dot{n}/dz$ (Figure 80)

allows a second quadratic relationship to be seen, and at this point is defined

$$\Delta C^2_{n,3} = \Delta C^2_{n,2} - VGC_2 \left(\frac{d\dot{n}}{dz} \right). \tag{140}$$

A final VGC_3 was defined and related to dT/dz, but the correlation in this was extremely weak, and no good physical explanation was given for to relationship. It is believed that this relationship was happenstance.

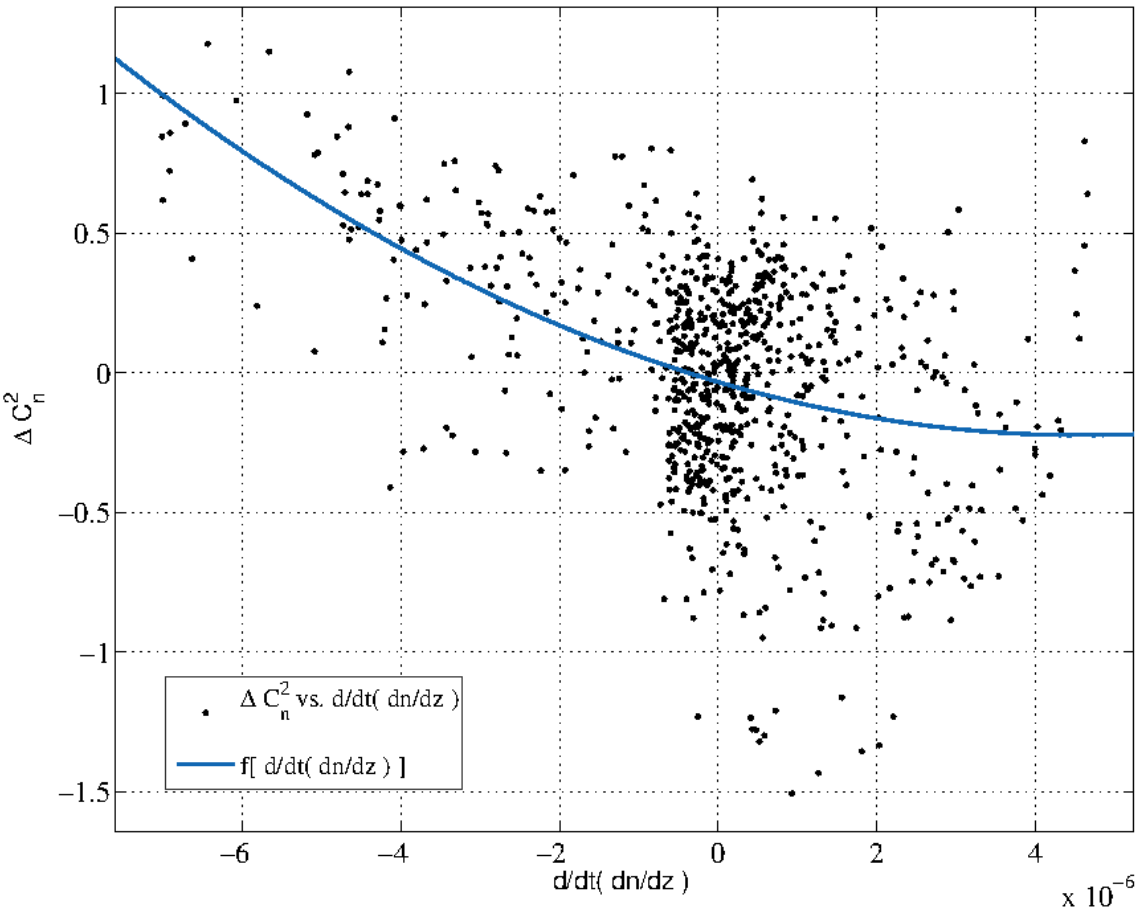

Figure 80. Scatter plot of $\Delta C^2_{n,2}$ as a function of $d\dot{n}/dz$. It can be seen that there is very different behavior for $d\dot{n}/dz > 0$, $d\dot{n}/dz > 0$, and $d\dot{n}/dz \approx 0$.

The relationship of the radar signal to dn/dz has reasonable phenomenological basis. Increased ground clutter in radar measurements is the result of variation of the

path of the radar's main beam and its side-lobes in response to changes in dn/dz. The radar beam, to first order, bends downward from a straight ray path creating an arc with a curvature radius of about four-thirds of the Earth's radius [16]. Variations in the vertical temperature and vapor pressure profiles cause the radar beam curvature to deviate from its typical arc. When the magnitude of dn/dz is reduced, the radar beam is said to be *sub-refracted* resulting in a greater height of the beam. Conversely, when the magnitude of dn/dz is greater than normal, the beam is *super-refracted* bending the beam down toward the ground. Like the main lobe, the diffraction-induced side-lobes of the radar are super-refracted or sub-refracted. This vertical deviation of the lobes changes the amount of energy that reflects off the ground and back into the radar. As a result, the apparent energy in the radar's main beam can be increased by super-refraction of the beam. By tracking the relative changes in dn/dz, the amount of ground returns due to super-refraction were corrected to some degree. This trend can be seen in Figures 78 and 79, with the exception that for very negative dn/dz (strong bending, recall $dn/dz < 0$) the radar begins to do a better job estimating C_n^2 again. During these times, the PBL is very stable which affects the thickness of the PBL as well as Turbulent Kinetic Energy (TKE) production. These processes are described next and are believed to be counteracting the increased ground clutter.

Vertical stability may also affect $\Delta C_{n,1}^2$. PBL stability affects the production or loss of TKE and the overall depth of the PBL. It is apparent from Figure 20 that the upper portion of the radar beam is around one kilometer above the ground. In a stable atmosphere, the potential temperature increases with height. Under these conditions, buoyant forces are reduced and TKE production is restricted. This creates a shallow, stable PBL that may be less than $500m$ in depth with a "residual" neutrally buoyant layer from the previous afternoon above it to a depth of approximately $1.5km$ [66]. Under these conditions, the radar beam and side-lobes are refracted strongly. While

the ground clutter does increase the radar return, the boundary layer is relatively thin, so much of the radar's main beam would be in the residual layer. In this layer turbulence is significantly weaker, so the radar's C_n^2 will be reduced compared with the scintillometer's. This explains the behavior on the left side of Figure 79 where ΔC_n^2 returns to zero despite increased ground clutter. As night progresses, C_n^2 tends to increase steadily as wind speeds increase and greater shear production is present in the TKE budget. Looking at the top plot (ΔC_n^2 vs. time) of Figure 78, this pattern can be readily seen as ΔC_n^2 tends to head toward zero during several of the nights.

It was noted that there are different behaviors of $\Delta C_{n,2}^2$ depending on whether dn/dz is increasing, constant, or decreasing over time. This behavior may suggests that TKE dynamics are affecting $\Delta C_{n,2}^2$. For constant dn/dz, $\Delta C_{n,2}^2 \approx 0$. It was apparent that $\Delta C_{n,2}^2$ was significant when the local temperature gradient was transitioning between stable and unstable conditions. At dawn, heating of the Earth's surface by the sun causes dn/dz to increase toward 0 as the lower layer of the PBL becomes warmer and the atmosphere becomes more unstable (Figure 78). During this time, the radar beam begins to rise and receives less ground clutter decreasing its apparent C_n^2. Concurrently, the buoyant production of TKE begins to increase C_n^2 measured by both instruments and thickens the PBL. During this time, ΔC_n^2 goes through zero to its daytime value where the radar is slightly underestimating the turbulence. While both the radar and scintillometer C_n^2 are gradually increasing, $\Delta C_{n,2}^2$ approaches a constant value for positive $d\dot{n}/dz$. This indicates a lag between the response of both instruments. This could be a combination of phenomenological effects based on the location of the scintillometer path and radar beam, as well as the unknown lag between when the NEXRAD made its measurement, and when its measurement volumes were compressed and time-stamped.

As dusk approaches and the angle of the sun decreases, the heating of the ground

slows down. During this time, dn/dz becomes more negative and the radar beam begins to bend down toward the ground. Before the ground clutter becomes significant, there is a large drop in the scintillometer C_n^2 but only a slight roll-off in the radar C_n^2. At this time the PBL is quickly becoming stable and buoyant forces now damp vertical motions, reducing the TKE. Evidence of this process can be seen in the left side of Figure 80 where $\Delta C_{n,2}$ increases with $d\dot{n}/dz$.

As mentioned, the fits shown here did not translate well to other times and locations. In addition, examination of the C_n^2 volumes over time show that NEXRAD systems often see elevated nocturnal C_n^2. It may be that part of this effect is the increased ground clutter. However, without reflections off turbulent eddies, it is difficult to explain the behavior in Figures 79 and 80. The shapes of these correlations suggest that a portion of the reflected energy, at least, is due to scattering off turbulent eddies and another portion is ground clutter.

Bibliography

1. Randall J. Allis and Billy D. Felton. Numerical simulations of optical turbulence using an advanced atmospheric prediction model: Implications for adaptive optics design. In *Proceedings of the Advanced Maui Optical and Space Surveillance Technologies Conference*, Wailea, Hawaii, September 9-12 2014.

2. Randall J. Allis and Billy D. Felton. Validation of optical turbulence simulations from a numerical weather prediction model in support of adaptive optics design. In *International Conference on Space Optical Systems and Applications (ICSOS)*, pages S2–3, Kobe, Japan, May 7-9 2014.

3. R. W. Astheimer. The remote detection of clear air turbulence by infrared radiation. *Applied Optics*, 9(8):1789–1797, August 1970.

4. Santasri Basu, Lee Burchett, Jack McCrae, and Steven Fiorino. Comparison of the path-weighted C_n^2 derived from time-lapse imagery and weather radar. In *Proceedings of the 2016 IEEE Aerospace Conference*, 2016. Accepted Paper 2372 for Session 5.04 Atmospheric Turbulence: Propagation, Phenomenology, Measurement, Mitigation.

5. A. Berk, C. P. Anderson, P. K. Acharya, L. S. Bernstein, L. Muratov, J. Lee, M. Fox, S. M. Adler-Golden, J. H. Chetwind, M. L. Hoke, R. B. Lockwood, J. A. Gardner, T. W. Cooley, C. C. Borel, P. E. Lewis, and E. P. Shettle. Modtran 2006 update. In *Proc. SPIE*, volume 6233, 2006.

6. Carmelo Peter Bonsignore and Charlie Bellamy. Daily activity and flight behaviour of adults of capnodis tenebrionis (coleoptera: Buprestidae). *European Journal of Entomology*, 104(3):425–431, 2007.

7. Robert A. Briers, Helen M. Cariss, and John H. R. Gee. Flight activity of adult stoneflies in relation to weather. *Ecological Entomology*, 28(1):31–40, 2003.

8. Lee Burchett. Turbulence measurement in the atmospheric boundary layer using cellular telephone signals. Master's thesis, Air Force Institute of Technology, March 2012.

9. Lee R. Burchett and Steven T. Fiorino. Wavelength correction of refractivity variation measurements. *Opt. Express*, 21(26):31990–31997, Dec 2013.

10. Lee R. Burchett, Steven T. Fiorino, and Matthew Buchanan. Automation of C_n^2 profile extraction from weather radar images. In Linda M. Wasiczko Thomas; Earl J. Spillar, editor, *Atmospheric Propagation IX*, volume 8380, May 7 2012.

11. Cedar Lake Ventures, Inc. Weatherspark beta, averages. Website, November 2015. `https://weatherspark.com/`.

12. N. Blaustein & C. G. Christoddoulou. *Radio Propagation and Adaptive Antennas for Wireless Communication Links*. John Wiley & Sons, Inc., Hoboken, New Jersery, 2007.

13. Philip E. Ciddor. Refractive index of air: new equations for the visible and near infrared. *Applied Optics*, 35(9):1566–1573, 20 March 1996.

14. S. F. Clifford and L. Lading. Monostatic diffraction-limited lidars: the impact of optical refractive turbulence. *Appl. Opt.*, 22(11):1696–1701, Jun 1983.

15. J. Jean Cohen. Demonstration and verification of a broad spectrum anomalous dispersion effects tool for index of refraction and optical turbulence calculations. Master's thesis, Air Force Institute of Technology, March 2009.

16. R. J. Doviak and D. S. Zrnic. *Doppler Radar and Weather Observations*. Academic Press, Inc., San Diego, California, 1993.

17. J. A. Elliott. Microscale pressure fluctuations measured within the lower atmospheric boundary layer. *Journal of Fluid Mechanics*, 53:351–384, 5 1972.

18. Patrick Feneyrou, Jean-Claude Lehureau, and Hervé Barny. Performance evaluation for long-range turbulence-detection using ultraviolet lidar. *Appl. Opt.*, 48(19):3750–3759, Jul 2009.

19. S.T. Fiorino, R.M. Randall, A.D. Downs, R.J. Bartell, M.J. Krizo, and S.J. Cusumano. Three-dimensional optical turbulence assessments from doppler weather radar for laser applications. In *6th DEPS Systems Symposium*, March 2011.

20. Steven T. Fiorino. Satellite and radar measurement of C_T^2, C_n^2, and C_v^2. In *Imaging and Applied Optics Conference*, volume Propagation through and Characterization of Distributed Volume Turbulence (pcDVT), Seattle, WA, 13-17 July 2014 Invited.

21. Steven T. Fiorino, Richard J Bartell, Matthew J. Krizo, Brandon T. McClung, J. Jean Cohen, Robb M. Randall, and Salvitore J Cusumano. Broad-spectrum optical turbulence assessments from climatological temperature, pressure, humidity, and wind. *Journal of Directed Energy*, 3:223–228, Winter 2009.

22. Steven T Fiorino and Robb M Randall. Validation of a uv-to-rf high-spectral-resolution atmospheric boundary layer characterization tool. *J. Appl. Meteor. Climatol.*, 53:136–156, 2014.

23. Sidney A. Gauthreaux Jr. and Carroll G. Belser. Displays of bird movements on the wsr-88d: Patterns and quantification. *Wea. Forecasting*, 13:453–464, 1998.

24. Joseph W. Goodman. *Introduction to Fourier Optics, Third Edition*. Roberts and Company, Englewood, Colorado, 2005.

25. E. Gossard. Power spectra of temperature, humidity and refractive index from aircraft and tethered balloon measurements. *IRE Transactions on Antennas and Propagation*, 8(2):186–201, March 1960.

26. Kenneth R. Hardy, David Atlas, and Kenneth M. Glover. Multiwavelength backscatter from the clear atmosphere. *Journal of Geophysical Research*, 71(6):1537–1552, 1966.

27. R. J. Hill, S. F. Clifford, and R. S. Lawrence. Refractive-index and absorption fluctuations in the infrared caused by temperature, humidity, and pressure fluctuations. *J. Opt. Soc. Am.*, 70(10):1192–1205, Oct 1980.

28. Reginald J. Hill. Comparison of scintillation methods for measuring the inner scale of turbulence. *Appl. Opt.*, 27(11):2187–2193, Jun 1988.

29. Richard B. Holmes and Williams M. Hughes. Pupil plane imager for estimation of turbulence over long horizontal paths. *Appl. Opt.*, 46(23):5979–5986, Aug 2007.

30. James R. Holton and Gregory J. Hakim. *An Introduction to Dynamic Meteorology Fifth Edition*. Academic Press, Waltham, Massachusetts, 2013.

31. Jason W. Horn and Thomas H. Kunz. Analyzing NEXRAD doppler radar images to assess nightly dispersal patterns and population trends in brazilian free-tailed bats (tadarida brasiliensis). *Integrative and Comparative Biology*, 48(1):24–39, 2008.

32. A. Ishimaru. *Wave Propagation and Scattering in Random Media*. Academic Press, New York, New York, 1978.

33. Mark Z. Jacobson. *Fundamentals of Atmospheric Modeling*. Cambridge University Press, New York, second edition edition, 2005.

34. Joseph P. Gerrity Jr., Thomas L. Black, and Russell E. Treadon. The numerical solution of the mellor-yamada level 2.5 turbulent kinetic energy equation in the eta model. *Mon. Wea. Rev.*, 122:1640–1646, 1994.

35. Zhao Junwei, Qiang Xiwen, Feng Shuanglian, and Zhang ZhiGang. Measurement of atmospheric refractive index structure constant near ground based on can bus. In *Electronic Measurement Instruments (ICEMI), 2011 10th International Conference on*, volume 2, pages 270 –273, aug. 2011.

36. A.N. Komolgorov. The local structure of turbulence in incompressible viscous fluid for very large reynolds' numbers. *Dokl. Akad. Nauk SSSR*, 30(4), 1940. Translation from Proc. R. Soc. Lond. A (1991) 434, 9-13.

37. A.N. Komolgorov. Dissipation of energy in locally isotropic turbulence. *Dokl. Akad. Nauk SSSR*, 32(1), 1941. Translation from Proc. R. Soc. Lond. A (1991) 434, 15-17.

38. J. Kondo, O. Kanechika, and N. Yasuda. Heat and momentum transfers under strong stability in the atmospheric surface layer. *J. Atmos. Sci*, 35:1012–1021, 1978.

39. Jean-Pierre Laussade, Amnon Yariv, and Jack Comly. Optical communication through random atmospheric turbulence. *Appl. Opt.*, 8(8):1607–1611, Aug 1969.

40. Jie Li, F. J. Lopez-Dekker, T. Ince, and S.J. S. J. Frasier. Volume-imaging uhf radar measurement of atmospheric turbulence. In *Geoscience and Remote Sensing Symposium, 2000 Proceedings*, volume 6, pages 2813 –2815, 2000.

41. Wang Li-Li, Xi Xiao-Li, and Huang Lei. Naturally derived turbulence measurement procedures. In *Antennas, Propagation EM Theory, 2006. ISAPE '06. 7th International Symposium on*, pages 1 –4, oct. 2006.

42. Lockheed Martin Corporation Ocean Radar and Sensor Systems. NEXRAD WSR-88D. Website, October 2015. `http://www.qsl.net/n9zia/pdf/wsr-88d.pdf`.

43. Edward N. Lorenz. Deterministic nonperiodic flow. *J. Atmos. Sci.*, 20:130–141, 1963.

44. M. K. Mazumder and D. L. Wankum. SNR and spectral broadening in turbulence structure measurement using a CW laser. *Appl. Opt.*, 9(3):633–637, Mar 1970.

45. David Meier. *Operational Exploitation of Satellite-Based Sounding Data and Numerical Weather Prediction Models for Directed Energy Applications*. PhD thesis, Air Force Institute of Technology, December 2015.

46. David C. Meier and Steven T. Fiorino. Comparison of index of refraction structure functio (C_n^2) profiles derived from polar-orbitiong satellite data and numerical weather prediction models". In *Propagation through and Characterization of Distributed Volume Turbulence (pcDVT)*, Arlington, VA, 7-11 June 2015. Imaging and Applied Optics Conference.

47. Sorana Melian, Kolja Brix, Siegfried Mller, and Gero Schieffer. Space-filling curve techniques for parallel, multiscale-based grid adaptation: Concepts and applications. In Alexander Kuzmin, editor, *Computational Fluid Dynamics 2010*, pages 591–597. Springer Berlin Heidelberg, 2011.

48. George L. Mellor and Tetsuji Yamada. Development of a turbulence closure model for geophysical fluid problems. *Reviews of Geophysics*, 20(4):851–875, 1982.

49. NASA Tropical Rainfall Measurement Mission. Radar software library. Website, August 2011. `http://trmm-fc.gsfc.nasa.gov/trmm_gv/software/rsl/`.

50. National Oceanic and Atmospheric Administration. Hdss access system. Website, October 2015. `http://www.ncdc.noaa.gov/has/HAS.DsSelect`.

51. NOAA Radar Operations Center. WSR-88D build 10/super resolution level II FAQs. Wedbsite, October 2015. http://www.roc.noaa.gov/wsr88d/buildinfo/build10faq.aspx.

52. A. M. Obukov. Structure of the temperature field in turbulent flow. *Ivz. Akad. Nauk SSSR*, 13(58), 1949. Translation 334, July 1969 Dept. of Army, Fort Detrick, MD.

53. The Cornell Lab of Ornithology. Birdcost, bird migration forecasts in real-time. Website, September 2015. http://birdcast.info/.

54. Y. P. Ostrovsky, F. J. Yanovsky, and H. Rohling. Turbulence and precipitation classification based on doppler-polarimetric radar data. In *Radar Symposium, 2006. IRS 2006. International*, pages 1 –4, may 2006.

55. R.K. Peng, C.R. Fletcher, and S.L. Sutton. The effect of microclimate on flying dipterans. *International Journal of Biometeorology*, 36(2):69–76, 1992.

56. Glen P. Perram, Salvatore J. Cusumano, Robert L. Hengehold, and Steven T. Fiorino. *An Introduction to Laser Weapon Systems*. Directed Energy Professional Society, 2010. 473 pp.

57. Grant W. Petty. *A First Course in Atmospheric Radiation*. Sun Dog Publishing, Madison, Wisconson, second edition, 2006.

58. G. S. Poulos, W. Blumen, D. C. Fritts, J. K. Lundquist, J. Sun, S. P. Burns, C. Nappo, R. Banta, R. Newsom, J. Cuxart, E. Terradellas, B. Balsley, and M. Jensen. Cases-99: A comprehensive investigation of the stable nocturnal boundary layer. *Bull. Amer. Meteor. Soc.*, 83:555–581, 2002.

59. Ronald E. Rinehart. *Radar for Meteorologists*. Rinehart Publishing, fifth edition, 2004.

60. S.M. Rytov, Yu.A.Kravtsov, and V.I. Tatarskii. *Principals of Statistical Radiophysics*. Springer-Verlag, Berlin, Heidelberg, 1989.

61. P. G. Saffman. *Vortex Dynamics*. Cambridge University Press, New York, NY, 1995.

62. Scintec AG, Wilhelm-Maybach-Str. 14, 72108 Rottenburg, Germany. *Scintec Boundary Layer Scintillometer Hardware Manual: BLS450, BLS900, BLS2000*, 2.03 edition, April 2009. www.scintec.com.

63. Joseph Sela. The implementation of sigma pressure hybrid coordinate into the gfs. Technical report, U.S. Department of Commerce, National Oceanic and Atmospheric Administration, National Wether Service, National Centers for Environmental Prediction, July 2009. http://www.emc.ncep.noaa.gov/officenotes/newernotes/on461.pdf.

64. Smithsonion National Museum of Natural History. Birds: National bird collection. Website, July 2015. http://vertebrates.si.edu/birds/.

65. Jack A Stone and Jay H Zimmerman. NIST physical measurement labratory, engineering metrology toolbox. website, November 2015. http://emtoolbox.nist.gov/Wavelength/Documentation.asp#Introduction.

66. R. B. Stull. *An Introduction to Boundary Layer Meteorology*. Kluwer Academic, 1988. 688 pp.

67. V. I. Tatarski. *Wave Propagation in a Turbulent Medium*. Dover Publications Inc., New York, New York, 1967.

68. V. Tatarskii. The effects of the turbulent atmosphere on wave propagation. translation, NOAA, Washington D.C., 1971. Israel Program for Scientific Translations.

69. G. I. Taylor. Diffusion by continuous movements. *Proceedings of the London Mathematical Society*, s2-20(1):196–212, 1922.

70. S. M. Torres and C. D. Curtis. Design considerations for improved tornado detection using super-resolution data on the nexrad network. In *Third European Conf. on Radar Meteorology and Hydrology (ERAD)*, Barcelona, Spain, Copernicus, 2006.

71. S. M. Torres and C. D. Curtis. Initial implementation of super-resolution data on the nexrad network. In *23rd Conf. on Interactive Information Processing Systems (IIPS) for Meteorology, Oceanography, and Hydrology*, San Antonio, TX, 2007.

72. National Oceanic U.S. Department of Commerce and Global Systems Division Atmospheric Administration, Earth System Research Laboratory. Rapid refresh (RAP). Website, November 2015. http://rapidrefresh.noaa.gov/.

73. U.S. Department of Transportation Federal Aviation Administartion. Faa wildlife strike database. Website, Feb 2015. http://wildlife.faa.gov/.

74. Marie-Thérèse Velluet, Mikhail Vorontsov, Piet Schwering, Gabriele Marchi, Stephane Nicolas, and Jim Riker. Turbulence characterization and image processing data sets from a NATO RTO SET 165 trial in Dayton, Ohio. In *Atmospheric Propagation IX Proc. of SPIE*, number 1 in 83800J, 2012.

75. A. J. Viterbi. *CDMA:Principals of Spread Spectrum Communication (1 ed.)*. Prentice Hall, 1995.

76. Melvin M. Weiner. Atmospheric turbulence in optical surveillance systems. *Appl. Opt.*, 6(11):1984–1991, Nov 1967.

77. Raphael Z. Yahel. Turbulence effects on high energy laser beam propagation in the atmosphere. *Appl. Opt.*, 29(21):3088–3095, Jul 1990.

78. Aziz Ziad, Matthias Schöck, Gary A. Chanan, Mitchell Troy, Richard Dekany, Benjamin F. Lane, Julien Borgnino, and François Martin. Comparison of measurements of the outer scale of turbulence by three different techniques. *Appl. Opt.*, 43(11):2316–2324, Apr 2004.

REPORT DOCUMENTATION PAGE

Form Approved
OMB No. 0704–0188

1. REPORT DATE *(DD–MM–YYYY)*	2. REPORT TYPE	3. DATES COVERED *(From — To)*
24–03–2016	Doctoral Dissertation	Jan 2012 — Mar 2016

4. TITLE AND SUBTITLE

Methods for Passive Remote Turbulence Characterization in the Planetary Boundary Layer

5a. CONTRACT NUMBER

5b. GRANT NUMBER

5c. PROGRAM ELEMENT NUMBER

6. AUTHOR(S)

Burchett, Lee R, Dr.

5d. PROJECT NUMBER

5e. TASK NUMBER

5f. WORK UNIT NUMBER

7. PERFORMING ORGANIZATION NAME(S) AND ADDRESS(ES)

Air Force Institute of Technology
Graduate School of Engineering and Management (AFIT/EN)
2950 Hobson Way
WPAFB OH 45433-7765

8. PERFORMING ORGANIZATION REPORT NUMBER

AFIT-ENP-DS-16-M-058

9. SPONSORING / MONITORING AGENCY NAME(S) AND ADDRESS(ES)

High Energy Laser Joint Technology Office
801 University Blvd SE
Albuquerque, NM 87106
(505)248-8209
Tisha.Mangold.ctr@jto.hpc.mil

Air Force Office of Scientific Research
Deep Turbulence MURI
875 N. Randolph St, Ste 325
Arlington Virginia, 22203

10. SPONSOR/MONITOR'S ACRONYM(S)

HEL-JTO, AFOSR

11. SPONSOR/MONITOR'S REPORT NUMBER(S)

12. DISTRIBUTION / AVAILABILITY STATEMENT

DISTRIBUTION STATEMENT A:
APPROVED FOR PUBLIC RELEASE; DISTRIBUTION UNLIMITED.

13. SUPPLEMENTARY NOTES

This work is declared a work of the U.S. Government and is not subject to copyright protection in the United States.

14. ABSTRACT

Several methods are presented which allow for the index of refraction structure function constant, C_n^2, for visible light or IR systems to be determined remotely and passively using a combination of Numerical Weather Prediction, radar, and/or cell phone signals. These methods build on and extend existing techniques and theory, and are shown to be more accurate throughout the year than standard methods. Comparisons are made to $880nm$ scintillometer measurements of C_n^2 in a temperate suburban and a rural high-desert environment.

15. SUBJECT TERMS

Turbulence, Turbulence Characterization, Planetary Boundary Layer Turbulence, Optical Turbulence

16. SECURITY CLASSIFICATION OF:			17. LIMITATION OF ABSTRACT	18. NUMBER OF PAGES	19a. NAME OF RESPONSIBLE PERSON
a. REPORT	b. ABSTRACT	c. THIS PAGE			Dr. S. T. Fiorino, AFIT/ENP
U	U	U	UU	256	19b. TELEPHONE NUMBER *(include area code)* (937) 785-3636 x4506steven.fiorino@afit.edu